A Study of Seismic Performance Evaluation and Design of Suspended Ceiling Systems Based on Shake-Table Tests

진동대 실험을 통한 천장시스템의
내진성능평가와 설계

August 2022

서울대학교 대학원
건축학과

전 수 찬

A Study of Seismic Performance Evaluation and Design of Suspended Ceiling Systems Based on Shake-Table Tests

지도교수 이 철 호

이 논문을 공학박사 학위논문으로 제출함

2022 년 8 월

서울대학교 대학원
건축학과

전 수 찬
Su-Chan Jun

전수찬의 공학박사 학위논문을 인준함
2022 년 8 월

위 원 장	홍 성 걸	(인)
부위원장	이 철 호	(인)
위 원	박 홍 근	(인)
위 원	강 현 구	(인)
위 원	조 봉 호	(인)

Abstract

The seismic design of nonstructural elements has become increasingly important due to the recent advancements in the performance-based design method and the increased awareness of significant economic losses and building functionality interruptions resulting from widespread nonstructural seismic damage. Suspended ceiling systems are one of the most frequently reported earthquake-vulnerable nonstructural elements which have suffered devastating losses during recent major earthquakes. Despite their importance, only limited information is currently available and lacks an effective seismic design method mainly due to its complicated dynamic behavior. In this study, a series of full-scale shake table tests were conducted on various suspended ceiling systems to evaluate their seismic performance and develop effective seismic design methods.

First, studies on the seismic demands on nonstructural elements were performed to analyze the key affecting parameters on the peak floor acceleration (PFA) and the peak component acceleration (PCA). Numerical analyses were implemented using four types of three-dimensional building models to discuss the effects of various structural properties on the PFA and PCA. The limitations of the equivalent static method prescribed by current design codes were addressed through the analysis re-

i

sults obtained from the numerical study and the up-to-date database of the instrumented buildings. The effects of structural and nonstructural nonlinearities were analyzed through shake-table tests conducted using a full-scale 2-story steel moment frame. The relationship between PFA reduction and structural ductility was experimentally evaluated, and the effects of pinching hysteretic behavior of steel rack specimens on the PCA reduction were discussed. The studies on the nonstructural seismic demands were utilized to establish a seismic design strategy for suspended ceiling systems.

Full- and small-scale shake-table tests were performed on suspended ceiling systems to identify their failure mechanism and key engineering parameters, including acceleration amplification, natural frequency, and the critical damping ratio of ceiling systems. Ceiling specimens with various configurations were utilized, and the behavioral characteristics of both direct- and indirect-hung ceiling specimens were addressed. For indirect-hung ceiling specimens, a simplified analytical model was developed to predict their natural frequency, which shows a single and double curvature bending deformation in their orthogonal direction, respectively. Also, damage propagation of the continuous ceiling specimens was discussed using full-scale ceiling specimens installed on an array of two shake tables. Details regarding the large-size test frame fabrication and synchronous shake table excitation were presented. A system-level full-scale ceiling specimen was fabricated, where various nonstructural elements such as partition walls and fire sprinklers were installed. Adverse effects of nonstructural element interactions were analyzed by comparing test results to the ceiling fragility data of previous studies.

Two seismic performance-enhancing methods for ceiling systems were provided, and their performance was experimentally demonstrated. The effectiveness of the proposed ceiling systems was shown through the performance comparison made using the conventional braced ceiling specimen fabricated following current design codes. A seismic design method was provided using grid reinforcements and lateral bracings. The proposed braced ceiling system was proven to be effective in enhancing the seismic performance for ceiling systems with a large area. The grid reinforcements increased the grid in-plane stiffness, thus, improving the restraining effect provided by the braces. A cost-effective friction-added ceiling system was proposed, where a novel rotational friction mechanism was added. The proposed friction damper exhibited a stable hysteretic behavior under various input motions and effectively improved the seismic performance. The friction damping parameters were experimentally calibrated, and a simplified SDOF model with bilinear hysteresis was developed for the friction-added ceiling system. A numerical case study was performed to evaluate the applicability of the proposed friction-added ceiling system based on an extensive dynamic analysis of steel moment frame buildings. Some useful design implications were presented through the analysis of 2-DOF model simulating the behavior of the linear supporting structure and nonlinear friction ceilings. The step-by-step procedure to design the friction-added ceiling system was also recommended.

Contents

List of Figures

xiii

xiv

List of Tables

Chapter 1. Introduction

1.1. Research Background

The seismic design of nonstructural elements has become considerably important due to the recent advancements in the performance-based design method (SEAOC 1995; ASCE 41-17 2017) and the increased awareness of significant economic losses and building functionality interruptions resulting from widespread nonstructural seismic damage. Although nonstructural elements constitute a major portion of the total construction cost (75 – 85 % for commercial buildings, FEMA E74 2011), due design considerations have not yet been given partly because of the complicated nature of the floor motions and the behavioral characteristics of nonstructural elements. For the understanding of the floor motions, the effect of ground motion characteristics and the structural dynamic responses should be fully taken into account. As for nonstructural elements, it is generally hard to predict their behavioral characteristics or seismic capacity because they are fabricated with heterogeneous materials with complicated configurations. Ideally, ensuring the satisfactory seismic performance of nonstructural elements requires explicit consideration of the entire

influence chain composed of input ground motion, supporting structure as well as nonstructural elements.

The failure of suspended ceilings has been one of the most frequently reported nonstructural damages during past earthquakes. Suspended ceilings suffered substantial damage during the recent 2016 Gyeongju and 2017 Pohang earthquakes in Korea, although the primary structural systems were rarely damaged (see Figure 1.1). Owing to their seismic vulnerability, suspended ceiling systems have received significant research attention in recent decades. These studies are usually conducted based on shake table tests rather than numerical studies because of challenges in accurately reflect the interactions between the various members within the ceiling system and the complexity of simulating the highly nonlinear behavior that occurs when the portion of the ceiling system experiences failure (e.g., dislodgement of ceiling panels, disconnection of grid joints).

Several previous studies have already been taken and some important behavioral characteristics of suspended ceilings were reported. These include the process of ceiling damage propagation (ANCO 1983; Ayres and Sun 1973; Badillo-Almaraz et al. 2004; Duozhi et al. 2016), effects of perimeter fixtures (Badillo-Almaraz et al. 2004; Soroushian et al. 2019), and the seismic performance improvement made by

Figure 1.1 Failure of suspended ceilings observed in Gyeongju ($M_w = 5.5$) and Pohang ($M_w = 5.4$) earthquakes in Korea.

the introduction of the ceiling lateral bracings (Gilani 2010; Pantoli et al. 2016; Ryu and Reinhorn 2019a). For the improvement of seismic performance ceiling systems, various types of retrofit or design methods have been proposed (Gilani et al. 2008; Pourali et al. 2017; Brandolese et al. 2019).

Recently, noticeable advancements in numerical studies have been made. Based on either dynamic or static tests, various numerical models for ceiling systems have been proposed. Using the dynamic shake-table tests, simplified numerical models were proposed by Yao (2000), Ryu and Reinhorn (2019b), which can predict the overall response of ceiling systems. Based on component-level static tests, more sophisticated models were proposed by Echevarraia et al. (2012), Zaghi et al. (2016), Motoyui et al. (2014), and Isobe et al. (2017), which can predict the overall damage propagation of ceiling systems.

Despite the improvements made from previous studies, there still remain problems to be solved. First, the studies based on shake-table tests are usually focused on the overall failure modes of the ceilings and their seismic performance, which are frequently reported using the fragility curves. Therefore, the dynamic response of ceiling systems is still not clearly understood. The numerical models are generally too complex to be utilized. Not just because of its mathematical complexity but, more importantly, due to the lack of information about the ceiling systems to utilize the proposed models. In the case of the seismic retrofit methods, focus has been given on developing the method to fully restrain the ceiling movements, which usually requires the strengthening of the whole ceiling grid joints. Because of the complex load path within the ceiling grids and the details of grid joints (generally formed without using bolts or screws), it is hard to design the ceiling based on the rational

engineering procedure, and the most of the proposed design methods ended up with presenting the detailing of the reinforcements. Furthermore, most of the previous studies utilized the direct-hung suspended T-bar ceiling systems, although a variety of ceiling system configurations are used in actual practice.

Therefore, a systematic study is much required to analyze and understand the behavioral characteristics and dynamic properties of typical suspended ceiling systems. Also, an effective seismic retrofit and design strategy for the ceiling systems needs to be developed, which can be applied to ceilings with diverse configurations and be designed based on the rational engineering procedure.

1.2. Scope and Objectives

The main objective of this thesis is to evaluate the seismic performance of suspended ceilings and propose rational seismic design methods based on full-scale shake table tests.

Firstly, studies on the seismic demand on nonstructural elements were conducted to investigate the characteristics of floor motions (or peak floor acceleration) to which the nonstructural elements will be subjected. Based on three-dimensional numerical models, the effects of structural properties on the nonstructural seismic demand were analyzed, and the seismic design forces calculated based on current design codes (ASCE 7 and Eurocode 8) were evaluated. The study on nonstructural seismic demand was followed by a full-scale 2-story steel moment frame shake-table test where the effects of structural and nonstructural nonlinearities were incorporated. These analytical and experimental studies provide the basis for understanding the

key affecting variables influencing the floor motions and assist in generating desirable test input motions for experimental-based performance evaluation of the ceiling systems. Also, they provide useful implications for establishing seismic design strategies for the suspended ceiling systems.

An experimental study on the suspended ceiling system was implemented based on shake-table tests utilizing specimens with various scales. A total of nine ceiling specimens were tested. Full-scale specimens comprising two uniaxially excited full-scale ceiling specimens and one system-level large-scale ceiling specimen installed with various nonstructural elements, which are expected to have possible interaction with the ceiling specimen. Small-scale ceiling specimens were also fabricated to evaluate the multidirectional effects on the ceiling seismic performance. Based on the test results, the seismic performance and key dynamic characteristics were analyzed. Also, a simplified SDOF model was also developed, which can be utilized to predict the natural frequency of suspended ceilings.

Two seismic performance enhancing methods were proposed, a strengthening method through grid reinforcements and a friction-added ceiling system where a novel rotational friction mechanism was utilized. The seismic specimens showed a highly improved seismic performances with only minor ceiling damage observed during all the shake-table input stages. A simplified analytical SDOF model of the friction-added ceiling system was developed and extensive nonlinear time history analyses were performed to illustrate the applicability of the friction ceiling system. Also, some useful design implications were made through the approximate solution obtained for linear-nonlinear 2-DOF system which simulate the behavior of linear supporting structure and nonlinear friction ceiling systems.

1.3. Outline of Dissertation

The contents of this thesis can be categorized into two parts, where the seismic demand on nonstructural elements was evaluated and the seismic design methods for the suspended ceiling systems were presented. Each subject contains two chapters discussing the results obtained from full-scale experimental and analytical studies.

Chapter 2 summarizes the seismic design methods of nonstructural elements provided by current design codes. The key parameters affecting the nonstructural seismic demands were discussed based on the previous studies conducted for evaluating the peak floor acceleration and peak component acceleration. For suspended ceiling systems, the seismic requirements given by ASTM E580 was reviewed with summaries of various experimental and analytical previous studies.

Chapter 3 conducted analytical studies for evaluating the effects of structural dynamic properties on the nonstructural seismic demand. Linear and nonlinear dynamic analyses were performed on a total of four types of three-dimensional numerical models to discuss the effects of structural period, structural irregularities, and nonlinearity on the peak floor acceleration and the peak component acceleration. Evaluation on the seismic forces determined following both the equivalent and dynamic analysis methods provided by ASCE 7 was also conducted.

Chapter 4 provides discussions made from shake-table tests, which were performed using a full-scale 2-story steel moment frame. This study focused on measuring the effects of structural and nonstructural nonlinearity on the peak floor and the peak component accelerations. The relationship between the peak floor acceleration reduction and structural nonlinearity was evaluated through the structure ductility factor measured from each step of the incremental experimental campaign.

Steel rack specimens mounted on access floors were utilized to measure the peak component acceleration. A pronounced pinched hysteretic behavior was observed for all the rack specimens and the consequences resulting from the inferior energy-dissipating capacities were discussed.

Chapter 5 evaluates the seismic performance of suspended ceiling specimens based on a series of shake-table tests. A total of nine full- and small-scale ceiling specimens were utilized, and uniaxial and triaxial excitation tests were performed, respectively. Based on test results, the damage propagation of the ceiling specimens was described, and the key dynamic properties of the ceilings were analyzed. Also, a simplified numerical model to predict the response of the ceiling systems was provided.

Chapter 6 proposed seismic design methods for the suspended ceiling systems. Two seismic design methods were provided, each fabricated using grid reinforcements and rotational friction dampers. The enhanced seismic performances of the ceiling specimens fabricated with the proposed methods were reported. The proposed friction ceiling exhibited a stable hysteretic behavior under various input motions, and an analytical SDOF model was developed for inelastic dynamic analysis. The results of the numerical case study were presented to illustrate the applicability of the friction ceiling system based on extensive time history analyses of steel moment frame buildings.

Chapter 2. Literature Review

2.1. General Characteristics of Nonstructural Seismic Demand

The damage to nonstructural elements can be triggered by ground shaking intensities much lower than those required to initiate structural damage, leaving the building structurally intact but no longer functional. Such a high vulnerability of nonstructural elements is caused not just by their poor structural configurations but, more importantly, by the highly amplified acceleration that acts on the nonstructural elements.

Figure 2.1 describes the amplification (or filtering) process of ground motions in a cascade manner. At first, the bedrock motion is filtered around the predominant frequency (ω_g) of a surface soil layer. Then the free-field motion is again amplified by structural resonance near the natural frequency of structure (ω_n). Finally, nonstructural elements are subjected to floor motion amplified by the resonance effect near their natural frequency (ω_p). It can also be observed that the extremely wide-banded bedrock motion becomes a narrow-banded (almost harmonic) floor motion
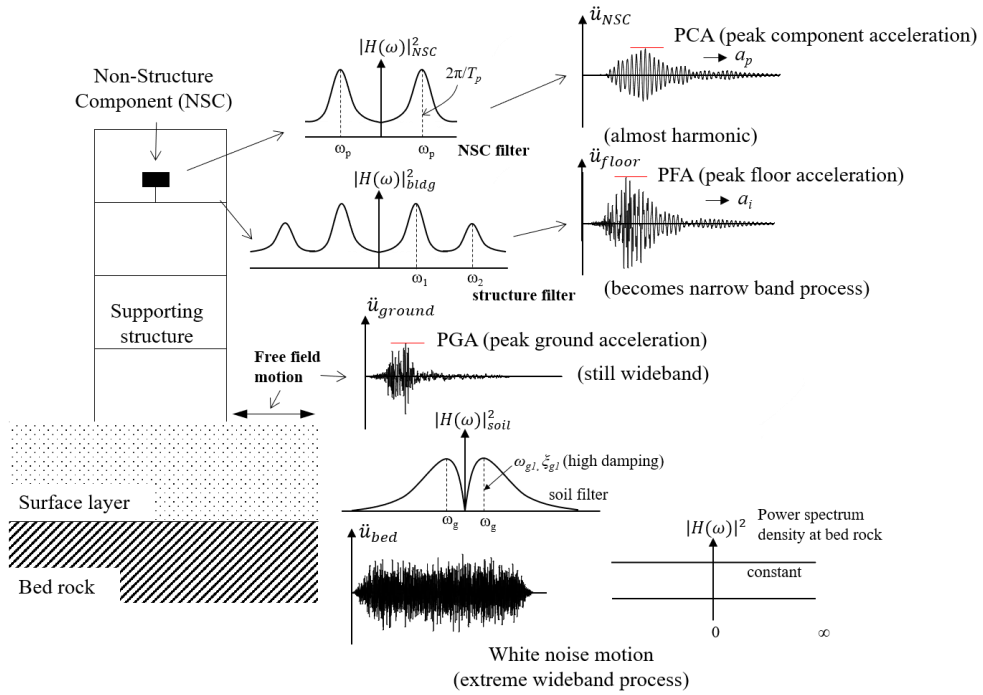
Figure 2.1 Amplification process of acceleration acting on nonstructural elements

during the filtering process. Since the amplification by the surface layer is already reflected in the design spectrum, the design of nonstructural elements needs to deal with the amplification caused by structure and the nonstructural element itself. These two amplification phenomena are generally referred to as in-structure amplification (or story amplification) and component amplification. If the rigorous dynamics is applied, such amplifications should be determined considering the effects of the structural and nonstructural dynamic properties (tuning effects), and the effects of structural-nonstructural interactions that vary depending on their mass ratio (= $m_{component}/m_{structure}$). Also, the problem should be solved using the nonclassical damping theory because the classical damping assumption is no longer valid because the critical damping ratio for general nonstructural elements is relatively lower ($\zeta_p \approx 1$ %) than that of the structure ($\zeta_n = 2 \sim 5$ %).

The researches on the nonstructural seismic demands have been conducted since the 1960s, led by nuclear power plant engineers. Numerous studies have already been conducted to understand the mechanisms of in-structure and component amplifications. The in-structure amplification is primarily affected by the seismic force-resisting system and its dynamic properties (for example, Fathali and Lizundia 2011; Miranda and Taghavi 2009; Kehoe and Freeman 1998; Medina et al. 1998; Singh et al. 2006). The magnitude of the in-structure amplification has known to decrease as the building nonlinear response increases (Anajafi and Medina 2018; Politopoulos and Feau 2007; Oropeze et al. 2010; Sullivan et al. 2013; Vukobratović and Fajfar 2016). Regarding the component amplification, it is highly dependent on the period ratio between the supporting structure and nonstructural elements. A very narrow-banded high amplification could occur if the component period is close to or equal to one of the natural periods of the supporting structure (Singh et al. 2006; Miranda and Taghavi 2009; Flores et al. 2015). It was also reported that the nonlinearities in supporting structures and nonstructural elements generally have an effect of reducing the component amplification, especially when the component are tuned to the fundamental period of the supporting structures (Lin and Mahin 1985; Surana et al. 2018; Chaudhuri and Villaverde 2008). Further extensive studies have been made to identify the key affecting parameters and their interrelationships, and several design methods to predict seismic demand on NSEs have been proposed; some on a largely empirical basis and others on a more rigorous dynamic basis.

Ideally, ensuring the satisfactory seismic performance of nonstructural elements requires explicit consideration of the entire influence chain composed of input ground motion, supporting structure as well as the nonstructural element itself. To

this end, a number of advanced design methods have been suggested ever since; some on a largely empirical basis and others on a more rigorous dynamics basis. However, due to the mathematical complexity inherent in the rigorous analysis methods and difficulties regarding the identification of dynamic properties of both the structure and nonstructural elements, major building codes suggest the equivalent static method in favor of its practical simplicity.

2.2. Seismic Design of Nonstructural Elements

This section summarized the design equations proposed by ASCE 7 and Eurocode 8 (2004), which have been popular in practice for their simplicity. As for ASCE 7, equations of both ASCE 7-16 (2017) and 7-22 (2022) were presented.

The basic form of design equations can be written as follows:

$$F_p = I_p \times PGA \times (\frac{PFA}{PGA}) \times (\frac{PCA}{PFA}) \times W_p \qquad (2.1)$$

where F_p = seismic design force to be applied at the center of gravity and distributed relative to component's mass distribution; PGA = peak ground acceleration; PFA = peak floor acceleration; PCA = peak component acceleration; W_p = component operating weight.

As for the peak ground acceleration (PGA), it is determined by $0.4S_{DS}$ which is intended to be the same as the design ground acceleration for the supporting structure, determined considering the seismic hazard and the soil condition of the building site.

The PGA is then multiplied by a factor (PFA/PFA) to represent the in-structure amplification of PFA, which occurs along the height of the supporting structure. Lastly, the PFA is multiplied by a factor (PCA/PFA) to account for the amplification of the PFA caused when the fundamental period of nonstructural elements is close to that of the supporting structure. The design equation methods for equivalent static method given by ASCE 7-16, ASEC 7-22 and Eurocode 8 can be defined as follows. Original parameters prescribed in Eurocode 8 were replaced with those of ASCE 7 for convenience.

$$F_p = I_p \times 0.4 S_{DS} \times (1 + 2\frac{z}{h}) \times (\frac{a_p}{R_p}) \times W_p \qquad \text{(ASCE 7-16)} \quad \text{(2.2a)}$$

$$F_p = I_p \times 0.4 S_{DS} \times H_f \times (\frac{C_{AR}}{R_{po}}) \times W_p \qquad \text{(ASCE 7-22)} \quad \text{(2.2b)}$$

$$F_p = I_p \times 0.4 S_{DS} \times [\frac{3(1 + z/h)}{(1 + (1 - T_a/T_1)^2)} - 0.5] \times (\frac{1}{R_p}) \times W_p \quad \text{(Eurocode 8)} \quad \text{(2.3)}$$

Definitions of each parameters and the methods to determine the in-structure amplification, and component amplification are summarized in the following sections.

2.2.1. Peak floor acceleration

In ASCE 7, the in-structure amplification is reflected as below.

$$\frac{PFA}{PGA} = 1 + 2.0(\frac{z}{h}) \qquad \text{(ASCE 7-16)} \qquad \text{(2.4a)}$$

$$H_f = 1 + 2.5(\frac{z}{h}) \qquad \text{(ASCE 7-22)} \qquad \text{(2.4b)}$$

$$H_f = 1 + a_1(\frac{z}{h}) + a_2(\frac{z}{h})^{10} \qquad \text{(2.4c)}$$

where $a_1 = 1/T_a \leq 2.5$; $a_2 = [1 - (0.4/T_a)^2] > 0$; z = height in structure of the highest point of attachment of component with respect to the base; h = average roof elevation of structure above the base; T_a = lowest approximate fundamental period of supporting building in either orthogonal direction.

Note that the in-structure amplification given by Eq. (2.4a) and Eq. (2.4b) are basically the same in that both equations adopted linearly distributed PFA along the building height. The in-structure amplification in Eq. (2.4a) was based on the database of the instrumented buildings from the Californian earthquakes available up to 1995 (Drake and Bachman 1996) (see Figure 2.2). Since it is well known that the linearly assumed PFA distribution is more suitable for short-period (low-rise) buildings, ASCE 7-22 newly proposed structural period-dependent equation that yield PFA distribution more favorable to longer-period buildings. The equation is based on both the records from the instrumented buildings and the analytical studies conducted by Taghavi and Miranda (2006) and Alonso-Rodriguez and Miranda (2016),
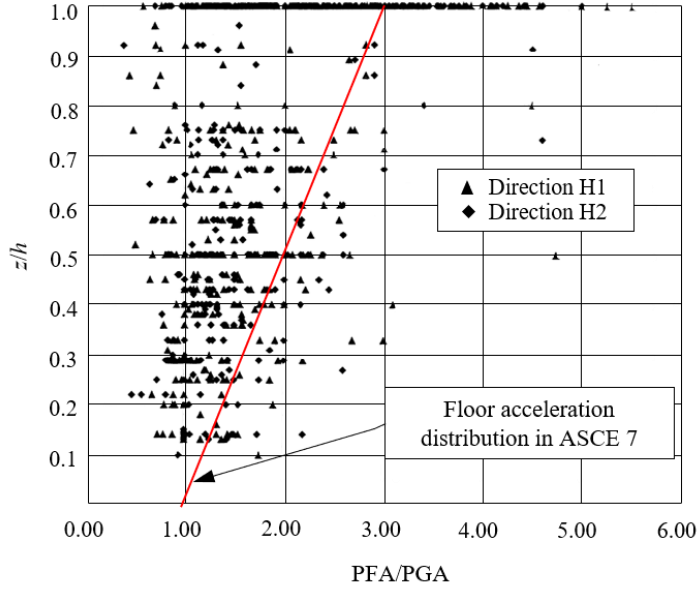
Figure 2.2 Instrumented floor acceleration data for PFA > 0.1 g (Drake and
Bachman 1996)

where they implemented time-history analysis using a simplified continuous model
consisting on a flexural beam laterally coupled with a shear beam (see Figure 2.3).

In the case of Eurocode 8, similar to the Eqs. (2.4a) and (2.4b), the linearly
distributed PFA assumption was adopted with the maximum in-structure amplifica-
tion given lower than that of ASCE 7. The in-structure amplification can be deter-
mined as follows.

$$\frac{PFA}{PGA} = 1.5(1 + \frac{z}{h}) - 0.5 \tag{2.5}$$

Figure 2.4 shows the in-structure amplification distribution given by Eqs. (2.4)
and (2.5). As mentioned previously, Eqs. (2.4a), (2.4b) and (2.5) showed same linear
PFA distribution except for the maximum level of the amplification where Eurocode
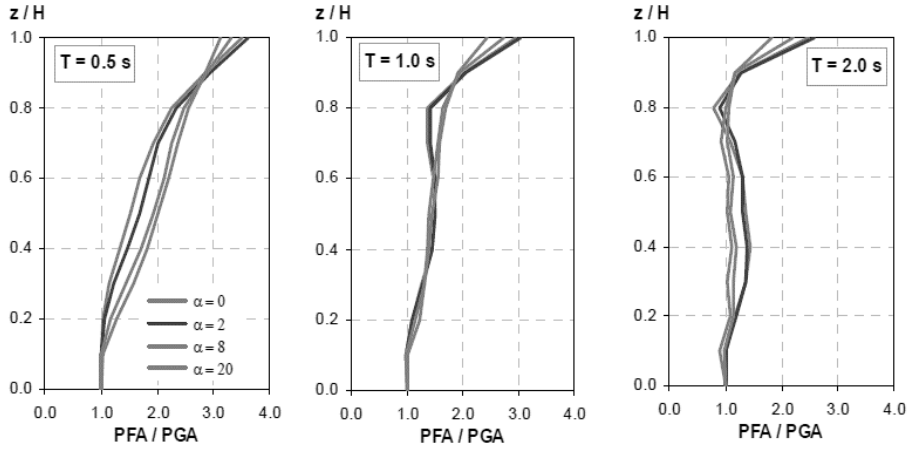
Figure 2.3 Effects of structural period and lateral stiffness ratio on peak floor acceleration ($a_0 = 0$ represents a pure flexural model) (Miranda and Taghavi 2009)

8 gives the lower PFA amplification than that of ASCE 7. The PFA distribution given by Eq. (2.4c) becomes more vertical as the fundamental period of the structure increases which is intended to capture the increasing higher mode effect of the long-period buildings.

Effect of structural nonlinearity

One of the major improvements made in ASCE 7-22 is the reduction of the component acceleration considering the structure and component ductility level. The reduction in PFA resulting from structural nonlinearity is accounted for through the factor R_μ which is determined as follows.

$$R_\mu = [\frac{1.1R}{I_e\Omega_0}]^{1/2} \geq 1 \tag{2.6}$$
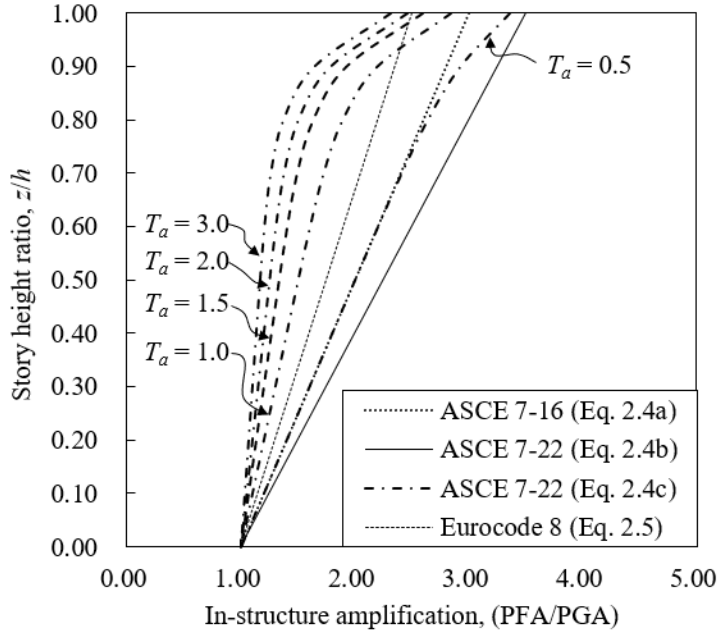
Figure 2.4 In-structure amplification along building height according to ASCE 7 and Eurocode 8

where R = structure response modification factor; I_e = structure importance factor; Ω_0 = structure overstrength factor.

Eq. (2.6) indicates that the PFA reduction is related to both the structure response modification factor (R) and the structural overstrength factor (Ω_0). The structure response modification factor R can be expressed, according to SEAOC (1999) as follows.

$$R = R_D \times R_o = R_D \times (\frac{\Omega_0}{1.1}) \tag{2.7}$$

where R_D = global ductility factor at design earthquake level; R_o = global over-strength factor or lower bound strength factor of lateral system; Ω_0 = upper bound strength factor of lateral system.

Using the relationship given in Eq. (2.7) and taking the structure importance factor (I_e) as 1.0, Eq. (4) can be reduced as below.

$$R_{\mu} = [\frac{1.1R}{I_e\Omega_0}]^{\frac{1}{2}} = [(\frac{1.1}{\Omega_0}) \times R_o \times R_D]^{\frac{1}{2}} = [R_D]^{\frac{1}{2}} \simeq [u_m / u_y]^{\frac{1}{2}} \qquad (2.8)$$

where u_m = maximum roof displacement of supporting structure; u_y = yield roof displacement of supporting structure.

Eq. (2.8) reveals that the PFA reduction is proportional to the square root of the structure global ductility factor (R_D). The relationship between PFA reduction and R_D is based on studies conducted for eight different types of structures (NIST 2018); R_D was approximated as the ratio of the maximum roof displacement normalized by the yield roof displacement of the structures.

2.2.2. Peak component acceleration

The component acceleration tends to increase significantly depend on the period ratio between nonstructural elements and the supporting structure. A very high acceleration amplification occurs if nonstructural elements in-tuned to the one of the

natural periods of the supporting structure. In ASCE 7-16, the component amplification factor (a_p) is assigned as 1.0 for rigid components and 2.5 for flexible components with somewhat arbitrary definition of 0.06 sec (16.6 Hz) as the borderline period to separate them. Therefore, the given empirical factors have limited ability to capture the actual variation trend of the component amplification and can be much higher than 2.5. However, the value of a_p was capped at 2.5 considering several reasons including the following. During strong ground shaking, the nonlinear behavior of the supporting structures and the nonstructural elements, if any will shift their fundamental period in an unpredictable manner, may increase or reduce the component amplification. Further, even though the nonstructural elements are tuned to one of the natural periods of a supporting structure, the effects would likely be transient, as the period of components will shift if yielding occurs (NIST 2017).

The component response modification factor (R_p) represents the seismic force reduction linked to the cyclic ductility capacity of the component and anchorage. Like the component amplification factor (a_p), R_p factor was also proposed based on engineering judgments without sufficient technical background.

Table 2.1 Component ductility categories (ASCE 7-22)

Ductility category	Assumed component ductility	PCA/PFA ($= C_{AR}$)
Elastic	1.00	4.00
Low	1.25	2.80
Moderate	1.50	2.20
High	2.00	1.40

In ASCE 7-22, the component amplification factor was newly prescribed as the component resonance ductility factor (C_{AR}), where the effect of component nonlinearity (μ_{comp}) was included. Firstly, the elastic component amplification factor, which was previously described as 2.5, was increased to 4.0. Then, a lower C_{AR} is assigned to the component of higher ductility (see Table 2.1).

The C_{AR} given in Table 2.1 represents the capped value of the analysis results conducted by NIST (2018). As previously discussed, component resonance amplification is a very narrow-banded phenomenon, and the likelihood that nonstructural elements belong to this band is relatively low. In this regard, NIST (2018) conducted a probabilistic analysis utilizing the database of instrumented buildings and a natural frequency database of nonstructural elements (see Figures 2.5 – 2.6). Based on the cumulative distribution function given as a period ratio function (T_{comp}/T_{bldg}), they set a resonance bandwidth where the nonstructural elements have a 10 % probability of being within the range. Then, the period range was used as a baseline to set C_{AR} for nonstructural elements (see Figure 2.7).
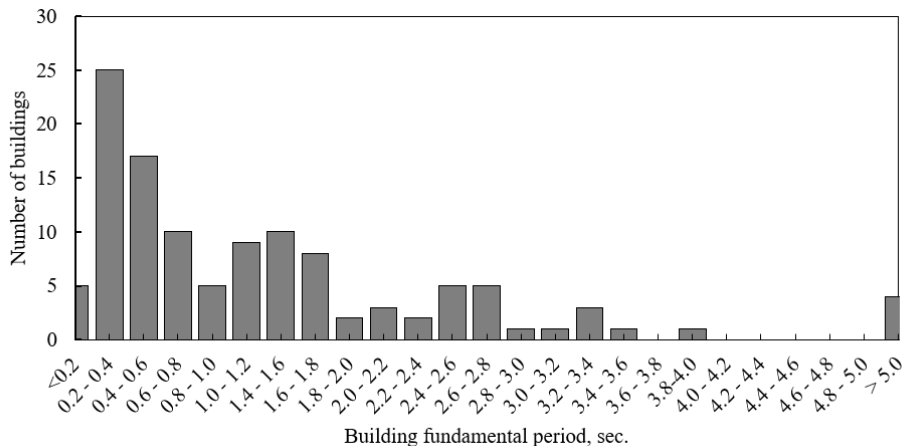
Figure 2.5 Database of instrumented buildings for probabilistic study to derive C_{AR} (NIST 2018)
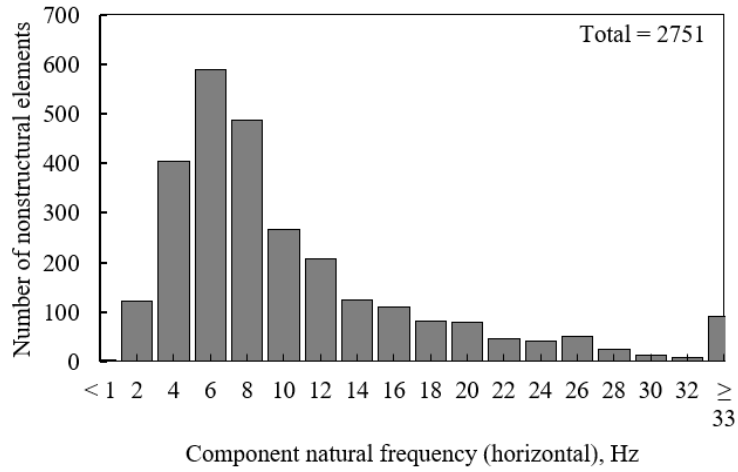
(a) Horizontal component frequency
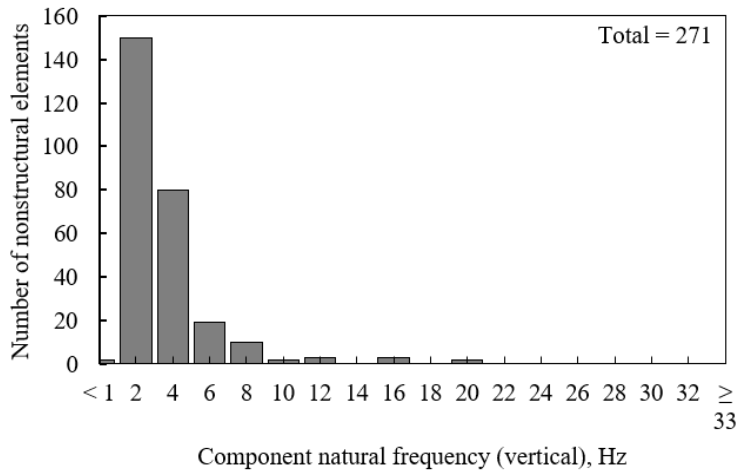
(b) Vertical component frequency

Figure 2.6 Database of nonstructural element for probabilistic study to derive C_{AR} (NIST 2018)
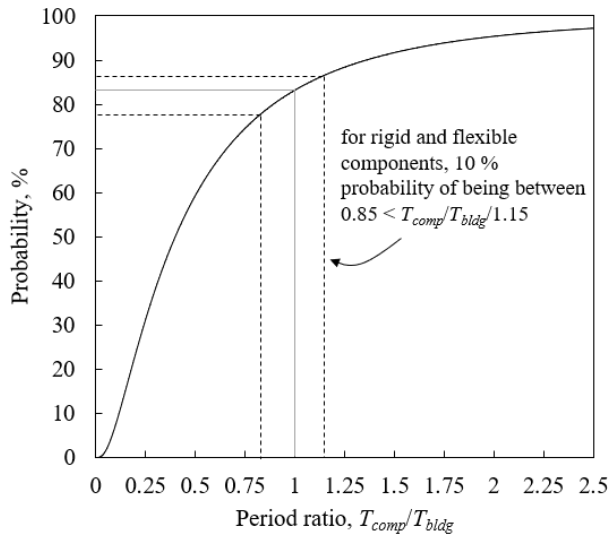
(a) Cumulative distribution function for T_{comp}/T_{bldg}
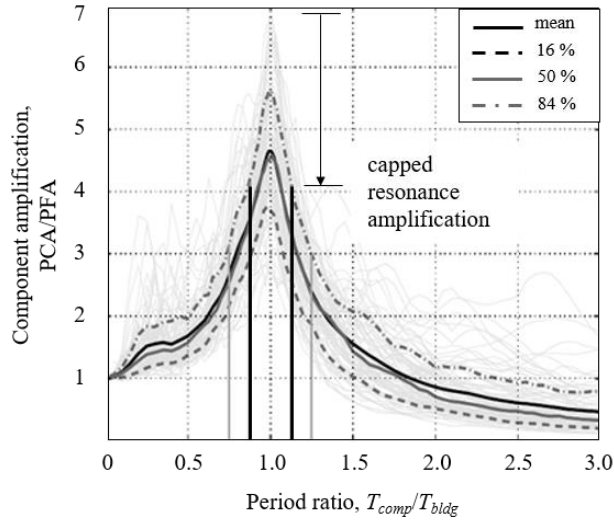
(b) Component amplification and capping of PCA/PFA

Figure 2.7 Probabilistic study for capping narrow-banded component resonance amplification (NIST 2018)
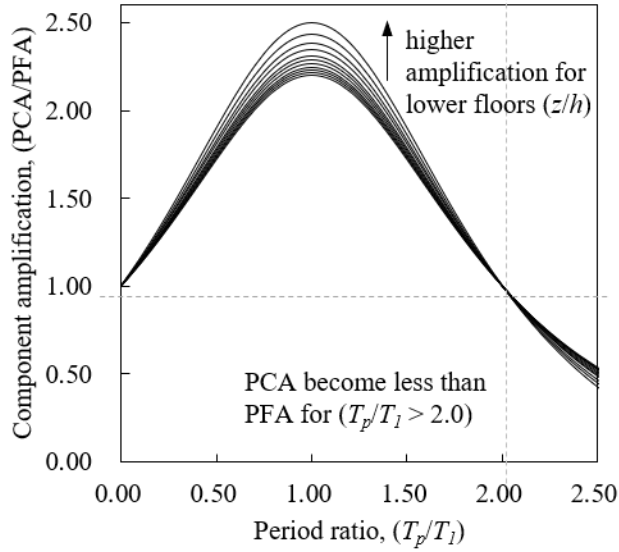
Figure 2.8 Component amplification factor according Eurocode 8

Eurocode 8 provides a period ratio-dependent component amplification relationship that can be expressed as follows.

$$\frac{PCA}{PFA} = \frac{6(1+\frac{z}{h}) - [1 + (1 - T_p / T_1)^2]}{[3(1+\frac{z}{h}) - 1] \times [1 + (1 - T_p / T_1)^2]} \tag{2.9}$$

where T_1 = fundamental period of the building in the relevant direction

As can be seen from Eq. (2.9) and Figure 2.8, the component amplification given by Eurocode 8 depends not only on the period ratio between nonstructural elements and the supporting structure (T_p/T_1) but also on the story height ratio (z/h). The component amplification tends to become higher if the nonstructural elements

23

are located on the lower floor. Also, the PCA becomes less than PFA if T_p is larger than two times T_1.

2.2.3. Dynamic analysis methods

In lieu of the equivalent static method discussed previously, the acceleration demand on nonstructural elements can be calculated using one of the following dynamic analysis methods: the response spectrum analysis method, linear/nonlinear time history analysis methods, the floor response spectrum method, and alternate floor response spectrum method. Depending on the types of analysis output obtained from the dynamic methods, the in-structure amplification or component amplification factors can be conveniently be replaced by the analysis results. The analyzed peak floor acceleration can be utilized instead of the in-structure amplification factor, and both the in-structure and component amplification factors can be replaced if the floor response spectrum method is used.

2.3. Seismic Design and Performance Evaluation of Suspended Ceiling System

2.3.1. Configuration of suspended ceiling systems

Suspended ceiling systems are composed mainly of hanger members, ceiling grids, ceiling panels, and perimeter closure channels (or molding). Among these, the main structural parts include the ceiling grids which provide in-plane stiffness, and
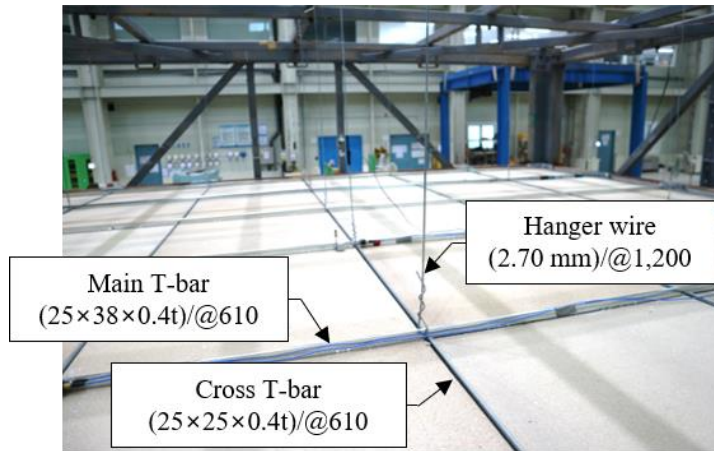
(a) Direct-hung lay-in T-bar ceiling system
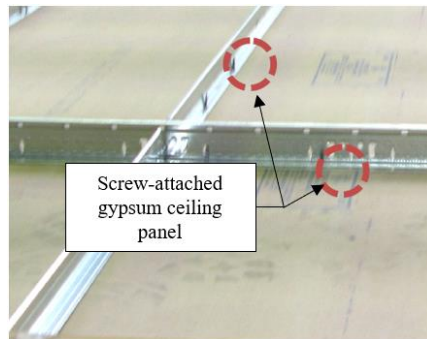
(b) Screw-attached continuous T-bar ceiling system (Gilani et al. 2008)

Figure 2.9 Configuration of direct-hung suspended ceiling system

hanger members which provide lateral stiffness to ceiling systems. Therefore, sus-

pended ceilings generally classified based on the types of grid and hanger members.

Perimeter closure channels are generally regarded as aesthetic elements that do not

have any structural role (ASTM-E580-E80 2017). Their main function is to prevent

the unseating of ceiling grids or panels at the perimeter of suspended ceilings. The

main characteristics of each ceiling system are summarized below.

(a) 1994 Northridge earthquake ($M_w = 6.7$)   (b) 2017 Pohang earthquake ($M_w = 5.4$)

Figure 2.10 Typical seismic damage observed for lay-in panel ceiling systems

Direct-hung suspended ceiling system

A direct-hung T-bar suspended ceiling system is one of the most popular ceiling systems worldwide. In this system, the grids are fabricated with main ($L = 4,000$ mm) and cross T-bars ($L = 610$ mm), which are placed at every 610 mm intervals. The ceiling panels are placed within the 610 mm $\times$ 610 mm ceiling grids without any positive attachments to the grid members (lay-in ceiling). Instead of the square lay-in panels, gypsum ceiling panels are often utilized. In such case, the gypsum panels are screw-attached to the ceiling grids. The fabricated ceiling grids are then suspended by hanger wires, which are directly looped through a hole in the main T-bars (direct-hung) and connected to the floor above. These wires are usually installed at intervals of 1,200 mm (see Figure 2.9).

Generally, direct-hung ceiling systems utilize lay-in ceiling panels. Therefore, many lay-in direct-hung ceilings were reported to suffer significant seismic damage during past major earthquakes (see Figure 2.10). Since the ceiling panels were not mechanically fixed to the grids, the damage was mostly concentrated on the loss of ceiling panels and member joint disconnections.
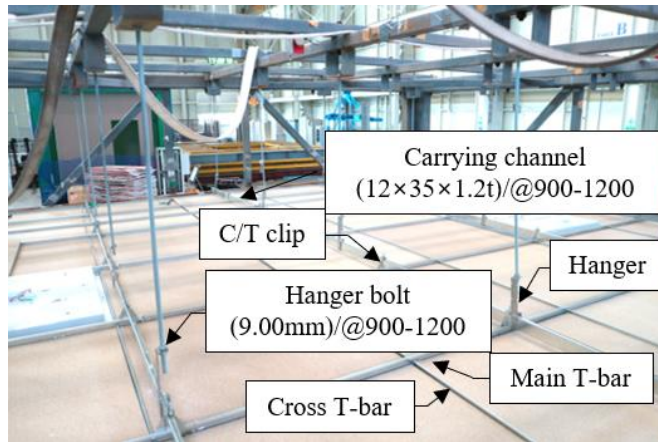
(a) Indirect-hung lay-in T-bar ceiling system
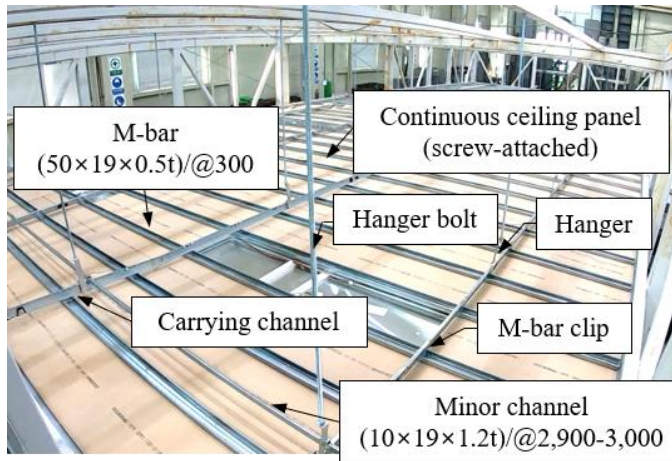
(b) Indirect-hung continuous M-bar ceiling system

Figure 2.11 Configuration of indirect-hung suspended ceiling system

Indirect-hung suspended ceiling system

In Korea, as well as in other countries, several types of suspended ceiling systems are commonly used apart from the direct-hung suspended ceiling system. The major differences lie in the hanger members and the details of the connection of the ceiling grids to the floor above. Figure 2.11(a) shows the configuration of the lay-in T-bar indirect-hung ceiling system. In this system, the ceiling grids are composed of main and cross T-bars are utilized but attached with additional C-section members,

(a) 2017 Pohang earthquake ($M_w = 5.4$)   (b) 2011 Tohoku earthquake ($M_w = 9.1$)

Figure 2.12 Typical seismic damage observed for continuous panel ceiling systems

often called a carrying channel, using C/T clips. Carrying channels are usually installed to main T-bars at intervals of 900 - 1,200 mm, and above the channels, minor channels are added to prevent the spreading of the carrying channels. Instead of hanger wires, hanger bolts are used to connect the grid system to the floor slab. Because the entire ceiling grid is hung through the carrying channel, it is also classified as an indirect-hung suspended ceiling system.

A grid system composed of M-section member (M-bars) is widely used for continuous panel ceiling systems. As shown in Figure 2.11(b), the grid is formed without any cross members, and the ceiling panels are screw-attached to the M-bars that are densely placed through whole ceiling area (300 mm intervals).

For continuous M-bar ceiling systems, seismic damage often occurs on a more global and drastic scale, as shown in Figure 2.12. Because the ceiling panels were mechanically fixed to the grid members, rather than dislodgement of partial ceiling panels, both the grid members and ceiling panels simultaneously collapsed, which can cause a severe threat to the safety of the residents.

2.3.2. Capacity of ceiling grid members

In this section, details of grid members used for direct- and indirect-hung ceiling systems were discussed. General capacity requirements for grid members given by Korean Standard (KS 3609 2015), British Standard (BS EN 13964 2014), and American Standard (ASTM C635 2017; ASTM E580 2017) were summarized and the main characteristics of direct-hung and indirect-hung grid members were discussed based on the test results of previous studies.

Tables 2.2 - 2.5 summarizes the certification criteria for ceiling grid members. It can be observed that the all the strength requirements for grid members were given with regard to the gravity load. ASTM E580 prescribed additional capacity requirements for ceiling systems subjected to earthquake loading. For such case, all the joints (splices and connections) of the grid system should be verified to have enough tensile and compressive strength.

Cho 2014 conducted a series of static component tests for an indirect-hung continuous M-bar ceiling system. It was demonstrated that all the joints and members have enough strength for gravity load, but the strength under lateral loads was not investigated, which is essential for investigating the capacity of ceiling systems under seismic load.

Table 2.2 Required capacity for M-bar ceiling members (KS 3609)

Loading direction	Member		Force, N	Maximum deflection, mm	Permanent deflection, mm
Downward force	M-bar	19type	294.2	≤ 10	≤ 2
		25type	490.3		
	Carrying channel		735.5	≤ 5	≤ 2
Upward force	M-bar		294.2	≤ 5	-

Table 2.3 Member classification for T-bar ceilings according to BS EN 13964

Class	Target Deflection, mm	Permanent deflection, mm
1	L/500 and not greater than 4.0	< 0.2
2	L/300	< 0.2
3	No limit	< 0.2

*L = span between the suspension points

Table 2.4 Minimum load-carrying capabilities of main runners (ASTM C635)

Suspension system	Duty classification	Applied load, N	Allowable midspan deflection, mm
Direct Hung	Light	22.7	3.33
	Intermediate	54.3	3.33
	Heavy	72.5	3.33
Indirect Hung	Light	9.1	3.33
	Intermediate	15.9	3.33
	Heavy	36.3	3.33

Table 2.5 Minimum component strength required for seismic ceilings (ASTM E580)

Component	SDC C		SDC D, E, and F	
	Tension	Compression	Tension	Compression
Splices	265	265	441	441
Connection	265	265	441	441

Soroushian et al. (2015a, 2016a) conducted static component tests for the grid members composing a direct-hung T-bar ceiling system. The focus was given on investigating the axial, shear, and flexural capacity of the several types of grid latches (joints). It was observed that all the joints have sufficient axial and shear capacity. But, it was highlighted that sudden partial failure of ceiling systems is probable when the bending demand on ceiling joints is high. Almost no rotational strength was observed within the joints except for one or two single peaks (see Figure 2.13).
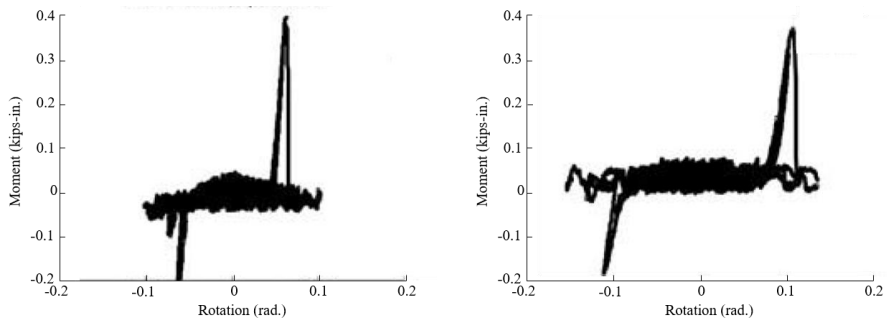
Figure 2.13 Low bending capacity of 2 ft and 4 ft cross T-bars joints (Soroushian et al. 2015a)

2.3.3. Seismic requirements for suspended ceilings

Since the 1980s, a number of experimental studies using shake tables have been conducted to assess the seismic performance of suspended ceiling systems and identify the failure mechanism. Early studies (for example, Ayres and Sun 1973; ANCO 1983) found that the most critical part of suspended ceiling systems includes the grid
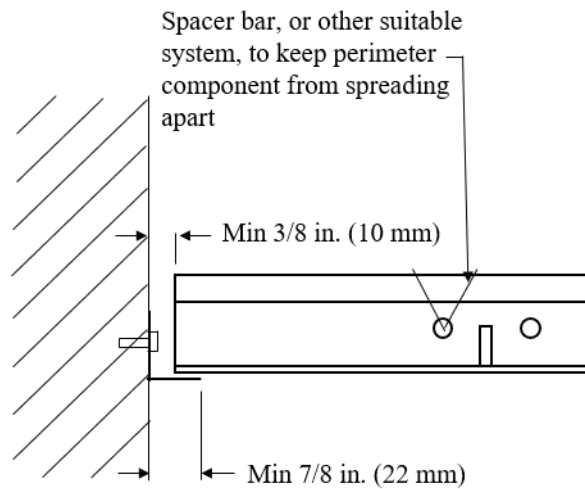
Figure 2.14 Seismic requirements for suspended ceilings installed on SDC C building (ASTM E580)
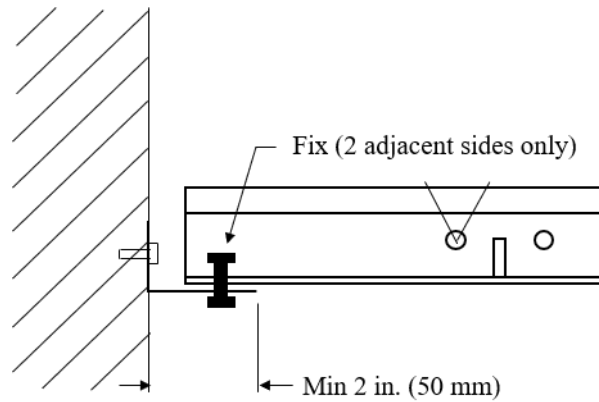
(a) Fixed perimeter detail
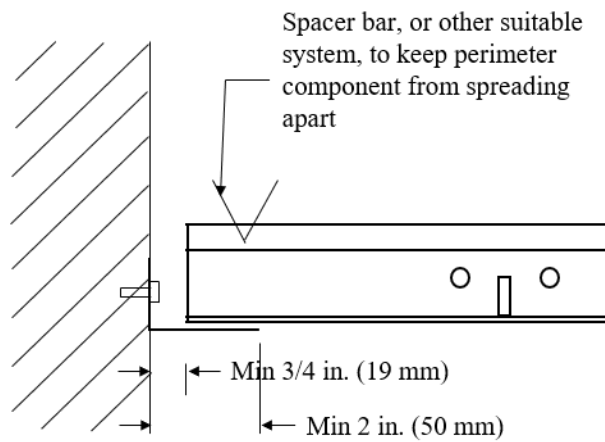
(b) Free (floating) perimeter detail

Figure 2.15 Seismic requirements for suspended ceilings installed on SDC
D, E, and F building (ASTM E580)

members at the ceiling perimeters. As the ceiling system collided with the surround-

ing walls, the perimeter grid members were easily damaged by pounding forces. De-

spite that their failure mechanism and causes of damage have been identified, the

seismic design of suspended ceiling systems is still largely empirical and lacks ra-

tional engineering procedures because of their complex dynamic behavior.
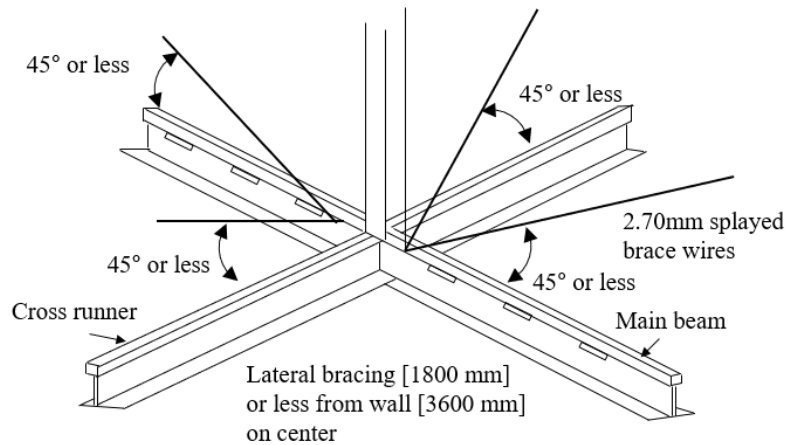
Figure 2.16 Lateral bracing requirement for large area ceiling installed on SDC D, E, and F building (ASTM E580)

Generally, suspended ceiling systems are designed following the seismic requirements prescribed by ASTM E580 (ASTM-E580-E80 2017). ASTM E580 provides recommendations for reducing the seismic damage of ceiling systems based on the Seismic Design Category (SDC) of the building that the ceilings were to be installed. Under moderate earthquake intensities (SDC C), providing a minimum clearance of 10 mm at all the edges of ceilings is recommended to accommodate ceiling displacement and minimize the pounding forces (see Figure 2.14). Under severe earthquake intensities (SDC D, E, F), the movement of ceilings should be restrained by attaching perimeter grid members to the perimeter closure channels on two adjacent walls using pop rivets or seismic clips. In the opposite sides, a minimum clearance of 19 mm should be provided to accommodate ceiling movement (Figure 2.15). Ceiling braces consisting of 45° splay wires and a compressive strut should be used if the area of ceiling exceed 100 m^2, as shown in Figure 2.16.

2.3.4. Shake-table test protocol for suspended ceiling system

Generally, shake-table testing of suspended ceiling systems (also for general nonstructural elements) is performed following the ICC-ES-AC 156 (2010) loading protocol. However, as the protocol was originally intended for performance evaluation of the floor-mounted nonstructural elements, additional considerations should be given when testing the suspended ceiling systems (also, other suspended nonstructural elements).

AC 156 provides procedures to generate an artificial ground motion that envelopes the required response spectrum. The required response spectrum in horizontal input direction can be defined as follows.

$$A_{FLX-H} = S_{DS}(1 + 2\frac{z}{h}) \leq 1.6 S_{DS} \tag{2.10}$$

$$A_{RIG-H} = 0.4 S_{DS}(1 + 2\frac{z}{h}) \tag{2.11}$$

For vertical direction, z may be taken to be 0.0 for all attachment heights, with overall acceleration given 2/3 of that for the horizontal direction. The vertical required response spectrum can be defined as follows.

$$A_{FLX-V} = 0.67 S_{DS} \tag{2.12}$$

$$A_{RIG-V} = 0.27 S_{DS} \tag{2.13}$$
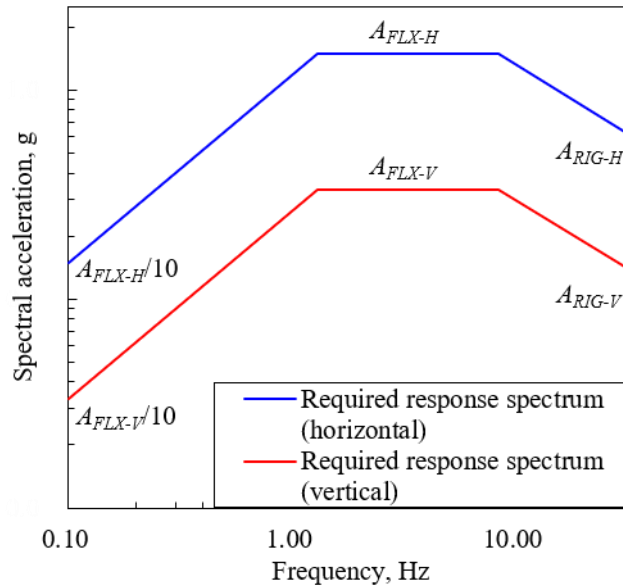
Figure 2.17 Horizonal and vertical required response spectrum for nonstructural element shake-table test (AC 156, 2010)

The required response spectrum given by AC 156 presents the floor response spectrum for general buildings (Figure 2.17). In these equations, the in-structure and component amplification factors are adopted from ASCE 7-16.

The required response spectrum given by AC 156 has a very wide-banded spectral feature that generates input motion with much higher energy than narrow-band floor motions. Correspondingly, higher seismic capacities are generally required for the tested nonstructural elements to receive performance certification. This wide-banded spectral feature of the input motion was given because the structural dynamic properties for the tested nonstructural elements are generally not given in advance. If the dynamic properties of the structure where the nonstructural elements will be installed are known in advance, shaking table tests can be implemented by generation floor motions based on the dynamic analysis methods given in Section 2.2.3.

Shake-table test of suspended ceiling systems requires a test frame to hang the ceiling systems. Therefore, in generating input motions, the structural dynamic response of the test frame should be considered to prevent the overamplification of the input motion. The simplest method is to construct a highly rigid test frame so that the test frame will not amplify the shake-table motion. Generally, a test frame with a 16.6 Hz natural frequency is deemed satisfactory because the input motion will not amplify within such a high stiffness structure, and also the generated floor response spectrum (or response spectrum obtained from the top of the test frame) will not have a high resonance peak within the amplified region (1.3 ~ 8.3 Hz) of the required response spectrum.

Alternatively, the input motion can be initially modified considering probable acceleration amplification such as the open-loop compensation procedure proposed by Maddaloni et al. (2010). Both the amplitude and signal compensations are required in the adjustment procedure where these compensations can be implemented using the transfer function of the desired (or target) and the achieved floor motion defined as follows.

$$x_{base} = H_{s,j}^{-1} \times \overline{x} \tag{2.14}$$

$$\overline{y}_j = H_{s,j} \times x_{base} = H_{s,j} \times H_{s,j}^{-1} \times \overline{x} \simeq \overline{x} \tag{2.15}$$

where x_{base} = input motion; $\overline{x}$ = target motion; $\overline{y}$ = achieved motion; $H_{s,j}$ = transfer function referred to the jth floor of structure.

2.3.5. Previous studies on suspended ceiling systems

Suspended ceiling systems are composed of combinations of discrete components with high diversity in their cross-sectional properties and joint details. Such a high diversity has posed a considerable challenge in identifying their failure mechanism and seismic capacities and generalizing their dynamic behavior. Generally, research on suspended ceilings is conducted based on shake-table tests. Based on test results, previous studies evaluate the effectiveness of the design method provided by ASTM E580 and proposed fragility curves, numerical models, and novel retrofit or design methods for effectively enhancing the ceiling seismic performance. Their findings can be summarized as below.

Yao (2000) performed shake-table tests on direct-hung lay-in suspended ceiling systems to identify their dynamic behavior and evaluate the effectiveness of compression posts given by ASTM E580. It was observed that the direct-hung ceiling systems have very low natural frequencies that can be effectively predicted by a pendulum theory. Also, it was identified that the ceiling systems have about a 5 to 7 % critical damping ratio. Specimen with compression posts did not contribute much to enhancing the ceiling seismic performance, but rather it was highlighted that the presence of transverse bars used to prevent grid spreading is more important for their seismic performance.

Badillo-Almaraz et al. (2007) conducted shake-table tests on direct-hung lay-in suspended ceiling systems where six types of ceiling configurations were utilized: specimen with 1) non-seismic (normal) detail, 2) recycled cross tees, 3) undersized ceiling panels, 4) retainer clips, 5) perimeter rivets, and 6) compression posts. They
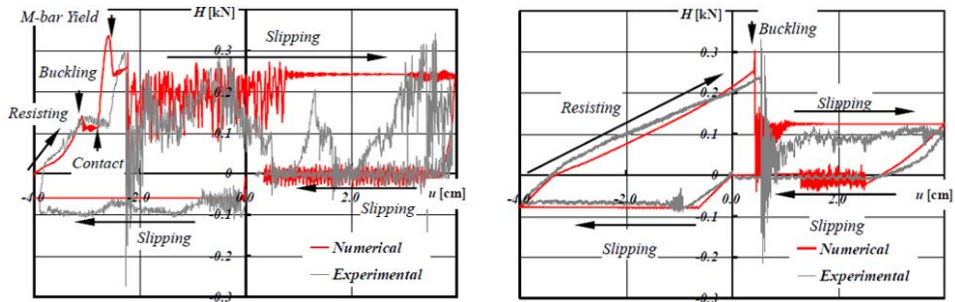
(a) For ceiling with small plenum depth   (b) For ceiling with large plenum depth

Figure 2.18 Load-displacement relationship of grid member (Motoyui and Sato 2014)

found that the recycled and undersized panel specimens were highly vulnerable to seismic damage compared to a normal ceiling specimen. Regarding the seismic specimens (specimens with retainer clips, perimeter rivets, and compression posts), they concluded that the perimeter clips and compression posts are highly effective in enhancing the overall ceiling seismic performances, but the retainer clips caused the failure of grid members as they increase the inertial load on the grids. They also proposed the four types of limit states that can be used for constructing ceiling fragility curves.

Gilani et al. (2010) evaluated the seismic performance of ceiling systems with compression posts based on ceilings with 4.9 m × 4.9 m dimensions. It was concluded that although the overall performance was enhanced, the specimen showed an unexpected failure mode where most of the center ceiling panels were dislodged.

Huang et al. (2013a) conducted shake-table tests on non-seismic and perimeter fixed ceiling systems. Along with their seismic performance, the energy dissipating characteristics of suspended ceiling systems were analyzed. It was concluded that
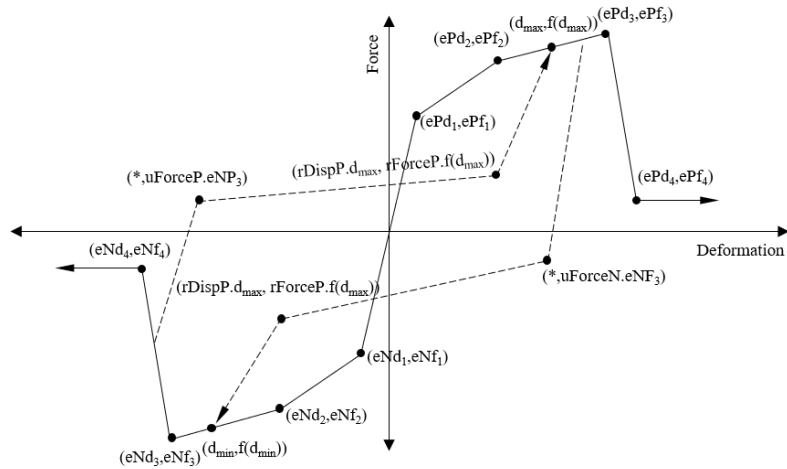
Figure 2.19 Pinching hysteresis model utilized for simulating ceiling grid joints behavior (Soroushian 2015b)

the energy dissipating mechanism for the free-floating ceiling systems is mainly provided by the frictional resistance that occurs between ceiling perimeter and wall moldings. The frictional coefficients were reported as around 0.2 to 0.4.

Motoyui and Sato (2014) developed a numerical model for ceiling systems based on static testing of ceiling grid members. In this study, they utilized indirect-hung suspended ceiling systems. The proposed numerical model can capture the horizontal displacement of the ceiling by taking into account the joint nonlinear behavior such as slipping, buckling, and contact (Figure 2.18).

Soroushian et al. (2015c, 2016a) conducted cyclic tests on individual ceiling joints. The objective of the tests was to capture the load-displacement relationships between all the grid joints and develop fragility curves for each ceiling member. Based on the study, Soroushian et al. (2015b) developed 32 component level analytical models that can capture the axial behavior of ceiling wires, the interactions between ceiling panels and sprinkler heads, and the shear and bending behavior of

grid connections. The hysteretic behavior of the grid latch joint was developed based on "Pinching 4" properties of OpenSees (Figure 2.19).

Zaghi et al. (2016) conducted full-scale analytical studies which was to simulate the actual damage of ceiling systems. The analysis was conducted using OpenSees, where the load-displacement relationships of member joints were adopted from the study of Soroushian et al. (2015b). They validated that the complex ceiling failure mechanism can be effectively simulated based on the proposed numerical model.

Soroushian et al. (2016b) conducted full-scale 5-story steel moment frame shake table tests to evaluate the performance of suspended ceiling systems. They analyzed the acceleration amplification factor for ceiling systems and observed that about 2.6 to 2.8 times acceleration amplification occurs during the tests. Also, they highlighted a high vertical acceleration amplification of ceiling systems which was caused by the flexibility of the floor slabs. They concluded that the use of lateral bracing with compression posts may not improve the seismic response of the ceiling when subjected to strong vertical excitation.

Pantoli et al. (2016) implemented system-level shake table tests based on a full-scale five-story reinforced concrete building. The main focus of the study was to advance the understanding of the seismic behavior of nonstructural elements, including their dynamic interactions amongst each other and with the structure. First, they observed that the seismic recommendations given by ASTM E580 are highly effective in preventing seismic damage. Also, they underlined the importance of dynamic interactions among nonstructural elements as most of the tested ceiling systems were damaged due to the interaction of the ceiling boundaries with structural elements and other nonstructural elements (in this study, balloon framing).

40
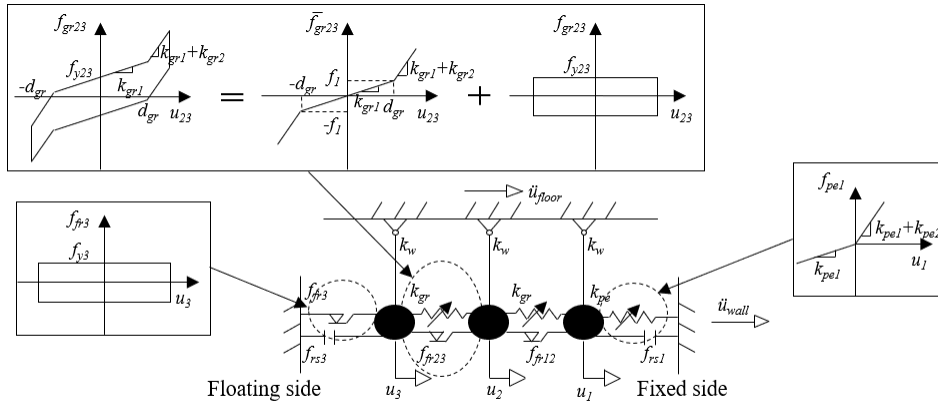
Figure 2.20 Lumped mass-spring ceiling nonlinear model (Ryu and Reinhorn 2019b)

Dhakal et al. (2016) conducted experimental studies on the ceiling components to provide fragility data. The objective of the study was to identify the most critical elements of the ceilings that govern the system capacity. The static component tests showed that the most critical components of the perimeter-fixed ceiling could be identified as single rivet connections.

Pourali et al. (2017) performed shake-table testing on free-floating suspended ceiling systems. They identified that the dynamic behavior of free-floating can be described by utilizing the equation of motion for a simple pendulum. Also, it was observed that the system has a very low critical damping ratio of 1 %. They proposed a fully-floating design concept of suspended ceiling systems where the excessive resonance displacement response can be effectively mitigated by perimeter isolation gap fillers which provide additional damping to the system
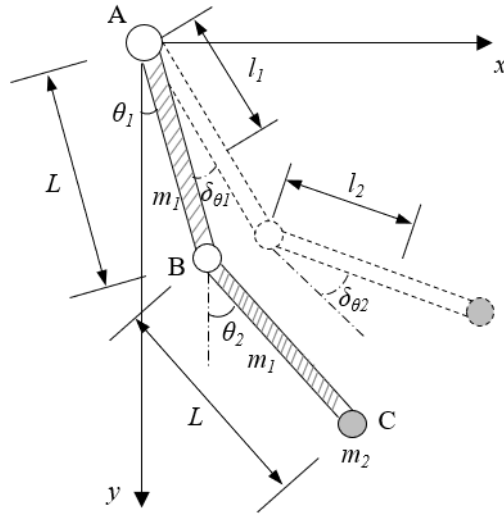
Figure 2.21 Double pendulum model for indirect-hung suspended ceilings
(Luo et al. 2018)

Ryu and Reinhorn (2019a) conducted full-scale shake-table tests on suspended ceiling systems based on 20 ft × 53 ft test frame. Tests results showed the effectiveness of lateral bracings in enhancing the seismic performance of ceiling systems. Based on test results, Ryu and Reinhorn (2019b) analyzed the dynamic characteristics of suspended ceilings. They estimated a large damping ratio of ceiling systems that resulted from the friction between the ceiling perimeters and wall moldings. About 30 % equivalent damping ratio was reported. Also, they proposed a simplified numerical model that linearized the 3-DOF ceiling model consisting of various non-linear properties (Figure 2.20).

Luo et al. (2018) conducted experimental studies on indirect-hung suspended ceiling systems and proposed a numerical model for calculating the fundamental frequencies of indirect-hung ceiling systems using a double pendulum model (Figure 2.21). However, the double pendulum model did not show a noticeable difference

compared to a single pendulum model because the mass of ceiling rods is much smaller than that of the ceiling grids and panels. Consequently, the measured natural frequencies of tested ceilings showed significant differences from those calculated from the proposed model.

Qi et al. (2020) proposed theoretically derived equations for predicting the natural frequency of suspended nonstructural elements. They evaluated a seismic performance of a two-elevation integrated ceiling system and proposed a numerical model with friction-gap elements to model the connections between ceiling panels and integrated equipment.

Soroushian et al. (2019) conducted extensive fragility studies for suspended ceilings having various configurations. They showed that the ceilings with pop rivet connections have the lowest probability of failure compared to other ceiling system variables.

Brandolese et al. (2019) conducted cyclic quasi-static tests on braced ceiling systems to characterize the behavior of the bracing systems. Further, they performed seismic performance evaluation using the capacity spectrum method, assuming elastic ceiling behavior. They highlighted that the elastic displacement demand for ceilings is lower for high period supporting structures and evaluated the appropriateness of perimeter clearance requirements given by ASTM E580.

Summary of previous studies

Previous studies have provided useful insights into the seismic behavior of suspended ceiling systems. However, several aspects of suspended ceiling systems
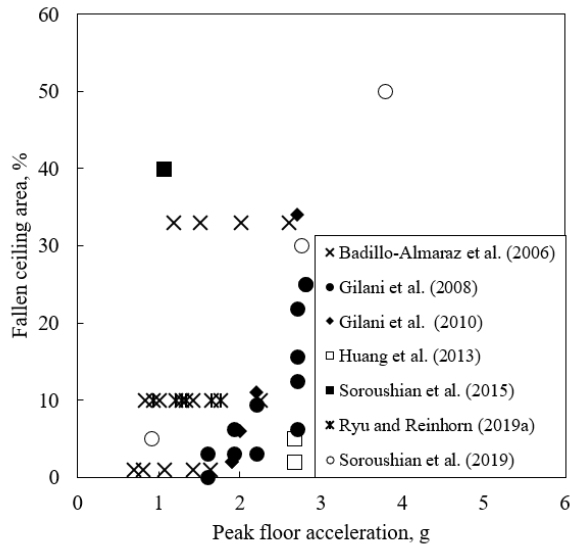
Figure 2.22 Different fragility of braced ceilings reported among different researchers

needed to be further investigated. Firstly, most of the previous studies were conducted using direct-hung lay-in suspended ceiling systems whereas ceilings with various configurations are utilized in common practice. Studies on ceiling systems needed to be conducted based on various types of suspended ceilings so that the derived design implications could be applied on more general ceiling systems. The numerical models for predicting the ceiling seismic behavior are too complicated to be used in engineering practice. More refined and simplified numerical models needed to be proposed. Lastly, the results of studies assessing effectiveness of ceiling lateral bracing are not consistent. For example, studies of Rihal and Granneman (1984), Badillo-Almaraz et al. (2007) and Huang et al. (2013b) showed that the presence of ceiling braces effectively reduced the seismic damage of ceiling specimens. Whereas, Yao (2000), Ryu and Reinhorn (2019a) demonstrated that the restraining effect of ceiling braces is very limited, and no observable performance enhancement

was identified. As shown in Figure 2.22, it is very difficult to draw a meaningful relationship between PFA and ceiling damage. Also, most of the previous studies mainly focused on the global failure modes and overall seismic performance, detailed dynamic responses of braced ceiling system have not been reported and are still not clearly understood. Therefore, more systematic experimental testing of bracing ceiling systems is required.

Chapter 3. Evaluation of Equivalent Static and Dynamic Analysis Methods

3.1. Introduction

The damage to nonstructural elements can be triggered by ground shaking intensities much lower than those required to initiate structural damage, leaving the building structurally intact but no longer functional. One of the main reasons for the higher vulnerability of nonstructural elements lies in the fact that most elements are attached on the elevated portion of a building and, thus, subjected to amplified ground motion generated by the dynamic response of the building. Therefore, the dynamic properties of both the building and nonstructural elements should be considered as key parameters in estimating the acceleration demand on nonstructural elements. However, in common practice, the relevant information may not be readily available to design engineers. The engineer in charge of the nonstructural element design usually does not have access to detailed information about the dynamic properties of the supporting structures.

Recognizing the reality that the dynamic properties of supporting structures and nonstructural elements are not generally available to design engineers at the relevant stage, and also based on the floor acceleration data observed in the past earthquakes, ASCE 7-16 (ASCE/SEI 2017) suggests the equivalent static approach, which can be implemented without knowing the dynamic properties of supporting structures, Despite its empirical and simplistic nature, the equivalent static method has been the most popular method in design practice. When the dynamic properties of the supporting structures and nonstructural elements are known, a more rational acceleration demand can be obtained using one of the dynamic analysis methods given in ASCE 7-16.

Several studies have already been conducted in order to evaluate the effects of dynamic characteristics of supporting structures on the acceleration demand on nonstructural elements. It is now well recognized that the ASCE 7-16 equivalent static method has several limitations. First, the peak floor acceleration and its distribution along the height of the building based on the equivalent static approach may significantly be different from the dynamic results in the case of tall, long-period structures (Kehoe and Freeman 1998). Second, the code-prescribed component amplification factor cannot capture the actual trend of the component amplification (Miranda and Taghavi 2009; Wieser et al. 2013). The effect of the nonlinear behavior of the supporting structure under the design earthquake is neglected (Rodriguez et al. 2002; Chaudhuri and Villaverde 2008). Furthermore, it has also been pointed out that the amplification of the floor acceleration by torsion might be appreciable and should be considered to avoid the unconservative design of nonstructural elements (Villaverde 1997; Anajafi and Medina 2019).
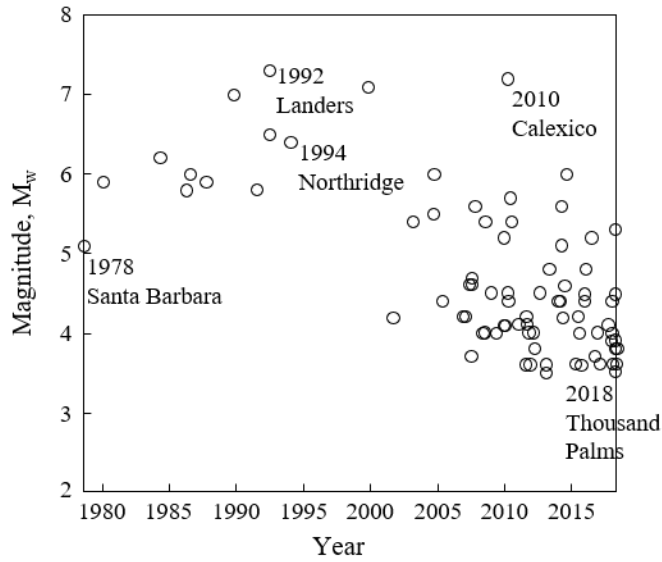
Figure 3.1 Earthquake database used for instrumented building database analysis

Although past studies provided valuable insights regarding the key parameters affecting the seismic demand on nonstructural elements, a more comprehensive and systematic evaluation of the equivalent static and dynamic methods is needed to better understand the effect of the influential parameters and draw useful design recommendations.

3.2. Effects of Supporting Structure Parameters

3.2.1. Floor acceleration from measured data and elementary structural dynamics

During a seismic event, nonstructural elements mounted on the elevated portion of a building are subjected to the amplified motion resulting from the dynamic re-

sponse of the building and the shaking associated with the element itself. The modification of shaking by the building response is one of the most important physical characteristics, which accounts for a significant portion of the acceleration demand on NSEs. Thus, the in-structure amplification due to a supporting structure is first investigated.

Simplified numerical building models often fail to capture the response characteristics of real buildings related to the flexibility of the floor diaphragm, torsional response (accidental/inherent), actual distribution of damage, contribution of infill and partitions, soil-foundation-structure interactions, damping effect, and interaction between nonstructural elements and supporting structure (Anajafi and Medina 2018). Analysis of up-to-date database of instrumented buildings using CESMD (Center for Engineering Strong Motion Data) was conducted. Preliminary analysis results for the peak floor acceleration (PFA) are presented in this section. The up-to-date database of the instrumented buildings comprising approximately 3,000 records was analyzed based on 63 Californian earthquakes, including Santa Barbara (5.1 M_w), 1992
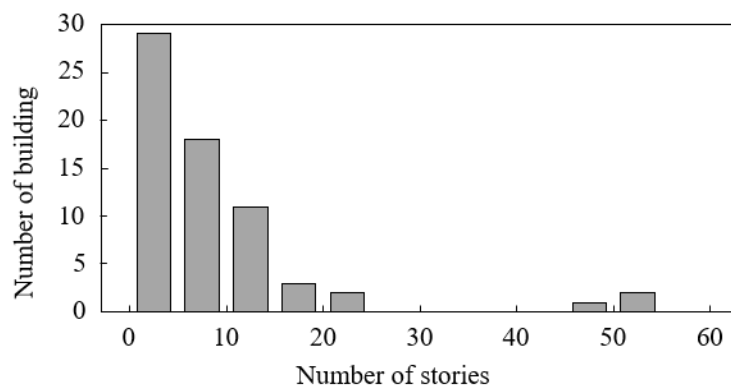
Figure 3.2 Database of instrumented buildings categorized by number of building stories

50
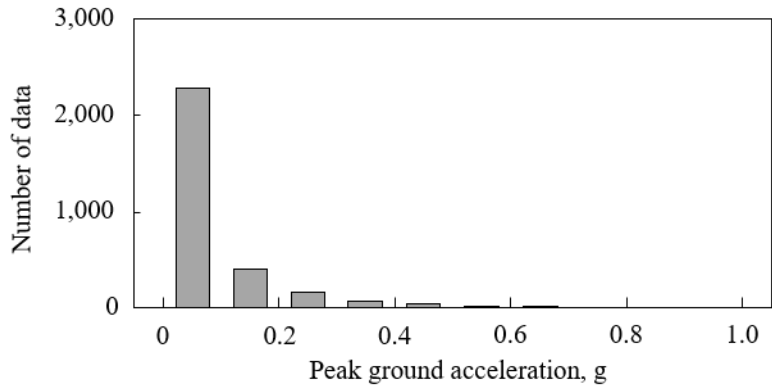
(a) Total nuber of instrumented building data
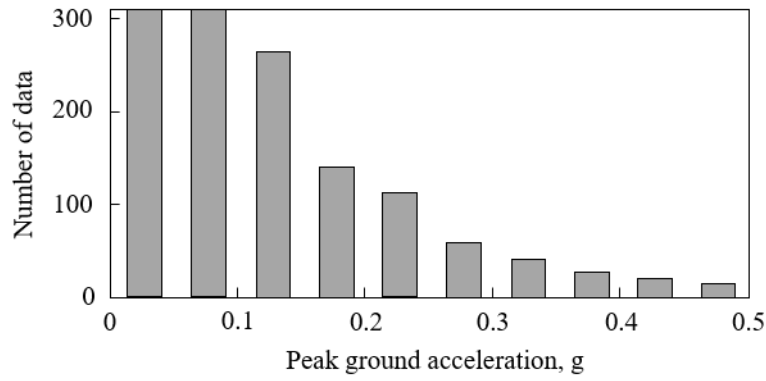
(b) Number of data with PFA within 0.0 to 0.50 g
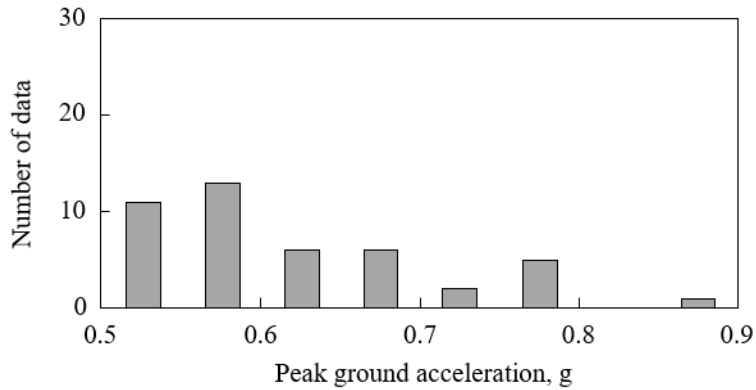
(c) Number of data with PGA over 0.50 g

Figure 3.3 Database of instrumented buildings categorized by peak ground acceleration
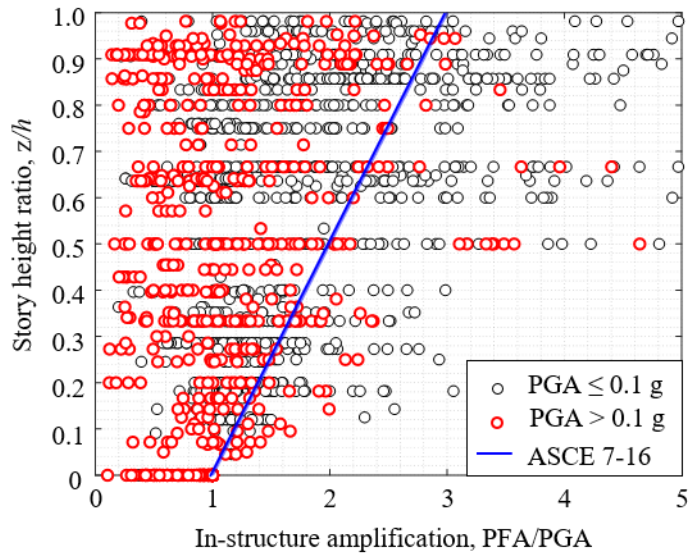
(a) All data
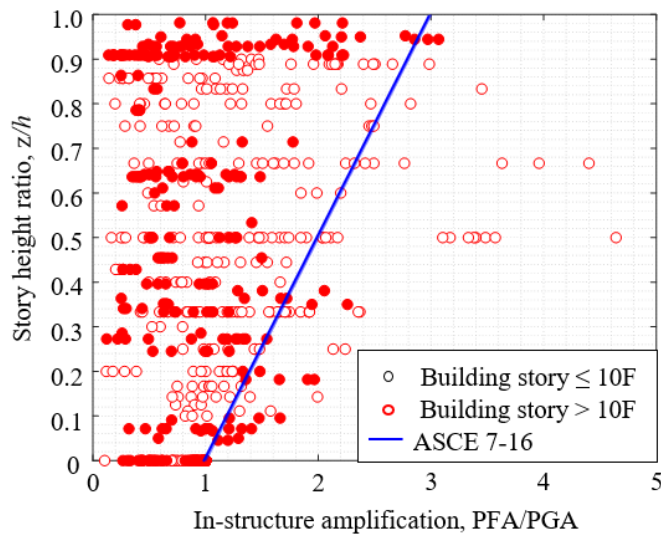
(b) Distribution based on building story

Figure 3.4 PFA distribution obtained from analysis of 63 Californian earthquakes

Landers (7.3 M_w), 1994 Northridge (6.7 M_w), and 2018 Thousand Palms (3.8 M_w), and 66 buildings, single- to 54-story high (see Figures 3.1 – 3.3).

Figure 3.4 compares the measured PFA normalized to PGA with the linear acceleration profile given in ASCE 7-16. First, it is observed from Figure 3.4 that for
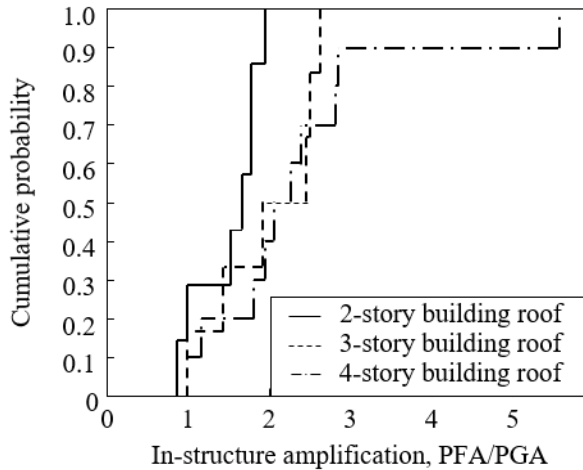
(a) Cumulative distribution function for 3-, 4-, 5-story building
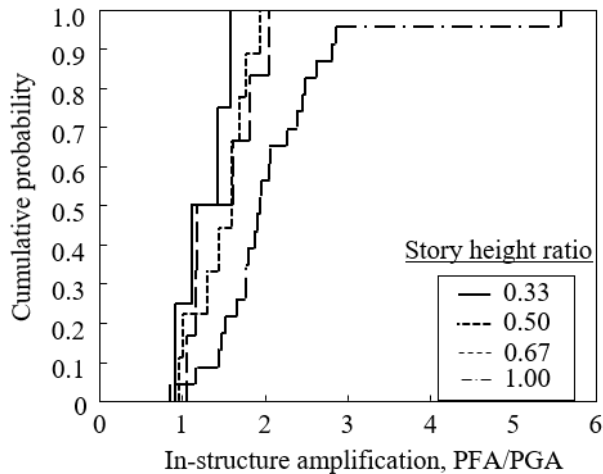
(b) Cumulative distribution function for different story height ratio

Figure 3.5 Cumulative distribution function drawn with respect to in-structure amplification

higher ground motion intensity (PGA > 0.10 g), PFA response is reduced, indicating the effect of supporting structure nonlinearity. In Figure 3.4 (b), it is noted that PFA in the building more than 10-story high is smaller than that in the lower-story buildings, implying the reduction of the spectral acceleration for the longer structural pe-

riod. These observations can also be found in Figure 3.5, which shows the cumulative distribution function obtained from the data with PGA over 0.10 g. These preliminary analysis results clearly indicate that the up-to-date database of the instrumented buildings does not well corroborate the design force formulation by the equivalent static approach.

Before evaluating the equivalent static method through numerical case studies, the theoretical equation for predicting the peak absolute floor acceleration is approximately derived to demonstrate some basic limitations existing in the current equivalent static approach. Just elementary structural dynamics (Chopra 2001) is sufficient for the derivation as shown below.

Consider a lightly damped single degree of freedom (SDOF) ($c \approx 0$) subjected to earthquake excitation $\ddot{u}_g(t)$.

$$\ddot{u}(t) + \omega_n^2 u(t) = -u_g(t) \tag{3.1}$$

In this case, the maximum absolute acceleration response can be obtained as

$$\ddot{u}_t = \ddot{u}(t) + \ddot{u}_g(t) = -\omega_n^2 u(t) \tag{3.2}$$

$$\ddot{u}_t = \omega_n^2 u_{max} \tag{3.3}$$

Given the design response spectrum, the maximum value ($\ddot{u}_{g,max}$) can be expressed as

$$\ddot{u}_{t,\max} = \omega_n^2 S_D(T_n, \zeta_n) = S_A(T_n, \zeta_n) \qquad (3.4)$$

where S_D and S_A, respectively, represent the ordinate in the displacement and acceleration response spectrum of the input excitation for a natural period T_n $(= 2\pi/\omega_n)$ and damping ratio ζ_n.

A similar approach can be extended to multi degree of freedom (MDOF) systems. The nth mode equation of motion for lightly damped MDOF structures can be approximated as,

$$\ddot{z}_n(t) + \omega_n^2 z_n(t) = -\Gamma_n \ddot{u}_g(t) \qquad (3.5)$$

where ω_n and ζ_n respectively represent the natural frequency and damping ratio of the system in its nth mode of vibration, $z_n(t)$ denotes the nth modal displacement response, and Γ_n represents the modal participation factor in its nth mode of vibration.

The maximum absolute floor acceleration at floor level j contributed by the nth mode is given as,

$$\ddot{u}_{n,j,\max}^t = \phi_{n,j}\Gamma_n \omega_n^2 S_D(T_n, \zeta_n) = [\Gamma_n S_A(T_n, \zeta_n)] \times [\phi_{n,j}] \qquad (3.6)$$

Combining all the modal contribution per SRSS rule yields,

$$\ddot{u}^t_{j,\max} = \sqrt{\sum_{n=1}^{N}[\phi_{n,\mathrm{j}}\Gamma_n\omega_n^2 S_D(T_n,\zeta_n)]^2}$$

$$= \sqrt{\sum_{n=1}^{N}[\phi_{n,\mathrm{j}}\Gamma_n S_A(T_n,\zeta_n)]^2} \tag{3.7}$$

Several observations can be made based on Eqs. (3.6) and (3.7). First, the PFA implied in Eq. (2.1) can be extracted as

$$PFA = [0.4 S_{DS}] \times [1 + 2\frac{z}{h}] \tag{3.8}$$

Comparing Eqs. (3.6) and (3.8) reveals that PFA in principle should be based on the structural-period dependent spectral acceleration (S_A) rather than S_{DS}, which is the short-period spectral acceleration independent of the structural period. It is well known from Newmark's spectrum theory (Newmark and Hall 1982) that when structures belong to the velocity-sensitive region, S_A is inversely proportional to the structural period (T_n). When T_n becomes longer (say, 0.5 sec or more), the PFA can be much smaller than that based on $0.4 S_{DS}$ in Eq. (3.8). It is also observed that the distribution of PFA along the building height should follow structural mode shape (φ_n) rather than the linear distribution ($1+2z/h$) in ASCE 7 or Eurocode 8. The combined modal response in Eq. (3.7) indicates that the floor acceleration is proportional to the squared frequency (ω_n^2). Thus, the contribution of the higher modes is more influential, even though the modal participation factor (Γ_n) reduces for higher modes

3.2.2. Numerical case studies

This section evaluates the effects of several supporting parameters on the response of the floor acceleration. A total of four three-dimensional building models (Figure 3.6) were analyzed using ETABS 2016 (ETABS 2017). In the first set of analyses, three SAC steel moment frame buildings (SAC MRFs) designed according to the UBC 1994 for the Los Angeles area (Gupta and Krawinkler 1999) were adopted. In these buildings, the perimeter moment frames provided the seismic resistance needed. These SAC MRFs were used to investigate the effect of the structural period, higher modes, and structural nonlinearity. In the next analysis, a 4-story building was selected from the telecommunication center buildings in Korea to investigate the effect of the torsional behavior. The center of mass (CoM) and the center of rigidity (CoR) were marked on the floor plan, as shown in Figure 3.6(d). The building had severe torsional irregularity, and the distance between CoM and CoR was 40.5 % of the transverse dimension of the building. The fundamental periods obtained from the eigenvalue analysis of these four building models are summarized in Table 3.1.

Table 3.1 Summary of fundamental periods of analyzed building models

Story	T_n, sec.	Structural system
3	1.16	Perimeter steel moment resisting frame
9	2.37	Perimeter steel moment resisting frame
20	3.87	Perimeter steel moment resisting frame
4	0.66	RC moment frame with eccentric staircase shaft

(a) 3-story SAC MRF
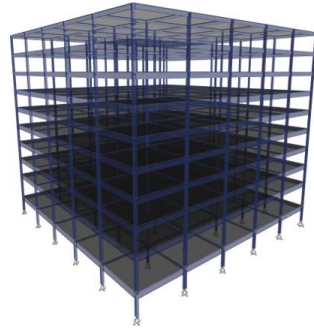
(b) 9-story SAC MRF

(c) 20-story SAC MRF
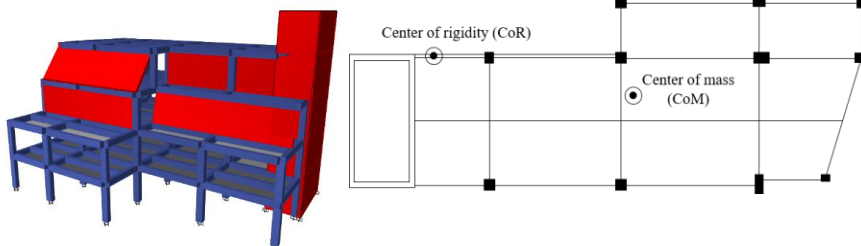
(d) 4-story RC frame with torsional irregularity

Figure 3.6 Three-dimensional case study buildings
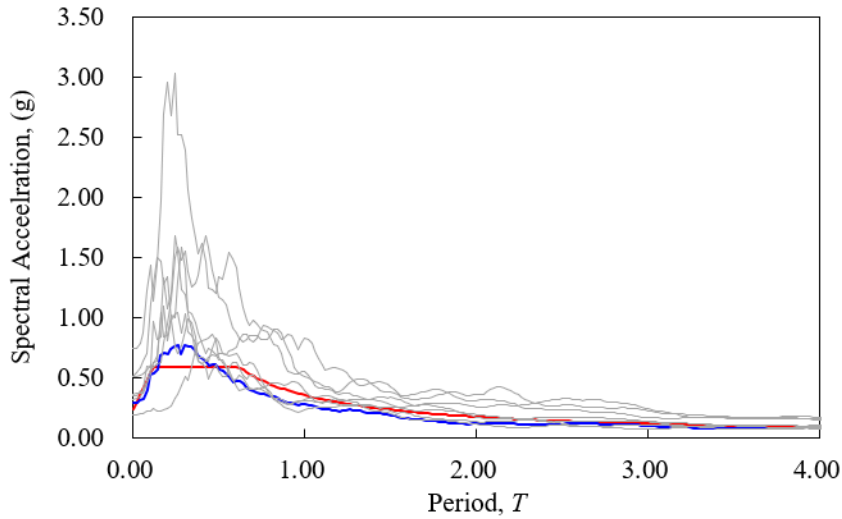
Figure 3.7 Input earthquakes scaled to match design spectrum

In this study, linear and nonlinear time history analyses were conducted using a suite of seven far-field ground motions selected from PEER-NGA strong-motion database. The lists of the ground motions are summarized in Table 3.2. The amplitudes of ground motions were scaled to be compatible with the design spectrum per

Table 3.2 Ground motion records selected

Earthquake	Year	Station	Magnitude, M_w	Epicentral distance, km
Chuetsu-oki, Japan	2007	Sanjo	6.8	21.40
Chuetsu-oki, Japan	2007	Niigata Nishi Kaba District	6.8	27.83
Imperial Valley	1979	El Centro Array # 11	6.5	12.56
Loma Prieta	1989	Fremont – Mission San Jose	6.5	39.32
Iwata, Japan	2008	Misato Miyagi Kitaura - A	6.9	38.04
Chi-Chi, Taiwan	1999	TCU070	6.2	45.94
Kobe, Japan	1995	Tadoka	6.9	31.69

ASCE 41-13 (ASCE/SEI 2013) (see Figure 3.7). The intensity of the ground motions was arbitrarily increased to induce different degrees of nonlinearity in the structure when studying the effect of nonlinearity. The lumped plastic hinges were introduced at each end of the beam and column elements, and the fiber hinges were used for the wall elements. The modeling parameters for the plastic hinges were determined according to ASCE 41-13. Bi-directional dynamic analyses were conducted for all the building models.

Effect of structural period and higher modes

Figure 3.8 shows the results of the linear time history analysis for SAC MRFs. The ordinate was normalized to PGA in order to evaluate the in-structure amplification of the acceleration along the building height. First, it is observed that the floor acceleration response is highly scattered because of the stochastic nature of the input motions. As mentioned previously, the floor acceleration is increasingly overestimated by the equivalent static method as the fundamental period of the building becomes longer (see Figures 3.8(b) and (c)). Regarding the spatial distribution, due to the increased higher mode effect, the floor accelerations are more or less constant along the building height as the building becomes taller. It is interesting to note that for the 20-story building, the ratio PFA/PGA is almost unity in the mean sense, except for the top and bottom stories, indicating that the in-structure amplification is almost negligible.
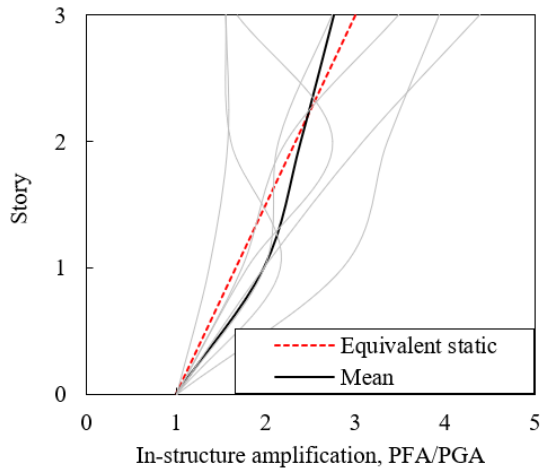
(a) 3-story SAC MRF ($T_n = 1.16$ sec.)
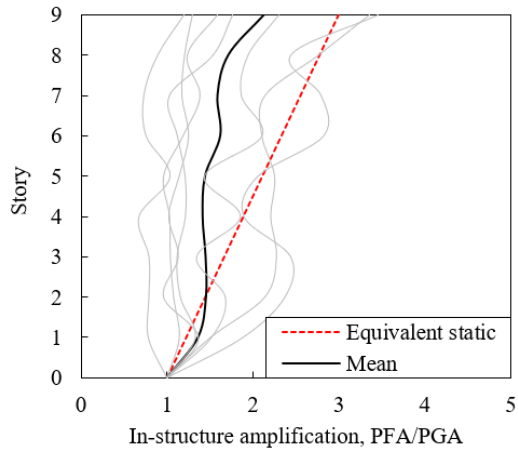
(b) 9-story SAC MRF ($T_n = 2.37$ sec.)
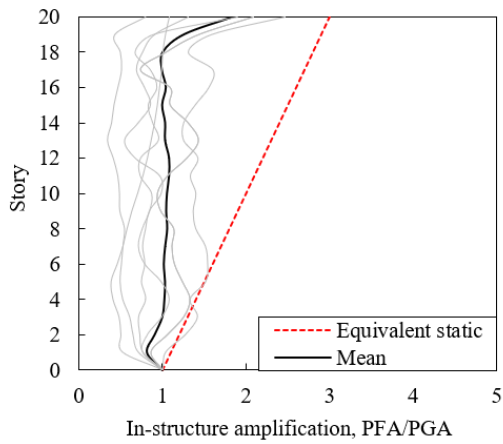
(c) 20-story SAC MRF ($T_n = 3.87$ sec.)

Figure 3.8 Effects of structural period on floor acceleration amplification and profile

Effect of structural nonlinearity

In Figure 3.9, the results of the incremental nonlinear time history analysis are presented. The ground intensity up to 100 % of the design earthquake did not cause significant nonlinear behavior for 9- and 20-story buildings. It is observed in Figure 3.9 that as the intensity of the ground motion increases, the floor acceleration is also reduced because of the period lengthening due to yielding. It is interesting to note that the PFA of the 20-story building becomes even smaller than PGA when subjected to 250 % of the design earthquakes.

Effect of torsional irregularity

In Figure 3.10, the results of the linear time history analysis for the torsionally irregular building (Figure 3.6(d)) are presented. The results were reported using the maximum floor acceleration, which is generally observed at the farthest point from the CoR, and the acceleration at the CoR where the effect of torsional amplification is minimized. The in-plane torsional amplification is measured by dividing the maximum floor acceleration by the acceleration at the CoR.

First, it is observed from Figure 3.10 that the maximum floor acceleration is highly underestimated by the equivalent static method, and the vertical profile is neither linear nor constant, which is probably caused by the combined effect of the in-structure and torsional amplifications. In this torsionally irregular building, a maximum torsional amplification of approximately 250 % was observed (Figure 3.10(c)). Figure 3.11 shows that PFA, as well as the torsional amplification, tend to decrease as the nonlinearity increases. However, PFA was still underestimated by the equivalent static method even though the building experienced significant nonlinearity.
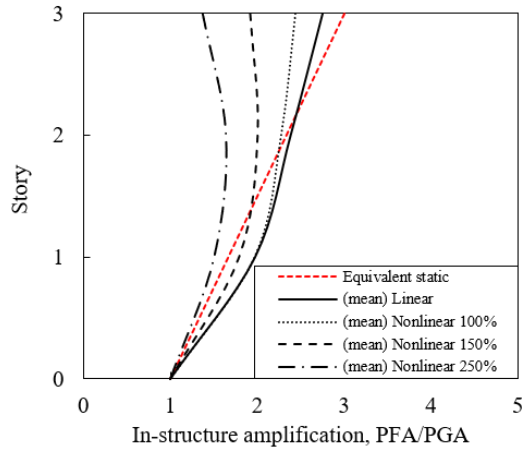
(a) 3-story SAC MRF (T_n = 1.16 sec.)
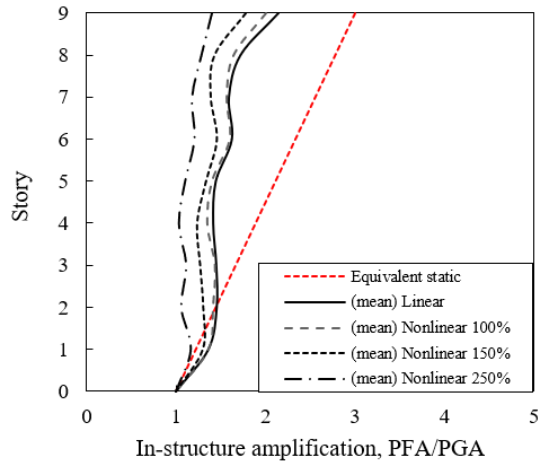
(b) 9-story SAC MRF (T_n = 2.37sec.)
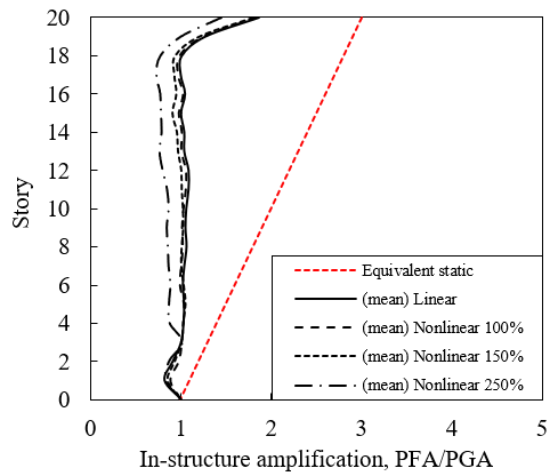
(c) 20-story SAC MRF (T_n = 3.87 sec.)

Figure 3.9 Effects of structural nonlinearity on floor acceleration amplification and profile
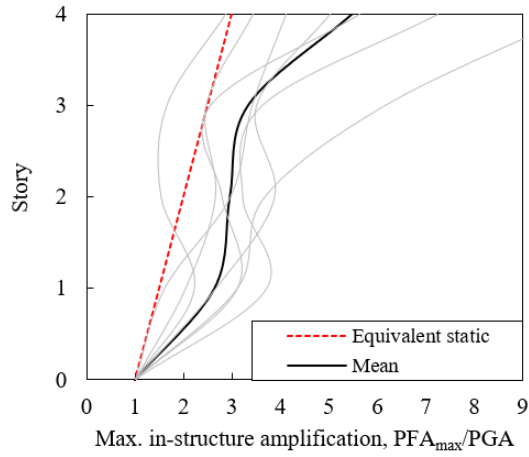
(a) Maximum acceleration at the farthest point from CoR
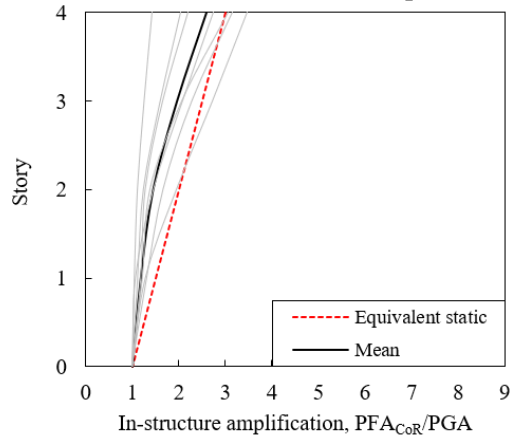
(b) Acceleration at CoR
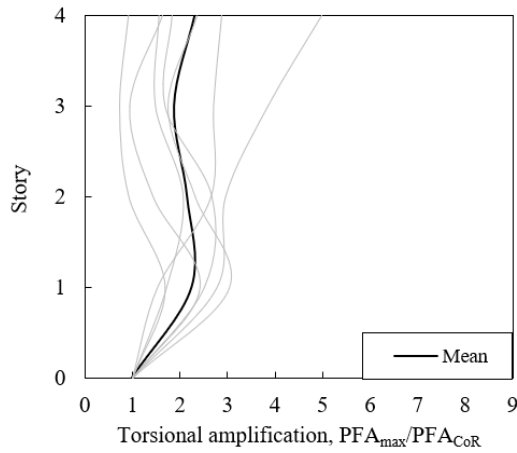
(c) Torsional amplification

Figure 3.10 Effects of torsional irregularity on floor acceleration amplification and profile
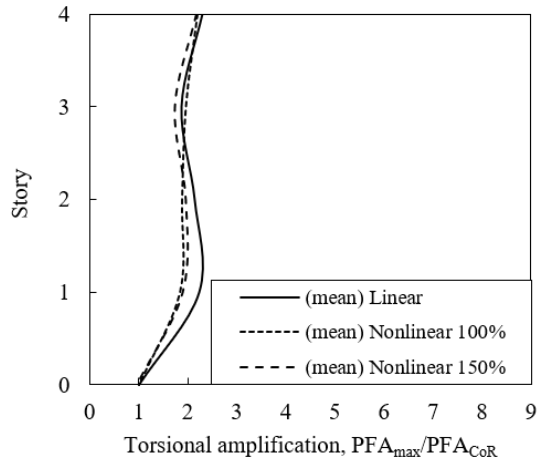
(a) Maximum acceleration at the farthest point from CoR
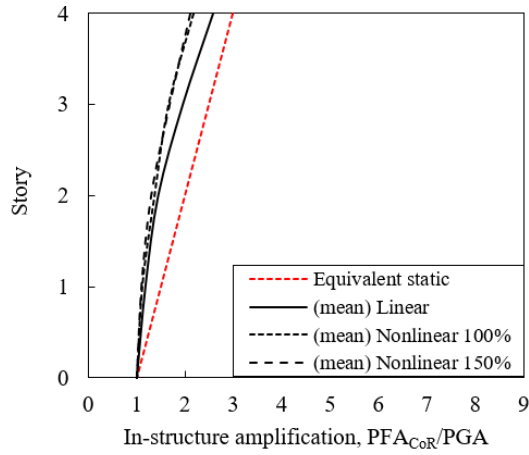
(b) Acceleration at CoR
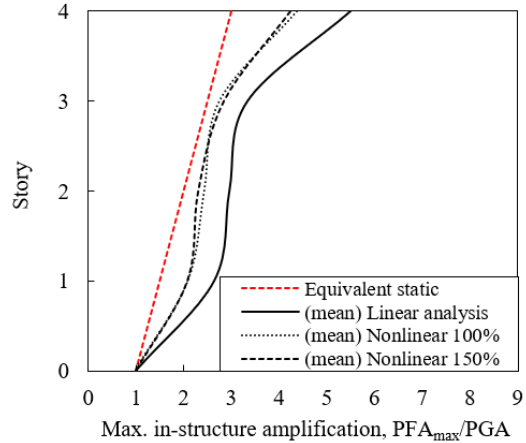
(c) Torsional amplification

Figure 3.11 Effects of nonlinearity on floor acceleration amplification and profile of torsionally irregular building

3.3. Evaluation of Component Amplification

In this section, the effect of the supporting structural characteristics on the peak component amplification is evaluated. The evaluation was based on the 5 %-damped mean floor response spectrum calculated from the seven ground records in Table 3.2. the floor response spectrum ordinate normalized by PFA represents the component amplification factor when the behavior of NSEs is assumed as elastic.

Effect of component period

Figures 3.12 – 3.14 show the component amplification obtained from the SAC MRF buildings. The mean floor response spectrum at several different locations, including the nonlinear analysis results, are presented in these figures. It is first observed that the component amplification is significantly affected by the component period (T_p), in some cases reaching as high as 6.0. In all the buildings analyzed, the highest component amplification corresponded to the higher modes of the supporting structure rather than the fundamental mode. The shape of the component amplification spectrum in the 3-story building changed slightly along the building height (see Figure 3.12). However, as can be seen in Figure 3.14, the spectrum shape significantly changed depending on the floor location (z/h) when it came to the 20-story building because of the increased higher mode effect. The component amplification tends to decrease as the period of the structure increases. However, the amplification factor recommended by ASCE 7-16 for flexible components ($a_p = 2.5$) significantly underestimates the component amplification when the fundamental periods of NSEs are tuned to the structural periods of higher modes.
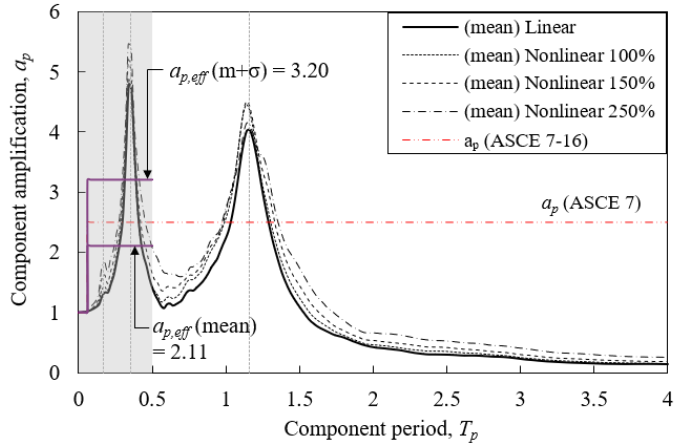
(a) Roof ($z/h = 1.0$)
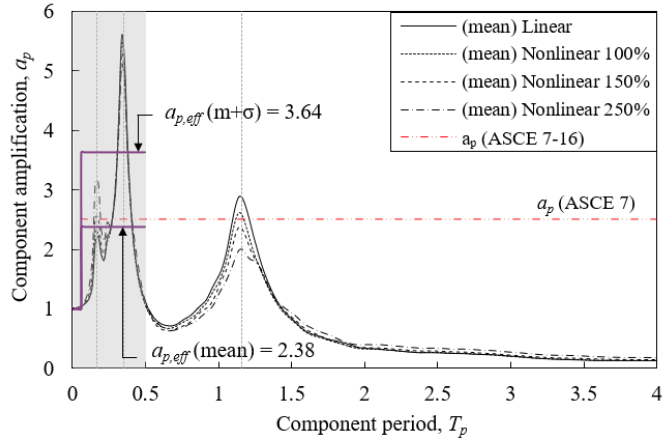
(b) 2nd floor ($z/h = 0.7$)
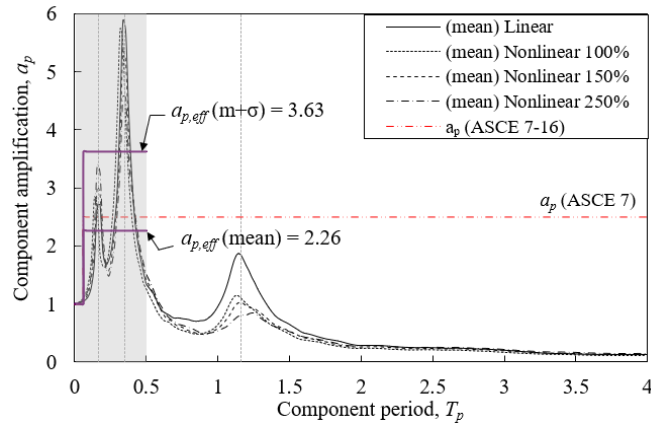
(c) 1st floor ($z/h = 0.3$)

Figure 3.12 Variation of component amplification factor (a_p) depending on floor location and component period (T_p) (3-story SAC MRF)
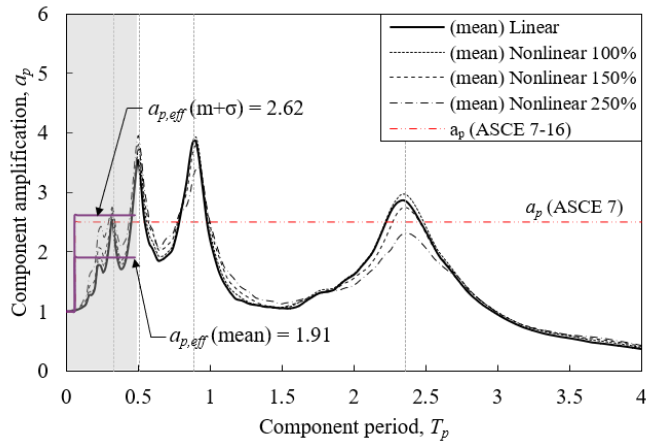
(a) Roof ($z/h = 1.0$)
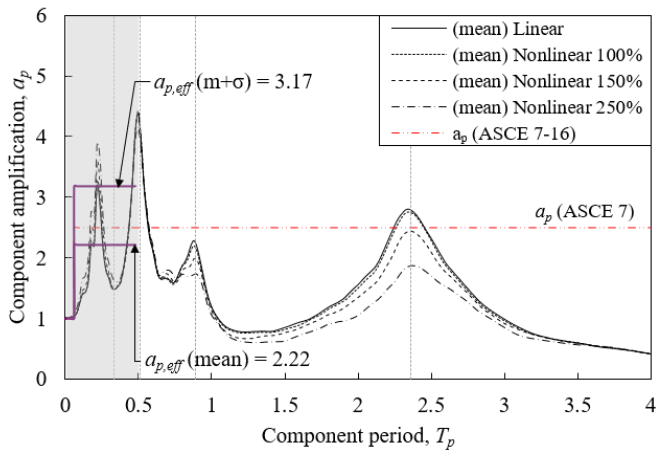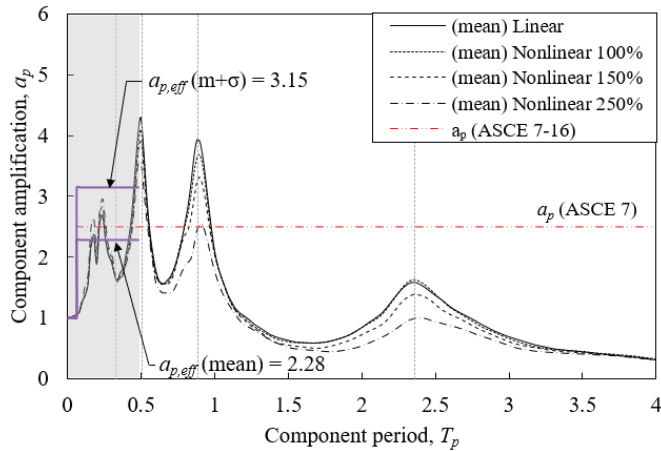
(b) 2nd floor ($z/h = 0.7$)

(c) 1st floor ($z/h = 0.3$)

Figure 3.13 Variation of component amplification factor (a_p) depending on floor location and component period (T_p) (9-story SAC MRF)
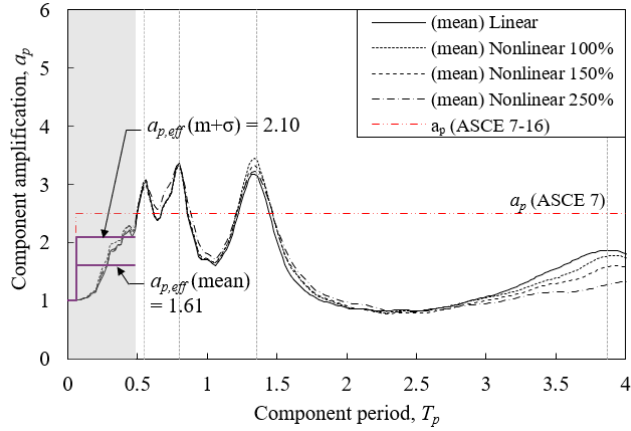
(a) Roof ($z/h = 1.0$)
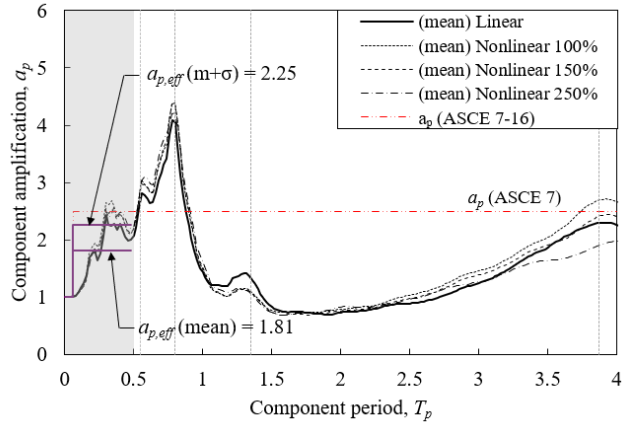
(b) 2nd floor ($z/h = 0.7$)
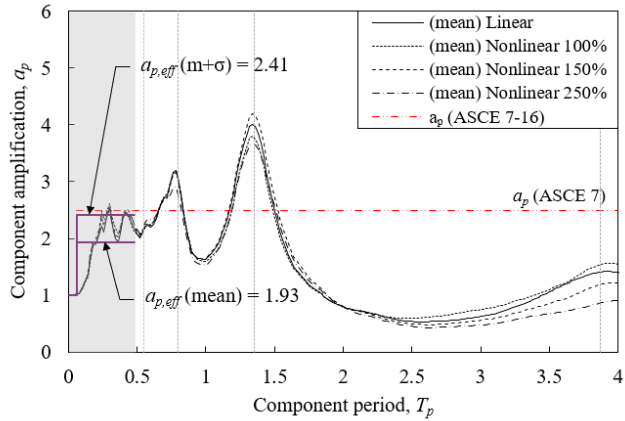
(c) 1st floor ($z/h = 0.3$)

Figure 3.14 Variation of component amplification factor (a_p) depending on floor location and component period (T_p) (20-story SAC MRF)

Overall, the code-prescribed a_p does not well describe the actual variation of the component amplification because of its inherent simplicity. However, as mentioned previously, in many cases, the design should be conducted without knowing information about the dynamic properties of the supporting structures and nonstructural elements. In such cases, the use of a simple a_p factor is inevitable. In this context, the concept of the *effective* component amplification factor ($\underline{a_{p,eff}}$) is proposed considering the practical range of the component period T_p as follows. The component amplification factor a_p is calculated as the ratio of PCA to PFA.

$$a_p = \frac{PCA}{PFA} \tag{3.9}$$

Figures 3.12-14 summarize the a_p values obtained from the extensive dynamic analysis of SAC MRFs using the seven input motions in Table 3.2. The effective PCA is defined as the average of a_p values in the component period range between $0.06 - 0.5$ sec as follows.

$$a_{p,eff} = \frac{\int_{0.06}^{0.5} a_p(T)dT}{0.5 - 0.06} \tag{3.10}$$

The period range for defining $a_{p,eff}$ was chosen based on the natural frequency database of nonstructural elements reported by ATC (NIST 2017). The database was accumulated from the dynamic test results of a variety of nonstructural elements used in California hospitals. The database showed that all the tested nonstructural elements (mechanical and electrical units) had a natural frequency higher than 2 Hz

70
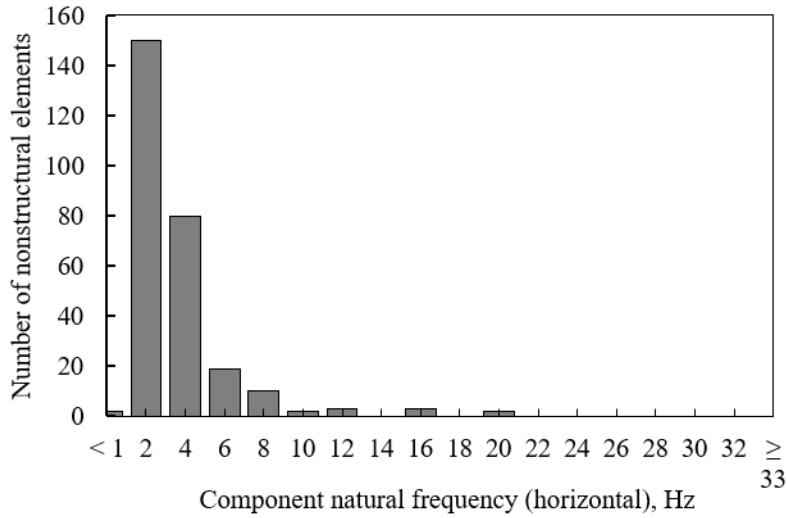
Figure 3.15 Database of natural frequency for spring-isolated nonstructural element (NIST 2017)

(less than 0.5 sec), and 84 % of the rigidly-mounted (see Figure 2.5) and 100 % of the spring-isolated nonstructural elements (see Figure 3.15) were classified as flexible according to the criterion of ASCE 7-16 ($T_p \geq 0.06$ sec). Thus, the component amplification in the T_p range of 0.06 sec to 0.5 sec should be the focus of investigation (refer to the gray band for $T_p < 0.5$ sec in Figure 3.12-14). In calculating $a_{p,eff}$ according to Eq. (3.10), only $a_p(T)$ values obtained from the linear dynamic analysis of the supporting structures were considered because the difference between the elastic and nonlinear analysis results was negligible. The mean and mean plus one sigma values of $a_{p,eff}$ are marked as the horizontal solid lines in Figures 3.12-14.

Note that because of the randomness of the input motions and the small number of samples (seven cases), the standard deviation should be high. A more extensive investigation using large number of input motions and diverse structural systems is

beyond the scope of this study. Although $a_{p,eff}$ obtained in this study is based on limited analysis data for steel moment frames, several observations can still be made.

The value of $a_{p,eff}$ (mean) were lower than ASCE 7 recommended value of 2.5. The average of all $a_{p,eff}$ (mean) values was 1.88, whereas, the average of $a_{p,eff}$ (m+σ) for all the analyzed cases was 2.64, which is comparable to the value of 2.5 in ASCE 7.

Effect of structural nonlinearity

As can be seen in Figure 3.12-14, the nonlinear behavior of the supporting structures generally decreased the component amplification. A more noticeable decrease in the component amplification occurs only when the component period T_p is long and close to the fundamental period of the supporting structure. As noted above, considering that the component period (T_p) is mostly shorter than 0.5 sec, and thus, would belong to the period of higher modes, it may be concluded that the nonlinearity of the supporting structure would have a negligible effect on the acceleration demand on the typical nonstructural elements rigidly mounted on the floor.

Effect of torsional irregularity

For the 4-story torsionally irregular structure, a unique ap spectrum was obtained as shown in Figure 3.16. Pronounced second and third spikes were created in a band due to the closely spaced torsional modes of vibration. Thus, the nonstructural elements installed in the torsionally irregular buildings are expected to experience higher acceleration because of the torsionally-amplified floor acceleration and the band effect resulting from closely spaced modes of the torsional vibrations.
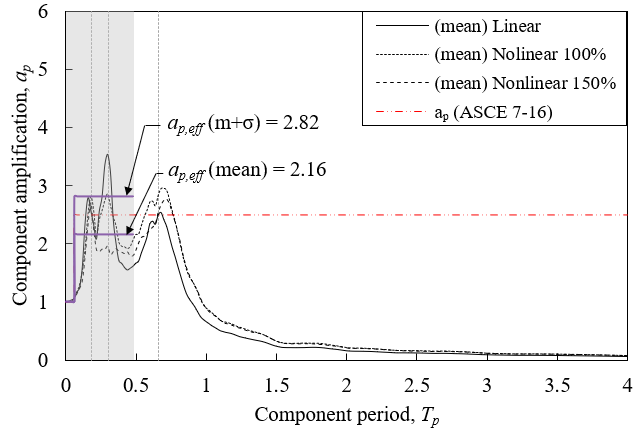
(a) Roof ($z/h = 1.0$)
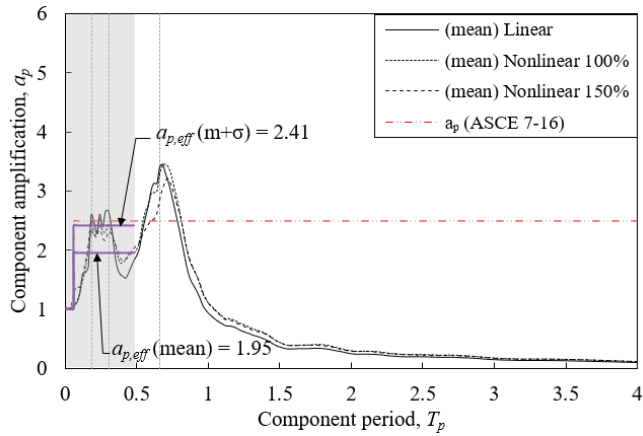
(b) 2nd floor ($z/h = 0.5$)

Figure 3.16 Variation of component amplification factor (a_p) depending on floor location and component period (T_p) (4-story torsionally irregular building)

3.4. Comparative Evaluation of Peak Component Acceleration

In this section, PCA was comparatively evaluated using the equivalent static and dynamic analysis methods permitted in ASCE 7-16. The dynamic methods include the response spectrum method, the floor response spectrum method, and the alternate floor response spectrum method. In this case study, the component response modification factor (R_p) was assumed as 1.0.

First, for the SAC MRFs, the alternate floor response spectrum method yielded a rough correlation with the floor response spectrum; however, it failed to predict the peak values. Table 3.3 shows the PFA values calculated according to the alternate floor response spectrum method for the 3-story SAC MRF. In this method, PFA at each mode is determined by multiplying the modal participation factor with the spectral acceleration corresponding to each modal period. The first-mode PFA is just equal to PGA, or no amplification at all, indicating that the effect of in-structure amplification was not well-captured by this method. Thus, even with a relatively high component amplification factor ($a_p = D_{AF} = 5.0$), the alternate floor response spectrum method generally showed unconservative results at the tuned period compared to the floor response spectrum method.

As can be seen in Figure 3.17, the equivalent static method generally showed much conservative results for all the SAC MRFs. Especially, for 9- and 20-story buildings, PCA was significantly overestimated mainly due to the assumption of the linear amplification of PFA in this method. However, according to ASCE 7-16, the design force should be governed by the upper limit ($1.6S_{DS}$), which is equal to 4 times the effective PGA ($0.4S_{DS}$). Without this upper limit, the design force can be amplified by up to 7.5 times PGA in these case studies.

However, as noted before, our investigation needs to focus on the component acceleration in the "practical" period range of $T_p \leq 0.5$ sec where most of the rigidly mounted nonstructural elements would belong. Thus, the mean and mean plus one sigma of effective PCA, $A_{p,eff}$ (mean) and $A_{p,eff}$ (m+σ) were calculated by averaging similar to Eq. (3.10). The $A_{p,eff}$ (m+σ) values obtained from the 3-, 9-, and 20-story SAC MRFs at the roof level were 6.1, 4.9, and 2.5 times PGA, respectively, showing fluctuation with higher values for short period buildings. However, the total average value of $4.5 \times$ PGA was comparable to the upper limit ($4.0 \times$ PGA) prescribed by ASCE 7-16.

In the case of the torsionally irregular 4-story building, the equivalent static method significantly underestimates the component acceleration because it neglects the effect of torsional amplification (see Figure 3.18). Enforcing the upper cap (4.0 $\times$ PGA) leads to further underestimation; $A_{p,eff}$ (mean) and $A_{p,eff}$ (m+σ) were 10.9 times and 14.2 times PGA, respectively. The response spectrum analysis method gave results comparable to the floor response spectrum method. As mentioned above,

Table 3.3 PFA calculated according to alternate floor response spectrum method (3-story SAC MRF, roof level)

	1st mode	2nd mode	3rd mode
Period	1.16	0.35	0.17
S_{ai} (spectral acceleration, g)	0.27	0.90	0.82
p_{ix} (participation factor – roof)	1.22	-0.31	0.07
PFA ($= S_{ai} \times p_{ix}$)	0.33 ($= 1.0 \times$ PGA)	0.28 ($= 0.8 \times$ PGA)	0.05 ($= 2 \times$ PGA)
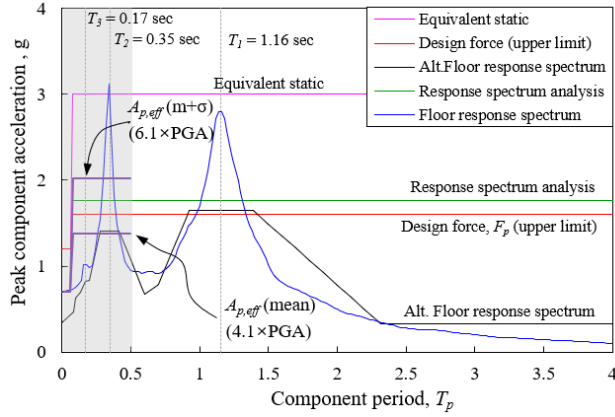
(a) 3-story SMRF
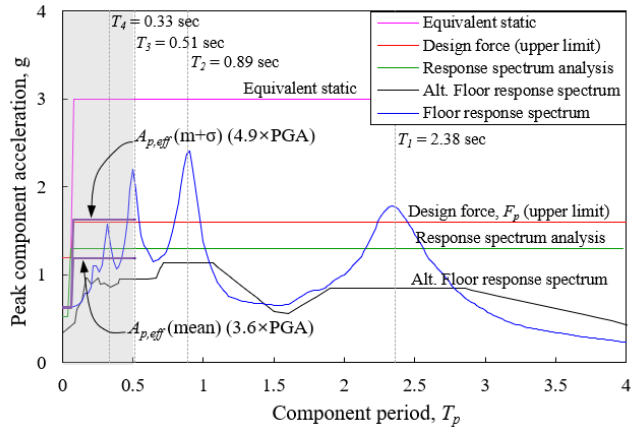
(b) 9-story SMRF
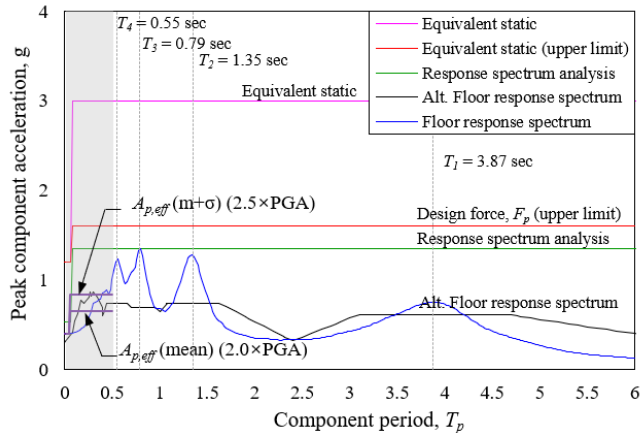
(c) 20-story SMRF

Figure 3.17 Comparison of PCA at roof level depending on analysis methods adopted (SAC MRFs)
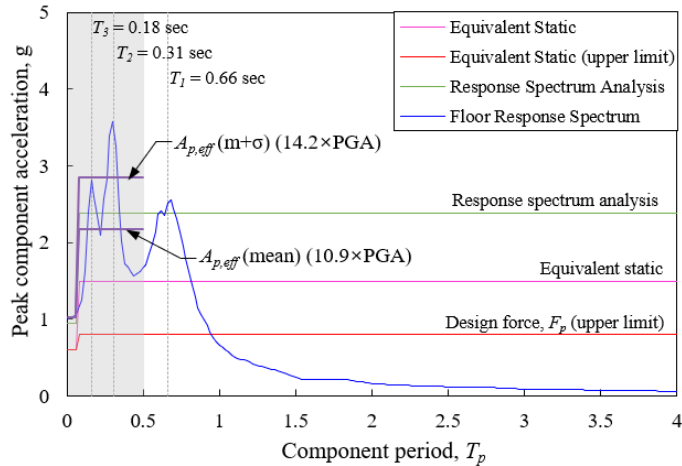
Figure 3.18 Comparison of PCA at roof level depending on analysis methods adopted (4-story torsionally irregular building)

because of the combined effects of the torsional amplification and closely spaced mode of vibrations, the PGA amplification in this torsionally irregular building was much higher than the regular SAC MRFs. Considering that the appropriate torsional amplification factor is not yet introduced in the equivalent static method, the dynamic methods should be preferred to avoid unconservative design if a building is severely irregular torsion-wise.

3.5. Summary and Conclusions

This study conducted a comparative evaluation of the equivalent static and dynamic methods suggested by ASCE 7-16 in order to better understand the effect of the potential influential parameters on the acceleration demand on nonstructural elements. The results are summarized as follows.

(1) The analysis of the up-to-date database of the instrumented building comprising approximately 3,000 records clearly showed that the measured PFA does not well corroborate with the PFA suggested by the ASCE 7-16 equivalent static approach. Elementary structural dynamics also indicated that the magnitude and profile of PFA should be determined based on the structural period-dependent spectral acceleration and structural mode shape.

(2) The numerical case study of this paper re-confirmed that PFA could be affected by the modal properties, nonlinearity, and torsional behavior of the supporting structures. The equivalent static method generally yielded conservative results for all the regular 3-, 9- and 20-story steel moment-resisting frame buildings. As the building became taller, the conservatism increased further, and the mean PFA distribution along the building height became almost uniform. In the 20-story building, the average ratio of PFA/PGA was very close to unity except for the top and bottom stories, indicating the in-structural amplification is negligible. However, the ASCE 7-16 design upper cap (4.0 × PGA) reduced the over-conservatism in the equivalent static method, and the resulting design acceleration was generally comparable to the *effective* PCA defined as the average of PCA for the practical period range between 0.06 sec and 0.5 sec, where the fundamental periods of most of the rigidly mounted nonstructural elements would belong.

(3) The floor response spectrum analysis of this study demonstrated that the component amplification is strongly dependent on the modal periods of the

supporting structures. Generally, a higher component amplification was observed when the component's period corresponded to higher modal periods of a supporting structure. However, the nonlinear behavior of the supporting structures was shown to have a negligible effect on the acceleration demand of the components whose periods corresponded to the higher modal periods of the supporting structures. The code-prescribed component amplification factor ($a_p = 2.5$) was generally unconservative around the tuning periods compared to the floor response spectrum approach, although it became more comparable to the component amplification in the practical period range between 0.06 sec and 0.50 sec.

(4) In the case of the torsionally irregular 4-story building, because of the combined effects of torsional amplification and closely spaced modes of vibration, the PCA predicted by the floor response spectrum approach was much higher than that predicted by the equivalent static method. The mean PCA in the practical period range between 0.06 sec and 0.50 sec was 2.50 times higher ($= 10.9 \times \text{PGA}$) than the ASCE 7-16 upper cap ($1.6S_{DS} = 4.0 \times \text{PGA}$). Considering that appropriate torsional amplification is not yet accounted for in the equivalent static method, the dynamic methods should be preferred to avoid unconservative design if a building is severely irregular in torsion-wise.

Chapter 4. Experimental Study on Seismic Demand of Nonstructural Elements

4.1. Introduction

A great research effort has been devoted over the last few decades to develop a rational seismic design method for nonstructural elements. For the most part, this effort has been given through numerical studies which tried to analyze the effects of structural and nonstructural dynamic properties on the seismic demand. Recently, ASCE 7-22 proposed a much more advanced nonstructural element seismic design procedure. As discussed in Chapter 2, the major efforts were given to reflect the effects of structural and component nonlinearity on the seismic demand. Despite the improvements made, however, there still remains room for further advancement because the proposed procedures were developed largely based on numerical studies, which were performed based on the simplified idealized structure and nonstructural mathematical models. Especially regarding the nonlinear behavior of nonstructural

elements, ASCE 7-22 still provides design factors that were largely based on engineering judgments because there is still a lack of experimental studies or instrumented nonstructural element databases to be utilized for the analysis. Also, it should be highlighted that despite some efforts given to evaluate the seismic performance of nonstructural elements based on a full-scale multi-story level building structures (for example, Pantoli et al 2016; Chen et al 2016; Matsuoka et al. 2008; Dao et al 2011; Sato et al. 2011) only a handful of studies were able to incorporate the nonstructural seismic demand on their research scope. Most studies focused on evaluating the seismic performance of individual nonstructural elements.

In this chapter, shaking table tests results based on a full-scale multi-story level structure were performed. This study was conducted as a part of a Korean government-funded joint research project in which 5 universities and more than 10 industry sponsors collaborated to systematically investigate the seismic performance of NSEs. A variety of architectural NSEs was installed in a full-scale two-story steel moment frame mounted on shake tables. This chapter focused on analyzing the seismic demand on nonstructural elements and evaluating the effects of component nonlinearity based on steel rack specimens installed on the roof floor of the testing frame.

4.2. Shake-Table Test of Full-Scale 2-Story Steel Moment Frame

A total of 10 types of nonstructural elements were installed in the 2-story test frame by the collaborative research team consisting of 5 universities and more than 10 industry partners. The nonstructural elements included stone and steel panel exterior claddings, metal panel and lightweight suspended ceiling systems, full- and
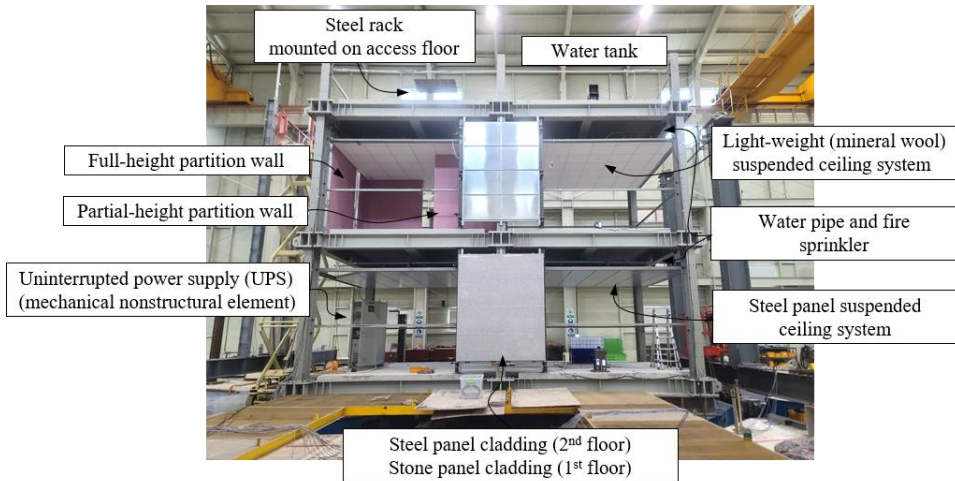
Figure 4.1 Overview of full-scale 2-story steel moment frame mounted on an array of two shake tables with various nonstructural elements.

partial-height partition walls, steel racks mounted on access floors, water tanks, pipes, fire sprinklers, and UPS (mechanical nonstructural elements) (see Figure 4.1). This chapter focused on analyzing the nonstructural seismic demand based on the floor and component responses measured during shake-table testing. The seismic performance of a suspended ceiling specimen will be presented in Chapter 5.

4.2.1. Full-scale 2-story steel moment frame

A two-by-one bay steel moment frame was fabricated, which had a plan dimension of 4.5 m × 9.0 m and a total height of 6.75 m as shown in Figure 4.2. The steel frame was mounted on an array of two isolated shake tables, and incremental uniaxial tests were conducted by shaking the two tables synchronously. The measurement plan using the accelerometers and LVDTs is shown in Figure 4.2.

※ Beam & Column : SS275 (F_y = 275 Mpa, F_u = 410 Mpa)
Concrete slab (t = 110 mm) : f_{ck} = 30 Mpa

■ : Measurements (A: Accelerometer, D: LVDT)
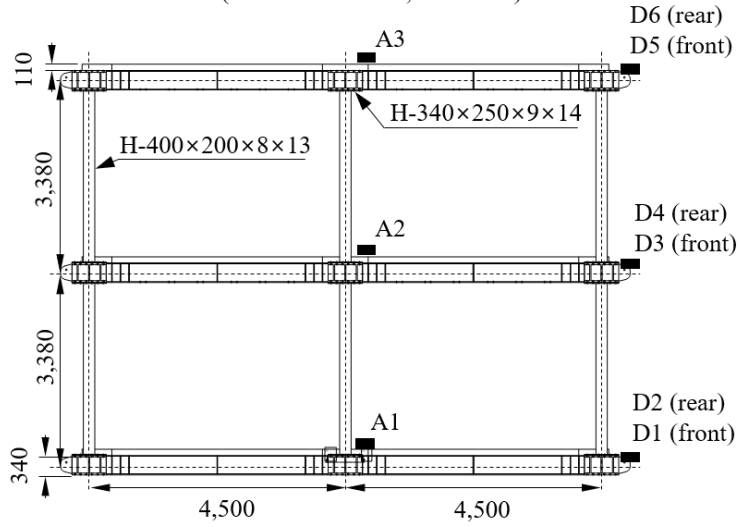
(a) Front view
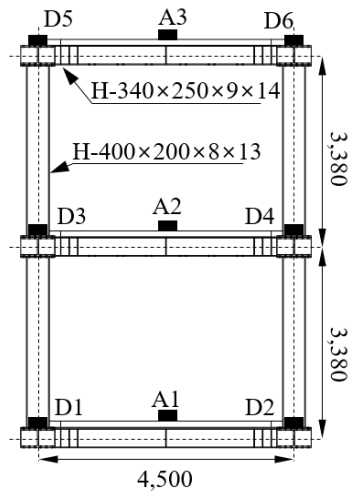
(b) Side view

Figure 4.2 Overall dimensions of test frame and measurement plan

84
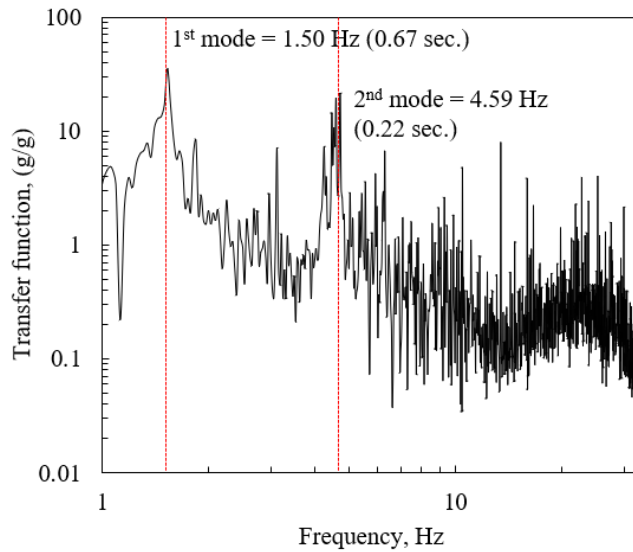
Figure 4.3 Transfer function of 2-story test frame obtained from white-noise excitation

The 1st- and 2nd-mode natural frequencies of the mounted moment frame measured from white-noise excitation test were 1.50 Hz (0.67 sec.) and 4.59 Hz (0.22 sec.), respectively (Figure 4.3). The measured damping of the 1st mode was 1.5 % of the critical damping.

4.2.2. Steel rack specimens mounted on access floor

A total of four access floor-mounted steel rack specimens were tested. The steel rack specimens were rigidly mounted on four different types of access floor. The steel rack had a plan dimension of 1.2 m × 0.8 m and a height of 1.0 m (see Figure 4.4). At the top of the steel rack, mass weight of 350 kgf was imposed to account for the mass of the mechanical elements located within the steel rack. The natural frequency of the steel rack was measured as 6.07 Hz, and the critical damping ratio was
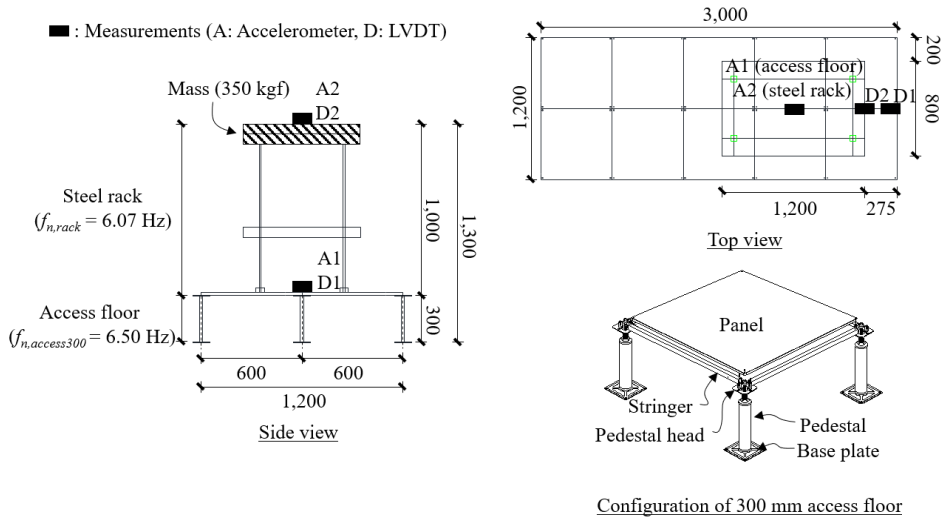
(a) Steel rack specimens mounted on 300 mm-high access floor (FH300-S and FH300-F)
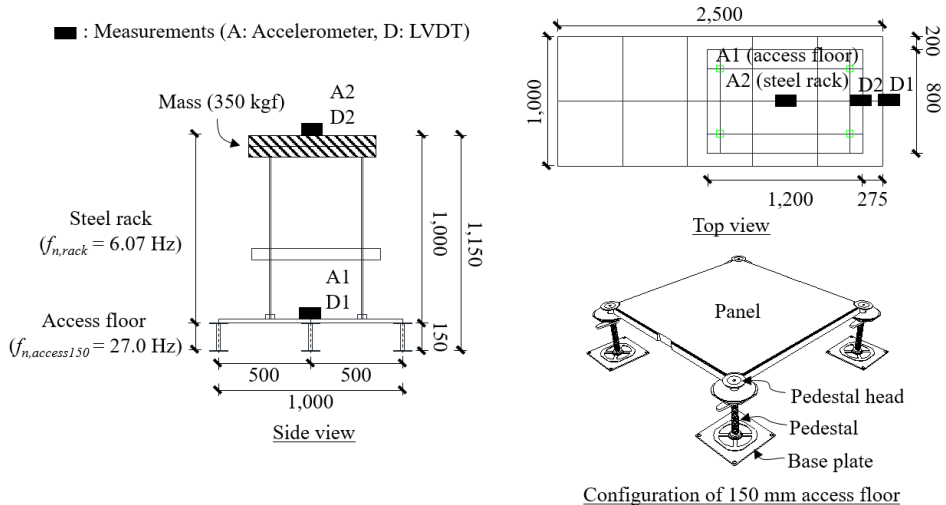
(b) Steel rack specimens mounted on 150 mm-high access floor (FH150-S and FH150-F)

Figure 4.4 Overall dimension of access floor-mounted steel rack specimens and measurement plan

approximately 1.0 %. The access floors had variations in their height and the base-fixing method. Specimens FH300-F and FH300-S utilized 300 mm-high flexible access floors, whereas the more rigid 150 mm-high access floors were employed for specimens FH150-F and FH150-S. The natural frequencies of the 300 mm- and 150

86

Figure 4.5 FH150-S and FH300-S specimens installed on the roof of 2-story steel frame

mm-high access floors were measured as 6.5 Hz and 27.0 Hz, respectively. The bases of the access floors in FH300-F and FH150-F were rigidly fixed to the concrete floor slab through concrete nails, whereas the access floors in FH300-S and FH150-S had no positive base fixtures such that some sliding movement could occur. The key

Table 4.1 Summary of key dynamic properties of access floor-mounted steel rack specimens

Specimen	Access floor properties		Base fixing condition
	Height, mm	Natural frequency, Hz	
FH300-F	300	6.5	Fixed
FH300-S	300	6.5	Sliding
FH150-F	150	27	Fixed
FH150-S	150	27	Sliding

* All the specimens utilized the same steel rack configuration ($f_{rack} = 6.07$ Hz, $\zeta_{rack} \approx 1.0$ %)
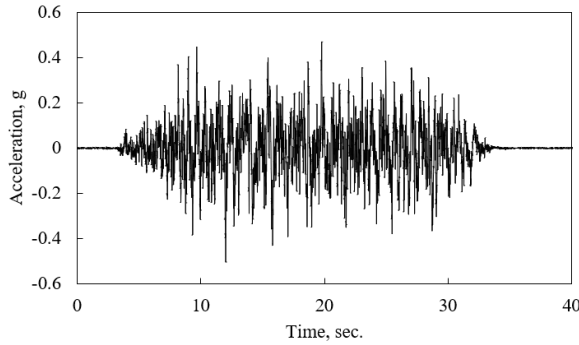
(a) Generated artificial input motion
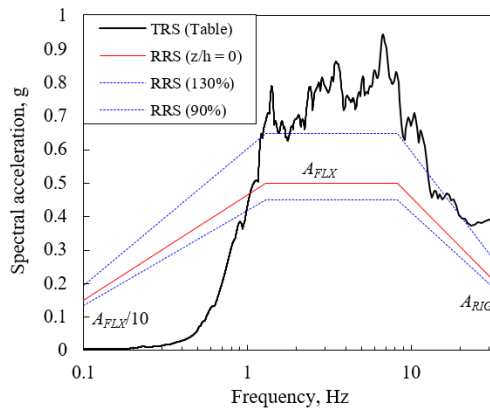
(b) Comparison of RRS and TRS for shaking table testing

Figure 4.6 Artificial input motion and TRS generated following AC 156 protocol

properties of access floor-mounted steel rack specimens are summarized in Table 4.1 and the configuration of the specimens installed on the roof floor are shown in Figure 4.5.

4.2.3. Input motion generation

Shake table tests were implemented following ICC-AC 156 (ICC 2010) proto-cols which, as previously mentioned, have been the most widely used for seismic

performance evaluation of nonstructural elements. Artificial input motions were generated to envelop the required response spectrum (RRS) specified by the protocol. The RRS was constructed based on the $S_{DS} = 0.50$ g, which corresponds to the highest seismic demand according to Korean Design Standards (KDS 41 17 00, 2019). The story amplification factor (z/h) was not applied because it will be automatically reflected through the dynamic behavior of the 2-story steel frame during testing. The generated artificial input motion had 20 seconds of strong-motion duration, and the test response spectrum (TRS) well enveloped the RRS as shown in Figure 4.6.

4.3. Evaluation of Peak Floor and Peak Component Acceleration

4.3.1. Effect of structural nonlinearity

The in-structure and component amplifications were analyzed using the floor response spectrum measured from each floor. The measured PFA was normalized by peak ground acceleration (PGA) to obtain the in-structure amplification, and the measured PCA was normalized by the measured PFA to obtain component amplification.

Figure 4.7 shows the PFA amplification distributions predicted by ASCE 7-22 (Eqs. 2.4b and 2.4c) and the distribution measured from the elastic test frame. It can be noticed that the measured PFA distribution did not strictly follow the linear trend, which is generally expected for short-period (low-rise) structures. The experimental PFA distribution was more related to the distribution obtained from the numerical
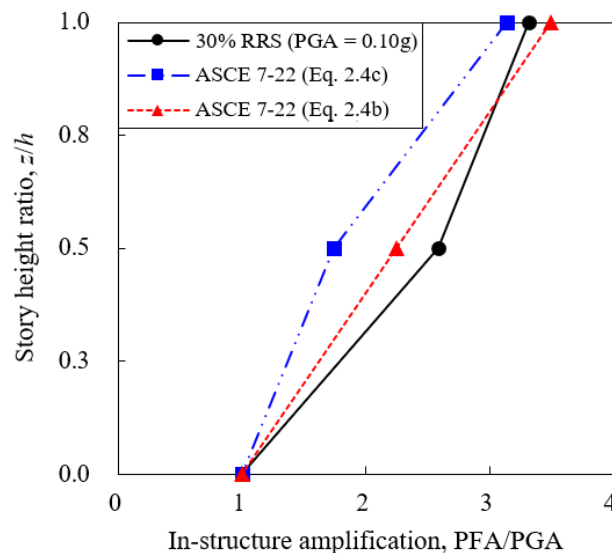
Figure 4.7 Comparison of in-structure amplification (PFA/PCA) under elastic behavior
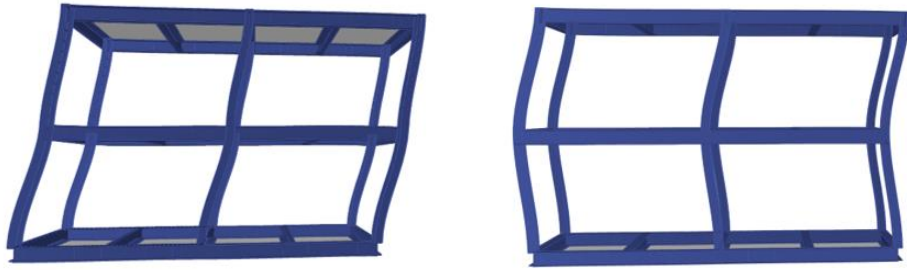
(a) 1st-mode shape (T_1 = 0.61 sec.);   (b) 2nd-mode shape (T_2 = 0.22 sec.);
effective modal mass = 94 % of total   effective modal mass = 6 % of total

Figure 4.8 Mode shapes and modal periods of 2-story test frame

case studies (see Figure 3.8(a)). Both the structural period-dependent (Eq. 2.4c) and independent (Eq. 2.4b) PFA predictions according to ASCE 7-22 underestimated the 2nd-floor PFA. This PFA underestimation was speculated to be caused by the contribution of the 2nd-mode shape of the tested frame as can be identified from the eigenvalue analysis results obtained using ETABS 2016 (see Figure 4.8); the combination of the 1st- and 2nd-mode shapes would provide a better correlation with the distribution observed in the test.

The 2-story steel frame showed yielding when subjected to 60 % RRS (PGA = 0.21 g) input motion. In order to evaluate the effects of structural nonlinearity on PFA reduction, the nonlinear response parameters used to define PFA reduction in ASCE 7-22 (see Eq. 2.8) were utilized. As discussed above, the structure global ductility factor (R_D) is calculated as the ratio of the maximum (u_{max}) to the yield displacement (u_y). These displacements were obtained based on the cyclic roof displacement and the base shear relationship of the tested frame (Figure. 4.9). The peaks in the displacement time histories and the corresponding base shear forces are marked with red dots to capture the yield and maximum displacements. It is observed that the measured peaks maintain a linear trend up to 30 % RRS excitation level.

91
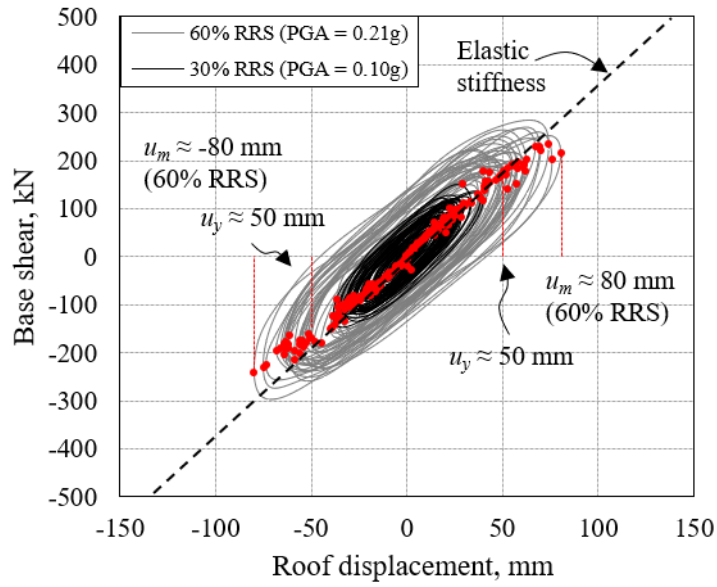
(a) Determination of yield displacement of test frame
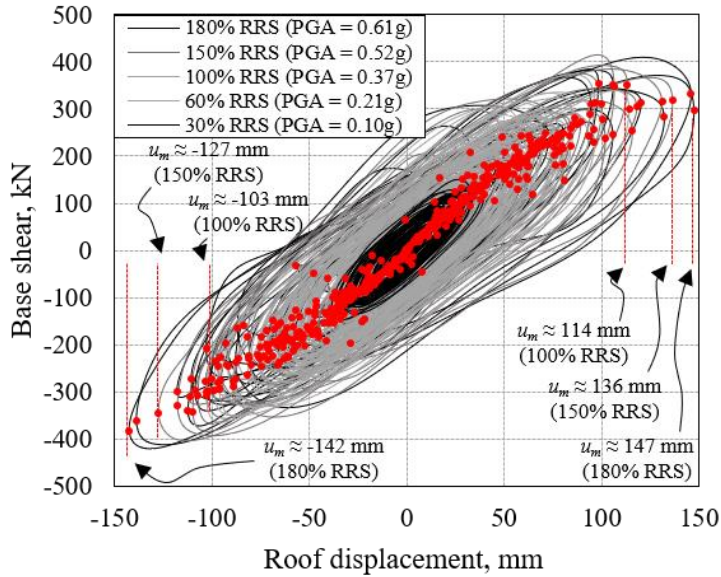
(b) Determination of maximum roof displacements

Figure 4.9 Determination of yield and maximum roof displacements of test frame
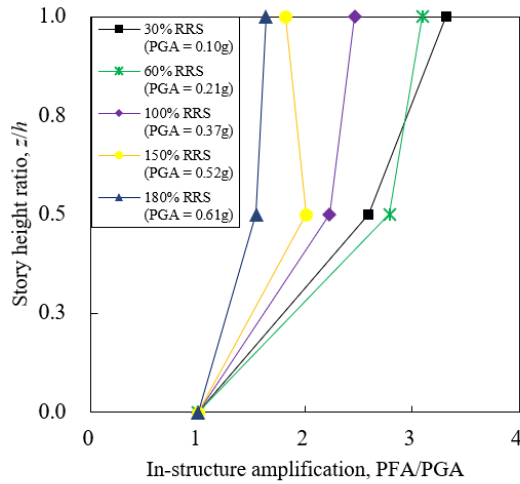
(a) Decreasing in-structure amplification with increasing nonlinear behavior
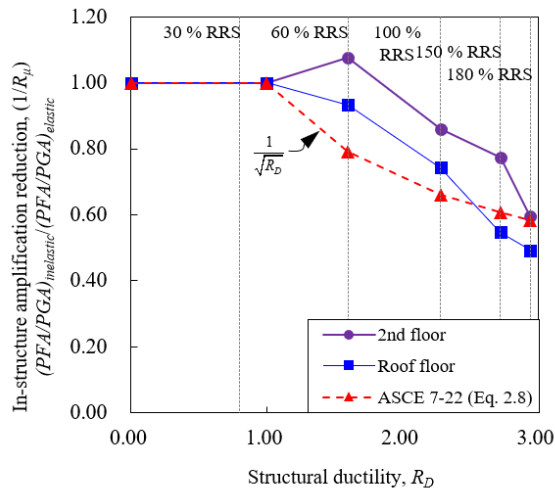
(b) Comparison of measured and ASCE 7-22 PFA reduction depending on structural ductility level

Figure 4.10 Effect of structural nonlinearity on PFA

The measured elastic stiffness is plotted in Figure 4.9(a) with a dashed line. Under a higher input intensity (60 % RRS), the peaks started to deviate from the measured elastic stiffness line, implying the yielding of the tested frame. The test frame had approximately 50 mm yield roof displacement, and the maximum displacements

measured at each input intensity were 80 mm (60 % RRS), 114 mm (100 % RRS), 136 mm (150 % RRS), and 147 m (180 % RRS). The experimental R_D and PFA amplifications are summarized in Table 4.2. The ratio of inelastic PFA amplification to elastic PFA amplification (measured at 30 % RRS) is also reported in the parentheses.

Figure 4.10 shows the reduced in-structure amplification observed during the tests. The relationship between the reduced PFA and the structural ductility (R_D) was compared with that predicted by Eq. (2.8). Overall, the PFA was much more reduced on the roof floor than on the 2nd floor. The PFA at a structure ductility level of about 3 was 40 % - 50 % of the elastic PFA. The difference in PFA reduction observed between 2nd and roof floors may have resulted from the non-uniform yielding of the test frame. The roof-floor PFA reductions were better predicted by ASCE 7-22 for all the developed structural ductility levels. However, the 2nd-floor PFA reductions

Table 4.2 Structural ductility and in-structure amplification measured during shake table testing

Input intensity	u_y, mm	u_m, mm	R_D	PFA/PGA	
				2nd floor	Roof floor
30% RRS		40	0.80 (elastic)	2.59 (1.00)	3.32 (1.00)
60% RRS		80	1.60	2.79 (1.08)	3.1 (0.93)
100% RRS	50	114	2.28	2.23 (0.86)	2.46 (0.74)
150% RRS		136	2.72	2.01 (0.78)	1.82 (0.55)
180% RRS		147	2.94	1.54 (0.59)	1.63 (0.49)

* Parenthesis = (inelastic amplification/elastic amplification)
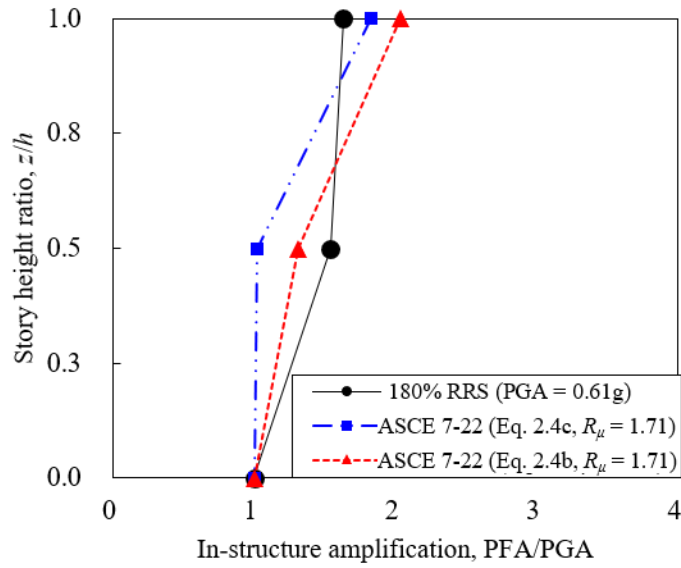
Figure 4.11 Comparison of measured and ASCE 7-22 PFA profiles for $u_m/u_y = 2.94$ (or $R_\mu = 1.71$)

were generally overestimated. The PFA overestimation for the 2nd floor became less as the structural nonlinearity increased. When the test frame achieved a low-to-moderate level of structural ductility ($R_D = 2.94$), the predicted 2nd-floor PFA became comparable to the measured response. Additional studies on structures having a moderate-to-high level of ductility seem desirable for a better understanding of the relationship between the structural ductility and PFA reduction and its variation along the building height.

Figure 4.11 shows a comparison of the measured and ASCE 7-22 PFA distributions corresponding to low-to-moderate ductility level, $u_m/u_y = 2.94$ at 180 % RRS. The 2nd-floor PFA is underestimated while the roof-floor PFA is overestimated by the ASCE 7-22 approach, implying that Eq. (2.4c) may not well capture the higher mode effect (the 2nd mode effect in this case, see Figure 4.8)
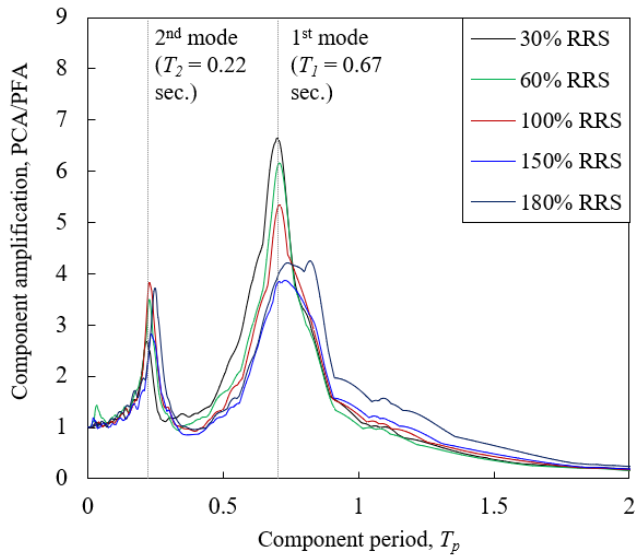
(a) 2nd floor
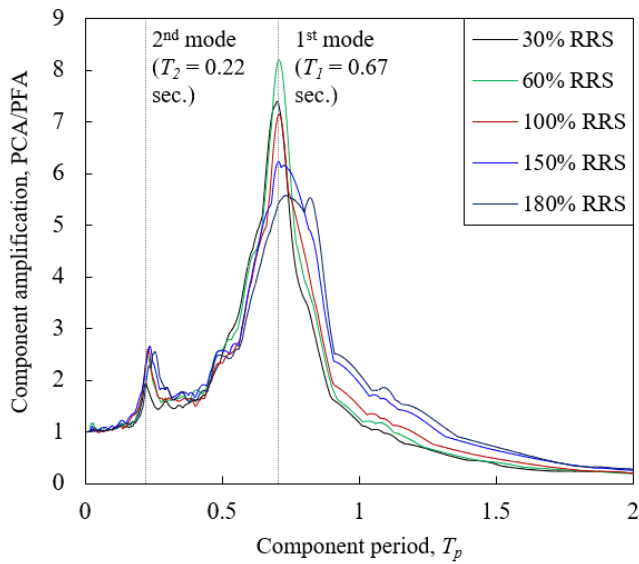
(b) Roof floor

Figure 4.12 Effect of structural nonlinearity on PCA
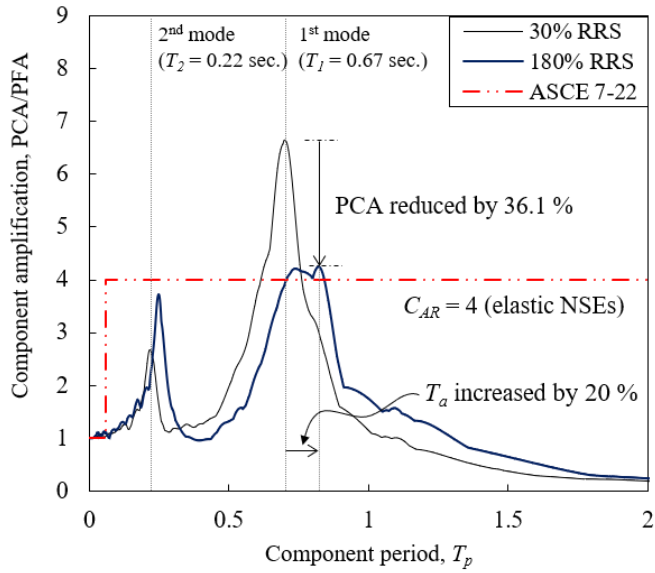
(a) 2nd floor
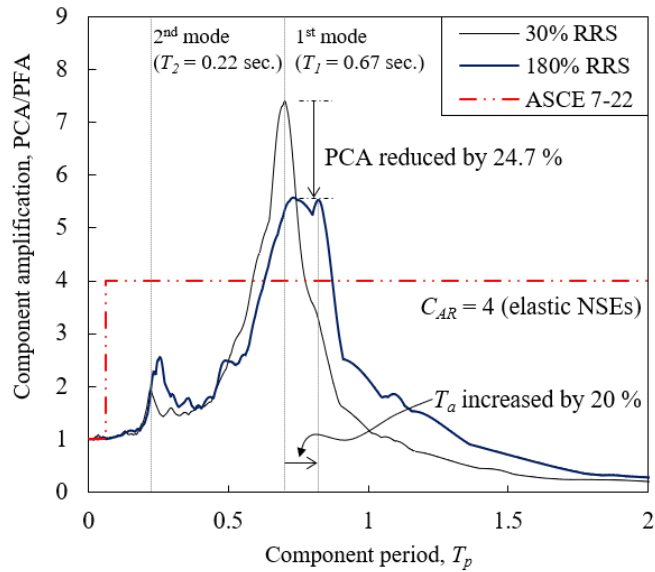
(b) Roof floor

Figure 4.13 Comparison of ASCE 7-22 elastic C_{AR} with PCA obtained by using floor motions of elastic and moderately yielded ($R_D = 2.94$) frame

The component amplification spectrum was constructed to evaluate the effect of structural nonlinearity on the PCA of elastic nonstructural elements. Figure 4.12 shows the variation in the component response spectrum with increasing input intensity or increasing structural nonlinearity. The yielding of the test frame caused a decrease in component amplification and the lengthening of the structural periods Under a low-to-moderate level of structural nonlinearity ($R_D = 2.94$ at 180 % RRS), the fundamental period increased by about 20 %, and widened the resonance amplification period range (see Figure 4.13). The elastic resonant PCA around the fundamental period was as high as 7 times the PFA, exceeding ASCE 7-22 elastic C_{AR} ($= 4.0$) by approximately 75 %. However, the reduction in PCA due to structural nonlinearity was most dominant around the 1st mode of the test frame; for $R_D = 2.94$, PCA was reduced by 36 % and 25 % on the 2nd and roof floor, respectively.

For a more comprehensive evaluation of the amplification factors for PFA and PCA given by ASCE 7-22, the nonstructural seismic demand was calculated using Eq. (2.2b) and compared with the floor response spectrum constructed from the measured floor motions. For comparison, elastic nonstructural elements with no overstrength was assumed ($C_{AR} = 4.0$, $R_{po} = 1.0$), and the peak input acceleration ($0.4S_{DS} = 0.61$ g) and R_D of 2.94 obtained from 180 % RRS input level was employed. Thus, the results in Figure 4.13 can be considered as an example representing the response of elastic nonstructural elements on a low-to-moderately yielded frame.

The design force determined from a simple component period-based resonance criterion ($T_p > 0.06$ sec.) inevitably overestimates the demand for many non-resonant components outside the resonant region. Such overestimation for the non-resonant components can be much relieved by employing the period ratio-based resonance
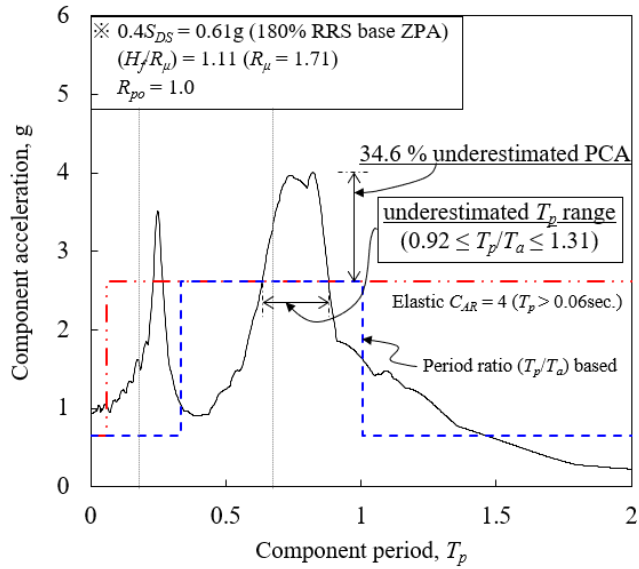
(a) 2nd floor
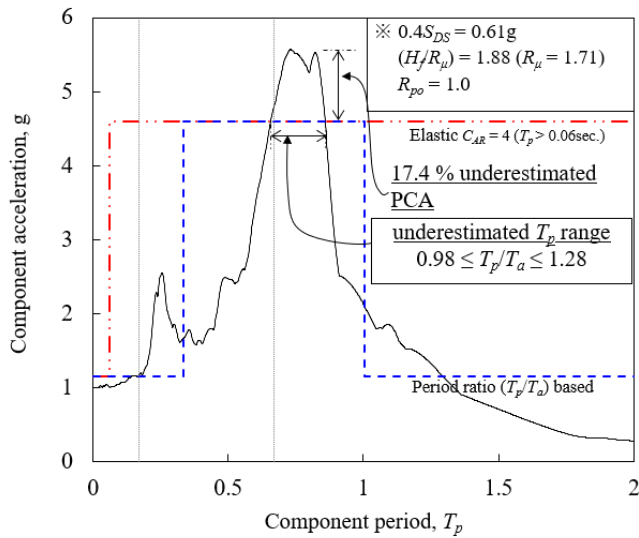
(b) Roof floor

Figure 4.14 PCA evaluation of elastic nonstructural elements mounted on low-to-moderately yielded structure ($R_D = 2.94$) using period ratio-based resonance criterion

criterion ($0.5 \leq T_p/T_a \leq 1.5$) given by the ASCE 7-22 commentary (ASCE/SEI 2022) (see Figure 4.14). The resonant period ratio range ($0.5 \leq T_p/T_a \leq 1.5$) given by the ASCE 7-22 commentary seems wide enough to cover the resonant region. The resonant bands underestimated were belonged to the ranges of $0.92 \leq T_p/T_a \leq 1.31$ and $0.98 \leq T_p/T_a \leq 1.28$ for the 2nd and roof floors, respectively.

4.3.2. Effect of component ductility

In this section, PCA obtained from access floor-mounted steel rack specimens is analyzed. All the specimens showed a highly pinched behavior caused by the loosely connected beam-to-column tab joints in access floor (see Figures 4.15-16). Specimen FH150-S exhibited slight sliding, as can be seen from the highly scattered hysteretic response caused by the sliding. Except for specimen FH150-S, all the specimens yielded as the input intensity increased. Specimens FH300-S and FH300-F yielded at 60 % RRS input intensity (PFA = 0.65 g); yielding occurred in the beam-column tab joints of access floors. In the case of FH150-F, the steel rack yielded at 180 % RRS input intensity (PFA = 1.00 g), and the rigid access floor remained intact. The natural frequencies based on the measurements at the top of FH150-F and FH300-F specimens are presented in Figure 4.16 to illustrate the variation in the natural frequency of the steel rack specimens caused by the access floor. The results for the sliding base specimens (FH150-S and FH300-S) are not presented because the results were largely the same as those for the fixed base specimens. As can be seen from Figure 4.17(a), the steel rack in specimen FH150-F shows just a minor change in its natural frequency ($f_n = 5.95$ Hz versus $f_n = 6.05$ Hz, see Figure 4.4),
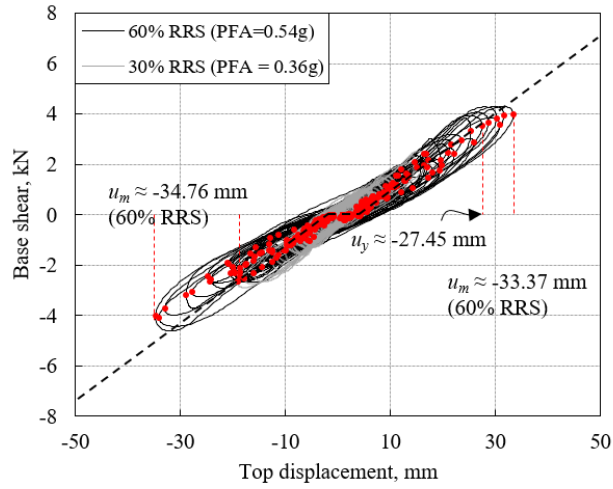
(a) Specimen FH300-S
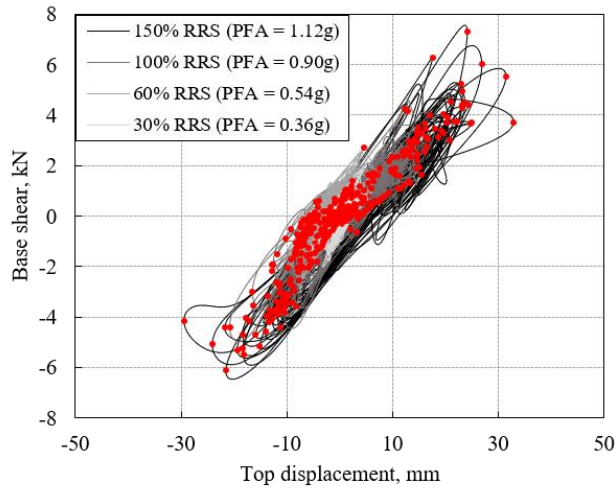
(b) Specimen FH150-S

Figure 4.15 Peak steel rack responses plotted from every measured hysteretic cycle for determining yield and maximum rack displacements (sliding base)
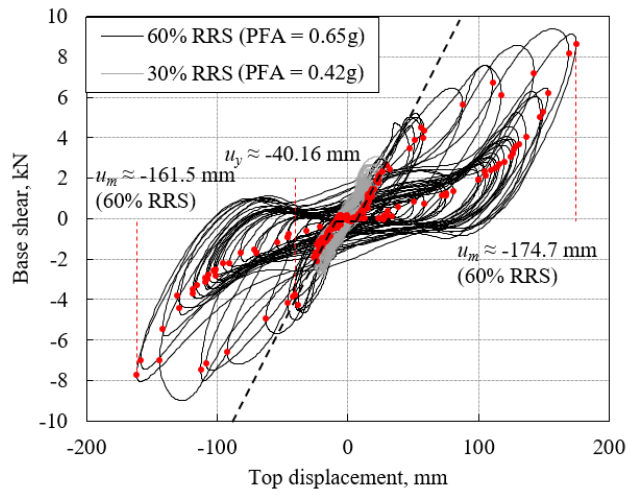
(a) Specimen FH300-F
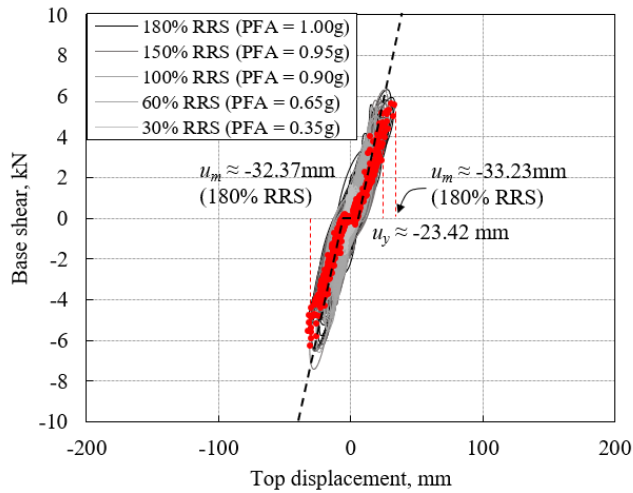
(b) Specimen FH150-F

Figure 4.16 Peak steel rack responses plotted from every measured hysteretic cycle for determining yield and maximum rack displacements (fixed base)
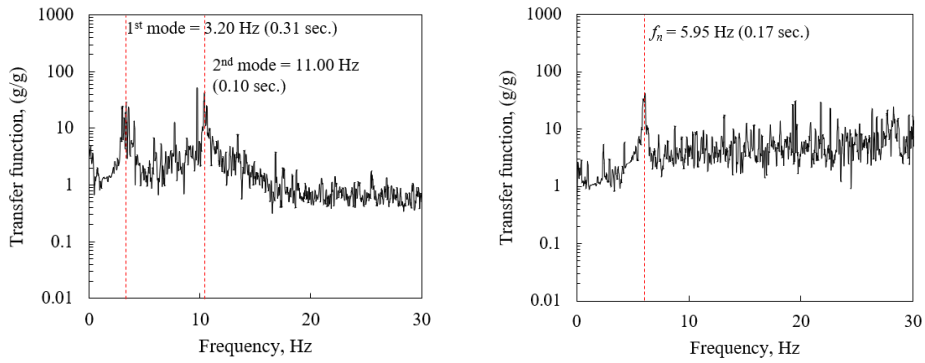
(a) Transfer function of FH300-F
measured at top of steel rack
(mounted on flexible access floor)

(b) Transfer function of FH150-F
measured at top of steel rack
(mounted on rigid access floor)

Figure 4.18 Effect of access floor on natural frequency of steel rack specimens
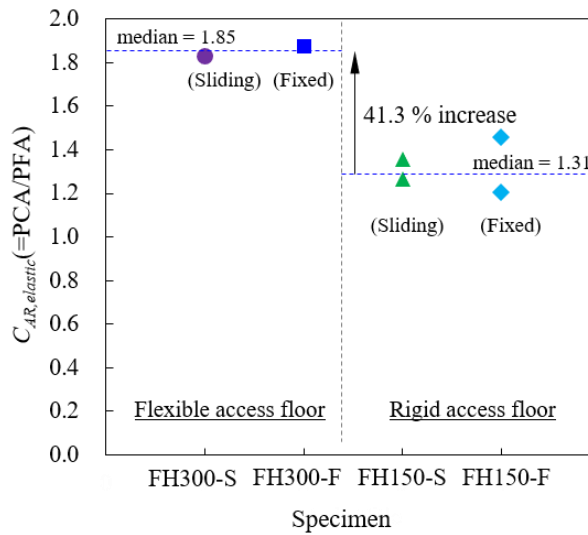
Figure 4.17 Comparison of elastic C_{AR} between FH150- and FH300-series specimens

implying negligible contribution of the very stiff (rigid) access floor ($f_{n,access150} = 27.0$ Hz) to the eigen property of the steel rack. Therefore, the dynamic behavior of the steel racks in FH150-series specimens was essentially that of steel racks rigidly
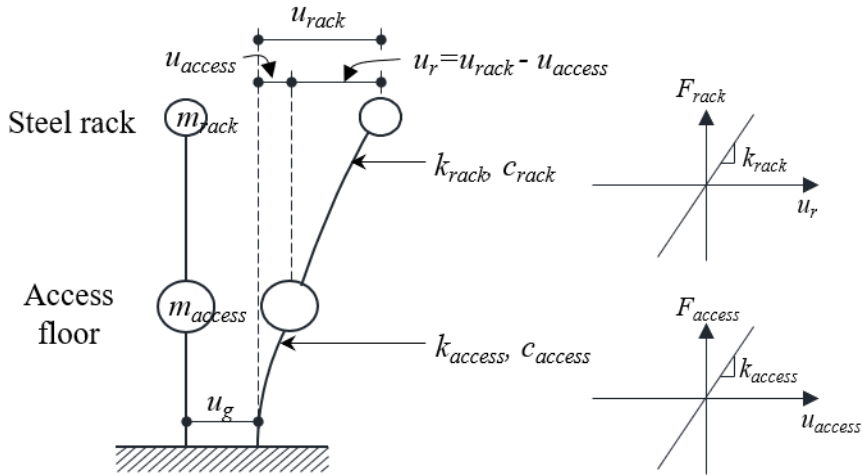
Figure 4.19 2-DOF numerical model for the yielded FH300-F specimen

mounted on the concrete floor slab. However, a significant contribution of the flexible access floor was observed in specimen FH300-F. The specimen effectively became a 2-DOF system, and the 1st and 2nd mode natural frequencies were measured as 3.20 Hz and 11.00 Hz, respectively. These resulted from the flexibility of the 300mm-high access floor ($f_{n,access300} = 6.5$ Hz, see Figure 4.4) and the high mass ratio between the steel rack and the access floor ($m_{rack}/m_{access300} = 2.19$).

Figure 4.18 presents the elastic component acceleration amplification (C_{AR}) which was evaluated before the specimens yielded. The PCA measured at the top of the steel rack was normalized by the PFA to calculate the elastic C_{AR}. First, from the results of FH150-series specimens, it was observed that the base sliding in FH150-S specimen seemed to have a minor effect on the component response; the magnitude of sliding was small, approximately 4 mm. The overall C_{AR} for FH300-series specimens was higher by about 40 % than that of FH150-series specimens because the fundamental period of the FH300-series specimens was closer to the 2nd mode of

the 2-story steel frame ($T_{1,FH300}/T_{2,frame}$ = 0.76). These results clearly indicate that possible interaction between nonstructural elements and non-rigid mounting needs to be properly considered in their seismic design.

To evaluate the relationship between C_{AR} and component ductility (μ_{comp}), the yield and maximum displacements of the yielded steel rack specimens were extracted based on the measured hysteretic responses (Figures 4.15-16), following the same procedure utilized for the PFA analysis. C_{AR} reduction was measured by normalizing inelastic C_{AR} by elastic C_{AR}. The low-to-moderately yielded specimens FH300-S and FH150-F (μ_{comp} = 1.22 – 1.42) showed only minor period elongation, implying that the tuning ratio of the specimens remained almost the same. C_{AR} reduction of specimens FH300-S and FH150-F was calculated as the ratio of the measured elastic and inelastic C_{AR}. However, a very high level of component ductility was developed for specimen FH300-F (see Figure 4.16(a)), and the specimen became more closely tuned to the 1st mode of the test frame (T_p/T_n = 1.08), resulting in a much higher C_{AR} (= 3.62) compared to the measured elastic C_{AR} (= 1.88). In order to obtain the elastic C_{AR} corresponding to the yielded FH300-F specimen, a linear time-history analysis of 2-DOF system corresponding to the yielded FH300-F specimen

Table 4.3 Verification of numerical 2-DOF model based on dynamic properties measured from yielded FH300-F specimen

	Access floor-mounted steel rack			
	1st mode		2nd mode	
	f_1 (Hz)	ζ_1 (%)	f_2 (Hz)	ζ_2 (%)
Shake table test	1.63	1.18	5.30	0.56
Numerical analysis	1.66	1.08	5.84	0.21

was conducted. The equation of motion for the 2-DOF model can be defined as follows.

$$m_{access}\ddot{u}_{access} + c_{access}\dot{u}_{access} + k_{access}u_{access} = -m_{access}[\ddot{u}_g + \frac{m_{rack}}{m_{access}}\ddot{u}_{rack}]$$

$$m_{rack}\ddot{u}_r + c_{rack}\dot{u}_r + k_{rack}u_r = -m_{rack}\ddot{u}_{access}$$

(4.1)

where $\ddot{u}_r = \ddot{u}_{rack} - \ddot{u}_{access}$; $u_r = u_{rack} - u_{access}$

The 2-DOF model was established by referring to the dynamic properties of the steel rack and the yielded access floor that were individually measured after the testing (Figure 4.19). The time-history analysis was implemented by MATLAB based on Newmark's method. The constructed 2-DOF numerical model was verified by comparing the analyzed dynamic properties with those measured from the yielded FH300-F specimen. As can be seen in Table 4.3, the numerical results correlated well with the measured properties of the test specimen.

Figure 4.20 shows the measured C_{AR} and the corresponding component ductility levels. The relationship between C_{AR} and component ductility given by ASCE 7-22 is also plotted. Overall, the measured C_{AR} is less than that predicted by ASCE 7-22. The C_{AR} underestimation made by ASCE 7-22 may be related to the difference between the component hysteretic model (bilinear hysteresis model with 3 % strain hardening) assumed by ASCE 7-22 (ASCE/SEI 2022) and the pinching hysteretic behavior generally exhibit inferior energy-dissipating capacities. Considering that many of the floor-mounted nonstructural elements such as steel racks (Jovanović et
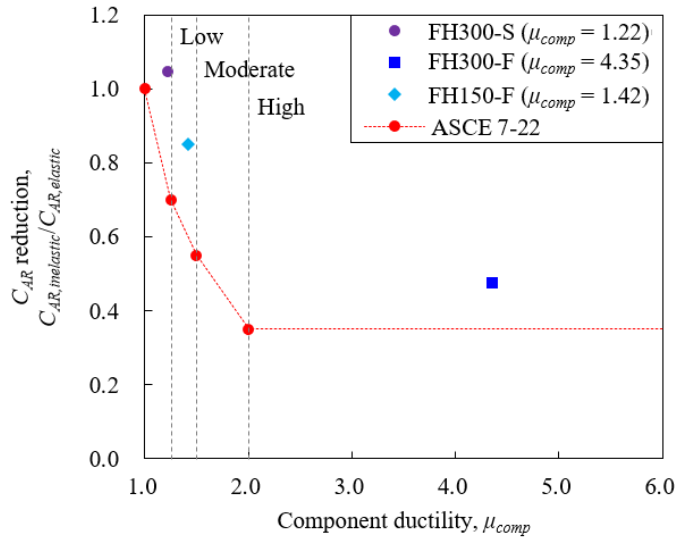
Figure 4.20 Comparison of measured and ASCE 7-22 C_{AR} reduction depending on component ductility level

al 2019; Dai et al. 2020) and partition walls (Petrone et al. 2016; Rahmanishamsi et al. 2017) frequently involve pinched hysteretic behavior of tabbed or hooked joints, further investigation including the pinching model is warranted to establish a more realistic relationship between the component ductility and C_{AR}.

4.4. Summary and Conclusions

In this study, shake-table testing of nonstructural elements using a full-scale 2-story steel moment frame was conducted. This chapter focused on analyzing the non-structural seismic demand based on the floor and component responses measured during the shake table testing. The results of this study can be summarized as follows

(1) The PFA measured from the 2-story moment frame at the elastic stage showed a distribution somewhat different from the structural period-considered PFA profile suggested by ASCE 7-22, implying that the higher mode effect (the 2nd mode effect in this case) may not be well captured by the ASCE 7-22 PFA profile.

(2) The PFA reduction suggested by ASCE 7-22 to account for structural nonlinearity was larger than the experimental results for low-to-moderate ductility level ($1.60 \leq R_D \leq 2.94$). The PFA measured from the moderately yielded test frame ($R_D = 2.94$) was about half of the elastic PFA. Additional studies including moderate-to-high structural ductility seem desirable to better understand the relationship between structural ductility and PFA reduction and its variation along the building height.

(3) The analysis on the resonant PCA showed that the elastic nonstructural elements installed on the inelastic test frame experienced a significant reduction in their acceleration responses due to the structural nonlinearity. For elastic NSEs resonating to the 1st mode of the elastic test frame, the PCA increased as high as 7 times PFA, whereas the PCA decreased by about 30 % as the test frame reached a moderate level of structural ductility ($R_D = 2.94$). The effect of structural nonlinearity on the response of elastic NSEs needs to be systematically addressed for the better estimation of nonstructural seismic demands.

(4) The design force determined from a simple component period-based resonance criterion ($T_P > 0.06$ sec.) tends to highly overestimate the demand for

nonstructural elements outside the resonant region. The use of a period ratio-based resonance criterion ($0.5 \leq T_p \leq 1.5$), in accordance with the ASCE 7-22 commentary, is recommended to relieve such overestimation if possible. For the structural ductility level of $R_D = 2.94$, the elastic component acceleration in the resonant band around $0.9 \leq T_p/T_a \leq 1.3$ exceeded the ASCE 7-22 maximum acceleration corresponding to $C_{AR} = 4.0$.

(5) Due to the flexibility of 300 mm-high access floors, steel racks in FH300-series specimen experienced a much higher PCA than those mounted on much stiffer (almost rigid) access floors (FH150-series specimen) and significantly yielded under a low level of input intensity (60 % RRS, PFA = 0.65 g), while rigid FH150-series specimens exhibited only minor yielding even under a much higher input intensity (180% RRS, PFA = 1.00 g). These test results clearly indicate that possible interactions between nonstructural elements and non-rigid mounting should be properly considered in design.

(6) The effect of component yielding on PCA was evaluated based on the test results of steel rack specimens mounted on flexible and rigid access floors. The PCA reduction depending on the component ductility level was generally less than that suggested by ASCE 7-22. It is speculated that the underestimation made by ASCE 7-22 might be related to the difference between the component hysteretic model (bilinear hysteresis model with 3% strain hardening) assumed therein, and the pinched hysteretic behavior actually observed in the testing. Considering that many of the floor-mounted nonstructural elements frequently exhibit pinched hysteretic behavior, a more

refined analysis including the pinching model is warranted to establish a more realistic relationship between component ductility and component acceleration.

Chapter 5. Seismic Performance Evaluation of Ceiling Systems Based on Full-Scale Shake-Table Tests

5.1. Introduction

Suspended ceiling system is one of the most earthquake-vulnerable non-structural elements. Even under moderate earthquake levels, suspended ceiling systems could suffer significant seismic damage which may lead to functional loss of buildings and threaten life safety by blocking the path during evacuation. Despite their high seismic fragility, the seismic design of suspended ceiling systems is largely empirical and lack of rational engineering procedure because of their complex details and dynamic behavior.

Several previous studies have provided useful insights into the seismic behavior of suspended ceiling systems. However, most of these studies focused on evaluating the seismic performance of ceiling systems rather than identifying their dynamic characteristics or behavior. Also, it should be noted that many of the studies were

conducted using a direct-hung suspended ceiling systems, although a variety of ceiling configurations are used in actual practice. Therefore, a systematic study analyzing and comparing the physical behavior and dynamic properties of typical suspended ceiling systems is much needed.

In this chapter, the results of shake table tests were discussed which were performed using direct and indirect-hung suspended ceilings with diverse configuration. In particular, a large-size test specimen (with size comparable to that of an actual ceilings) was tested using an array of two shake tables. Small-size ceiling specimens were also tested under multi-directional input. Based on the test results, the physical behavior of the tested ceilings was analytically modeled, the key dynamic properties were identified, and evolution of ceiling damage according to increments in the shake-table input intensity was traced.

5.2. Shake-Table Test of Non-Seismic Ceiling Systems

In this section, test frame features, ceiling specimen information, and dynamic loading protocol used for shake table testing are described.

5.2.1. Shake table test frames

In this study, ceiling specimens were tested using 3 types of test frames which are a large-size test frame, small-size test frame, and the full-scale 2-story steel moment frame. The information about the full-scale 2-story steel moment frame can be referred to Chapter 4.
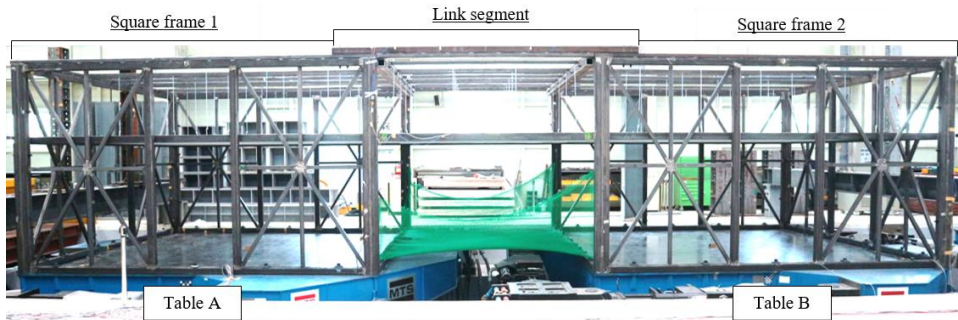
Figure 5.1 Large-size test frame for shake table testing of suspended ceiling systems and modular segments

A large-size test frame was specially designed and fabricated for conducting dynamic test using two isolated shake tables synchronously (see Figure 5.1). The overall dimension of the large-size test frame was 13.1 m (length) × 5.1 m (width) × 3 m (height). It was composed of three segments: 1) two identical stiff frames (5.1 m × 5.1 m) installed on two shake tables and 2) a 4.1 m × 5.1 m link segment, which connects the two frames rigidly at the roof level (see Figure 5.2).

Figures 5.3 – 5.5 present detailed information of the frame segments. Each 5.1 m × 5.1 m square frame composed of 2 side wall frames, 1 end wall frame, 1 opening frame and 1 top frame. All the wall frames were stiffly designed using diagonal braces in order to construct a rigid test frame. At the upper side of the wall frames, HSS-100×50×3.2 box beams were welded for installation of wall molding for ceiling systems. For installation of ceiling systems, HSS-50×50×3.2 box beams were densely located at the top of the square frame. As shown in Figure 00, the holes to hang ceiling systems were introduced where the intervals were determined for installing the ceiling systems with 610 mm interval hanger bolts and 900 mm interval

hanger bolts. To facilitate the assembly of the test frame, all the elements were bolt connected through the holes introduced at the sides and top of the elements.

The large-size test frame was intended to conduct uniaxial shake table test in the longitudinal direction. The test frame was designed to have a horizontal natural frequency of 24 Hz for each bare square frame and 17 Hz for the combined test frame including the mass of ceiling specimens. The natural frequency of the whole test frame was measured to be 16.8 Hz by the white noise test (see Figure 5.6). On this basis, the frame was considered to be sufficiently stiff for preventing unintended amplification of the table input motion at the test frame roof. The test frame was mounted on two 5.0 m× 5.0 m three degrees-of-freedom shake tables having a maximum acceleration capacity of 1.0 g.
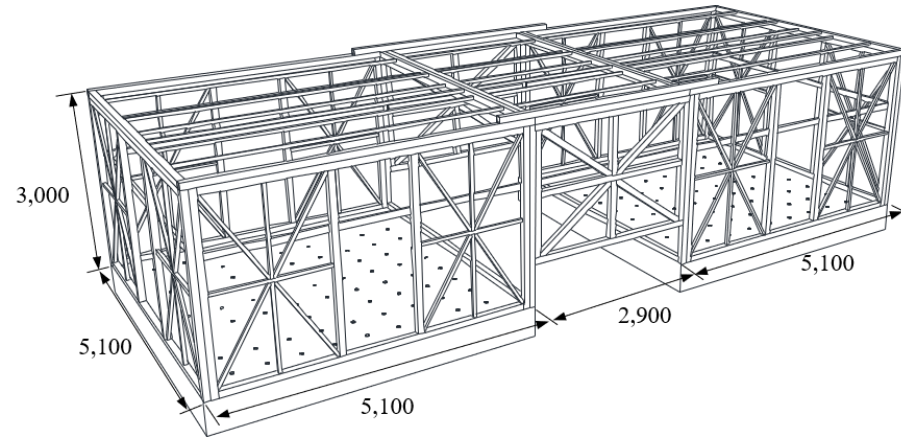
Figure 5.2 3D plan showing configuration of large-scale test frame
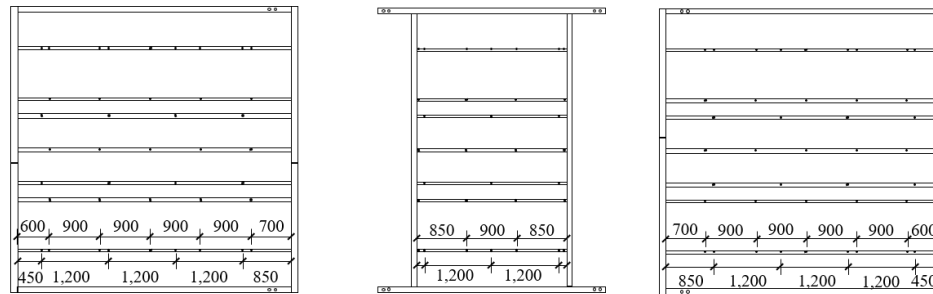
Figure 5.3 Top view of large-size test frame showing hanger bolt hole locations
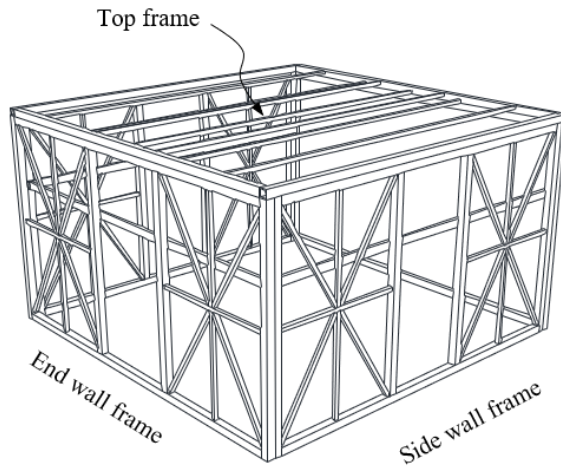
(a) 3-dimensional veiw of square frame

(b) Plan view of the top of square frame

116

for installing wall molding
HSS-100×50×3.2

HSS-100×100×9

1,000

1,450

1,450

HSS-100×100×9

HSS-50×50×3.2

1,900   1,100   1,900

4,900
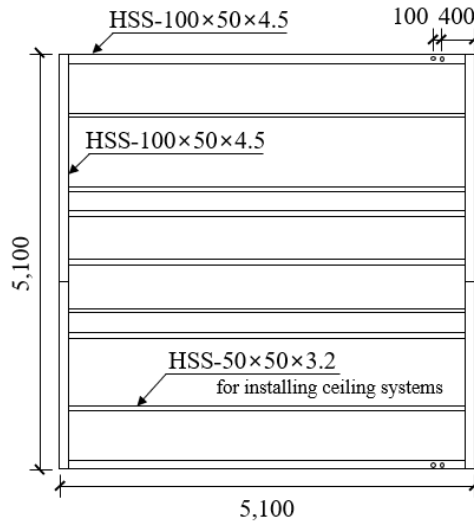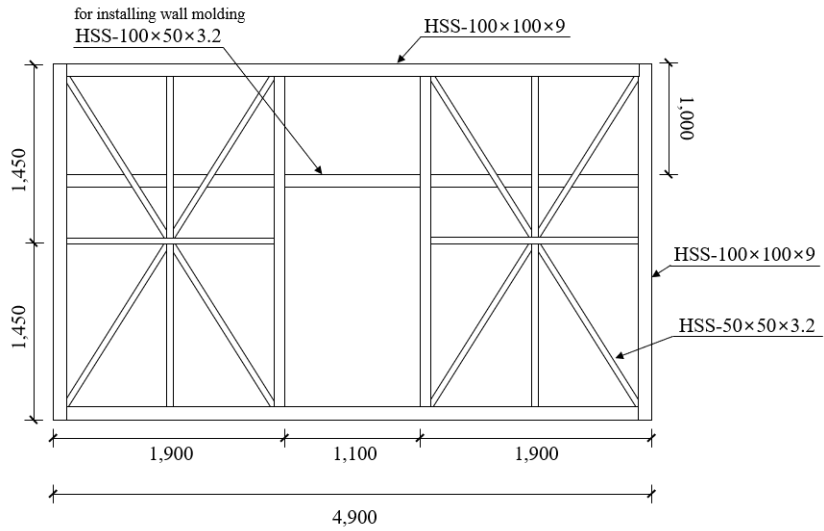
(c) Side view of square frame (side wall frame)

550   800   800   800   800   800   550

350 300 300 300 300 300 300

M24   HSS-100×100×9

2,900

5,100
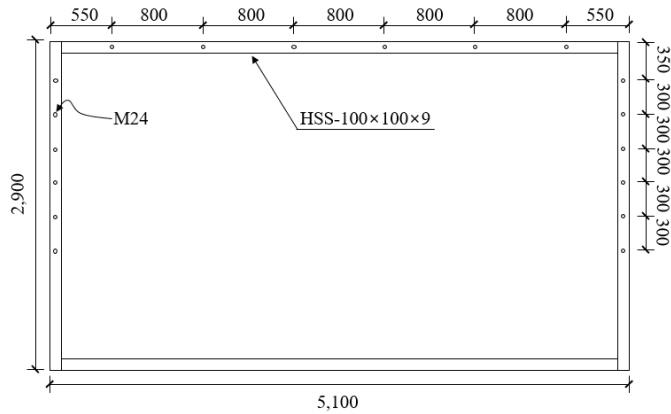
(d) Side view of square frame (opening frame)

Figure 5.4 Configuration and detailed plan for square frame
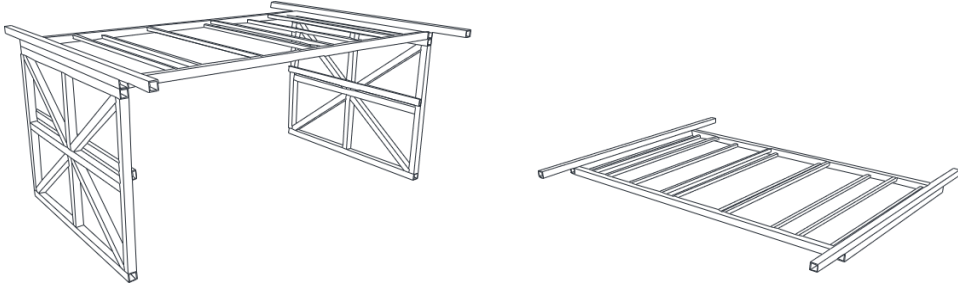
(a) 3-dimensional view of link segment
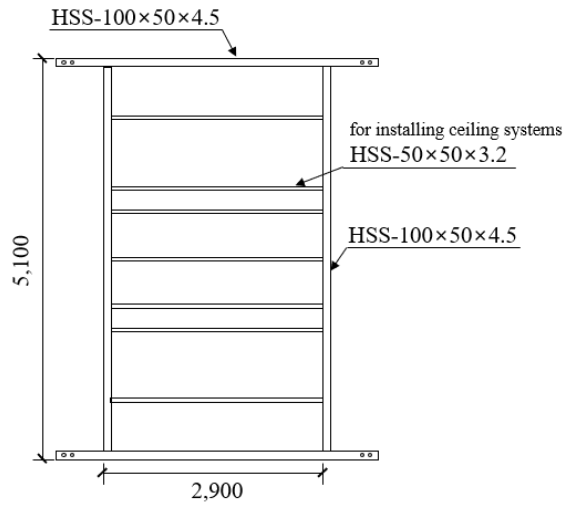
(b) Plan view of the top of square link segment
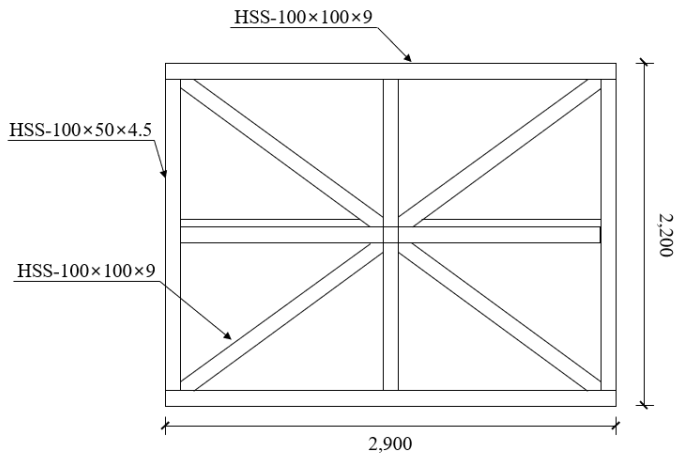
(c) Side view of link segment

Figure 5.5 Configuration and detailed plan for link segment
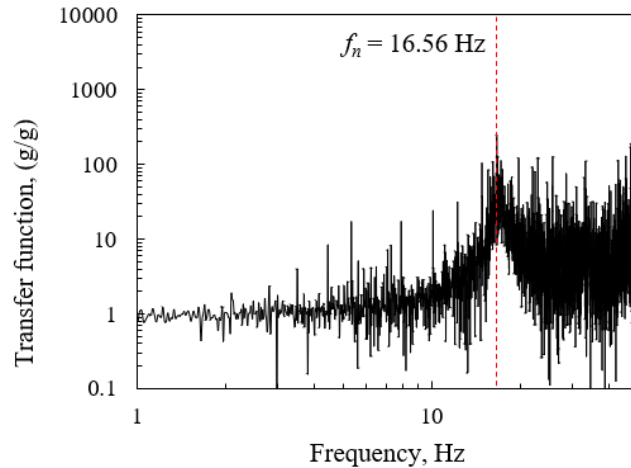
Figure 5.6 Transfer function measured at the top of large-size test frame

Small-size specimen tests were also conducted to supplement the large-size uni-axial shake table testing and evaluate the multi-directional input effects. A test frame with a size of 4.1 m (length) $\times$ 4.1 m (width) $\times$ 3.2 m (height) (see Figures 5.7 -5.8) was mounted on a six degrees-of-freedom shake table (4.0 $\times$ 4.0 m) having a maximum acceleration capacity of 1.5 g. The natural frequencies of the small-size test frames were measured to be 16.1 Hz in the horizontal direction and 9.0 Hz in the vertical direction (see Figure 5.9).
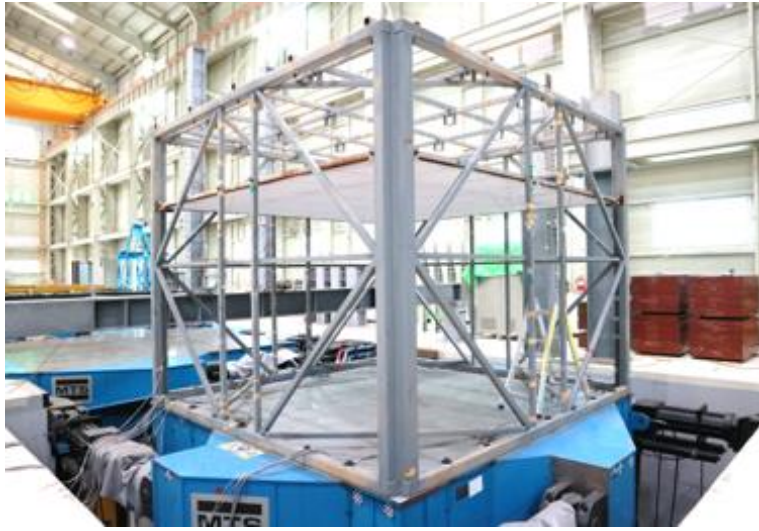
Figure 5.7 Small-size test frame for multi-directional shake-table test
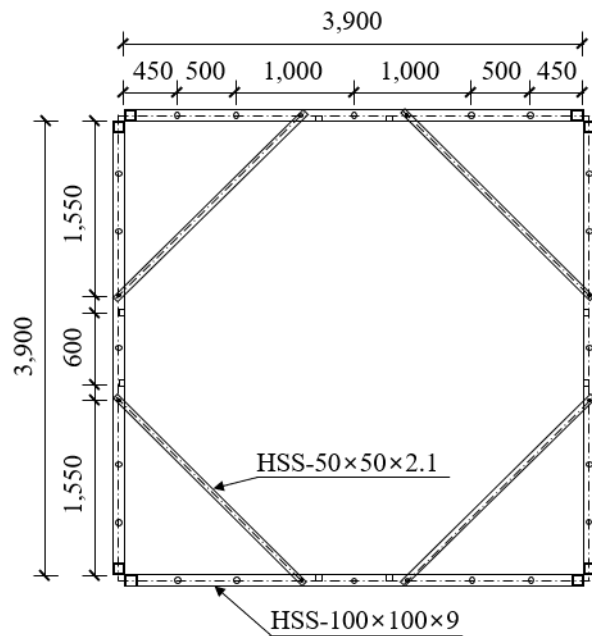
(a) Plane view of the bottom of small-size test frame
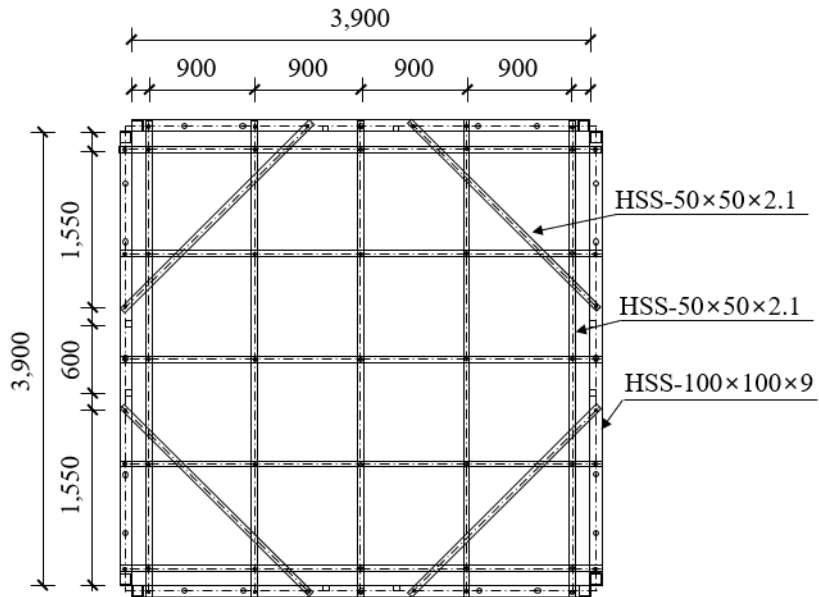
(b) Plan view of the top of small-size test frame
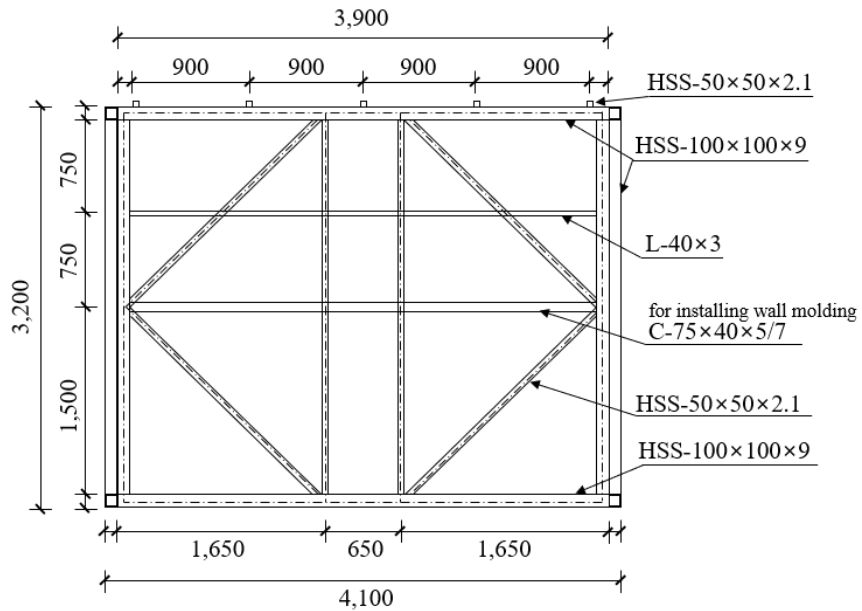
(c) Side view of small-size test frame

Figure 5.8 Detailed configuration and plan for small-size test frame
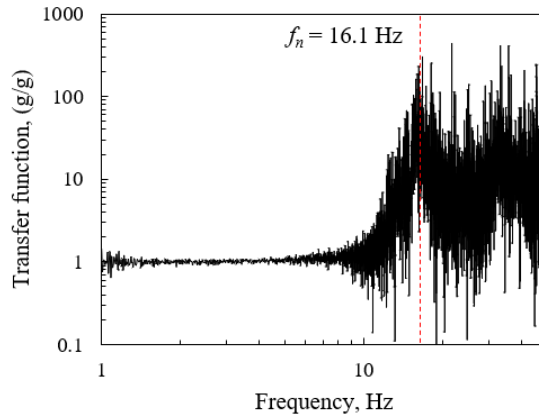
(a) Horizontal direction
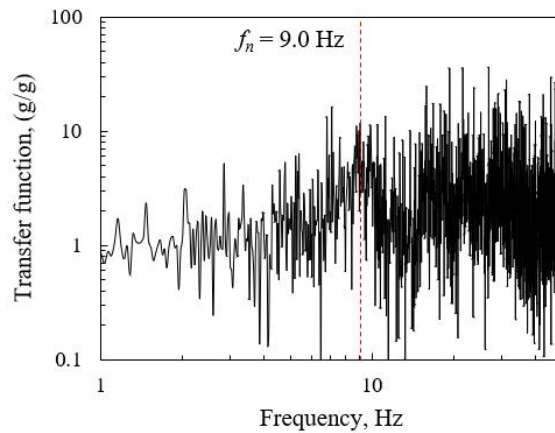
(b) Vertical direction

Figure 5.9 Transfer function measured at the top of small-size test frame

Before conduction tests for ceiling systems, a coherence function analysis was conducted for the large-size test frame to ensure that both the top of the square frame 1 and 2 exert identical floor motions without any differential movements. The coherence function is a statistical tool that can be used to examine the relation between two different signals. The coherence function can be determined as follows:
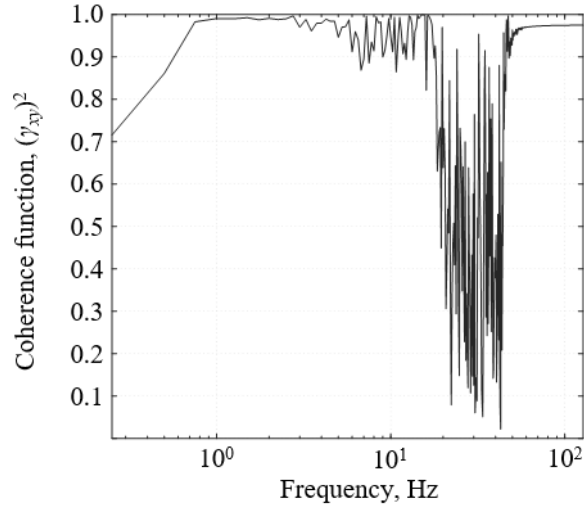
Figure 5.10 Coherence function measured at the top of large-size test frame

$$\gamma_{xy}^2 = \frac{\left|G_{xy}(f)\right|^2}{G_{xx}(f) \times G_{yy}(f)} \tag{5.1}$$

where $G_{xx}(f)$ = auto-correlation function of xth signal, $G_{yy}(f)$ = auto-correlation function of yth signal, $G_{xy}(f)$ = cross-correlation function of xth and y^{th} signals.

When the coherence function is equal to one, two signals are completely related, or two signals are completely identical in terms of their phase and frequency contents. If the coherence function is far from unity, it implies that the two signals have severe differences in their frequency contents; in this experimental study, the ceiling specimen installed on the square frame 1 and 2 was subjected to different floor motions (top frame acceleration response) caused by the differential movements between the square frames.

Figure 5.10 shows the coherence function measured from the recorded signals on the top of the square frames 1 and 2. It can be observed that the coherence function maintains almost unity in the whole frequency range except for around 20 Hz, where the coherence function highly fluctuated. Such a high fluctuation, around 20 Hz, is speculated to be caused by the local vibration of the beam members at the top frame and will not affect the global response of the ceiling specimens. Therefore, it can be concluded that the large-scale test frame installed on the two isolated shake tables was perfectly synchronized, and the whole suspended ceiling specimen installed on the large-size test frame is expected to be subjected to the same floor motions.

5.2.2. Test specimens and measurements

A total of 9 suspended ceiling specimens, one ceiling specimen using full-scale 2-story moment resisting frame (9.0 m × 4.07 m), two large-size (12.8 m × 4.85 m) and six small-size (3.87 m × 3.87 m), were fabricated. Four types of ceiling systems were utilized including direct-hung lay-in T-bar ceiling system, indirect-hung lay-in and continuous ceiling systems (see Figures 2.9 and 2.10). Also, an indirect-hung lay-in T&H bar ceiling system was used which composed of main and cross T-bars and additional H-bars as shown in Figure 5.11. This system is also widely used in many commercial buildings. In this grid system, cross T-bars and cross H-bars are installed between the main T-bars. Unlike the cross T-bars that are connected to the main T-bars, cross H-bars generally do not have any connection with the main T-bars.
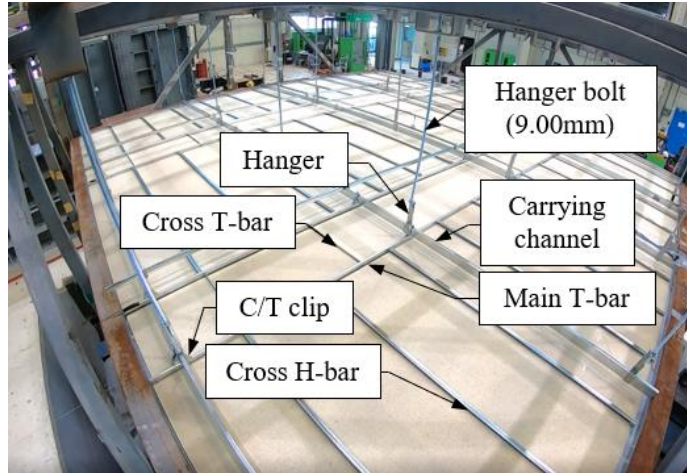
Figure 5.11 Configuration of indirect-hung suspended ceiling system (T&H-bar) (Lay-in panel)

All the boundaries of the test specimens were treated to have a 15 mm clearance between the grid members and the wall-attached perimeter closure channel to satisfy a minimum gap requirement (10 mm) for SDC C according to ASTM E580 (ASTM-E580-E80 2017). The key specimen information is summarized in Table 5.1.

In this experimental program, direct- and in-direct-hung T-bar ceiling systems (DTL and ITL specimens) were tested and compared to investigate the differences in their dynamic characteristics and seismic performance resulting from the difference in hanger members. Testing was conducted under more severe pounding conditions in the case of continuous panel ceilings, considering the robust restraint provided by the screw-attached ceiling panels as reported in previous studies (Gilani et al. 2015; Magliulo et al. 2012; McCormick et al 2008). The ceiling size (or the ceiling mass) was significantly increased in this case such that more sever pounding forces can be applied to ceiling systems. Two large-size ceiling specimens (IMC-L-

Table 5.1 Ceiling types and key properties of test specimens

Specimen	Ceiling type	Ceiling size, m	Input direction	Boundary type (clearance, mm)	Plenum depth, m	Panel type
DTL-FS	Direct-hung suspended T-bar ceiling	9.0 × 4.07	x	Free floating (15)	0.79	Lay-in
DTL	Direct-hung suspended T-bar ceiling	3.87 × 3.87	x, y, z	Free floating (15)	0.80	Lay-in
ITL	Indirect-hung suspended T-bar ceiling	3.87 × 3.87	x, y, z	Free floating (15)	0.75	Lay-in
ITL-R1	Indirect-hung suspended T-bar ceiling	3.87 × 3.87	x, y, z	Free floating (x-dir. 410, y-dir. 15)	0.75	Lay-in
ITL-R2	Indirect-hung suspended T-bar ceiling	3.87 × 3.87	x, y, z	Free floating (410)	0.75	Lay-in
ITHL	Indirect-hung suspended T&H-bar ceiling	3.87 × 3.87	x, y, z	Free floating (15)	0.75	Lay-in
IMC-L-M	Indirect-hung suspended M-bar ceiling	12.9 × 12.8	x	Free floating (15)	1.00	Screw-attached
IMC-L-C	Indirect-hung suspended M-bar ceiling	12.9 × 12.8	x	Free floating (15)	1.00	Screw-attached
IMC	Indirect-hung suspended M-bar ceiling	3.87 × 3.87	x, y, z	Free floating (15)	0.75	Screw-attached

M, IMC-L-C) were fabricated and uniaxially tested in the longitudinal direction using the test frame described in the preceding section (see Figure 5.1). IMC-L-M specimen was fabricated to evaluate the ceiling seismic performance along the M-bar direction. IMC-L-C specimen has same configuration with IMC-L-M specimen, but it was 90° rotated from IMC-L-M specimen to exert pounding forces on the carrying channel members. In addition, in order to evaluate the 3-dimensional input effects and the interaction with a nonstructural element installed within the ceiling, a small-size test specimen was also prepared by installing the air conditioner within the ceiling grid. The specimen and measurement plan for the tested ceilings are summarized in Figures 5.12 – 5.14.

While measuring the natural frequency and damping ratio of the ceiling systems by the since sweep or white noise test, the magnitude of the input acceleration (0.1 ± 0.05 g) was observed to be generally too low for generating enough dynamic forces that could overcome the initial frictional forces existing in the perimeter of the suspended ceilings. When a higher input was applied to overcome the friction, the acceleration data was disturbed, wherein undesired acceleration spikes caused by pounding upon the perimeter closure channels occurred. Therefore, a specimen with a sufficiently wide clearance (410 mm) in both the horizontal directions was fabricated (ITL-R2). Furthermore, another specimen with a 410 mm clearance (ITL-R1) in one horizontal direction was also fabricated to measure the additional damping effect caused by the friction between the ceiling grids and perimeter closure channels (see Figure 5.12(c) and 5.12(d)).

Various measuring devices including accelerometers, LVDTs, and strain gauges were installed to monitor the global and local responses of the test frame and specimen. The installation locations are shown in Figure 5.12 – 5.14.
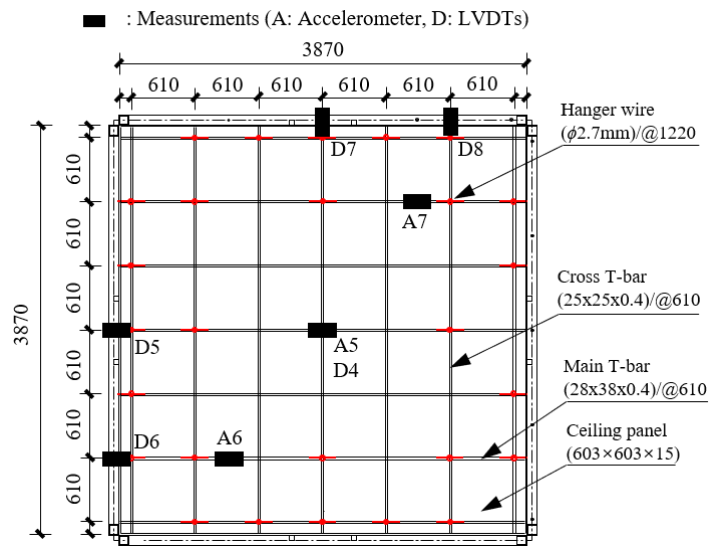
(a) Direct-hung T-bar ceiling specimen (DTL)
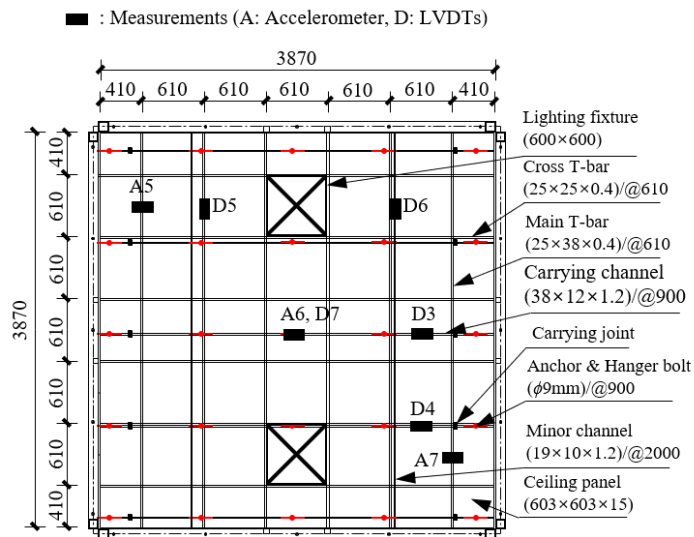
(b) Indirect-hung T-bar ceiling specimen (ITL)
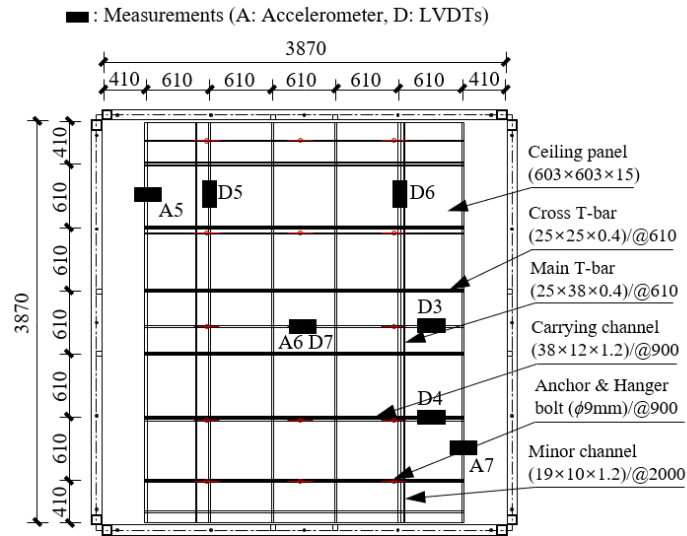
(c) Indirect-hung T-bar ceiling specimen with large clearance (ITL-R1)

(d) Indirect-hung T-bar ceiling specimen with large clearance (ITL-R2)

: Measurements (A: Accelerometer, D: LVDTs)

Steel cross H-bar
(20×20×0.45)/@300

Steel main T-bar
(25×38×0.4)/@1190

Carrying channel
(38×12×1.2)/@900

Anchor & Hanger bolt
(ϕ9mm)/@900

Minor channel
(19×10×1.2)/@2000

Ceiling panel
(300×1,210×15)
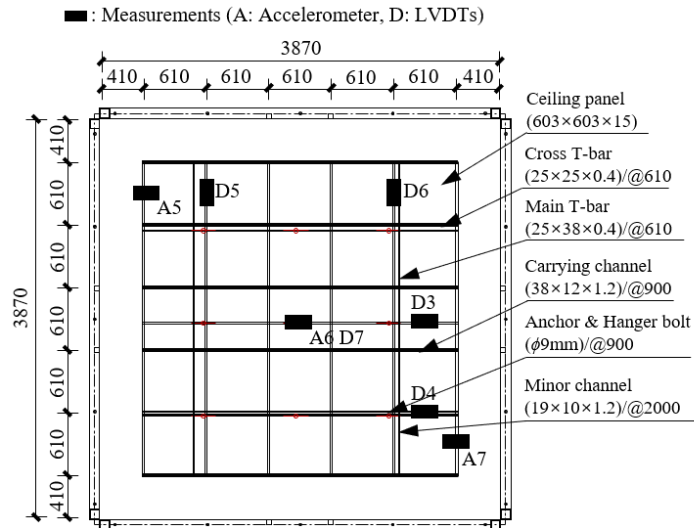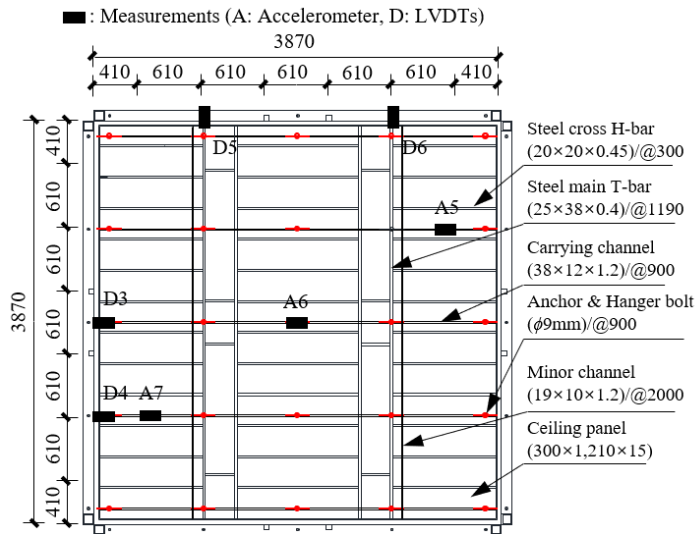
(e) Indirect-hung T&H-bar ceiling specimen (ITHL)

: Measurements (A: Accelerometer, D: LVDTs)

System A/C
(850×850×290)

M-bar
(50×19×0.5)/@300

Carrying channel
(38×12×1.2)/@900

Anchor & Hanger bolt
(ϕ9mm)/@900

Minor channel
(19×10×1.2)/@2000

Ceiling panel
(300×600×9.5)
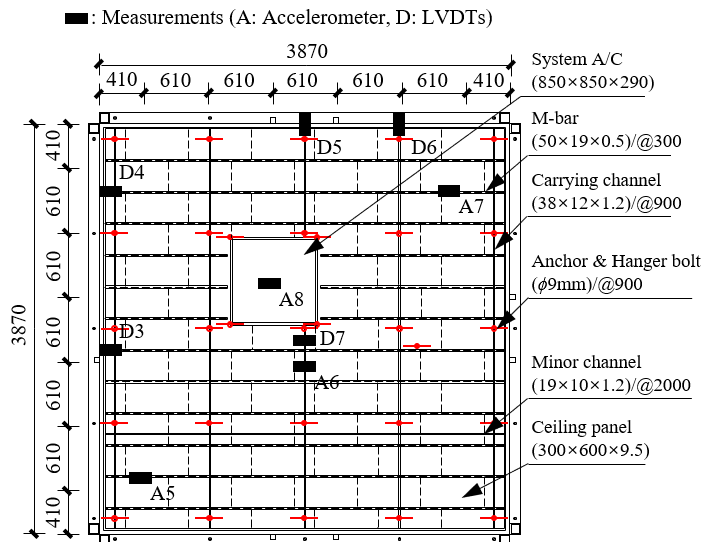
(f) Indirect-hung M-bar ceiling specimen (IMC)
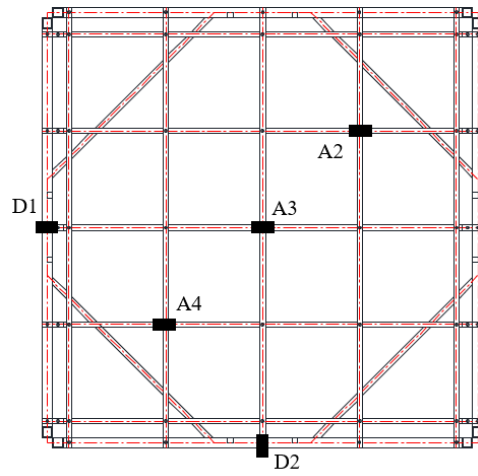
(g) Measurement plan at the top of test frame

Figure 5.12 Configuration of small-size shake table test ceiling specimens
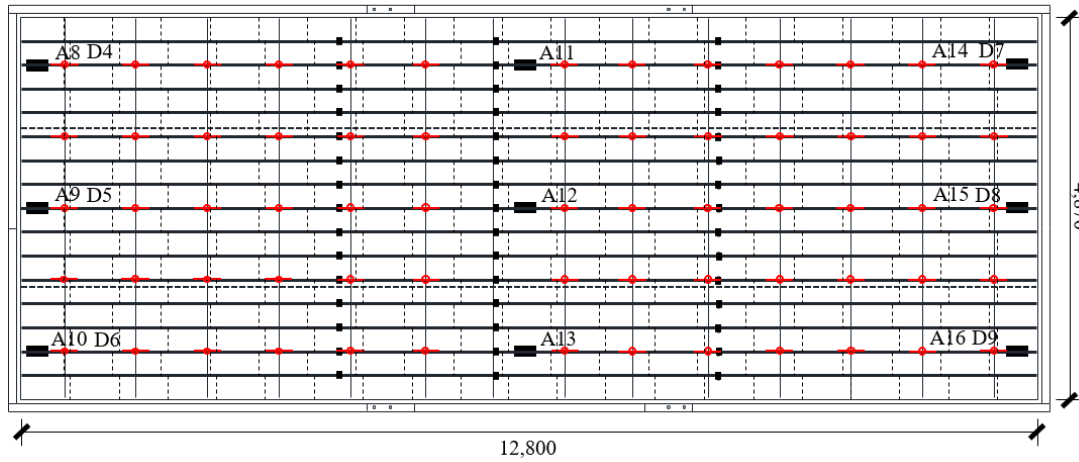
(a) Indirect-hung M-bar ceiling specimen excited along M-bar direction (IMC-L-M)
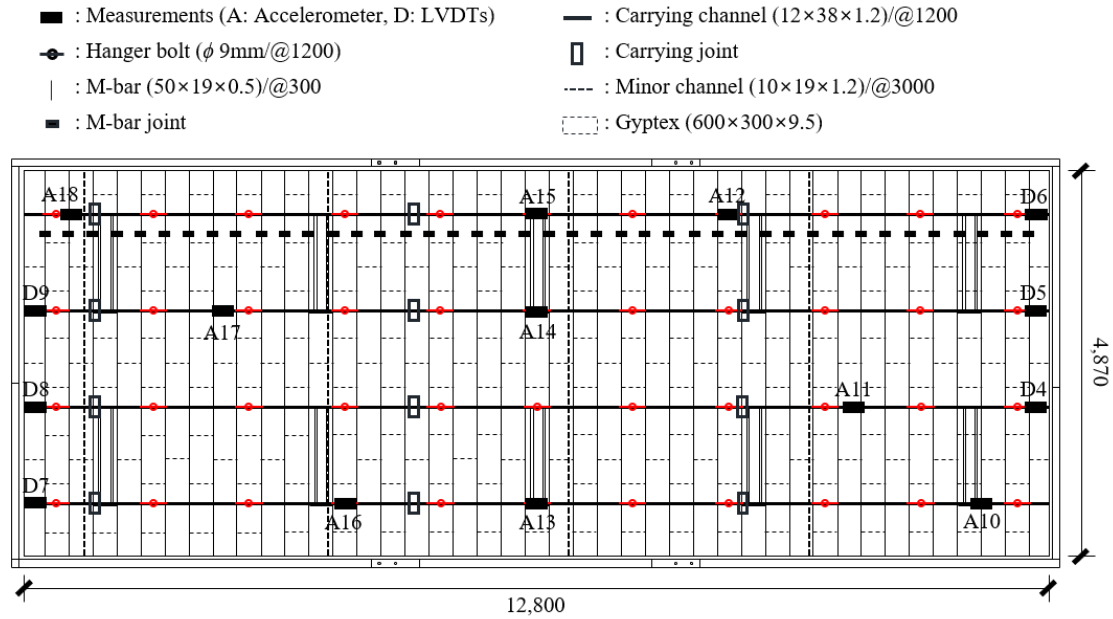
(b) Indirect-hung M-bar ceiling specimen excited along Carrying-channel direction (IMC-L-C)

: Measurements (A: Accelerometer, D: LVDTs) (for IMC-L-C specimen)

: Measurements (A: Accelerometer, D: LVDTs) (for IMC-L-M specimen, marked with *)

A3* D1*

A11

A9 A5*

A7

D2

A10

D2*

A8*

D1

A4*

A8 A6*

A6

D3

A9* A5

D3*

A7*
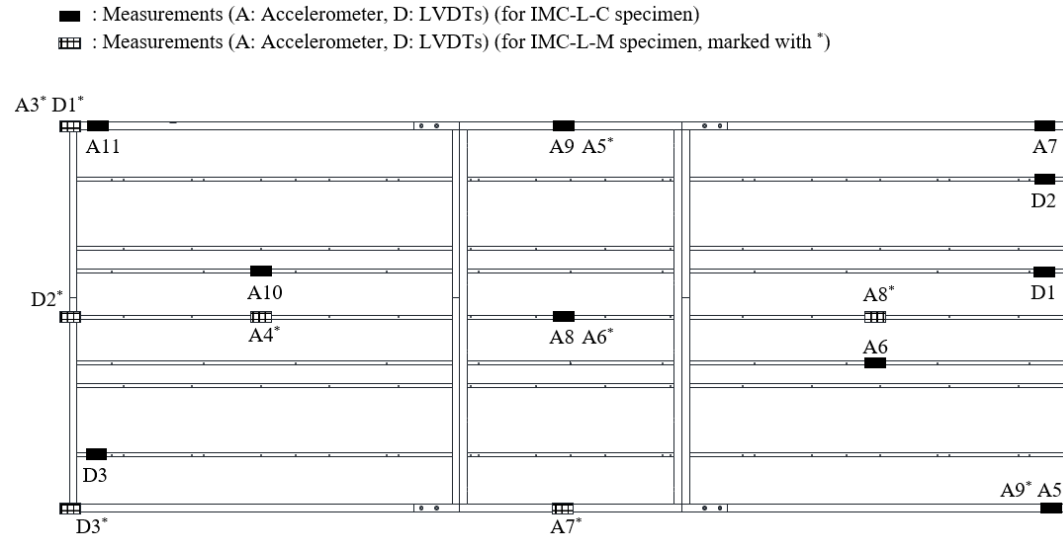
(c) Measurements plan at the top of large-size test frame

Figure 5.13 Configuration of large-size shake table test ceiling specimens

134

Specimen DTL-FS is a lay-in T-bar ceiling system which was installed on the full-scale 2-story steel moment frame which was discussed in Chapter 4 (see Figure 4.1). The specimen was fabricated to have a plan dimension of 9.0 m × 4.07 m. This specimen was specially prepared for evaluating the interaction effects that could be probable when the ceiling is installed with various nonstructural elements. For DTL-FS specimen, partition walls and fire sprinklers were incorporated to assess their interactions with the ceiling specimen. Full- and partial-height partition walls, with two cross-sectional types (rectangular and T-section), were installed at the side and center of the ceiling specimen, respectively. The top of the partial-height partition walls was connected to ceiling grids using ceiling screws ($d = 3.0$ mm), and concrete nails ($d = 3.5$ mm) were used to fix the wall base on the concrete floor slab (see Figure 5.14(b)). Fire sprinklers were provided above the ceiling specimen, penetrating the ceiling panels through flexible sprinkler drops. The sprinkler drops were branched from the water pipes that were suspended to the floor above by hanger bolts. No extra clearances were introduced around the sprinkler drops (see Figure 5.14(c)).

: Measurements (A: Accelerometer, D: LVDT)

Full-height partition

Hanger wire
(φ2.7mm)/@610

Main T-bar
(28×25×0.4)/@610

Cross T-bar
(25×25×0.4)/@610

Ceiling panel
(603×603×15)

D4

A2

D2

A1

D5

A4

D1

A3

Partial-height
partition

Sprinkler

Clearance (15mm)

Molding (50mm)

4,070

1,300

1,900

1,800

1,200

1,900

1,900

9,000
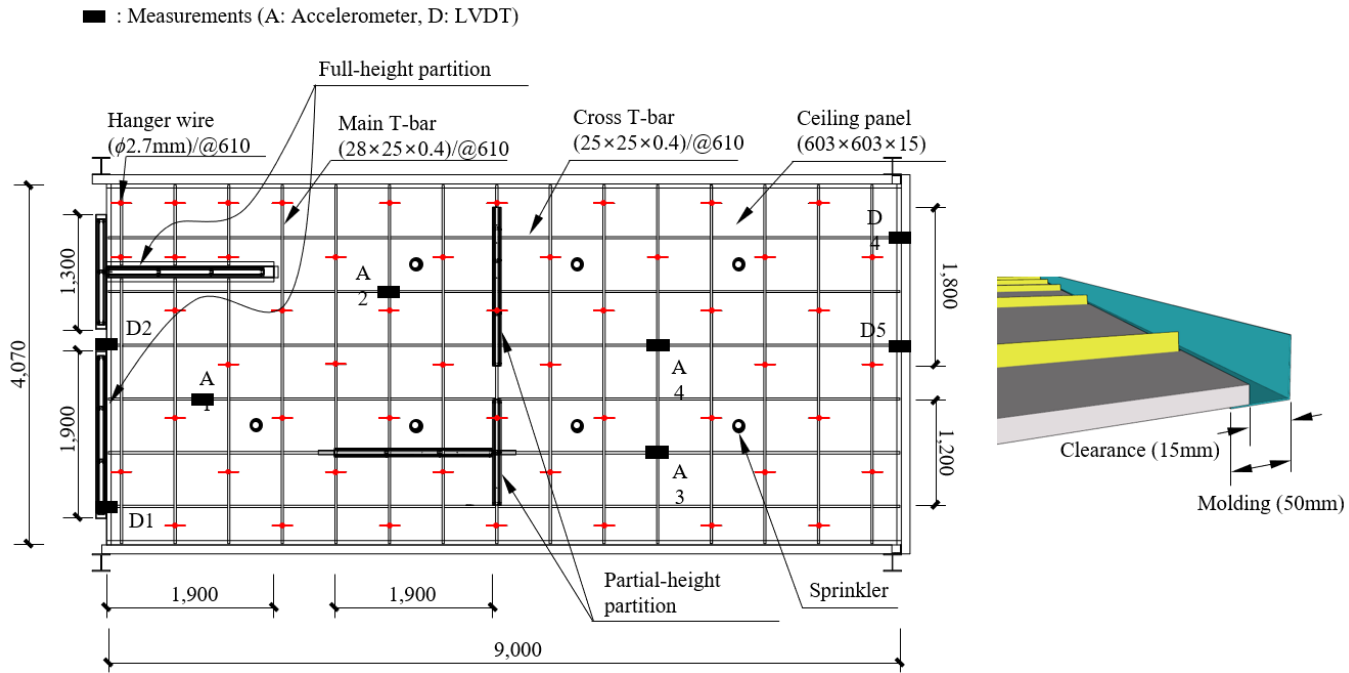
(a) Measurements plan for DTL-FS ceiling specimen

Fixed
(ceiling screw, $d = 3$mm/@600)

Fixed
(concrete nail, $d = 3.5$mm/@600)

ceiling screw
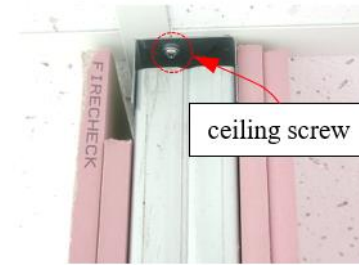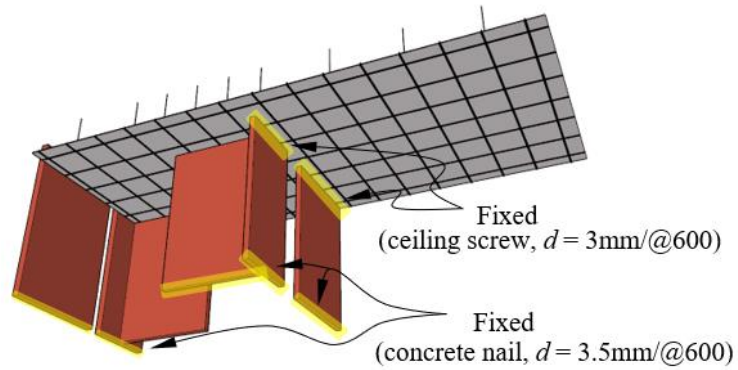
(b) Configuration of full- and partial-height partition walls

Hanger bolt

Sprinkler
branch pipe

Hanger bolt

Water pipe

Flexible sprinkler drop

Sprinkler head

Ceiling grid
mounting bracket
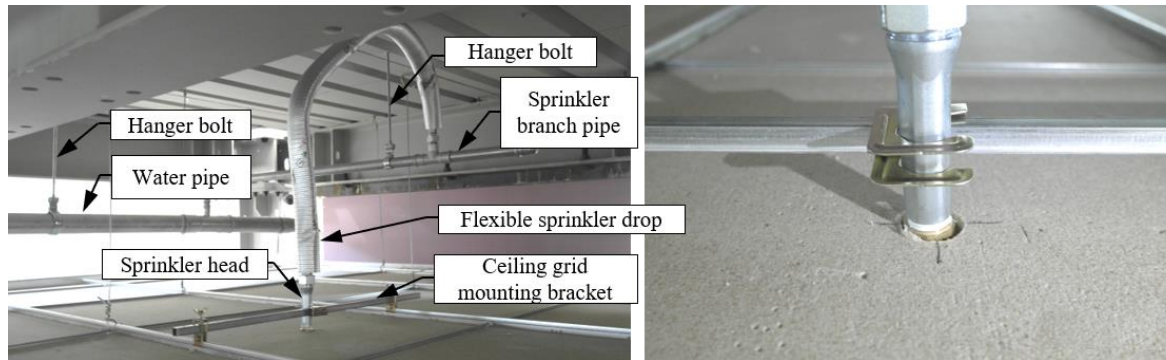
(c) Configuration of water pipes and fire sprinklers installed above ceiling specimen

Figure 5.14 Details of DTL-FS and nonstructural elements installed within ceiling specimen

5.2.3. Loading protocol

Artificial input motions were generated following the protocol recommended by ICC-ES-AC 156 (ICC 2010) discussed in Chapter 4. Figures 5.15 – 5.17 shows the RRS and the TRS obtained from the top of the large-scale and small-scale test frame. The TRS of the full-scale 2-story steel moment frame can be referred to Figure 4.5.

As shown in Figures 5.15(a), the TRS obtained from the small-size exceeded the RRS more than 30 %. It should be highlighted that for the shake table test to be qualified according to ICC-ES-AC 156, the TRS is required to envelope the amplified region (1.3 - 8.3 Hz) of the RRS. Also, the magnitude of the TRS should not exceed more than 30 % of the RRS in the amplified region. Such a higher TRS observed in this test program was to evaluate the performance of DTL specimen which was the most flexible among the specimens of this study. As discussed in Chapter 2.3, the natural frequency of DLT can be predicted using the pendulum formula (Pourali et al. 2017; Yao 2000). The estimated natural frequency of DTL specimen having a plenum depth of 750 mm was 0.56 Hz. The AC 156 protocol was originally
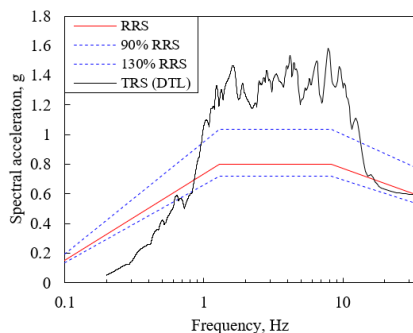
| (a) For direct-hung ceiling | (b) For indirect-hung ceilings |
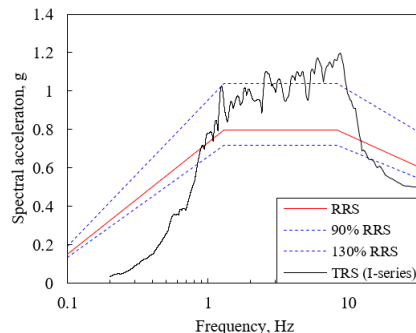
Figure 5.15 Horizontal TRS and RRS for small-size ceiling specimens
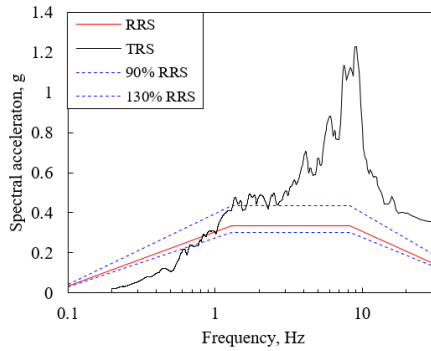
Figure 5.16 Vertical TRS and RRS for small-size ceiling specimens

proposed for testing of nonstructural elements that have fundamental frequencies greater than or equal to 1.3 Hz, or mainly for testing of acceleration-sensitive non-structural elements. However, there are not yet internationally accepted and widely used protocols for testing nonstructural components with low fundamental frequencies. Thus, in this study, the input motion for DTL specimen was generated to have sufficient power in the low-frequency band if possible, within the limit of shake-table capacity. Although the TRS exceeded the RRS amplified region (1.3 – 8.3 Hz) by more than 30 %, the effects of overmatching on the seismic performance of DTL specimen were deemed minor because the specimen's natural frequency was well below the amplified region. The authors thought that it could be acceptable since the primary purpose of this experimental testing was to investigate seismic behavior and damage patterns of the ceilings rather than qualify or certify the ceilings according to the AC 156 standard. The TRS shown in Figure 5.15(a) was used only for DTL specimen. For all the other small-size specimens (ITL, ITHL, IMC) which have natural frequencies within 1.5 – 4.0 Hz, the TRS was re-matched to satisfy the amplitude and envelope requirements given by the AC 156 standards (see Figure 5.15(b)).

| (a) From table A | (b) From table B |
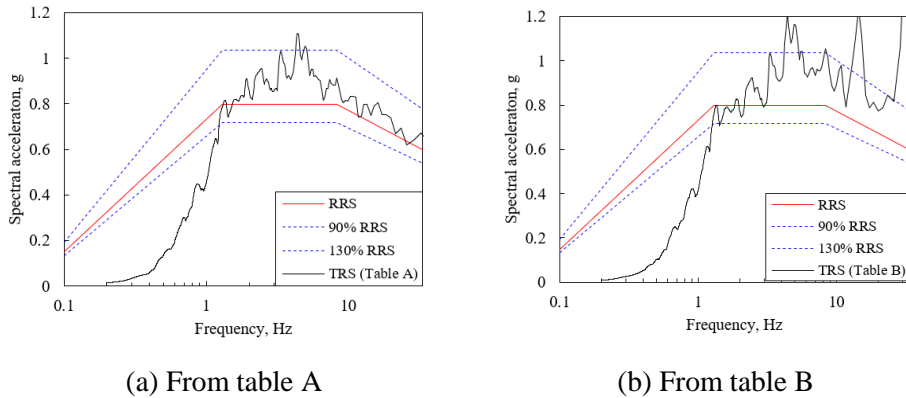
Figure 5.17 Comparison of RRS and TRS obtained from shake table A and B

5.3. Dynamic Properties and Seismic Performance of Ceiling Specimens

This section summarized the shake-table test results including the results of ceiling dynamic characteristics, damage observation.

5.3.1. Fundamental period of suspended ceilings

An analysis of the natural frequency of the tested suspended ceilings is described. In addition, the behavioral characteristics of each specimen are discussed. The analysis and discussion results can be used for developing an analytical model of the natural frequency of ceiling systems. Figure 5.18 shows the transfer function obtained from each test specimen. A low-pass filter with a cut-off frequency of 40 Hz was applied to obtain the transfer functions. The transfer function of specimen IMC was not reported in the figure; the natural frequencies of specimens IMC and IMC-L-series were very similar because the only difference between these specimens was the overall plan dimension and their mass and stiffness were proportional.
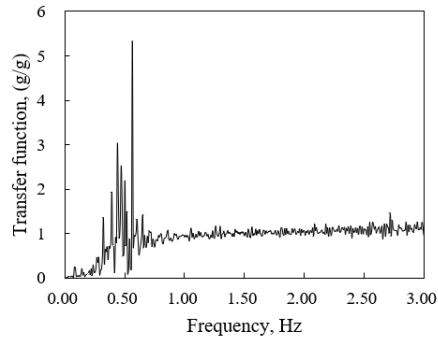
(a) DTL specimen
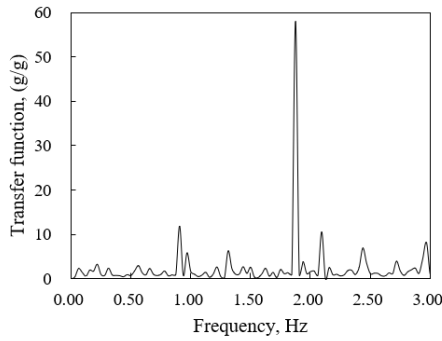
(b) ITL specimen

(single curvature direction)
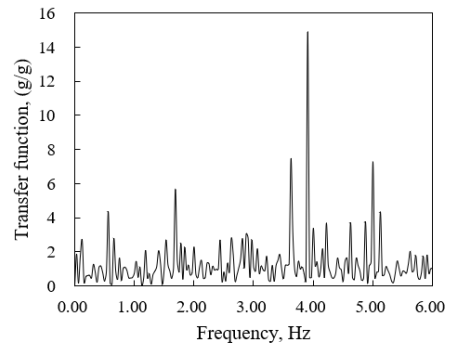
(c) ITL specimen

(double curvature direction)
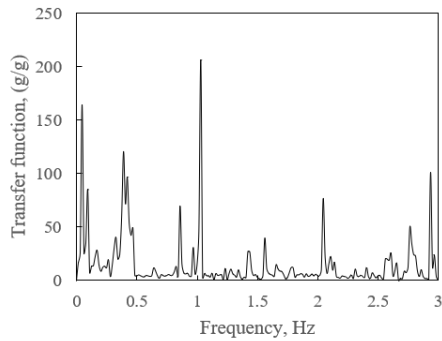
(d) IMC-L-C

(single curvature direction)
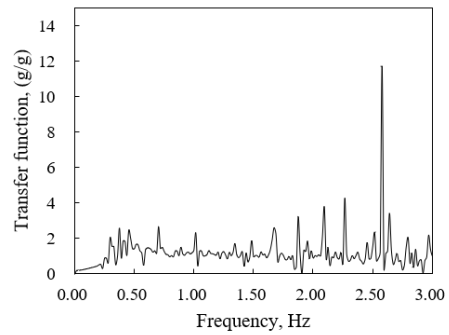
(e) IMC-L-M

(double curvature direction)
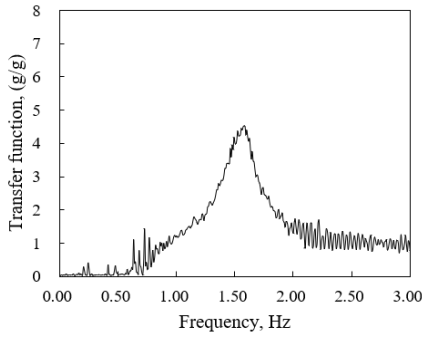
(f) ITL-R1 specimen
(single curvature direction)
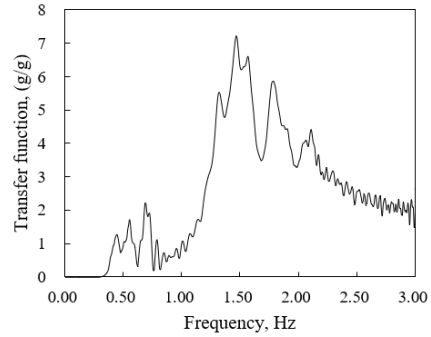
(g) ITL-R2 specimen
(single curvature direction)

Figure 5.18 Measured transfer functions for ceiling specimens

In the case of ITHL specimen, the specimen experienced some damage during the sine sweep test at a magnitude of 0.15 g. Thus, the specimen was re-fabricated and tested with skipping the sine sweep tests and its transfer function was not available.

The measured natural frequency of DTL specimen was 0.56 Hz (see Figure 5.18(a)). It was very close to the natural frequency calculated using the pendulum theory as reported in previous studies (Pourali et al. 2017; Yao 2000). The measured natural frequencies of the indirect-hung ceiling specimens (ITL, ITL-R1, ITL-R2, IMC-L-M, and IMC-L-C) were higher. In particular, it was observed that the specimens showed different natural frequencies in their orthogonal directions. As shown in Figures 5.18(b) – 5.18(e), the measured natural frequencies of ITC were 1.88 Hz and 3.91 Hz in the two orthogonal directions, and those of IMC-L-M and -C specimens were 1.03 Hz and 2.58 Hz, respectively.

These differences in the natural frequency were caused by the differences in the installation and fastening of the hanger members. As shown in Figure 5.19(a), the hanger wire was looped through the holes in the grids members at one end, and the

(a) Hanger wire details

Hanger bolt

Hanger

Carrying channel

Transverse direction

Longitudinal direction
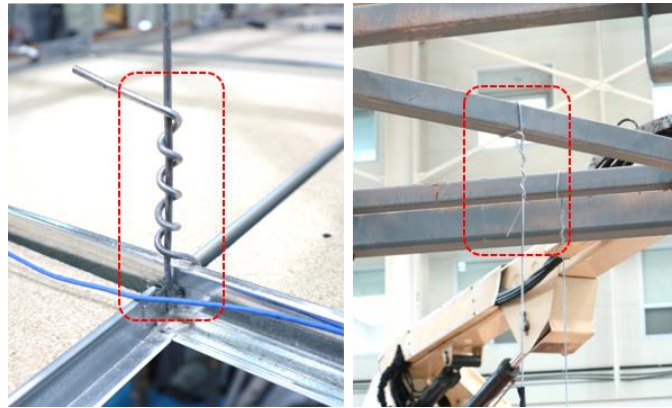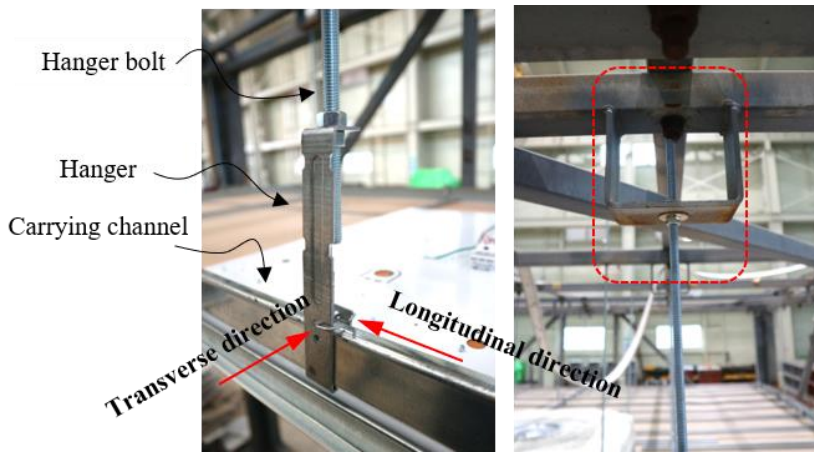
(b) Hanger bolt details

Figure 5.19 Comparison of installed connection details between hanger wire and hanger bolt

other end was looped around the roof members of the test frame. Therefore, the hanger wire was free to rotate at both the ends. Which enabled DTL specimen to respond similar to a pendulum.

In indirect-hung ceiling specimens, the rotational movement of the hanger bolt was restrained at the roof level in both directions. However, at the grid level, the
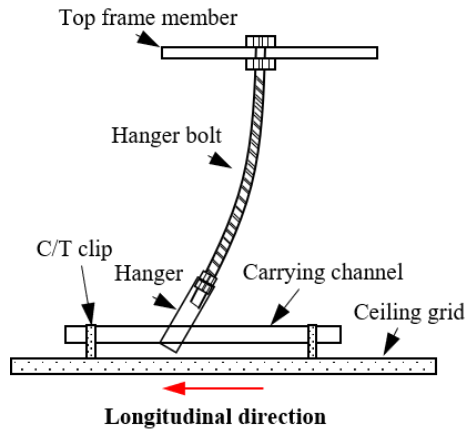
(a) Deformed behavior of hanger bolt in rotation free direction
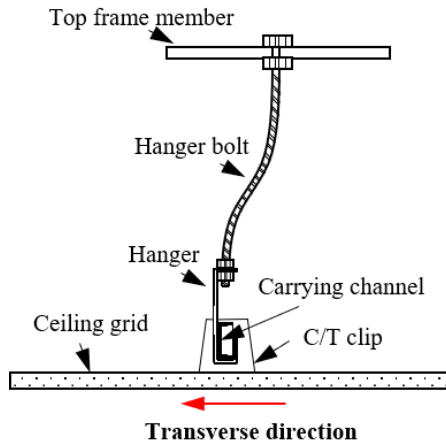
(b) Deformed behavior of hanger bolt in rotation restraiend direction

Figure 5.20 Deformed behavior of hanger bolt

rotational movement of the hanger bolt was restrained only in one (longitudinal) di-
rection (see Figure 5.19(b)). As shown in Figure 20, the hanger bolt showed a single
curvature bending deformation when the ceiling system was excited to the rotation-
free direction. However, a double curvature bending deformation occurred in the
hanger bolt when the excitation was in the rotation-restrained direction, due to the

restraining effect at both ends. Thus, all the indirect-hung ceiling specimens showed higher natural frequencies in their rotation-restrained direction.

The following method of calculating the lateral stiffness of the hanger bolt is recommend for simplified analytical modeling of the observed behavior in the indirect-hung suspended ceiling specimens:

$$k = \frac{3EI}{L^3} \qquad \text{(for single curvature bending)}$$

$$\text{(5.2)}$$

$$k = \frac{12EI}{L^3} \qquad \text{(for double curvature bending)}$$

Thus, the natural frequency of indirect-hung suspended ceilings can be determined as follows:

$$f_n = \frac{1}{2\pi} \sqrt{\frac{\sum k}{m_T}} \qquad \text{(for single curvature bending)} \qquad \text{(5.3)}$$

where $\sum k$ = sum of lateral stiffness of hanger bolt considering the curvature of bending, and m_T = total mass of ceiling system.

When the ceiling mass is uniformly distributed, fn may be calculated based on the lateral stiffness of a hanger bolt and its tributary mass. Table 5.2 compares the measured natural frequencies and those predicted using Eqs. (5.2) and (5.3). A uniform mass distribution was assumed for calculating the natural frequencies listed in Table 5.2. Also, it should be highlighted that the depth of the plenum should be taken

145

without the height of the hanger (in this study, a 100 mmm hanger was used). There-fore, the natural frequency of ceiling specimens with a 750 mm plenum depth was calculated using a plenum depth of 650 mm. From Table 5.2, it can be observed that the natural frequency of DTL specimen is predicted highly accurately by the pendu-lum formula. Also, the simplified analytical modeling in accordance with Eqs. (5.2) and (5.3) yields a satisfactory prediction of the natural frequencies of indirect-hung specimens. The maximum error observed between the measured and predicted value was kept within 10 %.

5.3.2. Damping ratio observed in indirect-hung suspended ceiling

An analysis of the damping ratio of the tested suspended ceilings is presented in this section. The damping ratio was measured using the half-power bandwidth method based on the transfer function measured for ITL-R1 and ITL-R2 specimens (see Figures 5.18(f) and (g)). The damping ratio of indirect-hung suspended ceilings having a wide clearance (410 mm) was measured because of the high acceleration spikes included in the transfer functions of specimens with a narrow clearance of 15 mm.

The measured damping ratio of the fully floating ceiling specimen (ITL-R1) was 7.0 %. This is significantly higher than those of direct-hung suspended ceilings reported by Pourali et al. (2017) (approximately 1 %). The higher damping ratio observed in ITL specimen might be attributed to the high energy dissipation caused by the cyclic frictions around the hanger connections (e.g., hangers and C/T clips)

146

Table 5.2 Comparison of measured and predicted natural frequencies

Specimen	Measured property		Predicted property		Error, %		Plenum depth, mm	Mass per hanger, N/hanger	Remark
	$f_{n,measured}$, Hz (Long.)	$f_{n,measured}$, Hz (Trans.)	$f_{n,calculated}$, Hz (Long.)	$f_{n,calculated}$, Hz (Trans.)	Longitu-dinal	Transverse			
DTL	0.56	0.55	0.56	0.56	0.00	1.79	800	44	Pendulum formula
ITL	1.88	3.91	2.02	4.03	6.93	2.98	650	44	Single (Long.) & double (Trans.) curvature bending
ITL-R1	1.59	-	1.76	-	9.66	-	650	57.8	Single curvature bending
ITL-R2	1.47	-	1.54	-	4.55	-	650	76	Single curvature bending
IMC-L-C	1.03	-	1.06	-	2.83	-	1000	59.7	Single curvature bending
IMC-L-M	-	2.58	-	2.49	-	3.61	900	43.6	Double curvature bending

Longitudinal = parallel to direction of carrying channel; Transverse = perpendicular to direction of carrying channel;
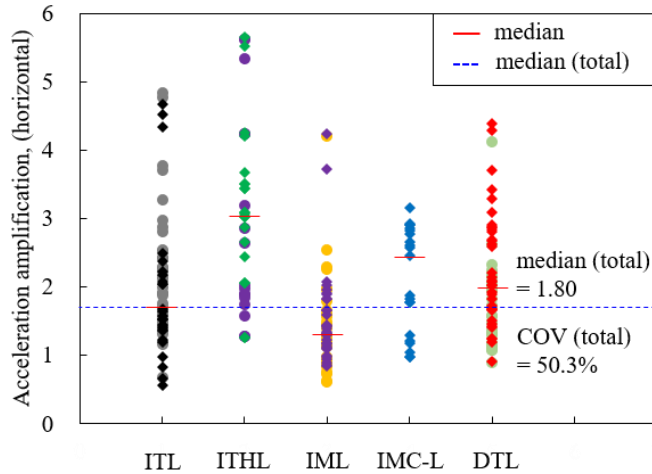
(a) Horizontal acceleration amplification
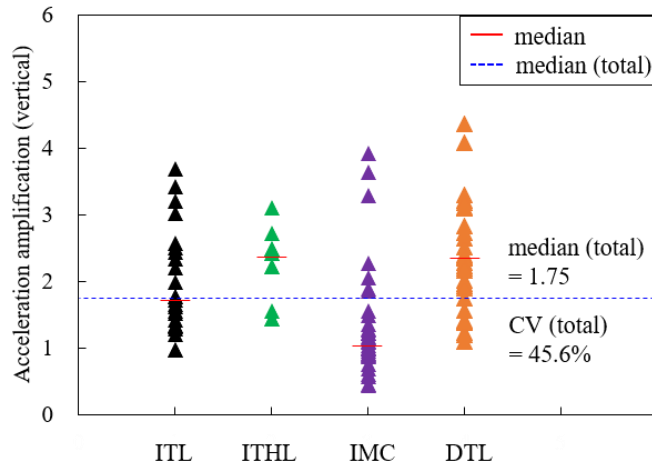
(b) Vertical acceleration amplification

Figure 5.21 Measured acceleration amplification factor

and member interfaces. The damping ratio was significantly increased when the ceiling grid members were laid on the perimeter closure channels, owing to the friction between these two members. The equivalent damping ratio measured in the uniaxial friction specimen (ITL-R1) was approximately 12 %. This could further increase if the friction exits in both the direction. Experimental study conducted by Ryu and

Reinhorn (2019b) showed that the equivalent damping ratio including perimeter friction could be as high as 30 % if the friction around all the perimeters is included. The dynamic frictional coefficients were reported to around 0.2 to 0.3 as reported from study of Huang et al. (2013a). However, for utilizing the perimeter friction effects in the numerical model, further experimental testing is required to better understand the friction damping mechanism attributed to ceiling perimeters.

5.3.3. Acceleration amplification factor

Figure 5.21 shows the acceleration amplification factor measured from each specimen in the horizontal and vertical directions. The amplification factors were determined by normalizing the peak acceleration measured at the ceiling grids, by the peak acceleration measured at the roof of the test frames. Because the low-pass-filtered data with a cut-off frequency of 40 Hz showed unrealistically high acceleration amplification possibly owing to the local vibration of grid members, low-pass filter with a cut-off frequency of 10 Hz was applied to obtain the amplification factors. The median acceleration amplification factor of the tested specimens fluctuated between 1.32 and 3.02, 1.1.3 and 2.43 in the horizontal and vertical directions, respectively.

The median amplification factor of all the indirect-hung ceiling specimens was 1.77, which was close to that of the direct-hung ceiling specimen (1.91). Under vertical excitation, direct-hung ceiling specimen showed a median acceleration amplification ($a_{vert,median} = 2.31$) higher than those of the indirect-hung ceiling specimens ($a_{vert,median} = 1.46$). Compiling all the data, the median amplification factors for the

horizontal and vertical directions were obtained as 1.80 and 1.75, respectively. These are almost two times the acceleration factor ($a_p = 1.0$) specified for the ceilings by ASCE 7 (ASCE/SEI 2017, 2022). The coefficient of variation (COV) obtained in both directions was as high as 50 %.

5.3.4. Damage observation

The main failure mechanism of the ceiling specimens during the incremental-intensity shake table tests are summarized in this section. Tests were initiated from RRS 50 % ($S_{DS} = 0.25$ g) and proceeded up to RRS 275 % ($S_{DS} = 1.38$ g). The peak acceleration measured at the roof center of the test frames, also known as peak floor acceleration, was summarized in conjunction with the accumulated damage states of the ceiling specimens.

In general, the ceiling damage started from the connections of the perimeter grid members because of the pounding forces as the ceiling system s collided with the surrounding walls. In all the small-size specimens, no significant pounding occurred until RRS 100 % ($S_{DS} = 0.50$ g). However, for the large-size test specimen (IMC-L-series), pounding was initiated at 50 % of RRS because of the larger inertia force caused by the larger mass of the ceiling system. Progressive failure of the inner grid members and ceiling panels was observed when significant damage had accumulated at the ceiling perimeter, including the fall of the perimeter ceiling panels. In direct-hung specimens, the damage was confined around ceiling perimeters owing to the higher in-plane stiffness of the grid systems.

Direct-hung suspended T-bar ceiling specimen (DTL)

Figure 5.22 shows the observed damage of DTL specimen during the shake table test. The specimen was substantially damaged owing to the low in-plane stiffness of ceiling grids and weak cross T-bar connections. As shown in Figure 5.25(c) the failure of latch connections caused dislodgement of perimeter ceiling panels. The dislodgement of partial perimeter ceiling panels triggered torsional irregularity in the grid system. This, in turn, caused the ceiling specimen to undergo torsional behavior. Owing to the torsional effect, the inner grid members and panels started to fail rapidly. Approximately 30 % of the ceiling panels were dislodged by the end of the test (see Figure 5.25(d)). The peak floor acceleration and its corresponding ceiling damage states is summarized in Table 5.5.
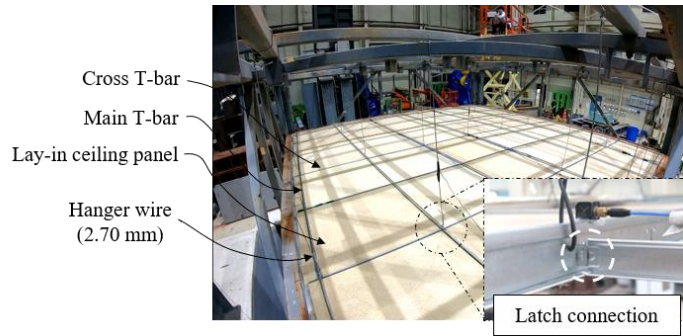
(a) Configuration of DTL specimen

(b) Perimeter ceiling panel displogement

(c) Failure of latch connections
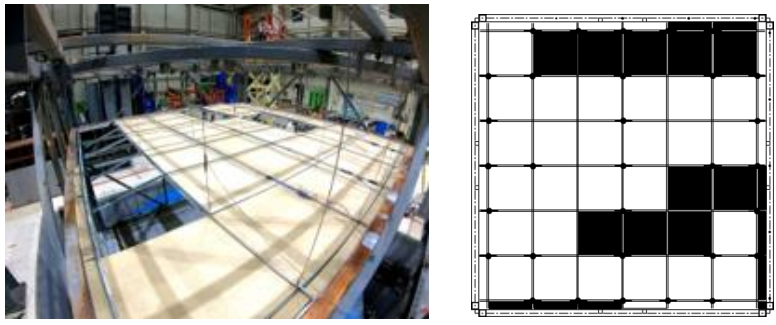
(d) Damage at the end of test

Figure 5.22 Failure pattern of DTL specimen observed during shake table test

Table 5.3 Accumulated damage observed in direct-hung suspended T-bar ceiling (DTL) specimen

Specimen	PFA, g			Damage observations	Fallen ceiling area percentage, %
	x-dir.	y-dir.	z-dir.		
DTL	0.31	0.24	0.09	-	-
	0.48	0.35	0.14	Perimeter cross T-bar connection failure (2 connections)	-
	0.65	0.46	0.18	Perimeter cross T-bar connection failure (4 connections)	-
	0.69	0.53	0.22	Perimeter cross T-bar connection failure (5 connections)	-
	0.86	0.64	0.25	Perimeter cross T-bar connection failure (6 connections) Perimeter ceiling panel dislodgement (3 panels)	1.28
	1.05	0.77	0.28	Perimeter cross T-bar connection failure (9 connections) Cross T-bar connection failure (3 connections) Perimeter & center ceiling panel dislodgement (5 panels) (3 panels)	9.59
	1.24	0.89	0.31	Perimeter cross T-bar connection failure (14 connections) Cross T-bar connection failure (6 connections) Perimeter & center ceiling panel dislodgement (8 panels) (6 panels)	22.44
	1.43	1.03	0.38	Perimeter cross T-bar connection failure (14 connections) Cross T-bar connection failure (12 connections) Perimeter & center ceiling panel dislodgement (10 panels) (10 panels)	29.12

Indirect-hung suspended T-bar ceiling specimen (ITL)

Test results of ITL specimen are summarized in Figure 5.23 and Table 5.4. For ITL specimen, much less damage was observed compared to that of DTL specimen. As the input intensity reaches PFA = 0.71 g, minor ceiling damage was observed (Figure 00). Similar to DTL specimen, the failure of the perimeter cross T-bars (disconnection of the cross T-bar from the main T-bar) caused the perimeter ceiling panel to dislodge (see Figure 00). However, the damage did not propagate into the inner grid members even after the specimen experienced higher intensity input motions than DTL specimen. The main reason for the lower damage observed in ITL specimen was due to the presence of the carrying channels across the main T-bars (see Figure 5.23(c)). The carrying channels (which connect the main T-bars along the entire length of the ceiling) served as a restraint for the cross T-bars (which were demonstrated to be the weakest link in DTL specimen). The carrying channels function as a stabilizer bar, whose installation in the direct-hung suspended ceilings is recommended by ASTM E580. Although stabilizer bars are generally not installed during ceiling seismic performance tests, it was reported by Yao (2000) that the installation of a stabilizer bar alone can enhance the seismic performance of direct-hung suspended ceilings by preventing the lateral spreading of the grid members, similar to the test results of ITL specimen.
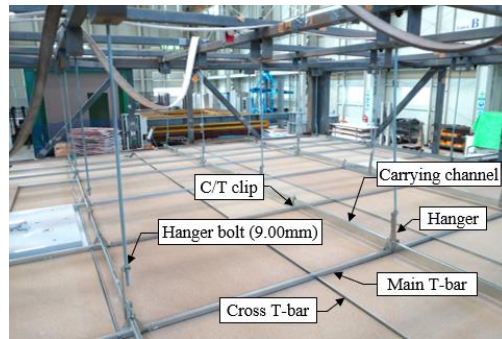
(a) Configuration of ITL specimen

(b) Damage obeserved at the end of test
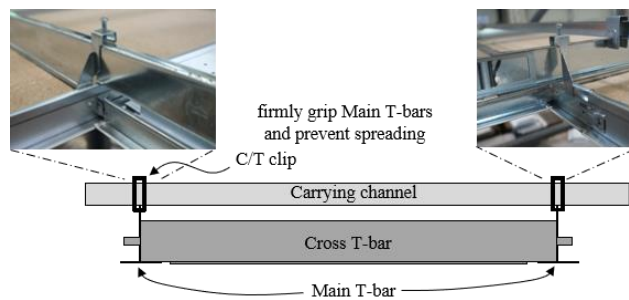
(c) T-bar spreading prevention provided by carrying channel
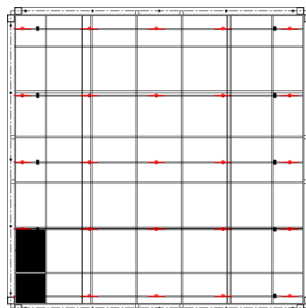
(d) Ceiling area dislodged at the end of test

Figure 5.23 Failure pattern of ITL specimen observed during shake table test

Indirect-hung suspended T&H-bar ceiling specimen (ITL)

In this testing program, the most premature failure was observed in ITHC specimen. As shown in Figure 5.24, most of the panels were unseated from the main T-bars at a low-intensity excitation ($S_{DS} = 0.50$ g). As mentioned previously, cross H-bars do not have any positive connection with the main T-bars. Once the panels started to fail, rapid progressive failure of the entire panels at the perimeter was observed (Figure 5.24(c)). At the end of the test, approximately 40 % of the ceiling panels were dislodged. As shown in Figure 5.27(c), the ceiling area, where the carrying channels prevent the spreading of Main T-bars, did not suffer any damage, which confirms the importance of carrying channels made in the ITL specimen.

Table 5.4 Accumulated damage observed in indirect-hung suspended T-bar ceiling (ITL) specimen

Speci-men	PFA, g			Damage observations	Fallen ceiling area percentage, %
	x-dir.	y-dir.	z-dir.		
ITL	0.84	0.79	0.40	Perimeter cross T-bar connection failure (1 connection)	-
	0.96	0.86	0.48	Perimeter cross T-bar connection failure (1 connection)	-
	1.11	1.02	0.54	Perimeter cross T-bar connection failure (2 connections)	-
	1.23	1.16	0.61	Perimeter cross T-bar connection failure (2 connections)	-
	1.48	1.42	0.71	Perimeter cross T-bar connection failure (2 connections)	-
	1.54	1.49	0.80	Perimeter cross T-bar connection failure (2 connections) Perimeter ceiling panel dislodgement (2 panels)	3.34
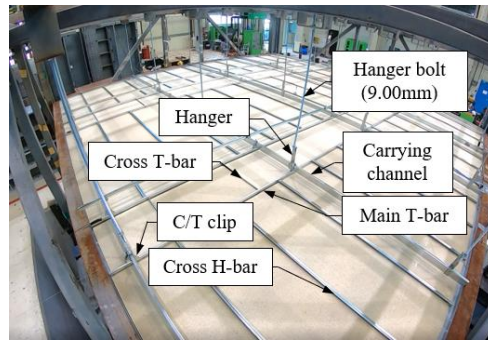
(a) Configuration of ITHL specimen
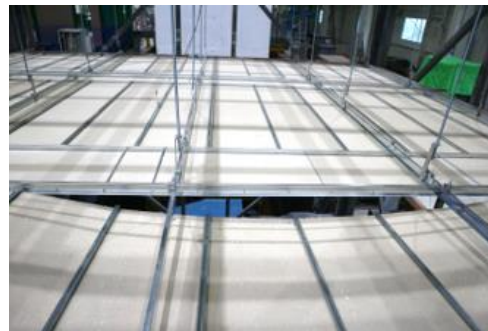
(b) Unseated H-bars
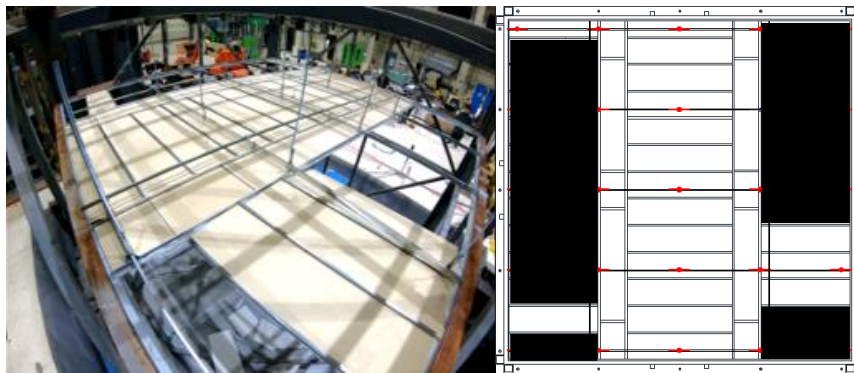
(c) Damage observation made at the end of test

Figure 5.24 Failure pattern of ITHL specimen observed during shake table test

Indirect-hung suspended M-bar Ceiling (IMC-series) specimen

In contrast to the lay-in panel ceiling systems, continuous panel ceiling speci-mens (IMC-series) experienced significantly less damage because of the continuous

restraining effects provided by the screw-attached panels on the grid members. For IMC specimen with triaxial excitation inputs, no observable damage occurred as shown in Figure 5.25. Only a single perimeter panel dislodged at very high input intensity (PFA = 1.61 g). In particular, the concentrated partial failure of ceiling panels was observed at the ceiling perimeter on the same grid line with the air conditioner probably owing to the increased inertial effect there.

The large-size ceiling specimen (IMC-L-M and IMC-L-C) showed significantly different seismic performances in their respective orthogonal directions. For the IMC-L-M specimen where the pounding occurred on the M-bars, there was only minor damage until the end of the test. However, the IMC-L-C specimen, which was excited to pounding along the carrying channels, experienced global ceiling failure due to the failure of the grid connections.

Table 5.5 Accumulated damage observed in indirect-hung suspended T&H-bar ceiling (ITHL) specimen

Speci-men	PFA, g			Damage observations	Fallen ceiling area per-centage, %
	x-dir.	y-dir.	z-dir.		
ITHL	0.57	0.55	0.29	Ceiling panel unseated	-
	0.72	0.74	0.33	Ceiling panel unseated	-
	0.85	0.87	0.49	Ceiling panel dislodgment (3 panels)	7.27
	0.97	0.97	0.38	Ceiling panel dislodgment (9 panels)	21.81
	1.09	1.14	0.50	Ceiling panel dislodgment (18 panels)	43.63
	1.27	1.32	0.54	Ceiling panel dislodgment (18 panels)	43.63

Figure 5.25 Failure pattern of IMC specimen observed during shake table test

Figure 5.26 shows the damage observed for the IMC-L-M specimen at the end of the test. Even after the specimen was subjected to significantly high input motions compared to those used for the other specimens, only partial crack of the perimeter ceiling panels and molding damage were observed because of the continuous restraining effects provided by the screw-attached panels on the M-bars.

Figure 5.27 summarizes the sequence of ceiling damage observed from the IMC-L-C specimen. As shown in Figure 5.27(a), the pounding at the ceiling perimeter initiated the failure of carrying channel joints which disarranged the location of the carrying members. The M-bar clips, which firmly connect ceiling panels and carrying members, were subjected to bending moment that was caused by the pounding forces and the disarranged carrying channels (150 % RRS, PFA = 0.85 g). The carrying channels restrained to M-bar clips which provide only one-sided restraining

Figure 5.26 Failure pattern of IMC-L-M specimen observed during shake table test

forces, caused underwent torsional behavior, which further accelerated the failure of all the joints connected to them (see Figure 5.27(b)). As the hanger (hanger bolt – carrying channel joint member) and the M-bar clips disconnected the whole ceiling grid system dislodged in enormous scale. About 1/4 of total ceiling area collapsed at the end of the test (see Figures 5.27(c)-(d)).
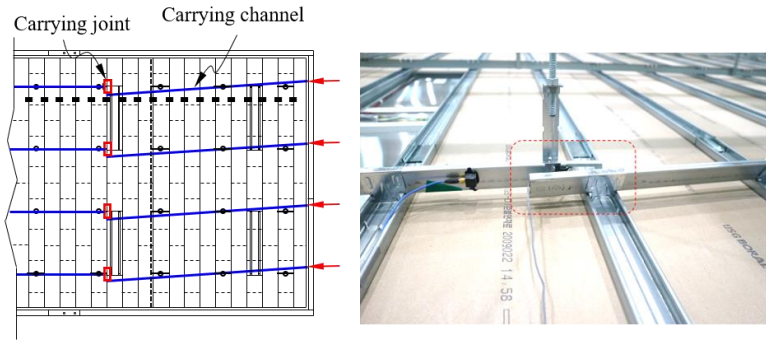
(a) Carrying joint failure
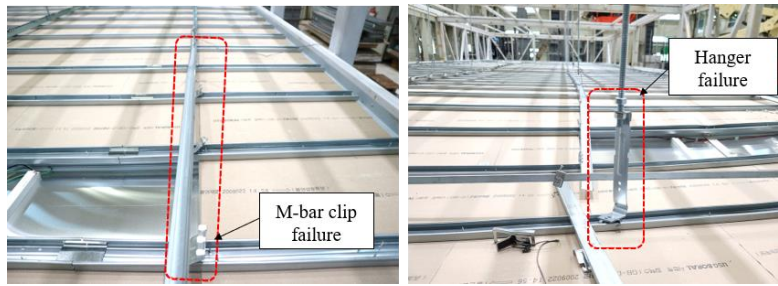
(b) M-bar clip and hanger failure

(c) Damage at the end of test

(d) Damage observation made at the end of test

Figure 5.27 Failure pattern of IMC-L-C specimen observed during shake table test

5.4. Effect of Component Interaction on Seismic Performance of Suspended Ceiling

The seismic performances of partition-attached ceiling (DTL-FS) specimen installed on the full-scale 2-story steel moment frame are presented in this section. The specimen was damaged at 30 % RRS input intensity, and about 55 ceiling panels were dislodged at the end of the test (150 % RRS).

Figure 5.28 shows the natural frequency of the non-seismic ceiling specimen. The specimen exhibited a higher natural frequency ($f_{n,ceiling}$ = 2.78 Hz) than that calculated according to the pendulum model for a free-floating ceiling system because of the lateral restraint provided by the attached partial-height partition walls. The kinematic interaction between the ceiling and partition walls adversely affected the ceiling seismic performance. The partitions experienced sever in-plan and out-of-plane rocking behavior because of the weak fixity provided at the bottom of the partitions. The fire sprinklers did not cause noticeable damage to the ceiling because the
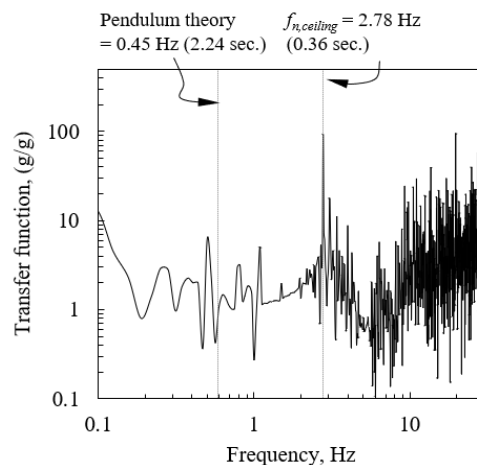
Figure 5.28 Increase of natural frequency of partition-connected (non-seismic) ceiling specimen

flexible sprinkler drops absorbed most of the relative displacements between the ceiling system and their main body (water pipes).

Table5.6 summarizes the ceiling damage observed during the test. Under 30 % RRS (PFA = 0.36 g) input level, about 50 % (7/14 panels) of the perimeter panels were dislodged, which was caused by the increased pounding forces resulting from the out-of-plane rocking of the rectangular partition. The T-section partition did not cause ceiling damage as the web partition prevented the rocking of the flange partition. Under 60 % and 100 % RRS input intensities, both the rectangular and the flange partitions overturned, causing widespread panel dislodgements at the ceiling perimeters. The pull-out forces developed when the partitions overturned seemed minor because the fastening between ceiling grids and the partitions was weak. Therefore, no significant damage was observed around the ceiling-partition joints (see Figures 5.29(a) – (d)). The occurrence of damage at the ceiling center was delayed to a higher intensity level (150 % RRS) (Figure 5.29(e)).

In Figure 5.33, the performance of the DTL-FS specimen is compared with previous test results to clearly show the effect of the partition-induced interaction on ceiling seismic performance. All the previous studies in Figure 5.30 utilized the same ceiling configurations as specimen DTL-FS, but partitions were not attached. It was observed that the seismic performance of suspended ceilings generally depends on the test input intensity and ceiling specimen area, as expected. In the tests conducted with approximately 20 m^2 ceiling area, damage was initiated around PFA = 1.50 g level, whereas a much inferior performance was reported in a test conducted with larger ceiling area (Ryu and Reinhorn 2019a). The specimen used in this study had
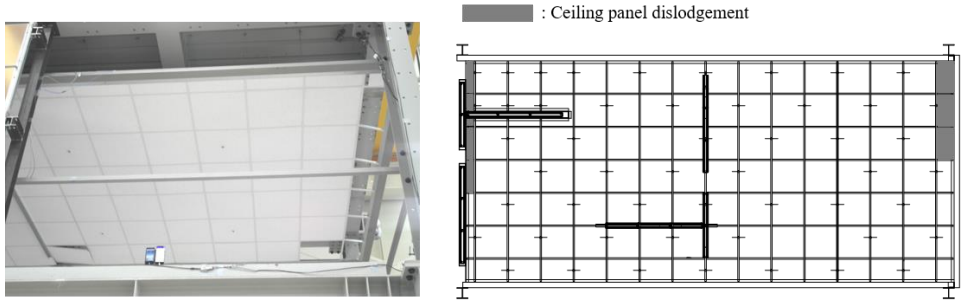
(a) Panel dislodgement at ceiling perimeter (60 % RRS, PFA = 0.54 g)
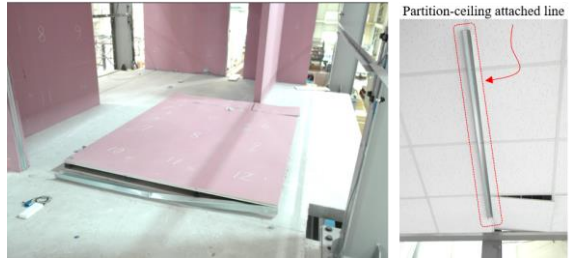
(b) Overturned rectangular partition and minor damage around partition-ceiling joint (60 % RRS, PFA = 0.54 g)
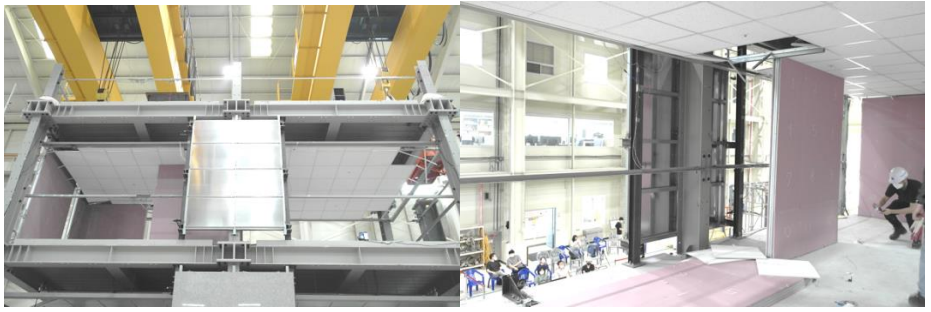
(c) Panel dislodgement at ceiling perimeter and T-section partition overturned (100 % RRS, PFA = 0.90 g)
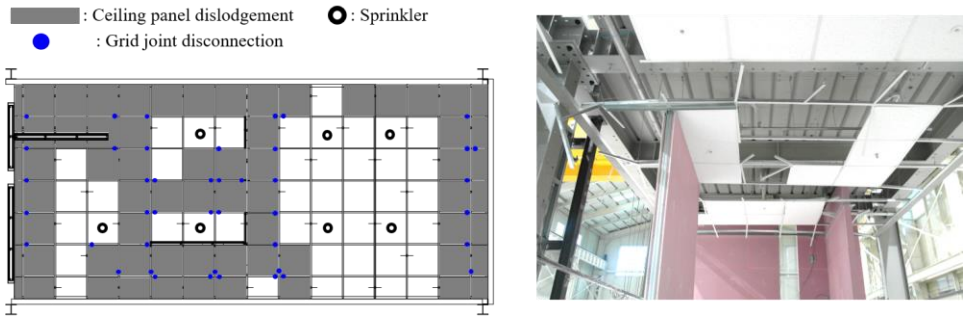
(d) Fallen ceiling area observed at the end of tests (PFA = 1.12g)

Figure 5.29 Failure pattern of DTL-FS specimen observed during shake table test
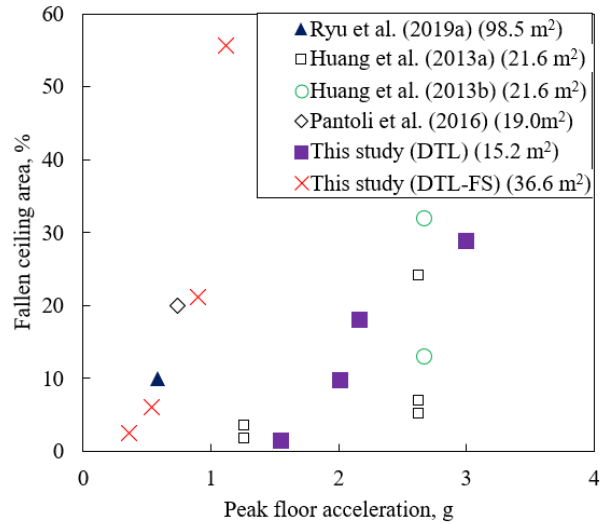
Figure 5.30 Effect of partition-induced interaction on ceiling fragility

an area smaller than half the area of the specimens tested by Ryu and Reinhorn (2019a) but showed comparable results, clearly indicating the performance degradation resulting from partition-induced interaction. Therefore, careful detailing considerations should be given when interactions between nonstructural elements are involved. However, considering the extra complexities and uncertainties in their dynamic behaviors, it would be more advantageous to design individual elements separately, as was done for the braced ceiling specimen which will be discussed in Chapter 6.

Table 5.6 Measured PFA and accumulated ceiling and partition damage observed

Specimen	Input level	PFA, g	Damage observations	Fallen ceiling area percentage, %
DTL-FS	30 % RRS	0.36	Perimeter panel dislodgement (7 panels)	2.53
	60 % RRS	0.54	Perimeter panel dislodgement (10 panels) Inner panel dislodgement (2 panels) Partial-height flat partition out-of-plane overturning	5.98
	100 % RRS	0.9	Perimeter panel dislodgement (14 panels) Inner panel dislodgment (17 panels) Partial-height rectangular partition overturning Partial-height T-section partition overturning	21.12
	150 % RRS	1.12	Perimeter panel dislodgement (14 panels) Inner panel dislodgment (54 panels) Partial-height rectangular partition overturning Partial-height T-section partition overturning	55.62

5.5. Summary and Conclusions

In this chapter, shake table tests of various types of suspended ceiling systems were conducted using two large-size uniaxial loading specimens and six small-size multi-directional loading specimens. The effects of interaction among nonstructural elements were also discussed through the partition-attached full-scale ceiling specimen. Based on the test results, their seismic performance and physical behavior were evaluated, and key dynamic properties were identified. The results of shake-table tests can be summarized as follows.

(1) The analysis of natural frequency of the test specimens clearly indicated that the behavior of suspended ceilings strongly depends on the connection details of the hanger members. The direct-hung suspended ceiling specimens with hanger wires showed the pendulum behavior because both ends of the hanger wire were free to rotate. The indirect-hung suspended ceiling specimens with hanger bolts showed a much higher natural frequency owing to the rotation-restrained characteristics of the connection between the hanger bolt and the frame top. Single and double curvature bending deformations were observed for each orthogonal direction because of the unidirectional rotation-restrained characteristics of the connection between the hanger bolt and the grid system. The calculated natural frequencies using the single and double curvature bending models proposed in this study showed good agreement with the measured natural frequencies. These be-

havioral characteristics found in direct- and indirect-hung suspended ceiling systems are essential for developing rational engineering design procedures for such ceiling systems.

(2) The indirect-hung suspended ceiling systems showed a higher damping ratio ($\zeta = 7$ %) than that of the indirect-hung suspended ceiling systems ($\zeta = 1$ %). The higher damping ratio observed in the indirect-hung ceiling specimen is attributed to the high energy dissipation caused by cyclic friction around the hanger connections and member interfaces. The damping ratio was significantly increased when the ceiling grid members were laid on the perimeter closure channels, owing to the friction between these two members. The equivalent damping ratio measured from the uniaxial friction specimen (ITL-R1) was estimated to be approximately 12 %.

(3) The measured acceleration amplification factors were generally higher than that given by ASCE 7, for both the horizonal and vertical directions. The median acceleration amplification factors in the horizontal and vertical directions were measured to be 1.80 and 1.75, respectively. The acceleration amplification factor needs to be prescribed more conservatively considering the high coefficient of variation observed (approximately 50 %). Assuming the suspended ceiling system as a rigid nonstructural element appears untenable unless all the ceiling perimeters are fixed to the surrounding walls.

(4) The direct-hung T-bar ceiling specimen suffered substantial damage mainly

because of the early damage to the cross T-bars and its low in-plane stiffness. Much less damage was observed in the indirect-hung T-bar ceiling specimens although the specimens experienced stronger input motions. This can be explained in terms of the presence of the carrying channels in the indirect-hung specimens, which restrain cross T-bars from spreading and thus enhance the in-plane stiffness of grid systems. The test results clearly show the importance of grid members, which contribute to maintaining the in-plane stiffness of ceiling systems by functioning as a stabilizer bar in direct-hung ceiling systems.

(5) The large-size continuous ceiling specimen showed different seismic performances in their respective orthogonal direction. IMC-L-M specimen showed only minor damage because of its continuous restraining effects provided by the screw-attached panels on the grid members. The triaxially excited specimen installed with an air conditioner also showed only minor damage. However, IMC-L-C specimen, which was excited to pounding along the carrying channels, experienced global ceiling failure mainly due to the failure of the carrying joints. The failure of the carrying joints initiated extensive joint failures within the ceiling specimen. It can be concluded that the high in-plane stiffness attributed to screw-attached ceiling panels is only effective on the M-bar layer of the ceiling specimen. Therefore, careful design consideration should be given on the ceiling grid layer composed of carrying channels, especially in regard to the joint strength.

(6) The partition-attached ceiling specimen suffered severe damage resulting

from the rocking behavior of the partial-height partition walls. The out-of-plane rocking of the partitions caused significant dislodgements and grid joint disconnections at the perimeters and the center of the ceiling. The ceiling damage started at a very low input intensity (30 % RRS, PGA = 0.10 g), and approximately 60 % of ceiling panels were dislodged at the end of the tests. The ceiling seismic performance were compared by collating previous studies, and the adverse effects of the nonstructural component interaction were discussed.

Chapter 6. Proposal of New Seismic Ceiling Systems

6.1. Introduction

Generally, seismic design of suspended ceiling systems has been performed based on ASTM E580, which provides seismic requirements that should be installed on ceilings during their construction. The main design strategy of ASTM E580 is to restrain the movement of ceilings by rigidly fixing all the perimeters to wall molding through seismic clips or pop rivets. For large area ceilings, a lateral bracing system is usually preferred. Details of the requirements is summarized in Chapter 2.

Numerous previous studies such as Rihal and Granneman (1984), Badillo-Almaraz et al. (2007), Soroushian et al. (2019) conducted experimental studies on evaluating the effectiveness of the seismic requirements given by ASTM E580. However, unanimous consent on the effectiveness of ceiling bracing have not been made as some of the studies reported inferiority of the braced ceiling system in improving the overall seismic performance. It is speculated that such different obser-

vations might be caused by various factors, such as the sensitivity of the tested ceiling systems to boundary conditions, specimen sizes, and the characteristics of input motions. As shown in Table 6.1, previous experimental studies were conducted on suspended ceiling specimens with different sizes and boundary conditions using different input motions. Because most of the studies mainly focused on the global failure modes and overall seismic performance, detailed dynamic responses of braced ceiling systems have not been reported and are still not clearly understood.

In this study, a series of shake table tests were first conducted using braced suspended ceiling specimens. Based on the test results, the seismic performances and

Table 6.1 Summary of previous studies evaluating seismic performance of braced ceiling systems

Authors	Excitation type	Loading directions	Size, m	Brace type	Boundary condition
Ryu and Rinhorn (2019a)	ICC-AC156	3-directional	6.10 × 15.2	comp. posts & splay wires	two-side rivet fixed
Rihal and Granneman (1984)	sinusoidal	uni-diretional	3.65 × 4.87	comp. posts & splay wires	two-side fixed
Badillo-Almaraz et al. (2007)	ICC-AC156	3-directional	4.90 × 4.90	comp. posts & splay wires	two-side rivet fixed
Huang et al. (2013a)	generated floor motion	3-directional	3.60 × 6.00	comp. posts & splay wires	two-side fixed & partial height partition installed
Yao (2000)	artificial ground motion	uni-diretional	1.20 × 4.00	comp. posts & splay wires	four-side free
Soroushian et al. (2016b)	recorded ground motion	3-directional	84 m2	comp. posts & splay wires	two-side fixed with seismic clip
Gilani et al. (2010)	ICC-AC156	3-directional	4.9 × 4.9	comp. posts & splay wires	two-side rivet fixed
Shimizu et al. (2018)	recorded ground motion	uni-diretional	1.8 × 2.4	rigid brace	four-side free
Brandolese et al. (2019)	cyclic test	uni-diretional	2.4 × 2.4	rigid brace	perimeter frictional bracket
Fiorino et al. (2020)	cyclic test	uni-diretional	-	comp. posts & splay wires	four-side free

172

response were analyzed. The limitations and side effects resulting from ceiling braces were discussed. In the purpose of enhancing the braced ceiling system, a seismic strengthening method using grid reinforcement was proposed and its performance was verified through the full-scale shake table tests. Also, as a cost-effective design or retrofit method, a rotational friction damper for suspended ceiling systems was developed, and its seismic performance was evaluated using shake table tests. The dynamic characteristics and mechanism of the proposed friction damper were experimentally calibrated, and a simple dynamic analysis model for the friction-added ceiling system was proposed. A numerical case study was performed to evaluate the applicability of the proposed ceiling system and draw useful design recommendations based on extensive time history analyses of steel moment-frame buildings.

6.2. Experimental Performance Evaluation of Proposed Seismic Ceiling Systems

Shake table tests were implement for three types of suspended ceiling specimens: braced, brace with grid reinforcement, and friction-mechanism added. All specimens belonged to a direct-hung T-bar ceiling system, which has a least seismic performance as discussed in Chapter 5. The test frames introduced in the previous chapter were utilized (small-size test frame and full-scale 2-story steel moment frame), therefore, will not be discussed in this section. The details of each test specimen are described below.

6.2.1. Test specimens and measurements

Table 6.2 summarizes the key information of the three specimens. The perimeter clearance introduced in each specimen was selected to satisfy the minimum requirement recommended by ASTM E580.

Specimen DTL-B is a braced ceiling specimen fabricated following the requirements for SDC D, E, and F ceilings. The braces were rigidly designed based on the equivalent static force prescribed by ASCE 7-16 (ASCE/SEI 2017). The equivalent static force was calculated by considering two parameters: the story height ratio ($z/h = 1.0$) and the design spectral acceleration at short periods ($S_{DS} = 0.50$ g), which correspond to the highest seismic demand according to the Korean Design Standards (KDS 41 17 00) (AIK 2019). A channel section of C-50 × 45 × 0.8 was used as a brace member. It had sufficient strength of more than three times the calculated equivalent static force. The calculated natural frequency of specimen DTL-B was approximately 28 Hz, and the specimen was almost rigid. The braces were installed at the top of the ceiling grid center using specially detailed bolted ceiling brackets, as shown in Figure 6.1. These brackets also contributed to strengthening the latch joint between the main and T-bars at the bracing locations where a large force concentration was expected.

Table 6.2 Seismic suspended ceiling test specimens used in this study

Specimen	ceiling size	Excitation	Perimeter clearance, mm	Plenum depth, m	Performance-enhancing feature
DTL-B	3.87 × 3.87	3-D	20	0.75	Rigid brace
DTL-FS-BS	4.06 × 8.99	1-D	20	0.79	Rigid brace with grid reinforcement
DTL-F	3.87 × 3.87	3-D	20	0.75	Friction damper
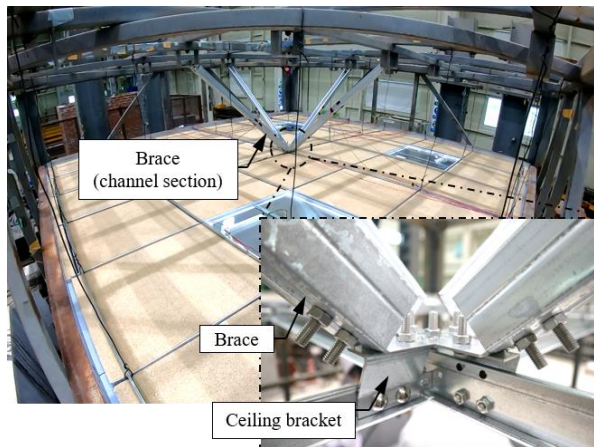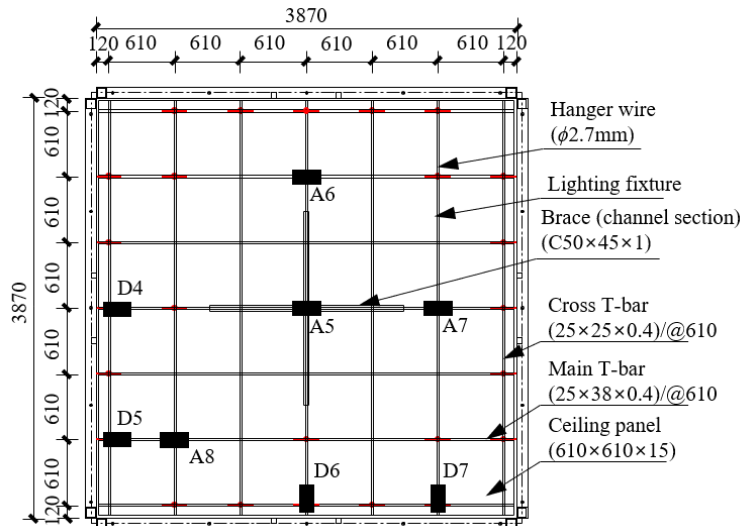
Figure 6.1 Configuration of braced direct-hung T-bar ceiling specimen (DTL-B)

Specimen DTL-FS-BS was also fabricated following the requirements used to design DTL-F specimen. A 20 mm clearance was introduced around the ceiling perimeters, and three lateral bracings were provided within the specimen. Grid reinforcement were added at each bracing location to promote the rigid diaphragm action of the ceiling grids (see Figure 6.2). Through the grid reinforcements, the inertial force provided by the ceiling mass can be more effectively collected and transmitted
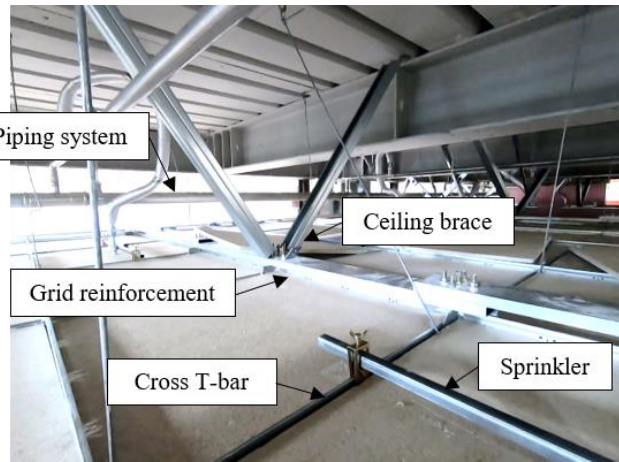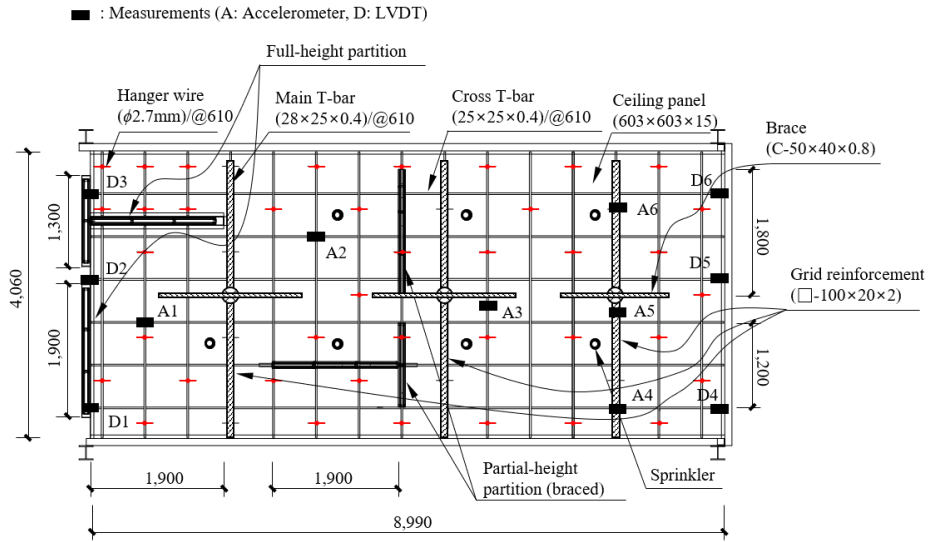
Figure 6.2 Configuration of braced ceiling specimen installed with grid rein-
forcements (DTL-FS-BS)

to the concrete floor slab (Figure 6.3). The reinforcement design can be conducted
by selecting the reinforcing member such that a displacement smaller than the intro-
duced clearance would occur. The lateral displacement of the reinforcement is cal-
culated by simplifying its behavior as that of the cantilever beam subjected to a uni-
formly distributed load (Figure 6.3). In this study, the reinforcement design was con-
ducted based on the same equivalent static force used for design DTL-F specimen.
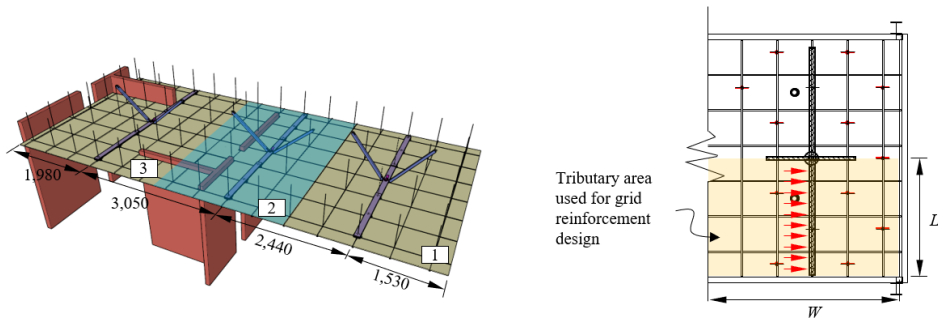
(a) Ceiling tributary area allocated for each grid reinforcement

$w = m \times W$

$\delta = \dfrac{wL^4}{8EI}$ $\leq$ clearance (20mm)
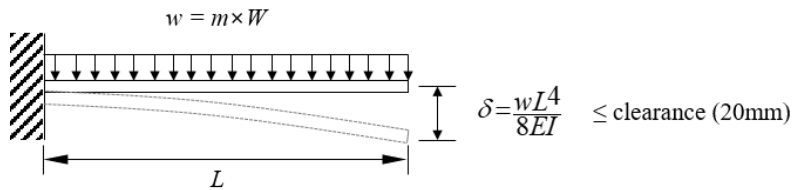
where
δ = maximum allowable deflection to avoid pounding
w = uniform load act on grid reinforcement
m = mass per unit ceiling area
L = length of grid reinforcement
W = width of tributary area

(b) Cantilever beam model employed for grid reinforcement design

Figure 6.3 Ceiling grid reinforcement design for inertial force provided from ceiling tributary area

The reinforcements were designed utilizing the mass that comes from their tributary area (Figure 6.3). A box channel section of $100 \times 20 \times 2$ (in mm) provided sufficient stiffness to avoid pounding.

A rotation friction damper was developed and included in the specimen DTL-F. The friction damper, which is frequently used in structural systems (for example, Mualla and Belev 2002; Monir and Zeynali 2013), was detailed to be operable under suspended ceiling systems and to maintain a consistent friction force for bi-directional excitation. Figure 6.5 shows the components of the proposed friction damper.
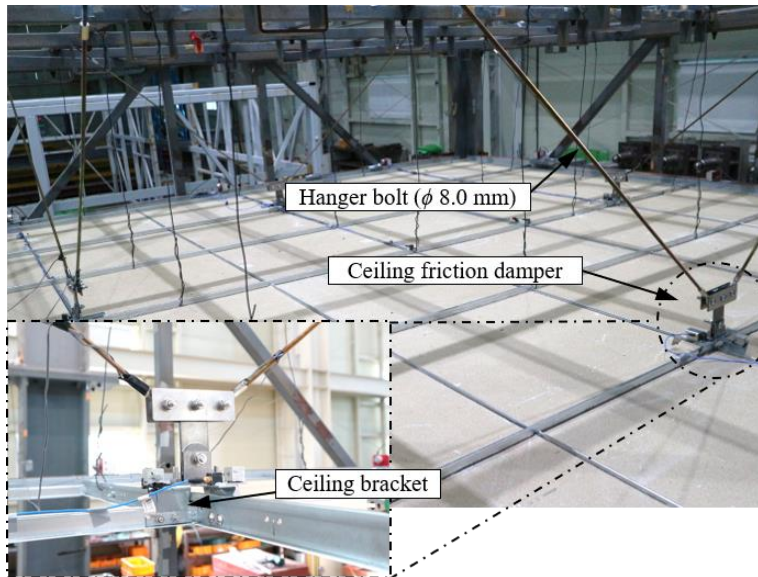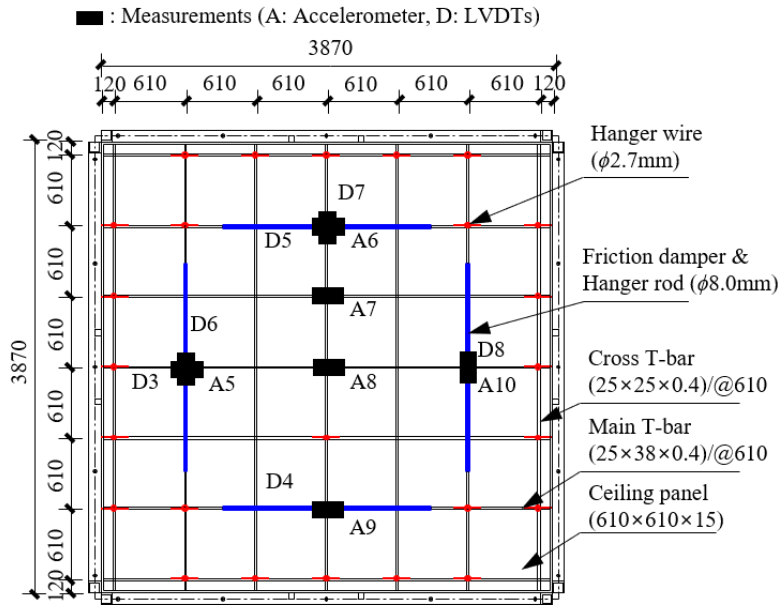
Figure 6.4 Configuration of ceiling specimen with friction mechanism added (DTL-F)
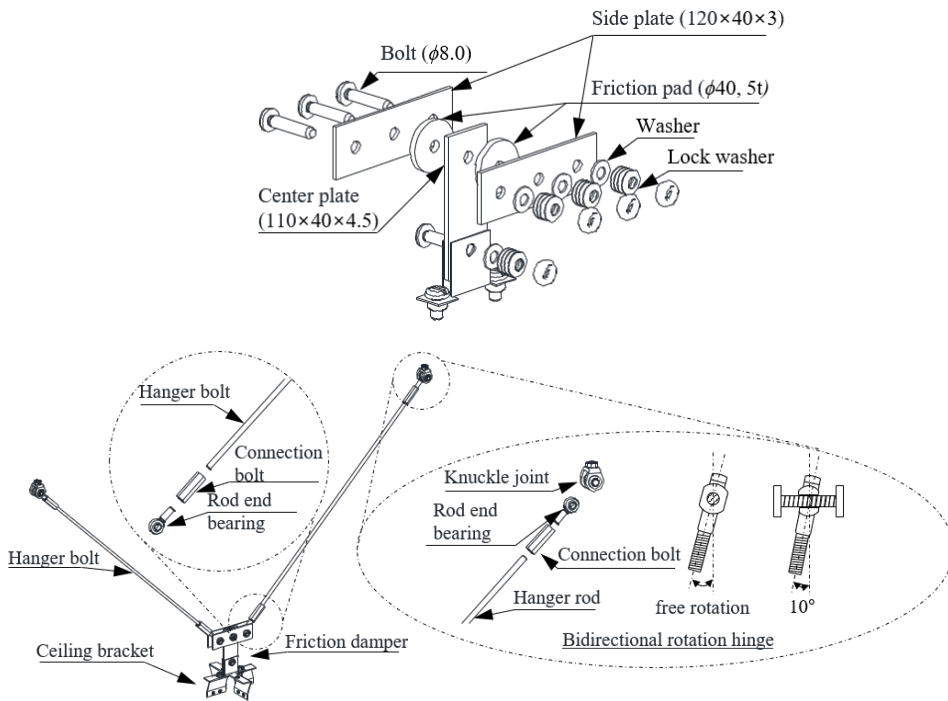
Figure 6.5 Components of ceiling friction damper proposed

The damper comprises one center plate, two side plates, circular friction pads made of mild steel plates and hanger bolts. When the ceiling is displaced horizontally by the seismic inertial force, the friction forces between the friction pads and the side plates dissipate seismic energy through the relative rotation between the center plate and the side plates (see Figure 6.6). Because the ceiling system is hung from the floor above, the use of rotation as a friction mechanism, instead of translational friction, was regarded to be kinematically more efficient in maintaining a uniform friction force. The maximum static friction force depends on the friction coefficient at the faying surface between the steel plates and the clamping force exerted by the center bolts. In this testing program, hanger bolts of typical size ($d = 8$ mm) were used as damper braces and were installed to form a 45 degrees diagonal angle. A sufficient
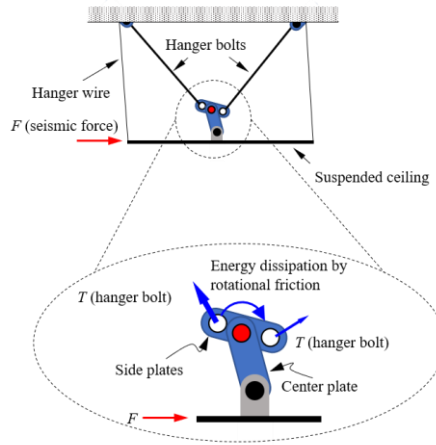
Figure 6.6 Mechanism of proposed friction damper

brace strength, in both tension and compression, was obtained using the typical hanger bolts because the tested specimens were composed of relatively lightweight ceiling panels. The clamping force was introduced by fastening the center bolt to a snug-tight condition; fully tightening by hands first, and one or two additional turns using a spud wrench.

The proposed friction damper was designed to work only for unidirectionally. The seismic input motion acting orthogonally to the working direction may degrade the functionality of the damper. The bending of the hanger bolts could keep the friction damper from maintaining a consistent frictional force owing to the bending moments induced at each end. To reduce the undesirable effects caused by the orthogonal excitation, the friction damper was pin-supported at both ends with rod end bearings, which allowed the hanger bolts to freely rotate bi-directionally. The rod end bearing used had a sufficient rotation capacity of 10 degrees.
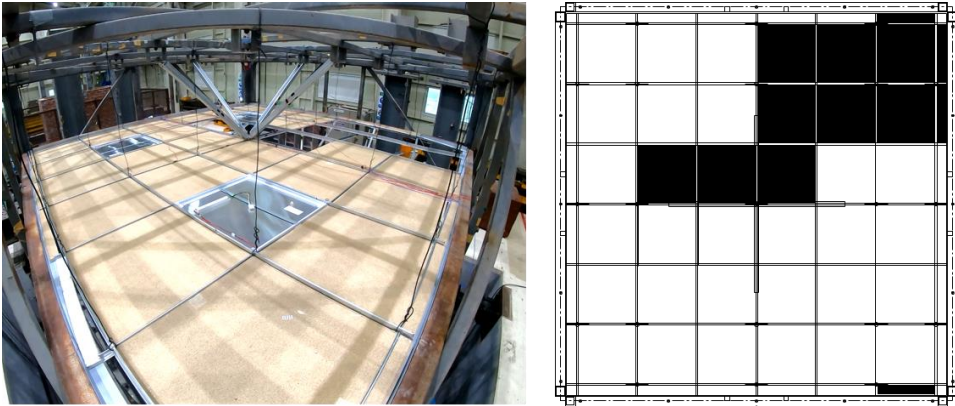
(a) Input intensity correponding to the maximum used for DTL specimen

(225 % RRS, PGA = 1.74 g)
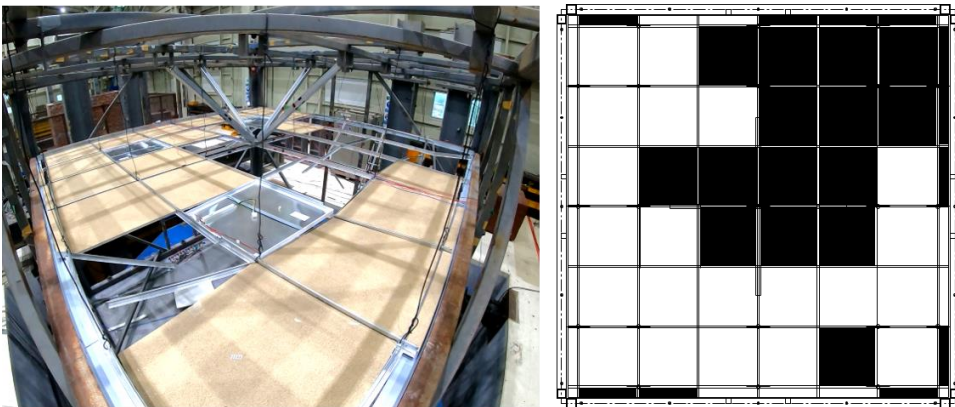
(b) At the end of test (275 % RRS, PFA = 2.41 g)

Figure 6.7 Fallen ceiling area of DTL-B specimen

6.3. Performance and Characteristics of Seismic Ceiling Speci-
      mens

In this section, the damage state of each specimen observed during the incremental-intensity testing is summarized in conjunction with the peak floor acceleration (PFA) measured at the roof of the mounting frame. The dynamic responses of each test specimen are described and comparatively analyzed.
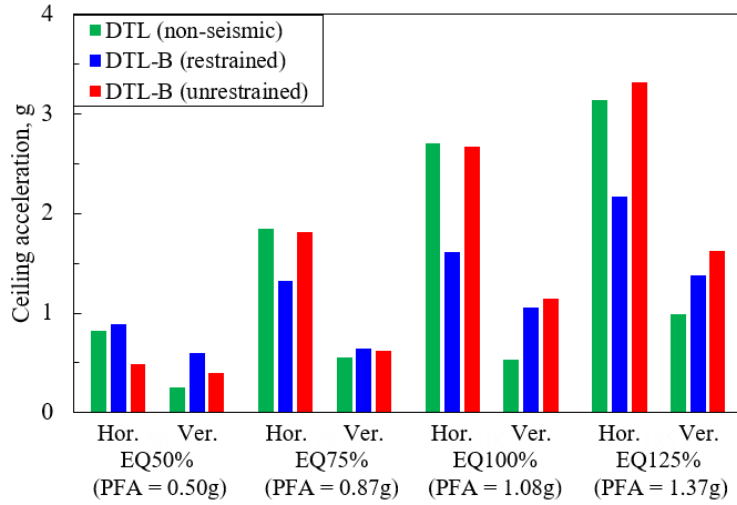
(a) Acceleration comparison between non-seismic and seismic (braced) specimens
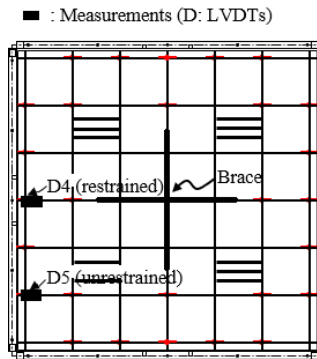
(b) Location of restrained (D4) and unrestraiend (D5) members

Figure 6.8 Comparison of measured acceleration from DTL & DTL-B

6.3.1. Braced ceiling specimen

Rigidly braced DTL-B exhibited only slightly improved seismic performance, comparable to specimen DTL, as shown in Figure 6.7. The limitations and side effects of rigid bracing are discussed by comparing the responses of DLT and DTL-B specimens.
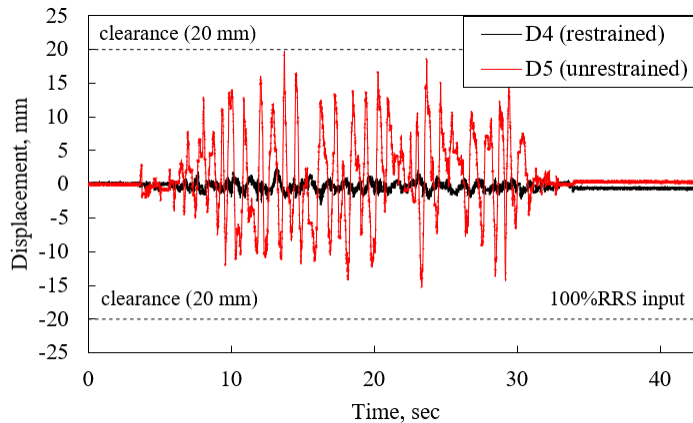
Figure 6.9 Comparison of displacement response time histories: restrained (D4) vs. unrestrained (D5)

Figure 6.8 compares the acceleration responses measured from specimens DTL and DTL-B. Figure 6.9 shows a comparison of the measured displacement response time histories for the 100 % RRS input. Note that two responses are reported for specimen DTL-B in Figures 6.8 and 6.9: the response measured at grid line D4 along which the bracing is provided (restrained response) and the response measured at grid line D5 along which the bracing is not available (unrestrained response). The location of the restrained and unrestrained members is shown in figure 6.8(b). First of all, the acceleration response of DTL-B along line D5 (unrestrained) rarely changed compared to that of DTL despite the provision of lateral bracing, whereas the acceleration response of DTL-B along line D4 (restrained) was significantly reduced (see Figure 6.8). Figure 6.9 indicates that the displacement response at grid line D5 is as large as 20 mm for 100 % RRS input, whereas the response at grid line D4 is almost null, or the response is effectively restrained by the braces. All these observations imply that the lateral bracing is only effective along the grid line where the bracing is located, and a desirable rigid diaphragm action of the ceiling grids is
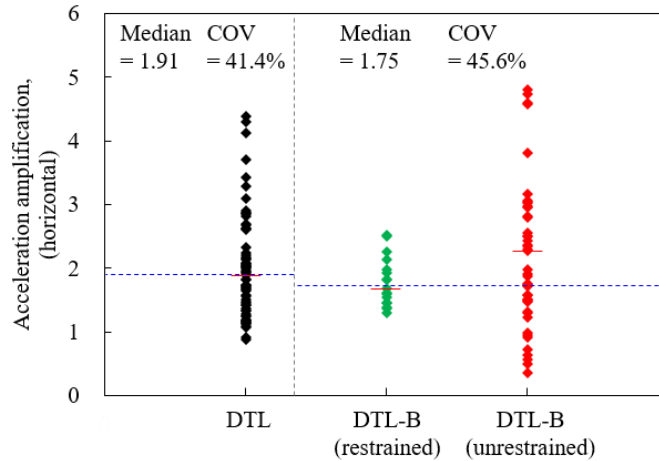
(a) Horizontal acceleration amplification
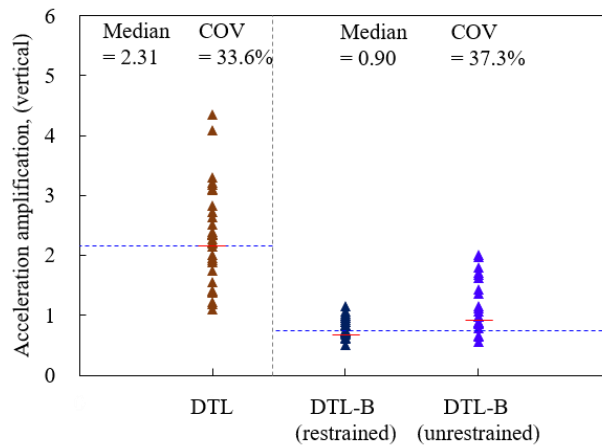
(b) Vertical acceleration amplification

Figure 6.10 Comparison of acceleration amplification measured from DTL and DTL-B specimens

rarely mobilized because of the low in-plane stiffness of direct-hung lay-in suspended ceiling systems.

In the early input stage (50 % RRS, before pounding occurred), the specimens DTL and DTL-B showed comparable acceleration responses. Under a higher input intensity (75 % RRS, PFA = 0.85 g), the acceleration response of the DTL increased drastically as the perimeter grid members started to collide with the surrounding

walls. The restrained members in specimen DTL-B showed an acceleration similar to that of PFA because the specimen locally underwent rigid body motion along the braced grid line. Specimen DTL-B was subjected pounding from PFA = 1.04 g (100 % RRS), showing a high acceleration response comparable to specimen DTL. In the vertical direction, the overall acceleration in specimen DTL-B was much higher than that in specimen DTL because of the high vertical stiffness induced by the bracing.

Figure 6.10 summarizes the measured acceleration amplification factors in the horizontal and vertical directions. The amplification factors were determined by normalizing the peak acceleration measured at the ceiling grids by PFA. Specimen DTL exhibited higher acceleration amplification due to pounding in both the horizontal and vertical directions ($a_{p,median} = 1.91$). In specimen DTL-B, much higher acceleration amplification was measured in the unrestrained grid members ($a_{p,median} = 2.25$) than in the restrained grid members. Such high acceleration amplifications may be attributed to the combined effect of the large displacement response and the resulting pounding. Compiling all the data for specimen DTL-B, the median acceleration amplification factor in the horizontal direction was obtained as 1.75, which is comparable to that of specimen DTL.

In summary, despite the provision of costly lateral bracing, the inherently low in-plane stiffness of direct-hung lay-in suspended ceilings permitted large relative displacements within the ceiling grids, thus causing high acceleration amplification. Furthermore, due to the highly increased vertical stiffness provided by the ceiling braces, the braced specimen was subjected to increased vertical acceleration, which is a surely undesirable side effect. In contrast to specimen DTL (see Figure 6.7) the

disconnection of grid members and dislodgement of ceiling panels were mostly con-

centrated around the center of the specimen where the braces were installed (Figure

6.8). At the end of the test, approximately 20 % of the ceiling panels were dislodged.

Table 6.3 Comparison of measured and predicted natural frequencies

Specimen	Input-level	PFA, g			Damage observation	Fallen ceiling area percentage, %
		x-dir.	y-dir.	z-dir.		
DTL-B	50 % RRS	0.60	0.58	0.35	-	-
	75 % RRS	0.93	0.91	0.36	-	-
	100% RRS	0.98	1.13	0.47	Ponding initiated	-
	125 % RRS	1.32	1.27	0.44	-	-
	150 % RRS	1.38	1.51	0.62	Cross T-bar connection failure (3 connections) Main T-bar connection failure (1 connection)	-
	175 % RRS	1.64	1.94	0.75	Cross T-bar connection failure (3 connections) Main T-bar connection failure (1 connection) Lightning fixture dislodgement (1 fixture)	2.48
	200 % RRS	1.92	1.94	0.94	Cross T-bar connection failure (8 connections) Main T-bar connection failure (1 connection) Lightning fixture dislodgement (1 fixture) Inner panel (5 panels) & perimeter panel (2 panels) dislodgement	15.88
	225 % RRS	1.92	2.08	1.00	Cross T-bar connection failure (12 connections) Main T-bar connection failure (1 connection) Lightning fixture dislodgement (1 fixture) Inner panel (8 panels) & perimeter panel (4 panels) dislodgement	24.32
	250 % RRS	1.96	2.04	1.69	Cross T-bar connection failure (13 connections) Main T-bar connection failure (2 connections) Lightning fixture dislodgement (1 fixture) Inner panel (8 panels) & perimeter panel (10 panels) dislodgement	27.25
	275 % RRS	2.05	2.41	1.92	Cross T-bar connection failure (13 connections) Main T-bar connection failure (2 connections) Lightning fixture dislodgement (1 fixture) Inner panel (14 panels) & perimeter panel (12 panels) dislodgement	43.13
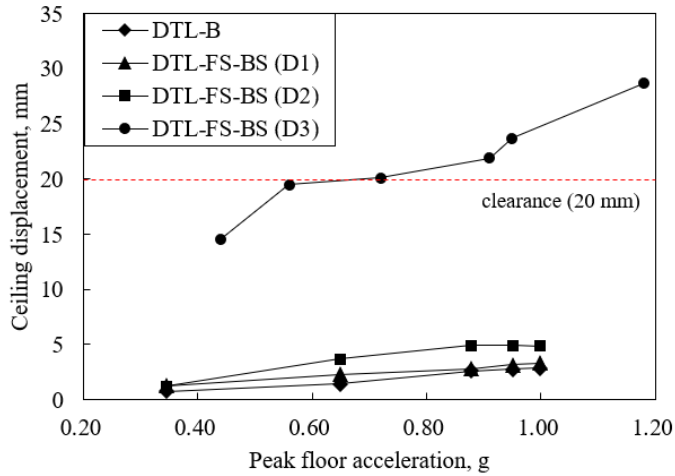
(a) Comparison of displacement response between DTL-B and DTL-FS-BS
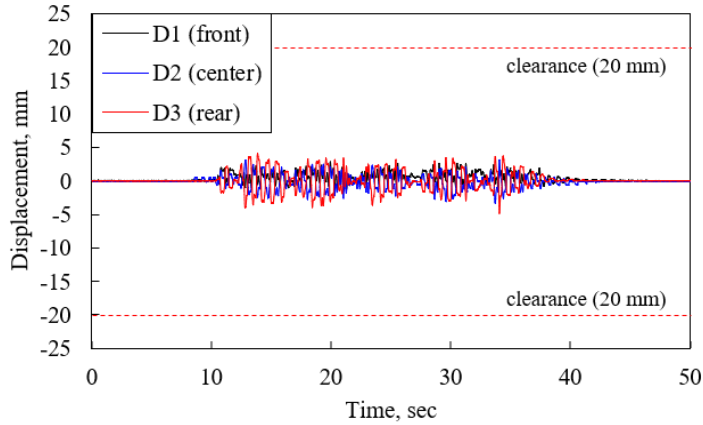
(b) Displacement measured from DTL-FS-BS

Figure 6.11 Effect of grid reinforcement on displacement response of DTL-FS-BS specimen

6.3.2. Braced ceiling specimen with grid reinforcement

The full-scale ceiling specimen installed with lateral bracings and grid reinforcements (specimen DTL-FS-BS) showed no damage until end of the test. By introducing grid reinforcements, the rigid diaphragm action of the ceiling grids was
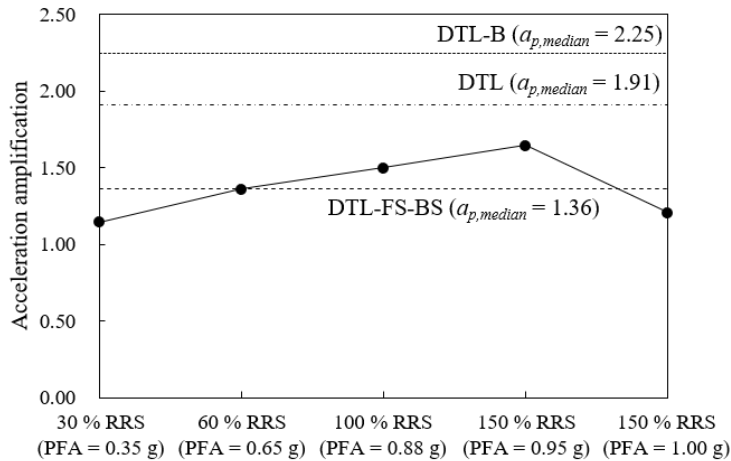
Figure 6.12 Effect of grid reinforcement on acceleration response of DTL-FS-BS specimen

fully developed, and the lateral bracings effectively restrained the overall movement of the ceiling specimen.

Figure 6.11(a) shows the measured displacement of DTL-FS-BS specimen where all the displacements measured in D1 (front), D2 (center), and D3 (rear) were plotted. Also, displacement of DTL-B was presented for comparison. First, it can be observed that DTL-FS-BS specimen responds as a monolithic system where almost no relative displacement within the ceiling grids was observed (see Figure 6.11(b)). The overall displacements of DTL-FS-BS tend to increase as the PFA increases, but they are far less than the clearance (20 mm) introduced at ceiling perimeters and the displacement of DTL-B specimen, which has a smaller specimen area. The same results can also be observed from the acceleration response of DTL-FS-BS specimen. As shown in Figure 6.12, through the formation of a rigid diaphragm in the DTL-FS-BS specimen grid, the resulting acceleration amplification was far less than the DTL and DTL-B specimen and was almost behaved rigidly ($a_{p,median} = 1.36$).

6.3.3. Friction-added suspended ceiling

Table 6.4 summarizes the damage evolution of the specimen DTL-F. There was no pounding observed until 125 % RRS (PFA = 1.20 g), and only minor damage at the ceiling perimeter was observed at the end of the tests, thus exhibiting much improved performance compared to the DTL and DTL-B specimens

The global responses of all three ceiling specimens are compare in Figure 6.13. It was observed that with the addition of the friction mechanism, the acceleration and displacement responses of specimen DTL-F were significantly reduced compared to those of the other specimens. Compare with specimen DTL-B, specimen DTL-F showed highly enhanced performance. In particular, as the damped ceiling specimen moves freely after reaching the maximum static friction force, the relative movements within the ceiling grids are significantly reduced, thus lowering the internal forces exerted on the ceiling grid connections.

Hysteretic characteristics of proposed friction mechanism

Before implementing seismic performance tests, low-level sine sweep tests were first conducted to evaluate the effect of the excitation frequency on the cyclic frictional response using 1 – 4 Hz sinusoidal waves. The objective of the test was to examine whether the proposed friction damper can develop a consistent frictional force regardless of excitation frequency, which is an already well-known feature of the Coulomb frictional damping as was noted in previous studies (for example, Mualla and Belev 2002; Ng and Xu 2006). The sweep rate was set to two octaves per minute (40-cycle excitation for every single Hz increment). The amplitude of the sine sweep waves was 0.1 g in order to prevent damage during the test. The measured
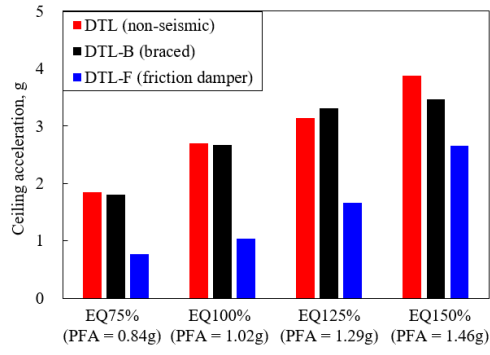
(a) Acceleration
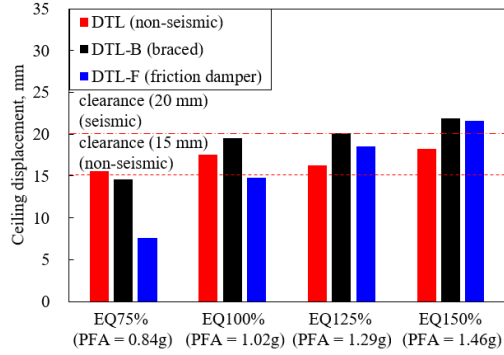
(b) Displacement
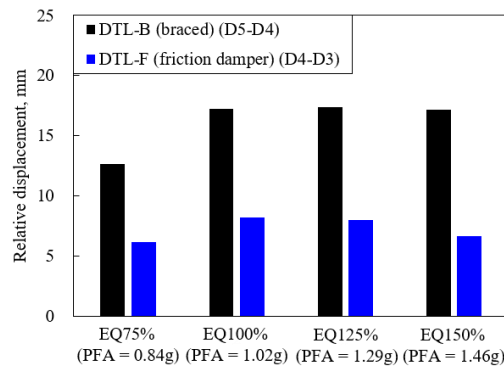
(c) Relative displacement
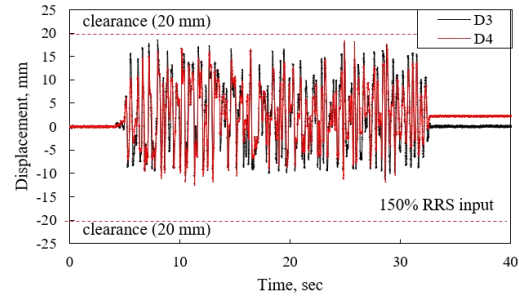
(d) Displacement time history

Figure 6.13 Response comparison of non-seismic (unbraced), braced, and friction added ceiling specimens.
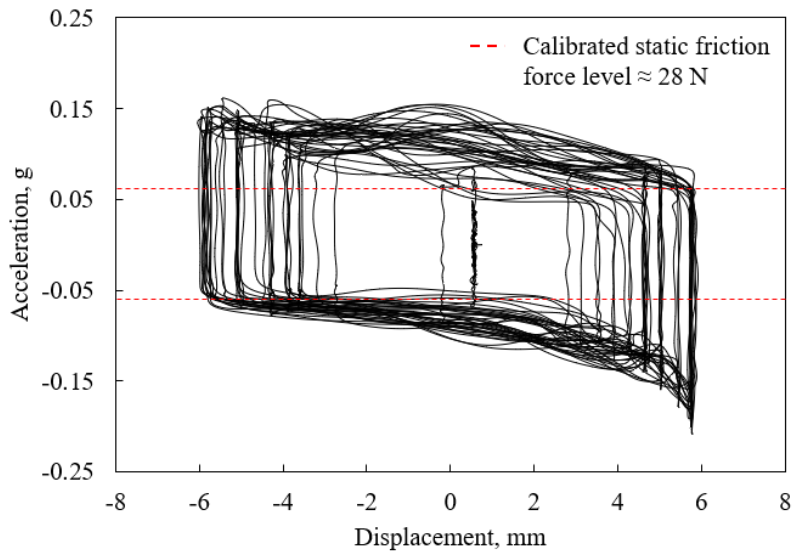
(a) Hysteresis loops measured for 1 – 2 Hz sinusoidal waves
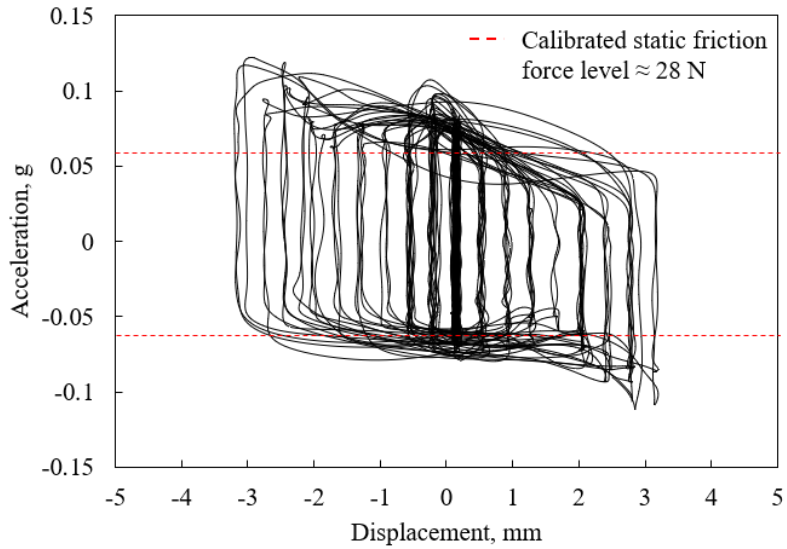
(b) Hysteresis loops measured for 2 – 4 Hz sinusoidal waves

Figure 6.14 Effect of excitation frequency on cyclic frictional response

hysteretic response for each octave increment was plotted separately for clear visualization, along with the calibrated static friction force obtained using a simplified analytical model. Detailed descriptions of the analytical model are provided in the next section. As shown in Figure 6.14, the proposed damper developed a consistent frictional force with a stable hysteresis response under the tested frequency range.

To assess the operability of the proposed damper under diverse input motions and input conditions, a series of preliminary tests were performed using artificial and recorded ground motions. Artificial input motions were generated from the RRS, as discussed in Chapter 5. To utilize more realistic input motions, the floor motions were obtained using the linear dynamic analysis of three-dimensional steel moment resisting frames (see Figure 3.6) using 20 recorded ground motions (see Table 6.4). Only single directional component records were used for the shake-table tests among the pair of recorded ground motions. Discussions based on the recorded ground motions will be conducted using the results obtained from Imperial Valley (1979) (LA06) and Sylmar (1994) (LA18) records. Detailed discussions about the floor motions will be presented in the numerical case study section below. The obtained floor motions were applied in one direction with their scale arbitrarily adjusted within the shake-table operation limit. To examine the effect of the input motion dimensionality on the damper friction force, both uniaxial and triaxial tests were conducted with artificial input motions. Figures 6.15 and 6.16 summarize the hysteresis responses obtained from the shake-table tests. High acceleration spikes in the hysteresis loops were formed when the specimen collided with the perimeter walls. Overall, DTL-F exhibited satisfactory hysteretic behavior under diverse input motions. In particular,

Table 6.4 List of ground motions used in shake-table test and numerical case study

Input name	Record	Duration, sec.	Magnitude, M_w	R, km	Scale	PGA, g
LA01	Imperial Valley, 1940, El Centro	39.38	6.9	10	2.01	0.46
LA02	Imperial Valley, 1940, El Centro	39.38	6.9	10	2.01	0.68
LA03	Imperial Valley, 1979, Array #05	39.38	6.5	4.1	1.01	0.39
LA04	Imperial Valley, 1979, Array #05	39.38	6.5	4.1	1.01	0.49
LA05	Imperial Valley, 1979, Array #06	39.08	6.5	1.2	0.84	0.3
LA06	Imperial Valley, 1979, Array #06	39.08	6.5	1.2	0.84	0.23
LA07	Landers, 1992, Barstow	79.98	7.3	36	3.2	0.42
LA08	Landers, 1992, Barstow	79.98	7.3	36	3.2	0.43
LA09	Landers, 1992, Yermo	79.98	7.3	25	2.17	0.52
LA10	Landers, 1992, Yermo	79.98	7.3	25	2.17	0.36
LA11	Loma Prieta, 1989, Gilroy	39.98	7.0	12.4	1.79	0.67
LA12	Loma Prieta, 1989, Gilroy	39.98	7.0	12.4	1.79	0.97
LA13	Northridge, 1994, Newhall	59.98	6.7	6.7	1.03	0.68
LA14	Northridge, 1994, Newhall	59.98	6.7	6.7	1.03	0.66
LA15	Northridge, 1994, Rinaldi	14.95	6.7	7.5	0.79	0.53
LA16	Northridge, 1994, Rinaldi	14.95	6.7	7.5	0.79	0.58
LA17	Northridge, 1994, Sylmar	59.98	6.7	6.4	0.99	0.57
LA18	Northridge, 1994, Sylmar	59.98	6.7	6.4	0.99	0.82
LA19	North Palm Springs, 1986	59.98	6.0	6.7	2.97	1.02
LA20	North Palm Springs, 1986	59.98	6.0	6.7	2.97	0.99
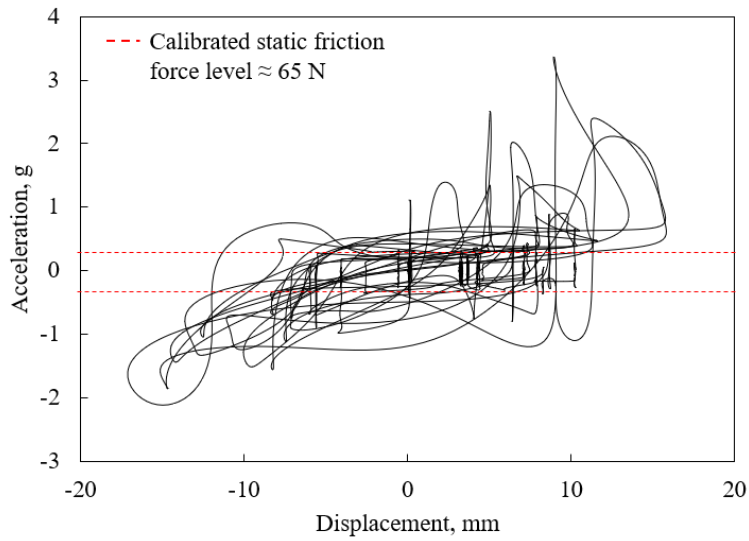
(a) Hysteresis loops measured under Imperial Valley (1979) (LA06) floor motion
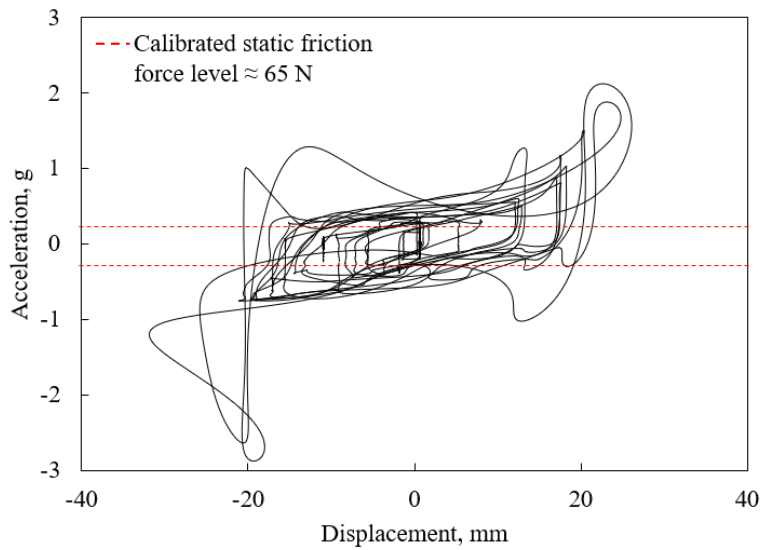
(b) Hysteresis loops measured under Sylmar (1994) (LA18) floor motion

Figure 6.15 Effect of input motion (6th floor motion obtained from a 9-story moment-resisting frame model)
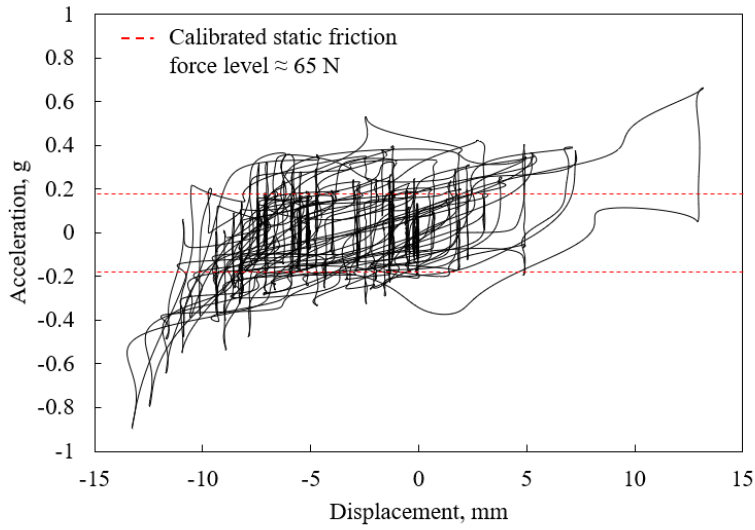
(a) Hysteresis loops measured from uniaxial excitation
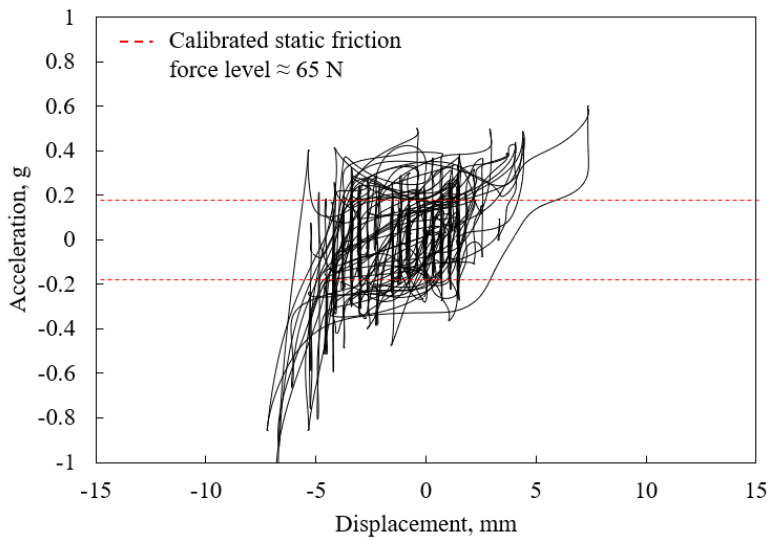
(b) Hysteresis loops measured from triaxial excitation

Figure 6.16 Effect of input dimensionality evaluated using artificial input motions

under both uniaxial and triaxial excitations, the damper developed comparable frictional hysteresis, demonstrating the robustness of the proposed damping mechanism regardless of the dimensionality of the input motions. The hysteresis response measured from all the recorded ground motion can be seen in Figure 6.17.
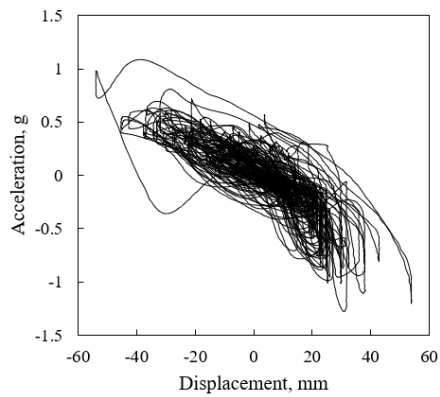
(a) LA02
(Imperial Valley 1940 floor motion)
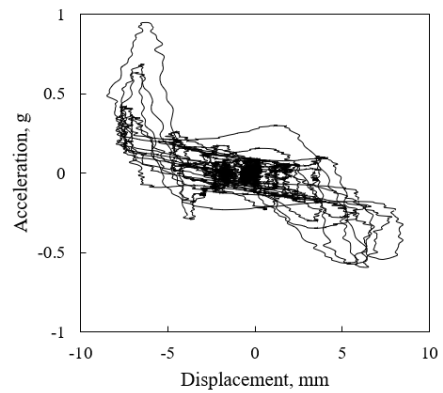
(b) LA04
(Imperial Valley 1979 floor motion)
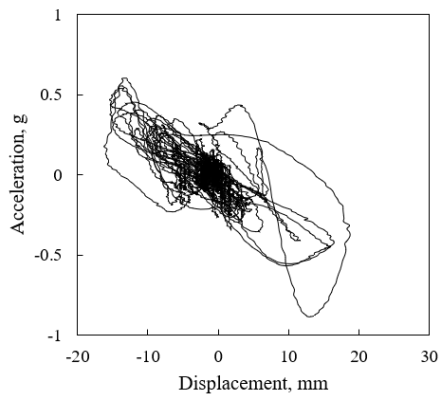
(c) LA08
(Landers 1992 floor motion)
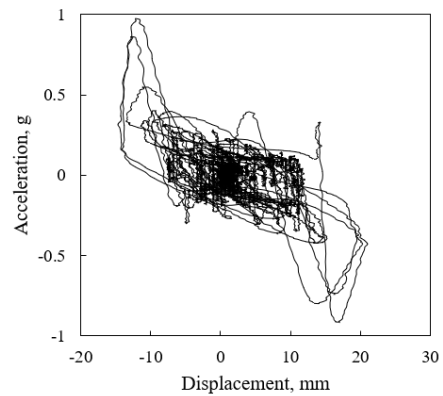
(d) LA10
(Landers 1992 floor motion)
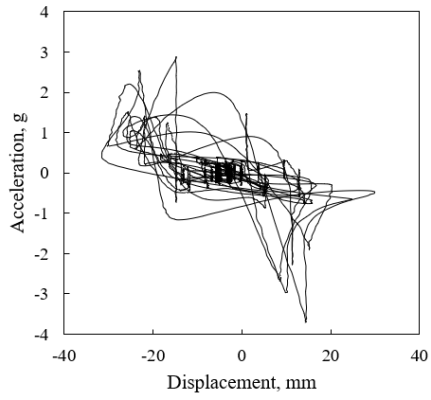
(e) LA12
(Loma Prieta 1989 floor motion)
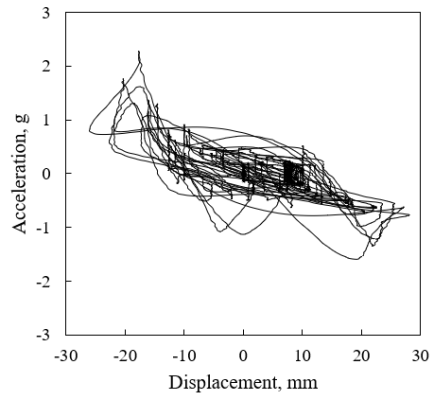
(f) LA14
(Northridge 1994 floor motion)
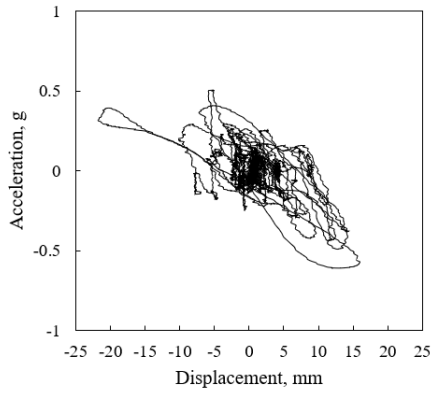
(g) LA16
(Northridge 1994 floor motion)
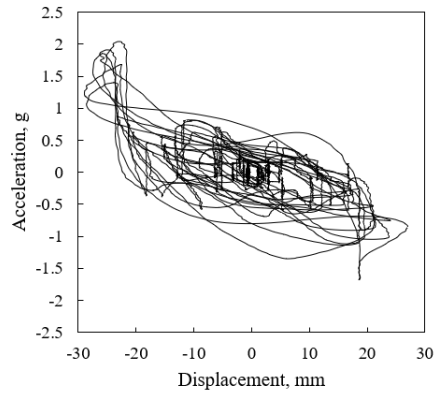
(h) LA20
(North Palm Spring 1986
floor motion)

Figure 6.17 Hysteresis loops measured from various floor motions
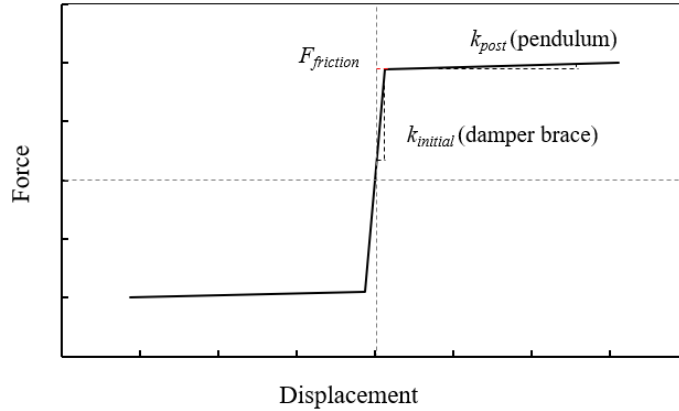
Figure 6.18 Bilinear hysteresis model for friction damper ceiling system

6.3.4. Simplified SDOF model for friction-added ceiling system

In this section, a simplified single degree of freedom (SODF) model with bilinear hysteresis is developed for the friction-added ceiling system proposed in this study. The envelope of the hysteresis can be idealized into two segments (Figure 6.18). Before reaching the maximum static friction force ($F_{friction}$), the ceiling would behave with the lateral stiffness contributed by the damper braces (hanger bolts) and the hanger members (hanger wires). Usually the lateral stiffness of direct-hung ceiling system is much less than that of the damper brace. Therefore, in this stage, the lateral stiffness contributed by hanger wires can be neglected. If the inertial force of the ceiling system exceeds the friction force, the ceiling became a pendulum, similar to the unbraced (non-seismic) ceiling specimen. Therefore, the post-friction stiffness can be calculated based on the pendulum theory with a small rotation assumption, and the equation of motion can be expressed as follows.

$$m_T \ddot{\theta} + \frac{c}{L} \dot{\theta} + m_T \frac{g}{L} \theta = 0 \qquad (6.1)$$

Thus, the post-friction stiffness is simply,

$$k_{post} = \frac{g}{L} m_T \qquad (6.2)$$

where c = viscous damping coefficient for ceiling system, g = gravitational acceleration, L = pendulum length (plenum depth of ceiling system), m_T = total mass of ceiling system.

The maximum static friction force ($F_{friction}$) was calibrated on a trial-and-error basis using the measured displacement and hysteresis loops of the DTL-F specimen. The viscous damping ratio was assumed as 1 % of the critical which was adopted from the value reported for unbraced (non-seismic) suspended ceiling systems (Pourali et al. 2017). In calibrating the SDOF model, uniaxial shake table test results from the artificial ground motions (75 % RRS) and Rinaldi (LA 16) floor motions were used because specimen DTL-F did not collide with the perimeter walls for these input motions. The maximum static friction force level identified experimentally was approximately 65 N, as shown in Figures 6.15 and 6.16.

Figures 6.19 – 6.20 shows the numerical analysis results which was conducted to validate the proposed SDOF model for the friction-added ceiling system. It can be observed that the proposed SDOF model well predicts the overall responses of the friction-added ceiling specimen. It is observed in Figure 6.21 that the proposed SDOF model successfully simulates the energy dissipation in a close match with the

shake table test results. The damped ceiling was shown to be highly effective in dissipating the earthquake input energy, and more than 80 % of the input energy was dissipated by the friction damper.
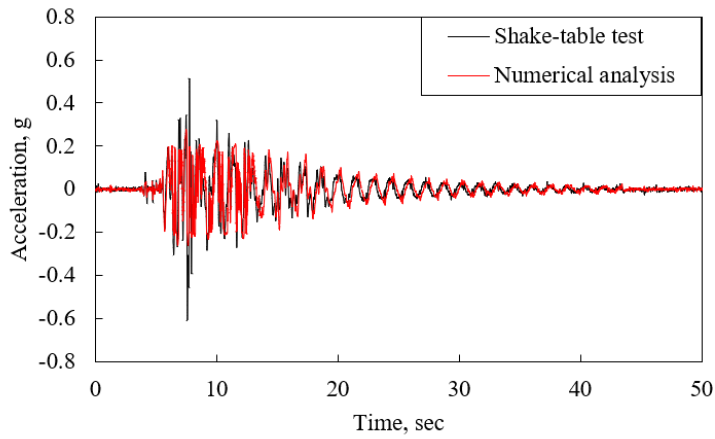
(a) Acceleration
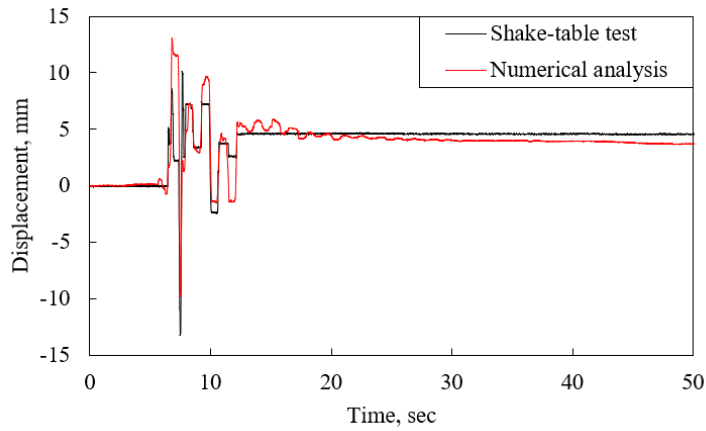
(b) Displacement
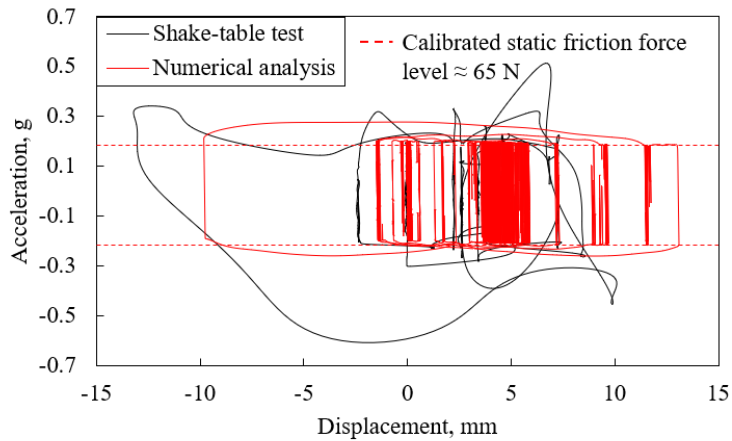
(c) Hysteresis response

Figure 6.19 Validation of proposed SDOF model using Rinaldi (1994) (LA16) input motion
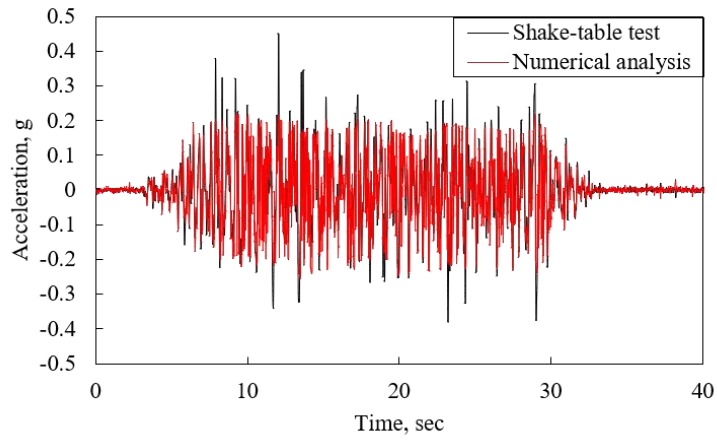
(a) Acceleration
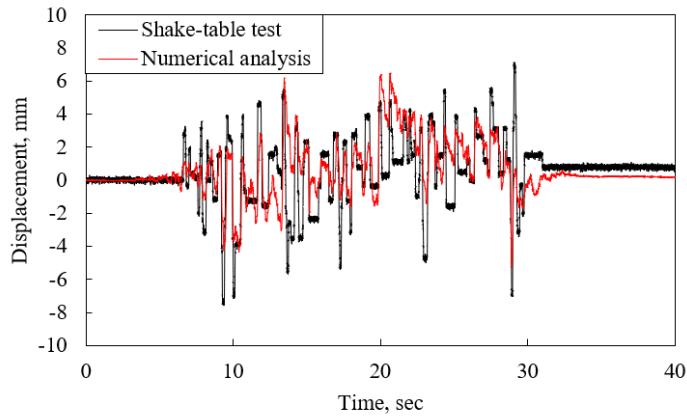
(b) Displacement
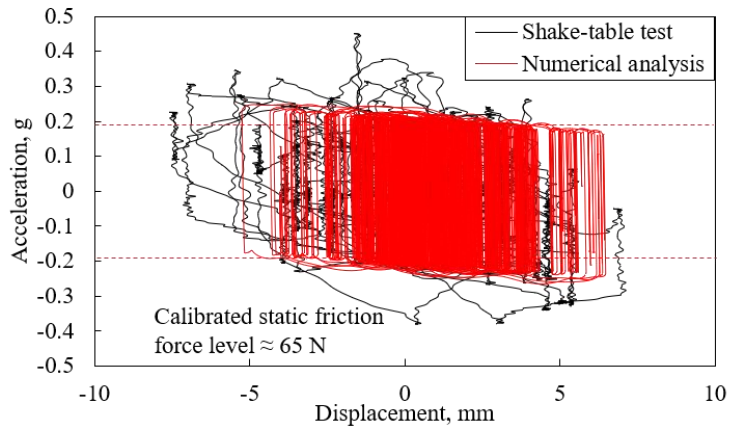
(c) Hysteresis response

Figure 6.20 Validation of proposed SDOF model using artificial input motion (ICC-AC156)

6.4. Comparative Seismic Performance Evaluation of Ceiling Specimens

In this section, the seismic performance of tested ceiling specimens was comparatively evaluated. Seismic performance level of suspended ceilings is usually defined based on diverse failure indices such as a number of ceiling panel loss, grid failure, and grid buckling. Table 6.5 shows the categorization of damage states and their corresponding damage description given by HAZUS-MH (FEMA 2005), which is widely used as a basis for the evaluation of the seismic performance of ceiling systems. Damage states are given, rather qualitatively, with respect to the degree of ceiling panel losses and grid damages.

Many previous studies have already been conducted to propose quantitative methods to evaluate the ceiling damage state and define the corresponding performance level. Generally, a slight damage state is related to Operational performance level, which requires only minor reconditioning. Moderate damage requires local

Table 6.5 Damage description for suspended ceiling given by HAZUS-MH (FEMA 2005)

Damage state	Description of damage
Slight	A few ceiling tiles have moved or fallen down
Moderate	Falling of tiles is more extensive; in addition, the ceiling support framing (T-bars) has disconnected and/or buckled at few locations; localized repairs are necessary
Extensive	The ceiling system exhibits extensive buckling, disconnected T-bars and falling ceiling tiles; ceiling partially collapse at few locations and some light fixtures fall; repair typically involves removal of most or all ceiling tiles.
Complete	The ceiling system is buckled throughout and/or fallen and requires complete replacement; many light fixtures fall

repair of ceiling systems, which can be associated with Position Retention performance level of ceiling systems. Extensive damage indicates Life Safety performance of ceiling systems where complete replacement of the ceilings is required.

Table 6.6 summarizes the damage states and the quantitative definition of each ceiling component damage given by previous studies. It can be observed that each damage state can be evaluated by either the comprehensive or single index criteria (ceiling tiles). Soroushian et al. (2009) proposed a distinctive method that allows for determining the fallen ceiling area by including both the ceiling panels and grid losses. A detailed description was given, which provides the method to equivalently calculate the grid loss in terms of the fallen ceiling area.

Table 6.6 Quantitative performance evaluation proposed by previous studies

Damage state	Items	HAZUS-MH	Ryu et al. 2019	Badillo-Almaraz et al. 2007	Soroushian et al[*]. 2019	Repair
Slight	Perimeter grid	-	< 10%	-	-	Minor recondition
	Grid	-	-	-	-	
	Ceiling tiles	Few	-	< 1%	< 5%	
Moderate	Perimeter grid	Few	> 10%	-	-	Local repair
	Grid	Few	< 10%	-	-	
	Ceiling tiles	Extensive	< 10%	< 10%	< 30%	
Extensive	Perimeter grid	Extensive	> 10%	-	-	Complete replacement
	Grid	Extensive	> 10%	-	-	
	Ceiling tiles	Extensive	> 10%	< 33%	< 50%	

* Grid loss was equivalently calculated in terms of ceiling tile loss
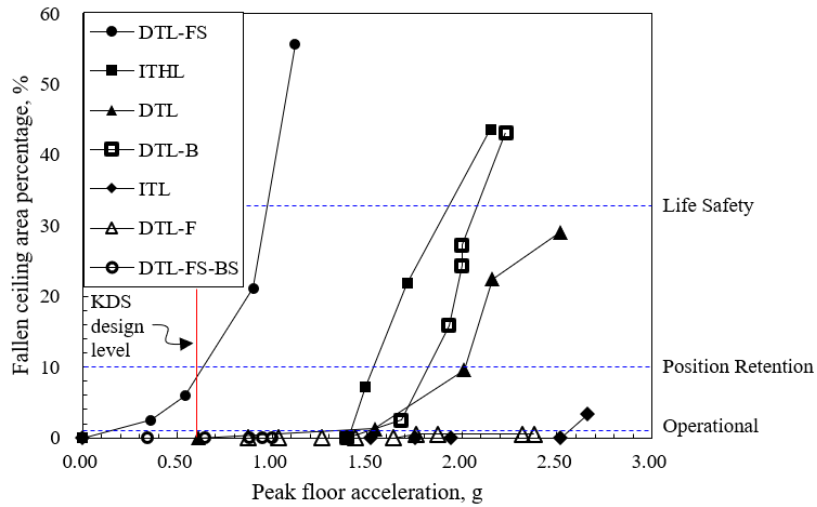
Figure 6.21 Performance evaluation results of tested ceiling specimens

Usually, the seismic performance of ceiling systems more or less depends on the area of panels loss, which is the most instinctive and apparent indicator of whether ceiling systems need to be repaired, replaced, or maintained. Therefore, in this study, the damage description given by Badillo-Almaraz et al. (2007) was adopted, and the performance of tested ceiling specimens was evaluated.

Figure 6.21 shows the performance evaluation results plotted with respect to the peak floor acceleration. It can be observed that the overall seismic performance is much lower for the direct-hung lay-in T-bar systems, as mentioned in the previous chapter. At the end of the tests, their seismic performance surpassed the Life Safety level, which requires the complete replacement of the whole system. Also, it should be noted that the braced ceiling fabricated by following the current seismic procedure showed inferior seismic performance comparable to non-seismic ceiling specimens. Seismic ceiling systems (specimen DTL-F and DTL-FS-BS) maintained superior seismic performance until the end of the tests. The Operational performance level was achieved for both seismic ceiling systems.

206
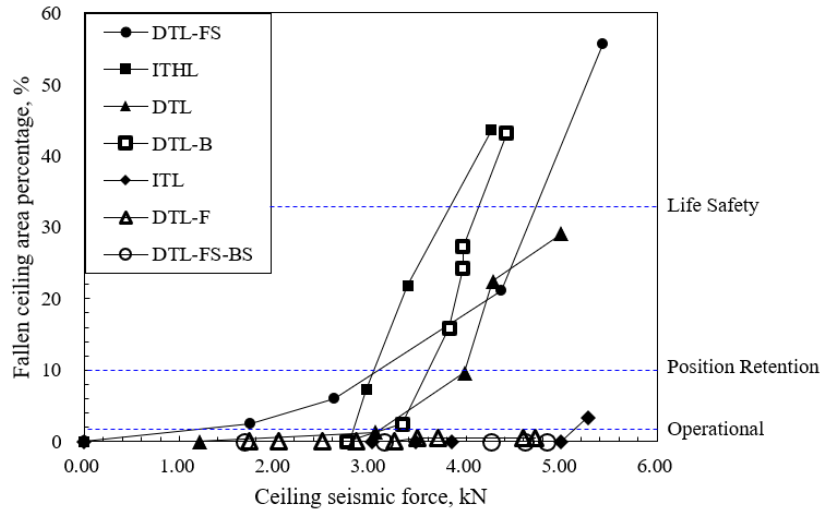
Figure 6.22 Performance evaluation based on ceiling seismic force including mass of ceiling specimens

Figure 6.22 replotted the test results with respect to the ceiling seismic forces to account for the mass differences among the ceiling specimens. The seismic forces were calculated based on the measured PFA, median acceleration amplification (see Section 5.3.3), and the mass of each specimen. It can be observed that the performance of DTL-FS specimen can be more suitably compared using the seismic force by including its mass. The partition-attached DTL-FS specimen showed inferior seismic performance compared to DTL specimen; showing twice the more damage under the same seismic force level.

The performance evaluation given by the peak floor acceleration provides convenient means to appraise whether or not the tested ceiling specimens will be safe under the design earthquake level. However, as mentioned, the performance of ceiling systems is very sensitive to the area of the ceiling specimen, which shows higher fragility for the specimen with a larger ceiling area (see DTL-FS). Therefore, the evaluation results imply that, except for DTL-FS specimen, all the ceiling specimens

can maintain the Operational performance under the design earthquake level, which is far from the seismic damage observed for ceiling systems during past major earthquakes (see Figures 2.10 – 2.11). To utilize the shake-table tests during design procedure, further studies need to be conducted to adjust the test results incorporating the scale (or mass) effect.

6.5. Numerical Case Study

A numerical case study was additionally conducted to evaluate the applicability of the proposed damping-added ceiling system. The floor motions were obtained from the linear time history analysis of three-dimensional building models using ETABS 2016 (ETABS 2017). Three SAC steel moment frame building discussed in Chapter 3 was adopted.

Figure 6.23 shows the 5 %-damped ground response spectrum. The mean floor response spectrum obtained from the dynamic analysis of the steel frames are shown
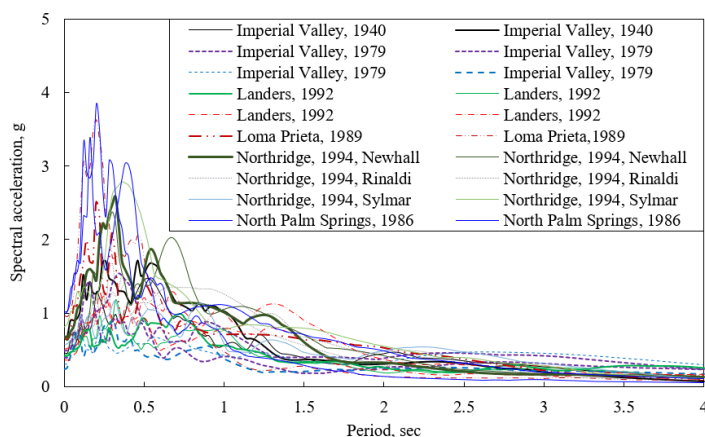
Figure 6.23 5%-damped ground input ground response spectrum used for numerical case study
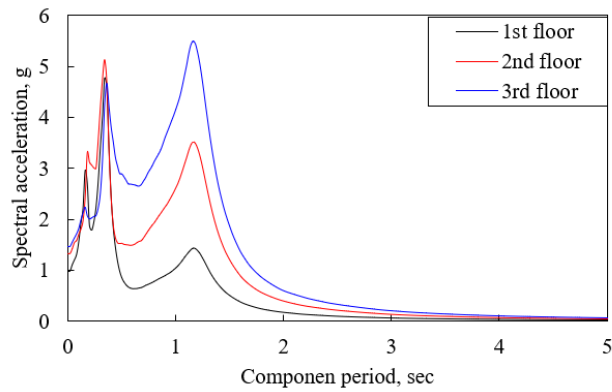
(a) 3-story steel moment frame
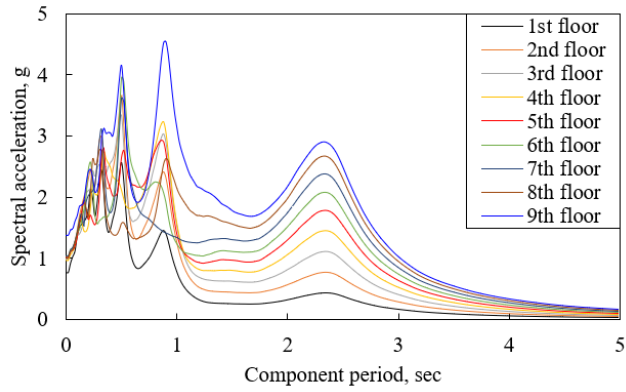
(b) 9-story steel moment frame
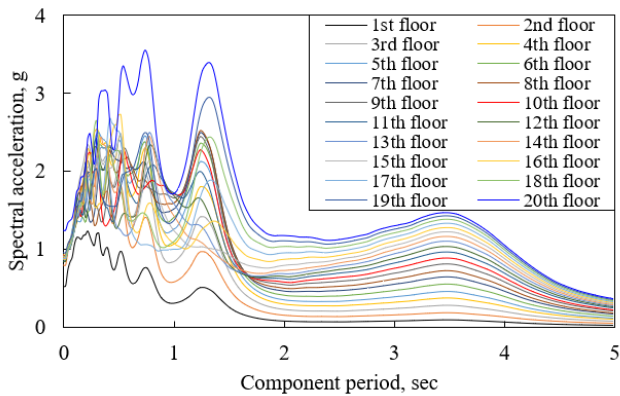
(c) 20-story steel moment frame

Figure 6.24 Mean floor acceleration response spectrum
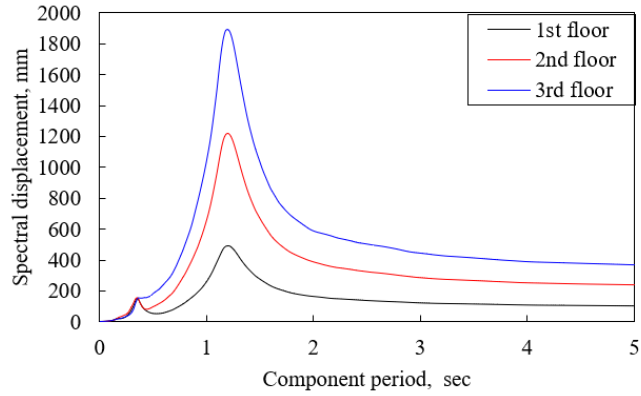
(a) 3-story steel moment frame
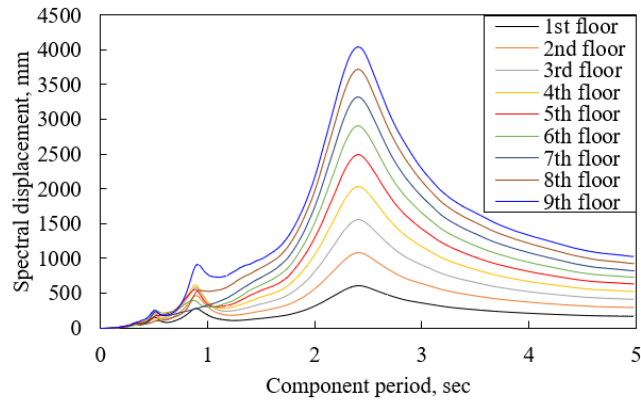
(b) 9-story steel moment frame
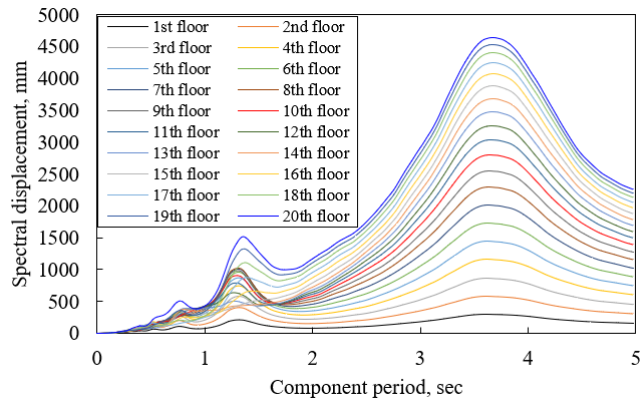
(c) 20-story steel moment frame

Figure 6.25 Mean floor displacement response spectrum

in Figures 6.24 and 6.25. Because of the filtering effect of the supporting structures, the floor response spectrum became much narrow-banded compared to the ground response spectrum. The response of nonstructural elements would increase around the lowest modes of the building model due to the tuning effects between the supporting structures and nonstructural elements.

Using the obtained floor motions as the input motions, an extensive nonlinear time history analysis based on the proposed SDOF model with bilinear hysteresis was conducted to obtain the ceiling acceleration (or peak component acceleration) and the ceiling lateral displacement along the building height. Newmark's method was implement using MATLAB to conduct the nonlinear dynamic SDOF analysis. In accordance with the basic design concept of ASTM E580, which recommends a minimum perimeter clearance in ceiling systems to minimize the ceiling pounding, one of the primary objectives was to **calculate** the estimate of the required perimeter clearance to calculate the estimate of the required perimeter clearance to minimize pounding. The SDOF ceiling model analyzed had the same geometry and configuration as specimen DTL-F (plenum depth = 750 mm, $W = 42.5$ N/m^2), and the maximum static friction force was set as 65 N, which is identical to the experimental calibration.

First of all, it is observed in Figure 6.26 that the ceiling acceleration tends to be more or less constant vertically as the building becomes taller. The median acceleration demand for friction ceiling is approximately 0.73 g for the 9 and 20-story buildings (see Figure 6.26). Figure 6.27 shows the displacement demand for non-seismic ceiling system. It implies that in order to avoid pounding for non-seismic ceiling systems, a highly excessive amount of perimeter clearance is required (more

than 280 mm for 3-story building), which is generally unacceptable using conventional ceiling details. Compared to the response shown in Figure 6.27, it can be observed that for the friction-added ceilings, a perimeter clearance of approximately 65 mm is required in the median sense to avoid pounding for all the case study buildings. Such an amount of the required perimeter clearance is fully feasible in practice using conventional ceiling perimeter channels.
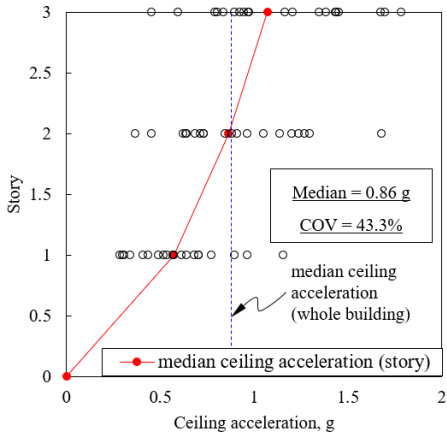
(a) 3-story building ceiling acceleration
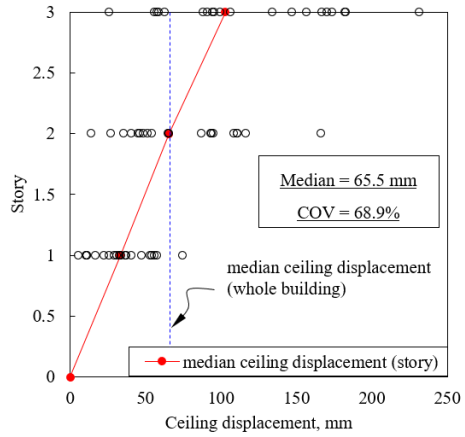
(b) 3-story building ceiling displacement
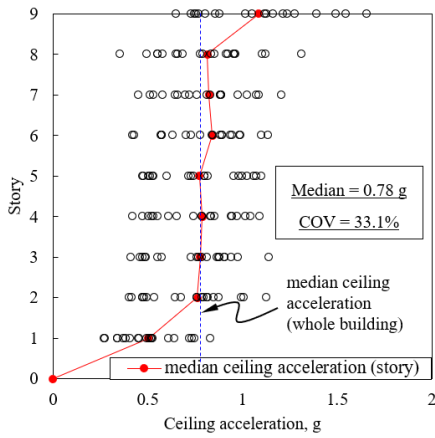
(c) 9-story building ceiling acceleration
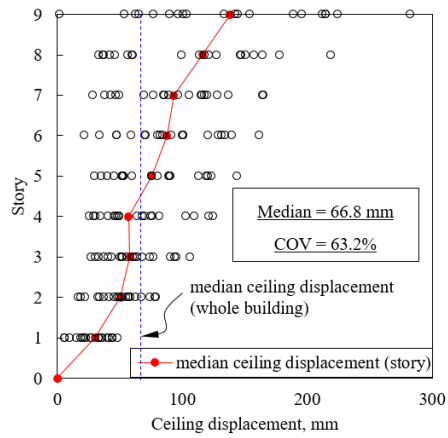
(d) 9-story building ceiling displacement
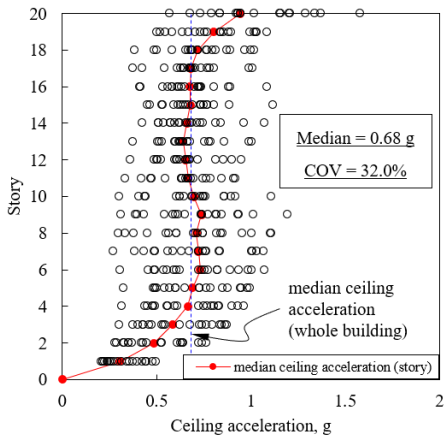
(e) 20-story building ceiling acceleration
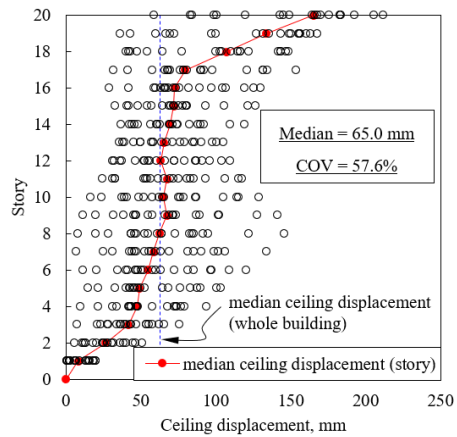
(f) 20-story building ceiling displacement

Figure 6.26 Distribution of friction-added ceiling acceleration and displacement along the building height calculated using 20 input motions
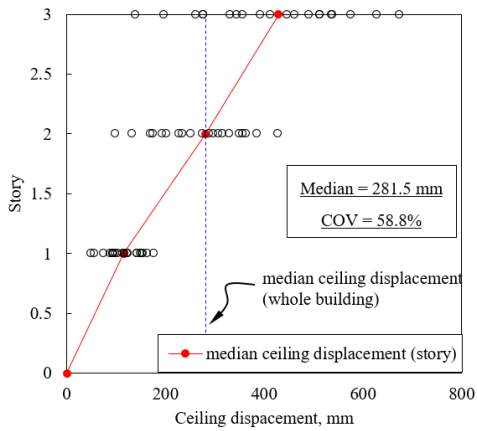
(a) 3-story building ceiling displacement
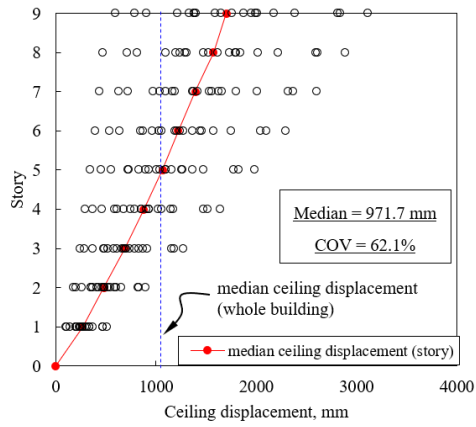
(b) 9-story building ceiling displacement
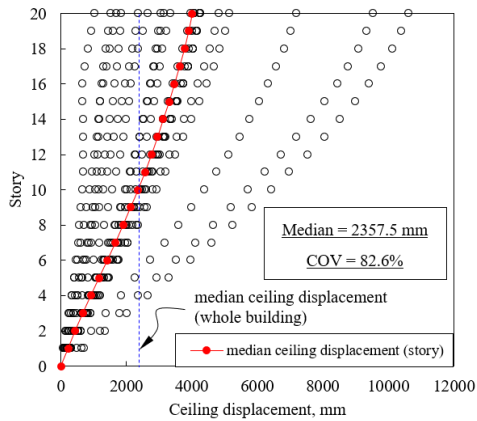
(c) 20-story building ceiling displacement

Figure 6.27 Distribution of non-seismic ceiling displacement along the building height calculated using 20 input motions

214
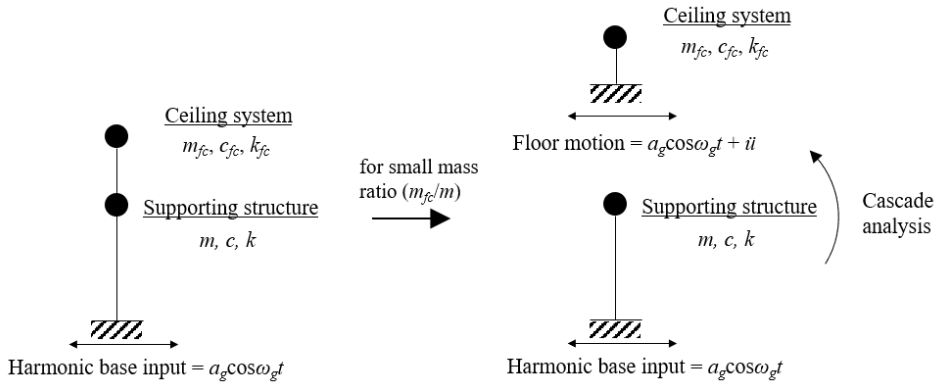
Figure 6.28 Coupled 2-DOF model for supporting structure and ceiling system

6.6. Study on Friction-Added Suspended Ceiling Subjected to Harmonic Excitation

In this section, the behavior of friction-added ceiling system mounted on a linear single-story supporting structure was discussed to address the basic information on the nature of the friction ceiling responses. The steady-state response of the friction ceiling subjected to harmonic base excitation was discussed.

Equation of motion for a coupled linear-linear 2-DOF system

First, the response of a linear ceiling system mounted on a linear single-story building was analyzed to discuss the characteristics of floor motions to which the ceiling system will be subjected. The equation of motion for the coupled linear-linear 2-DOF system (see Figure 6.28) can be described as follows.

$$
\begin{bmatrix} m & 0 \\ 0 & m_{fc} \end{bmatrix} \begin{Bmatrix} \ddot{u} \\ \ddot{u}_p \end{Bmatrix} + \begin{bmatrix} c + c_{fc} & -c_{fc} \\ -c_{fc} & c_{fc} \end{bmatrix} \begin{Bmatrix} \dot{u} \\ \dot{u}_p \end{Bmatrix} + \begin{bmatrix} k + k_{fc} & -k_{fc} \\ -k_{fc} & k_{fc} \end{bmatrix} \begin{Bmatrix} u \\ u_p \end{Bmatrix} = -\begin{Bmatrix} m \\ m_{fc} \end{Bmatrix} a_g \cos \omega_g t
$$

(6.3)

215

$$\begin{cases} m\ddot{u} + c\dot{u} - c_p\dot{u}_{fc} + ku - k_{fc}u_{fc} = -ma_g\cos\omega_g t \\ m_{fc}\ddot{u}_p + c_{fc}\dot{u}_{fc} + k_{fc}u_{fc} = -m_{fc}a_g\cos\omega_g t \end{cases} \qquad (6.4)$$

$$\begin{cases} m\ddot{u} + c\dot{u} + ku = -m[a_g\cos\omega_g t + \dfrac{m_{fc}}{m}(a_g\cos\omega_g t + \ddot{u}_p)] \\ m_{fc}\ddot{u}_{fc} + c_{fc}\dot{u}_{fc} + k_{fc}u_{fc} = -m_{fc}(a_g\cos\omega_g t + \ddot{u}) \end{cases} \qquad (6.5)$$

where m = mass of supporting structure; c = critical damping coefficient of support-ing structure; k = stiffness of supporting structure; a_g = magnitude of input motion; ω_g = excitation frequency; $u_{fc} = u_p - u$ (relative response of friction ceiling system). Properties denoted with a subscript fc implies the properties of friction ceiling system.

In Eq. (6.5), ($a_g\cos\omega t + \ddot{u}_p$) and ($a_g\cos\omega t + \ddot{u}$) can be replaced to $\ddot{u}_{ceiling}$ and $\ddot{u}_{floor}$, respectively. Each denotes absolute ceiling acceleration and absolute floor accelera-tion. Therefore, Eq. (6.5) implies that the ceiling system will be subjected to floor motion ($\ddot{u}_{floor}$), and the floor motion will be affected by the response of the ceiling system ($\ddot{u}_{ceiling}$). It should be highlighted that the effect of the ceiling system on the floor response depends on the mass ratio between the ceiling system and supporting structure (m_{fc}/m). In the case of a suspended ceiling system, its mass is usually much smaller than that of the supporting structure ($m_{fc}/m \ll 1.0$) and the coupled equation (6.5) can be simplified into two discrete equations that can be solved in a cascade manner (see Figure 6.28). Therefore, in order to analyze the steady-state response of friction-added ceiling system subjected to a harmonic base excitation, the linear re-sponse of supporting structure needs to be obtained in advance. In this section, the

216

problem was further simplified where the steady-state response of supporting structure was utilized to obtain the floor motion ($\ddot{u}_{floor}$). The steady-state response of the supporting structure can easily be obtained using fundamental dynamics (Chopra 2001), which can be expressed as follows.

$$\ddot{u}(t) = -a_g R_a \cos(\omega_g t - \phi) \tag{6.6}$$

where R_a = acceleration response factor; φ = phase angle defined as below.

$$R_a = \frac{(\omega_g / \omega_n)^2}{\sqrt{[1-(\omega_g / \omega_n)^2]^2 + [2\zeta_n(\omega_g / \omega_n)]^2}} \tag{6.7}$$

$$\phi = \tan^{-1} \frac{2\zeta(\omega_g / \omega_n)}{1-(\omega_g / \omega_n)^2} \tag{6.8}$$

where ω_n = circular natural frequency of supporting structure.

Response of friction-added ceiling with bilinear hysteresis

The equation of motion for friction-added ceiling system is presented which have a hysteresis curve of the type shown in Figure 6.29. The equation of motion for such type of bilinear hysteresis can be expressed as Eqs. (6.9) – (6.10). Suspended ceiling systems generally have a very low critical damping ratio ($\zeta \approx 1.0 \%$). Therefore, damping provided by ceiling system is neglected for simplicity.
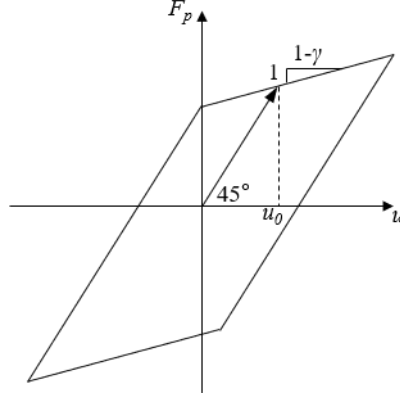
Figure 6.29 Bilinear hysteresis of friction-added ceiling system

$$m_{fc}\ddot{u}_r + k_{fc}F_{fc}(u_{fc},\gamma,t) = -m_{fc}\ddot{u}_{floor} \tag{6.9}$$

The hysteresis restoring force $F_p(u_p, \gamma, t)$ is defined as,

$$F_{fc}(u_{fc},\gamma,t) = \begin{bmatrix} u_{fc} & \text{if } (0 < u_{fc} < u_0) \\ u_0 + (\dfrac{k_c}{k_{fc}})(u_{fc} - u_0) & \text{if } (u_{fc} > u_0) \end{bmatrix} \tag{6.10}$$

where u_{fc} = displacement of ceiling system relative to floor; $u_0 = F_{fric}/k_d$ (displacement of friction damper required to initiate friction mechanism); $\gamma = k_d/k_{fc}$ (stiffness ratio between friction damper and friction ceiling); k_d = lateral stiffness of damper brace; k_c = lateral stiffness of unbraced ceiling; $k_{fc} = k_d + k_c$ (lateral stiffness of friction ceiling).

The nonlinear equation (Eq. 6.9) can be solved based on the method utilized by Caughey (1960), where the equation of motion for bilinear hysteresis was solved

218

based on the work of Kryloff and Bogoliuboff (Minorski 1947). The main theme of the first approximation theory of Kryloff and Bogoliuboff is to find an approximate solution for a quasi-linear system by applying the method of variation of constants to the basic steady-state solution for a linear SDOF system. Substituting the steady-state floor motion obtained in Eq. (6.6) to (6.9), the equation can be expressed as,

$$\ddot{u}_{fc}(\tau) + F_{fc}(u_{fc}, \gamma, \tau) = u_{fcs}[\cos(\eta\tau) + R_a \cos(\eta\tau - \phi)] \tag{6.11}$$

where ω_{fc} = cyclic natural frequency of friction ceiling; $\eta = \omega_g / \omega_{fc}$ (frequency ratio between ground input motion and friction ceiling); $u_{fcs} = a_g m_{fc}/k_{fc}$ (static displacement of friction ceiling); $\tau = t\omega_{fc}$.

In Eq. (6.11), terms are redefined as a function of τ to utilize the findings of the first approximation theory that in a quasi-linear system, the magnitude and phase change during a single cycle are very small, and it is appreciable to approximate them as a function of system period. For this reason, these are usually referred to as slow varying functions or the method of slowly varying parameters.

Eq. (6.11) can be solved assuming the solution to be of the form,

$$\begin{cases} u(\tau) = R(\tau)\cos(\eta\tau + \Phi(\tau)) \\ \dot{u}(\tau) = -R(\tau)\eta\sin(\eta\tau + \Phi(\tau)) \end{cases} \tag{6.12}$$

where $R(\tau)$ and $\Phi(\tau)$ are slow varying amplitude and phase of the friction ceiling.

The amplitude (R) and phase (Φ) can be obtained by differentiating Eq. (6.12), solved for Eq. (6.11) which results in following equations.

$$-\eta R' - \eta^2 R \sin\theta\cos\theta + F_{fc}(R\cos\theta,\gamma,\tau)\sin\theta$$
$$= u_{fcs}[R_a \cos(\eta\tau - \phi)\sin\theta + \cos(\eta\tau)\sin\theta] \tag{6.13}$$

$$-\eta R\Phi' - \eta^2 R\cos^2\theta + F_p(R\cos\theta,\gamma,\tau)\cos\theta$$
$$= u_{fcs}[R_a \cos(\eta\tau - \phi)\cos\theta + \cos(\eta\tau)\cos\theta] \tag{6.14}$$

where $\theta = \eta\tau + \Phi(\tau)$.

Since R and Φ are slowly varying, R' and Φ' can be regarded as a constant during a single cycle of motion. By integrating Eqs. (6.13) and (6.14) over one cycle, equations can be summarized as follows.

$$\left[\begin{array}{l} S_{(R_o)} = u_{fcs}[R_a \sin(\Phi + \phi) + \sin(\Phi)] \\ C_{(R_0)} - \eta^2 R_0 = u_{fcs}[R_a \cos(\Phi + \phi) + \cos(\Phi)] \end{array}\right. \tag{6.15}$$

$$\left[\begin{array}{l} S_{(R_o)} = \dfrac{1}{\pi}\displaystyle\int_0^{2\pi} F_{fc}(R\cos\theta,\gamma,\tau)\sin\theta\, d\theta \\[2mm] C_{(R_0)} = \dfrac{1}{\pi}\displaystyle\int_0^{2\pi} F_{fc}(R\cos\theta,\gamma,\tau)\cos\theta\, d\theta \end{array}\right. \tag{6.16}$$

During the derivation of Eq. (6.15), the results of integration for R' and Φ' are set to zero to obtain the steady-state response of the friction ceiling system, and R_0 denotes the steady-state amplitude of the system.

Eq. (6.16) can be solved using Figure 6.27, which yields (Caughey, 1960),

$$S_{(R_0)} = \begin{bmatrix} \dfrac{\gamma R_0}{\pi} \sin^2 \theta^* & \text{if } (R_0 > u_0) \\[2ex] 0 & \text{if } (R_0 < u_0) \end{bmatrix} \quad (6.17)$$

$$C_{(R_0)} = \begin{bmatrix} \dfrac{R_0}{\pi} \left[\gamma \theta^* + (1-\lambda)\pi - \dfrac{u}{2}\sin 2\theta^* \right] & \text{if } (R_0 > u_0) \\[2ex] R_0 & \text{if } (R_0 < u_0) \end{bmatrix} \quad (6.18)$$

$$\theta^* = \cos^{-1}(1 - \frac{2(u_0 / u_{fcs})}{(R_0 / u_{fcs})}) \quad (6.19)$$

Substituting Eqs. (6.17) – (6.18) into Eq. (6.15) the equation can be reduced as follows.

$$\eta^2 = \frac{C_{(R_o)}}{R_0} \pm \sqrt{(\frac{u_{fcs}}{R_0})^2 (R_a^2 + 2R_a \cos\phi + 1) - (\frac{S_{(R_0)}}{R_0})^2} \quad (6.20)$$

From the Eq. (6.20), the relationship between the amplitude of the friction ceiling and the frequency ratio ($\eta = \omega_g/\omega_{fc}$) at the given amplitude can be obtained similar to the relationship given in Eq. (6.7), which was described for a linear SDOF system. If the ceiling system undergoes a linear behavior, where the inertial force did not exceed the introduced friction force ($R_0 < u_0$), Eq. (6.20) reduces as

$$\eta^2 = 1 \pm \sqrt{(\frac{u_{fcs}}{R_0})^2 (R_a^2 + 2R_a \cos\phi + 1)} \quad (6.21)$$

Additionally, if it is assumed that the supporting structure has much higher natural frequency compared to the forcing frequency ($\omega_g/\omega_n \ll 1$) (thus, no acceleration amplification occurs), Eq. (6.21) becomes the steady-state dynamic response of an undamped linear SDOF system as shown below.

$$\frac{R_0}{u_{fcs}} = \frac{1}{\left|1-\eta^2\right|} \tag{6.22}$$

In the following, the equation for the resonance amplitude of the friction ceiling system was derived to analyze the governing parameters affecting the displacement response of friction ceilings.

The maximum amplitude of the friction ceiling will occur when Eq. (6.20) yields a double root solution for η, which gives the following relationship.

$$\left(\frac{u_{fcs}}{R_0}\right)^2 (R_a^2 + 2R_a \cos\phi + 1) = \left(\frac{S_{(R_0)}}{R_0}\right)^2 \tag{6.23}$$

Substituting Eq. (6.17) into Eq. (6.23) the system resonance amplitude can be obtained.

$$\frac{R_0}{u_{fcs}} = \frac{4(u_0/u_{fcs})^2}{4(u_0/u_{fcs}) - (\pi/\gamma)\sqrt{R_a^2 + 2R_a \cos\phi + 1}} \tag{6.24}$$

Eq. (6.24) can be redefined using the ceiling friction force (F_{fric}) as follows

$$\frac{R_0}{u_{fcs}} = \frac{(\frac{F_{fric}}{F_{fric,\min}})^2 (\frac{\pi}{\gamma})\sqrt{R_a^2 + 2R_a \cos\phi + 1}}{4(\frac{F_{fric}}{F_{fric,\min}} - 1)} \tag{6.25}$$

In Eq. (6.25), the ceiling friction force was normalized to the minimum friction force ($F_{fric,min}$). The minimum friction force represents the friction force that guarantees bounded ceiling resonance response. For the friction ceiling system to have a bounded response the following condition should be satisfied.

$$\frac{u_0}{u_{fcs}} > \frac{\pi}{4\gamma}\sqrt{R_a^2 + 2R_a \cos\phi + 1} \tag{6.26}$$

Describe in terms of system parameters, Eq. (6.26) can be given as follows.

$$\frac{F_{fric,\min}}{W_{fc}} > \frac{\pi}{4}(\frac{a_g}{g})\sqrt{R_a^2 + 2R_a \cos\phi + 1} \tag{6.27}$$

Eq. (6.25) reveals that the resonance amplitude of friction ceiling depends on the damper friction force (F_{fric}), stiffness ratio ($\gamma = k_d/k_{fc}$), period ratio between the ground motion and supporting structure (T_n/T_g), and the period ratio between the ground motion and friction-added ceiling (T_{fc}/T_g). Also, the required minimum friction force increases proportionally to the amplitude of the floor motion, which depends on the tuning ratio between the supporting structure and ground motions (ω_g/ω_n) (see Eq. (6.27)).
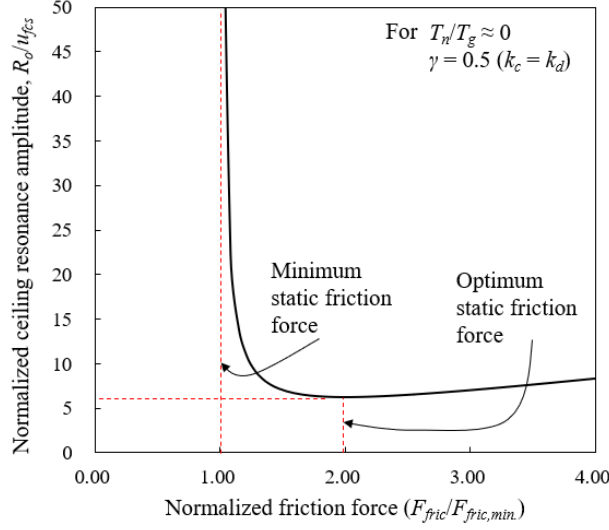
Figure 6.30 Relationship between static friction force and ceiling resonance
amplitude

First, the response of friction ceilings was analyzed assuming they are installed
on a very rigid structure ($\omega_g/\omega_n \approx 0$) where no acceleration amplification occurs.
Figure 6.30 shows the relationship given by Eq. (6.25) with assuming the friction
ceiling having $\lambda = 0.5$. It can be observed that the ceiling resonance amplitude tends
to decrease as the friction force increases. However, after reaching a minimum am-
plitude, it increases as the friction force increases. The friction force yielding a min-
imum resonance amplitude is known as the optimum static friction force, which can
be obtained by taking the partial derivative of Eq. (6.24).

$$\frac{\partial(R_0/u_{fcs})}{\partial(u_0/u_{fcs})} = 0 \tag{6.28}$$

$$\frac{F_{fric}}{W_{fc}} = \frac{\pi}{2}(\frac{a_g}{g})\sqrt{R_a^2 + 2R_a \cos\theta + 1} \tag{6.29}$$

224
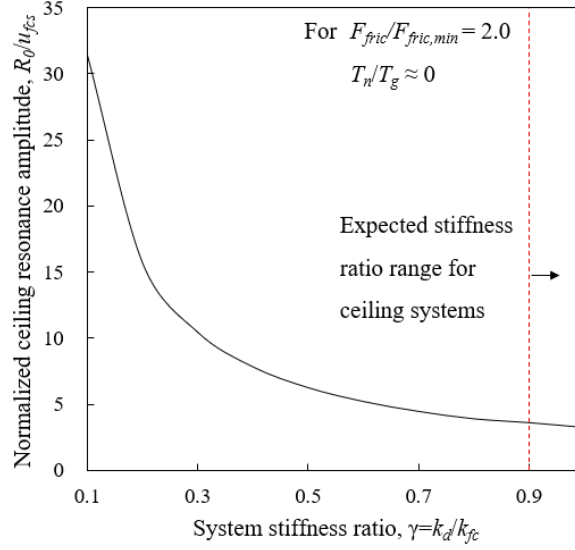
Figure 6.31 Effect of stiffness ratio ($\gamma = k_d/k_{fc}$)

As expected, the optimum slip load should also be adjusted take into account the amplification of input motion.

Figure 6.31 shows the effect of the stiffness ratio between the friction damper (k_d) and the friction ceiling ($k_{fc} = k_c + k_d$). It can be observed that for the given friction force ($F_{fric}/F_{fric,min} = 2.0$), the resonance amplitude of the ceiling system decreases more for the system with a higher stiffness ratio. Therefore, a high response reduction could be expected for the friction-added ceiling systems because the unbraced ceiling systems usually have very low lateral stiffness compared to that of the damper braces ($k_c << k_d$, $\gamma \geq 0.9$).

Figure 6.32 shows the displacement response spectrum of the friction-added ceiling system constructed from Eq. (6.20). The displacement amplitude was normalized to the static displacement of friction ceilings (u_{fcs}). For verification purpose, the results obtained from time-history analysis of the bilinear hysteresis nonlinear
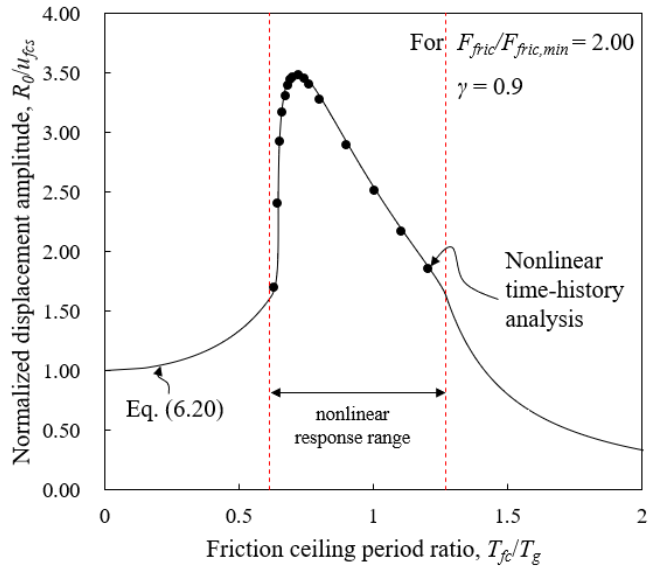
Figure 6.32 Displacement response spectrum for friction-added ceiling

model given in Figure 6.18 was also plotted with dots. It can be observed that the results obtained from Eq. (6.20) and the numerical analysis model are closely matched.

Figure 6.33 summarizes the response of the friction-added ceiling system with various stiffness ratios. As previously discussed, the overall responses are much smaller for the system with higher γ, implying that the displacement response of the ceiling system can be effectively reduced using the friction mechanism. Also, it can be observed that for the friction-added ceiling system with higher γ, the effect of the damper friction force on the resonance period becomes much significant, which requires careful consideration of resonance behavior for the friction-added ceiling system in its design process. The system became a fully-braced ceiling system when the high friction force was introduced. For a system with low friction force, the system behaves as an unbraced (non-seismic) fully-floating ceiling.
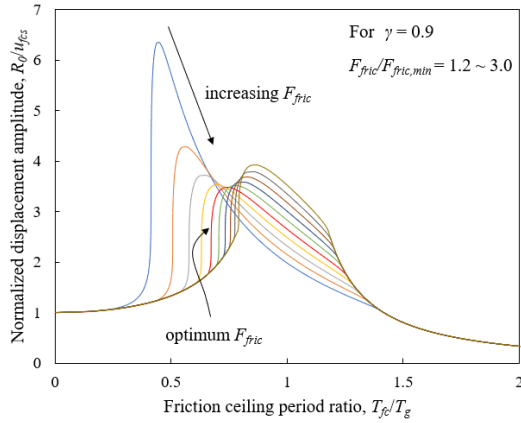
(a) Response of friction ceiling with $\gamma = 0.9$
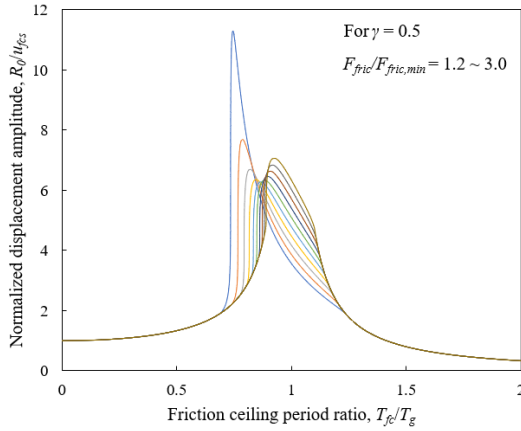
(b) Response of friction ceiling with $\gamma = 0.5$
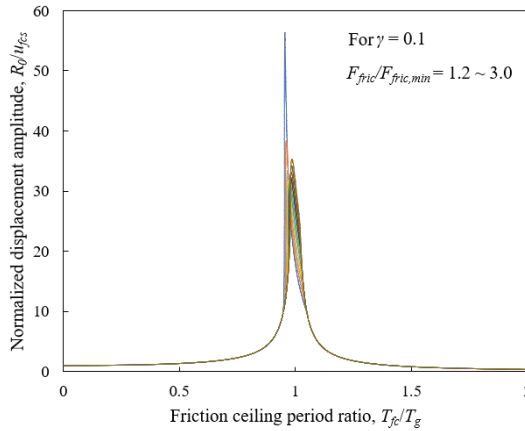
(c) Response of friction ceiling with $\gamma = 0.1$

Figure 6.33 Effect of stiffness ratio ($\gamma = k_d/k_{fc}$) on response of friction ceiling
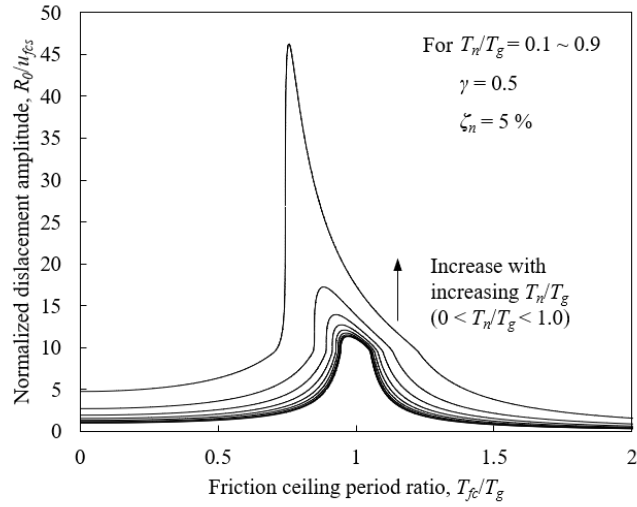
(a) For structure period $0 < T_n/T_g < 1.0$
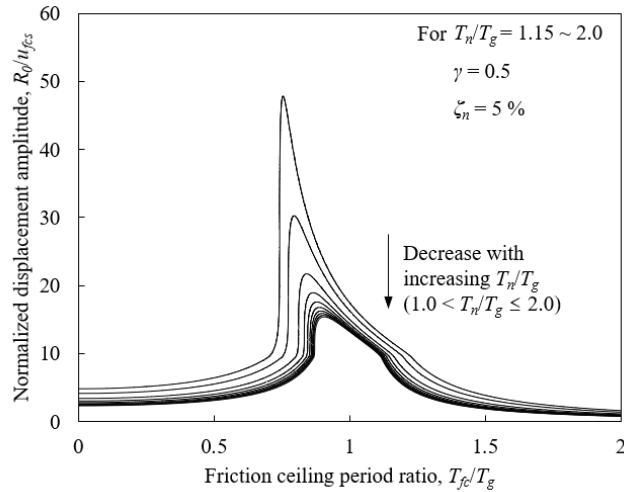
(b) For structure period $1.0 < T_n/T_g < 2.0$

Figure 6.34 Comparison of absolute ceiling response depending on structure period ratio (T_n/T_g)

The effects of structure period ratio (T_n/T_g) were discussed below using the response spectrum of the friction-added ceiling systems that are normalized to the static displacement of friction ceiling (u_{fcs}) and the static displacement of friction

ceiling incorporating the acceleration amplification resulting from the structural dynamic response ($u_{fcs,floor}$).

Figure 6.34 shows the response of friction ceilings normalized to static displacement of friction ceiling systems (u_{fcs}). It should be highlighted that u_{fcs} was defined with the un-amplified input magnitude ($u_{fcs} = m_{fc}a_g/k_{fc}$), which allows the comparison of the absolute response of friction ceilings depending on the structure period ratio (T_n/T_g). The analysis was conducted using a constant friction force ($F_{fric}/F_{fric,min}$ = 6.0), where the minimum friction force ($F_{fric,min}$) was determined for the case of $T_n/T_g = 0$ (see Eq. 6.27). The structure was assumed to have a critical damping ratio of 5 %.

First, it can be observed that the response of friction ceiling systems gradually increased as the structure period ratio (T_n/T_g) becomes close to unity, as expected, due to the effect of the amplified input motion resulted from structural filtering. Similar observation can also be made from the results of numerical case study (see Figure 6.24), where the overall ceiling displacements along the building height more or less follows the distribution of PFA amplification (see Figure 3.8).

The overall spectrum envelope varies because the analysis was conducted for a constant F_{fric} while the magnitude of the input motions increased or decreased depending on the structure period ratio (T_n/T_g). Therefore, for friction ceiling systems under higher floor acceleration (for $T_n/T_g \approx 1$), the overall response became more flexible and, thus, the resonance occurred at lower a T_n/T_g ratio. The variation in their resonance periods can be more clearly visible if the static displacement is determined considering the amplified input acceleration was utilized for the normalization (See Eq. 6.30)

$$u_{fcs,floor} = \frac{m_{fc}a_g}{k_{fc}} \sqrt{R_a^2 + 2R_a \cos\phi + 1} \tag{6.30}$$

Figure 6.35 shows that due to the increase or decrease in the floor acceleration caused by structural dynamic response (T_n/T_g), the friction ceilings experienced significant shift in their resonance periods. Also, the response of friction ceiling decreased as the T_n/T_g increased ($0.1 \leq T_n/T_g \leq 0.8$) and increased for $T_n/T_g = 0.9$ (see Figure 35(a)). For the T_n/T_g range of $1.15 - 2.0$, the response started to decrease and finally increased as T_n/T_g became higher than 1.5. Such variation in spectrum response resulted from the effects of input acceleration amplification which affect the friction force ratio ($F_{fric}/F_{fric,min}$).

As shown in Figure 6.28, the friction ceiling response decreased until F_{fric} reached the optimum friction force ($F_{fric}/F_{fric,min} = 2.0$) and increased proportionally to the friction force ratio. In the case of the spectrum shown in Figure 6.35(a), the friction force ratio was initially higher than the optimum friction force and started to decrease as the higher minimum friction force ($F_{fric,min}$) is required for T_n/T_g with close to unity. Correspondingly, the response of friction ceiling decreases until $F_{fric}/F_{fric,min}$ reaches the optimum friction force and increases as the $F_{fric}/F_{fric,min}$ pass through the optimum friction force (see Figure 6.35(b)).

The analysis for the effects of structure period ratio reveals that as the floor acceleration amplified for the structure closely tuned to the ground motion, the overall response of friction ceiling systems proportionally increased. However, it should
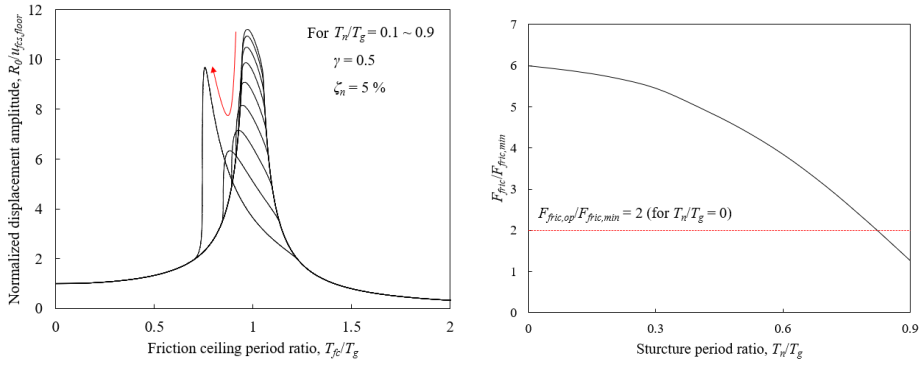
(a) For structure period $0 < T_n/T_g < 1.0$
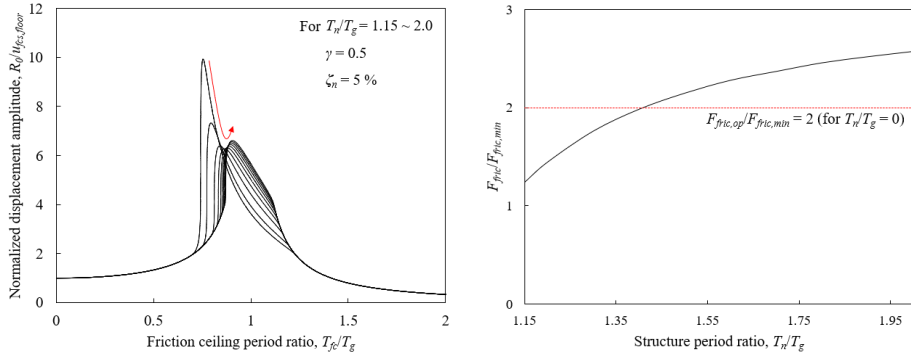
(b) For structure period $1.0 < T_n/T_g < 2.0$

Figure 6.35 Effect of structure period (T_n/T_g) on resonance period and response of friction-added ceiling system

be noted that the amount of the increment can be much higher than that of acceleration amplification because the resonance period of friction ceiling is also affected by the structure period ratio. If the friction force is kept constant, the friction ceiling system will behave more flexibly for the structure tuned to the ground motion (due to the highly amplified input acceleration), therefore, affecting the overall envelope of the response spectrum.

For simplification of the design process of friction-added ceiling systems, the static friction force needs to be proportionally adjusted by the amount of acceleration
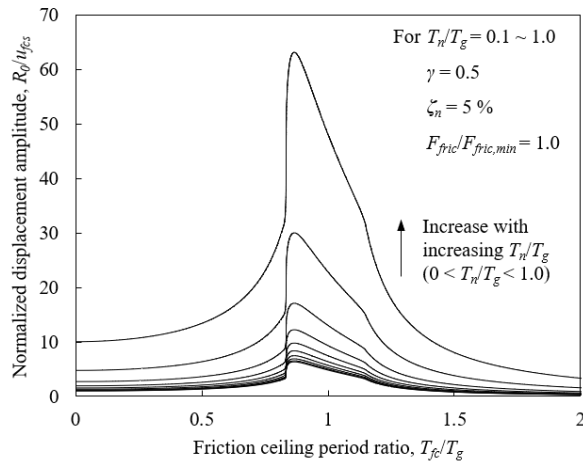
(a) Normalized to unamplified static displacement (u_{fcs})
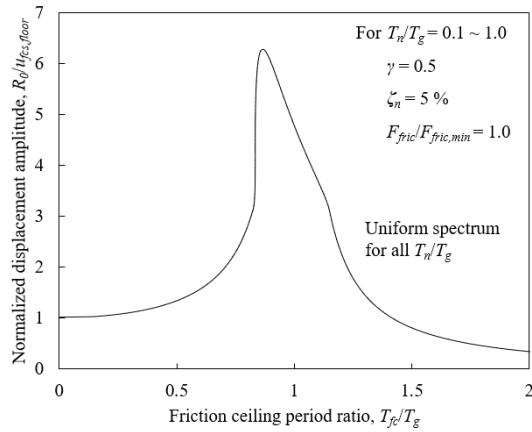
(b) Normalized to amplified static displacement ($u_{fcs,floor}$)

Figure 6.36 Response of friction ceilings with friction force proportionally increased by amount of acceleration amplification

amplification resulting from the structural dynamic response so that a uniform ceiling response spectrum can be utilized, as shown in Figure 6.36. It can be observed that the overall response spectrum envelope remains the same, and only the absolute ceiling response linearly increases proportionally to the amount of the acceleration amplification.

For further simplification, ideally, both the friction force level and the stiffness of friction ceilings could be proportionally adjusted, such that the same amount of ceiling displacement can be obtained such as the response shown in Figure 6.36(b). However, it is generally hard to adjust the stiffness of friction-added ceiling systems with keeping a constant stiffness ratio ($\gamma = k_d/k_{fc}$, $k_{fc} = k_d + k_c$) because not many options are available to adjust the stiffness of unbraced ceiling (k_c). Therefore, the formerly proposed adjustment method is expected to be more feasible option in controlling the response of friction-added ceiling systems installed along the building height.

The design implications made in this section are expected to be useful in adjusting the maximum static friction force in the design procedure, which will be presented in the following section.

6.7. Proposed Design Procedure

Figure 6.37 summarizes the step-by-step procedure to design the friction-added ceiling system proposed in this study. First, the plenum depth, mass per unit hanger wire, and the design response spectrum is determined. The selection and scaling of ground motions can be implemented following the standard procedure such as ASCE 7-22 (ASCE/SEI 2022). The damper bracing components may be designed based on the floor response spectrum method obtained from the linear or nonlinear time history analysis of supporting structures. Once the target perimeter clearance is established, the maximum static friction force can be determined through the iterative

```
                    ┌─────────────┐
                    │    Start    │
                    └─────────────┘
                           │
                           ▼
        ┌───────────────────────────────────────────┐
        │  Determine plenum depth, mass per unit     │
        │  hanger wire, and design response spectrum │
        └───────────────────────────────────────────┘
                           │
                           ▼
        ┌───────────────────────────────────────────┐
        │  Select spectrum-compatible ground motions │
        │  by following standard procedure such as   │
        │  ASCE 7-16                                  │
        └───────────────────────────────────────────┘
                           │
                           ▼
        ┌───────────────────────────────────────────┐
        │  Generate floor motions and floor response │
        │  spectrum                                   │
        └───────────────────────────────────────────┘
                           │
                           ▼
        ┌───────────────────────────────────────────┐
        │  Calculate maximum design seismic force    │
        │  and design damper bracing component       │
        └───────────────────────────────────────────┘
                           │
                           ▼
        ┌───────────────────────────────────────────┐
        │  Establish target perimeter clearance to   │
        │  avoid pounding                            │
        └───────────────────────────────────────────┘
                           │
                           ▼
        ┌───────────────────────────────────────────┐
        │  Assume initial maximum static friction    │
        │  force level                               │
        └───────────────────────────────────────────┘
                           │
                           ▼
        ┌───────────────────────────────────────────┐
        │  Perform nonlinear dynamic analysis using  │
        │  proposed bilinear-hysteresis SDOF model   │
        └───────────────────────────────────────────┘
                           │
                           ▼
                    Displacement
                   response within      ── No ──► Adjust maximum
                   target clearance?              static friction force
                           │
                          Yes
                           ▼
                    ┌─────────────┐
                    │     End     │
                    └─────────────┘
```

Either linear or nonlinear time history analysis may be used

Floor response spectrum method recommended

Figure 6.37 Recommended seismic design procedure for friction-added suspended ceilings

nonlinear analyses using the proposed bilinear hysteresis SDOF model until the ceiling displacement becomes less than the clearance level. The clamping force to develop the maximum static friction force should be determined experimentally.

6.8. Summary and Conclusions

In this study, shake table tests of a braced suspended ceiling specimen was first conducted to evaluate its seismic performance. The limitations resulting from the use of a ceiling brace were discussed. A new bracing system using grid reinforcement was proposed, which provides in-plane stiffness in the ceiling grid system. Higher in-plane stiffness of grid system could enhance the restraint effect of lateral bracing, therefore, and the overall seismic performance. Also, as a cost-effective design or retrofit method, a rotational friction damper for ceiling systems was developed, and its performance was evaluated through shake table tests. The dynamic characteristics and mechanism of the proposed friction damper were experimentally identified, and the simple analytical model for a friction-added ceiling system was developed. A numerical case study was implemented to evaluate the applicability of the proposed ceiling system and draw useful design recommendations based on an extensive time history analyses of steel moment frame buildings. The results of this study can be summarized as follows.

(1) Despite the provision of costly lateral bracing, the seismic performance was only slightly improved for the braced ceiling specimen due to the lack of a desirable rigid diaphragm action in ceiling grids. The large displacement response in the unrestrained grid line and the resulting pounding forces caused high acceleration amplification within the ceiling grids. Combined with high vertical acceleration, approximately 40 % of the panels were dislodged at the end of the test (PFA = 2.00 g).

(2) The braced ceiling specimen strengthened with grid reinforcements showed a highly improved seismic performance. Despite the fact that it has a larger ceiling area compared to the conventionally braced ceiling specimen, no damage was observed until the end of the test. All the displacement and acceleration responses measured in the specimen proved the effectiveness of grid reinforcements in strengthening the in-plane stiffness of the whole ceiling system and improving the restraining effect provided by the braces. Also, a simple design method was provided, which can be simply implemented using the equivalent static force prescribed in seismic design codes.

(3) The friction-added ceiling specimen exhibited highly enhanced performance compared to the non-seismic (unbraced) and conventionally braced specimens. By adding the friction mechanism, the acceleration and displacement responses were significantly reduced. Only a single ceiling panel was dislodged until the end of the test.

(4) The robustness and operability of the proposed ceiling friction damper were experimentally evaluated using diverse input motions. The proposed friction-damping mechanism showed a consistent friction force with stable hysteretic responses, regardless of the input motion characteristics. In addition, the damping mechanism developed a consistent frictional force for both the uniaxial and triaxial excitations because of allowed bi-directional rotations at the ends of the damper braces (hanger bolts).

(5) A simplified analytical SDOF model with bilinear hysteresis was developed

for the friction-added ceiling system. The proposed SDOF model accurately predicted the overall responses and satisfactorily simulated energy dissipation in a close match with the shake table test results.

(6) Seismic performance of all the tested ceiling specimens was evaluated based on the peak floor acceleration and the ceiling seismic force. It was shown that the performance of DTL-FS specimen showed the lowest seismic force, possibly due to the partition-induced dynamic interactions. Also, it was observed that all the non-seismic and the braced ceiling with conventional lateral bracing details reached almost life safety performance level at the end of the test. The seismic ceiling specimens (DTL-F and DTL-FS-BS) showed superior performance where operational performance level was achieved at the end of the test.

(7) This study conducted a performance level evaluation based on the area of the fallen ceiling panel area. Although such criteria are convenient and generally sufficient for the design purposes, further detailed performance level description or criteria based on the amount of introduced perimeter clearance needs to be developed as they are directly related to the pounding force, which is the main source of ceiling seismic damage.

(8) An extensive numerical case study was conducted to evaluate the applicability of the proposed friction-added ceiling system. The main objective was to estimate the ceiling displacements or the required perimeter clearance to avoid pounding. The floor motions obtained from the linear dynamic analysis of 3-, 9-, 20-story steel moment-resisting buildings were

used as input motions. Overall, the response of the friction-added ceiling system varied sensitively to the input motion and the dynamic characteristics of the supporting structures. The required perimeter clearance to avoid pounding was approximately 65 mm in the median sense for all the case study buildings, which is fully feasible in practice through using conventional ceiling perimeter channels.

(9) Behavioral characteristics of friction-added ceiling systems were analyzed based on the analytical solution obtained for the coupled 2-DOF system subjected to harmonic excitation. The 2-DOF simulates the friction ceiling with bilinear hysteresis installed on the linear supporting structure. Some of the key variables affecting the response of friction ceiling were analyzed, and the effect of acceleration amplification resulting from structural filtering was discussed. To obtain a uniform friction ceiling response regardless of the characteristics of supporting structure, both the friction force and the stiffness of the friction-added ceiling system needs to be proportionally adjusted by the amount of the acceleration amplification caused by structural filtering.

Chapter 7. Summary and Conclusions

This study conducted several experimental and numerical analyses to evaluate the seismic performance of suspended ceiling systems and to provide effective seismic design methods. Firstly, the studies on the seismic demands on nonstructural elements were implemented where discussions on the effects of key structural properties on the peak floor acceleration (PFA) and the peak component acceleration (PCA) were made. Based on a series of full-scale shake-table tests, the seismic performance of ceiling systems with various configurations was evaluated, and their key engineering parameters related to acceleration amplification and natural frequency were identified. Two seismic performance-enhancing methods were proposed, a strengthening method through grid reinforcements and a friction-added ceiling system where a novel rotational friction mechanism was utilized.

Chapters 3 and 4 provide results of experimental and numerical analyses conducted for evaluating the seismic demands on nonstructural elements. Numerical analysis was performed through the four types of three-dimensional building models to discuss the effects of various structural properties on the nonstructural seismic

demand. Also, shake-table tests were performed using a full-scale 2-story steel moment frame to evaluate the nonstructural seismic demand experimentally. The focus was given to estimating the effects of structural and nonstructural nonlinearities on the PFA and PCA. The results of this study can be summarized as follows.

(1) The key structural properties affecting the PFA were discussed through the elementary structural dynamics. The PFA given by ASCE 7-16 did not well corroborate with the PFA analyzed from the up-to-date database of the instrumented buildings.

(2) As for the PCA, the equivalent static method yielded conservative results for all the regular 3-, 9-, and 20-story steel moment frames mainly because they neglect the structural period effects on the PFA and the effects of the period ratio between the structure and nonstructural elements (T_p/T_n) on the PCA. For better prediction of the equivalent static force, the *effective* PCA defined as the average of PCA for the practical period range between 0.06 sec and 0.5 sec was proposed.

(3) The studies on the building model with torsional irregularity showed a much higher PCA than the predicted estimations made by ASCE 7-16 due to the combined effects of torsional amplification and closely spaced modes of vibration. Considering that appropriate torsional amplification is not yet accounted for in the equivalent static method, the dynamic methods should be preferred to avoid unconservative design if a building is severely irregular in torsion-wise.

(4) The overall PFA reduced significantly as the nonlinearity of the tested frame increased. The PFA reduction suggested by ASCE 7-22 was larger than the experimental results for low-to-moderate ductility level ($1.60 \leq R_D \leq 2.94$). The PFA measured from the moderately yielded test frame ($R_D = 2.94$) was about half of the elastic PFA.

(5) The analysis on resonant PCA showed that the magnitude of PCA amplification decreased by about 30 % when the test frame reached a moderate level of structural ductility ($R_D = 2.94$). The effect of structural nonlinearity on the response of elastic components needs to be systematically addressed for a better estimation of nonstructural seismic demands.

(6) The PCA further decreased due to the nonlinearity of the steel rack specimens mounted on flexible and rigid access floors. The relationship between the measured PCA and its corresponding component ductility did not well corroborate with that given by ASCE 7-22, which is speculated to be caused by the pinching hysteretic behavior of the steel rack specimens. Considering that many of the floor-mounted nonstructural (such as steel racks, partitions) exhibit pinched hysteretic behavior, a more refined analysis including the pinching model is warranted to establish a more realistic relationship between component ductility and component acceleration.

Chapter 5 presents the shake-table test results performed using a total of nine full- and small-size ceiling specimens. Based on the test results, their seismic performance and physical behavior were discussed, and key dynamic properties were iden-

tified. Also, the effects of interaction among nonstructural elements were also discussed through the partition-attached full-scale ceiling specimen. The main findings can be summarized as follows.

(1) The direct-hung suspended ceiling specimens with hanger wires showed the pendulum behavior because the both ends of hanger wires were free to rotate. The indirect-hung suspended ceiling specimens with hanger bolts showed a much higher natural frequency owing to the rotation-restrained characteristics of the connection between the hanger bolt and the frame top. Single and double curvature bending deformations were observed for each orthogonal direction because of the unidirectional rotation-restrained characteristics of the connection between the hanger bolt and the grid system. The single and double curvature bending models were proposed that can be utilized to developing rational engineering design procedures for such ceiling systems.

(2) A higher critical damping ratio ($\zeta = 7$ %) was observed for the indirect-suspended ceiling systems than that of direct-hung systems ($\zeta = 1$ %), which was attributed to the high energy dissipation caused by the cyclic friction around the hanger connections and member interfaces. The damping ratio was further increased when the effects of ceiling perimeter frictions were accounted. The equivalent damping ratio measured from the uniaxial perimeter friction specimen (ITL-R1) was estimated to be approximately 12 %.

(3) The analysis on the ceiling acceleration responses showed that the median acceleration amplification factors in the horizontal and vertical direction were measured to be 1.80 and 1.75, which were higher than those given by ASCE 7. Considering the high coefficient of variation observed (COV ≈ 50 %), the design acceleration amplification needs to be prescribed more conservatively.

(4) The direct-hung T-bar ceiling specimen suffered substantial damage mainly because of the early damage to the cross T-bars and its low in-plane stiffness. Much less damage was observed in the indirect-hung T-bar ceiling specimens due to the presence of the carrying channels which prevent the spreading of T-bar members and thus enhancing the in-plane stiffness of ceiling grid systems. The test results clearly show the importance of securing the sufficient in-plane stiffness of grid systems in obtaining high seismic performance of ceiling systems.

(5) The large-size continuous ceiling specimen showed different seismic performances in their respective orthogonal direction. The favorable continuous restraining effects provided by the screw-attached panels were only effective for the grid layer composed of M-bar members. In the orthogonal direction, where the pounding occurs on the carrying channels, global ceiling failure was observed initiated by the failure of the carrying joints. The carrying joints failure led to extensive disconnections of various joints installed within the ceiling specimen. Therefore, careful design consideration should be given to the ceiling grid layer composed of carrying channels,

243

especially in regard to the joint strength.

(6) The partition-attached ceiling specimen suffered severe damage resulting from the rocking behavior of the partial-height partition walls. The out-of-plane rocking of the partitions caused significant dislodgements and grid joint disconnections at the perimeters and the center of the ceiling resulting in approximately 60 % of ceiling panel dislodgements at the end of the tests. The ceiling seismic performance were compared by collating previous studies, and the adverse effects of the nonstructural component interaction were discussed.

Chapter 6 proposed seismic design methods for the suspended ceiling systems. Two seismic design methods were provided, each fabricated using grid reinforcements and rotational friction dampers. The enhanced seismic performances of the ceiling specimens fabricated with the proposed methods were reported. Also, the performance comparison was made using a braced ceiling specimen fabricated following the current design codes. The results of this study can be summarized as follows.

(1) The braced ceiling specimen showed only slightly improved seismic performance compared to the unbraced ceiling specimen due to the lack of desirable rigid diaphragm action in ceiling grids. The restraining effect provided by the lateral bracings was limited to the grid member directly attached to the bracings. Combined with high vertical acceleration, approximately 40 % of the panels were dislodged at the end of the test.

(2) The seismic performance of braced ceiling was highly improved by introducing grid reinforcements. Despite the fact that it has a larger ceiling area compared to the conventionally braced ceiling specimen, no damage was observed until the end of the test. The effectiveness of grid reinforcements in strengthening the in-plane stiffness of the ceiling grids were proved based on the measured acceleration and displacement responses. A simple design method was also provided, which can be implemented using the equivalent static force prescribed in seismic design codes.

(3) The friction-added ceiling specimen exhibited highly enhanced seismic performance with only minor damage observed until the end of the test. By adding the friction mechanism, the acceleration and displacement responses were significantly reduced, and the perimeter pounding was much delayed to occur under higher input intensity compared to that of the non-seismic ceiling specimen.

(4) The robustness and operability of the proposed ceiling friction damper were experimentally demonstrated using diverse input motions. The proposed friction-damping mechanism showed a stable hysteretic response by maintain consistent friction force regardless of the input motion characteristics.

(5) A simplified analytical SDOF model with bilinear hysteresis was developed for the friction-added ceiling system. The proposed SDOF model accurately predicted the overall responses and satisfactorily simulated energy dissipation in a close match with the shake table test results.

(6) An extensive numerical case study based on the floor motions of 3-, 9-, and

20-story steel moment buildings was performed to evaluate the applicability of the proposed friction-added ceiling system. The main objective was to estimate the ceiling displacements or the required perimeter clearance to avoid pounding. For all the analyzed buildings, the required perimeter clearance to avoid pounding was approximately 65 mm in the median sense for all the case study buildings, which is fully feasible in practice through using conventional ceiling perimeter channels.

(7) The behavioral characteristics of the friction-added ceiling system were discussed based on the approximate solution for the coupled 2-DOF model subjected to harmonic excitation. The coupled 2-DOF model was utilized to simulate the linear structure and nonlinear (bilinear hysteresis) ceiling behavior. Some useful design implications were made based on the analysis results of key affecting parameters.

(8) The step-by-step procedure to design the friction-added ceiling system proposed in this study was also recommended.

Bibliography

[1] AIK (Architectural Institue of Korea). *Seismic design code of buildings* (KDS 41 17 00). Ministry of Land, Infrastructure and Transport, Sejong, Korea (2019) (in Korean).

[2] Anajafi, H and Medina, RA. "Effects of supporting building characteristics on non-structural component acceleration demands". *Proceedings of 11th U.S. National Conference on Earthquake Engineering*, California, USA (2018).

[3] Anajafi H, Medina RA. "Lessons learned from evaluating the responses of instrumented buildings in the United State: The effects of supporting building characterstics on floor response spectra". *Earthquake Spectra* 35.1 (2019): pp. 159-191.

[4] ANCO. *Seismic harzard assessment of nonstructural ceiling components-Phase I*. Final report for National Science Foundation (1983).

[5] ASCE/SEI, 41-13. *Seismic evalaution and retrofit of existing buildings*. American Soceity of Civil Engineers (2013).

[6] ASCE/SEI, 41-17. *Seismic evalaution and retrofit of existing buildings*. American Soceity of Civil Engineers (2017).

[7] ASCE/SEI, 7-16. *Minimum design loads and associated criteria for buildings and other structures*. Reston, VA: American Society of Civil Engineering (2017).

[8] ASCE/SEI, 7-22. *Minimum design loads and associated criteria for buildings and other structure*. American Society of Civil Engienerign, VA, USA (2022).

[9] ASTM-E580-E80/ASTM-E580M-17. *Standard practice for installtaion of ceiling suspension systems for accoustical tile and lay-in panels in area subjected to earthquake ground motions*. West Conshohocken, PA, ASTM International (2017).

[10] ASTM C635/C635-17. Standard specification for manufacture, performance, and testing of metal suspension systems for acoustical tile and lay-in panel ceilings. West Conshohocken, PA, ASTM International (2017).

[11] Ayres JM and Sun TY. *Nonstructural damage: The San Fernando California earthquake of february 9, 1971*. US Departement of Commerce, National Ocean and Atmospheric Administration, NOAA, Washington, DC, 1(B) (1973): pp. 736-742.

[12] Badillo-Almaraz H, Whittaker AS, and Reinhorn AM. "Seismic fragility of suspended ceiling system". *Earthquake Spectra* 23 (1) (2007): pp. 21-40.

[13] Brandolese S, Fiorin L, Scotta R. "Seismic demand and capacity assessment of suspended ceiling systems". Engineering Structures 193 (2019): pp. 219-237.

[14] Caughey TK. "Sinusoidal excitation of a system with bilinear hysteresis". *Journal of Applied Mechanics* 27.4 (1960).

[15] CEN. Eurocode 8 – *Design of structures for earhtuqkae resistance. Part I: General rules, seismic actions and rules for building*. European standard EN1998-1, European Committee for Standardization, Burssels (2004).

[16] Chaudhuri SR, Villaverde R. "Effect of building nonlinearity on seismic response of nonstructural components: A parametric study". *Journal of Structural Engineering* 134.4 (2008): pp. 661-670.

[17] Chen C, Pantoli E, Wang X, Astroza R, Ebrahimian H, Hutchinson TC, Conte JP, Restrepo JI, Marin C, Walsh KD, Bachman RE, Hoehler MS, Englekirk R, Faghihi M. "Full-scale strcutural and nonstructural building system performance during earthquakes: Part I – Specimen description, test protocol, and structural response". Earthquake Spectra 32.2 (2016): pp. 737-770.

[18] Cho JE. Dynamic response characteristics of ceilings on shaking table test. MS thesis, Seoul National University (2015).

[19] Chopra AK. *Dynamics of Structure: theory and applications to earthquake engineering*. Prentic-Hall (2001).

[20] Dai L, Zhang P, Ren C. "Effects of pinching on seismic performances of unbraced steel storage pallet racks". Proceedings of the Cold-Formed Steel Research Consortium Colloquium (2020).

[21] Dao, N, Ryan, K, Sato, E, Okazaki, T, Mahin, S, Zaghi, A, Kajiwara, K, and Matsumori, T. "Experimental evaluation of an innovative isolation system for a lightweight steel moment frame building at E-Defense:. *Proceedings of ASCE Structures Congress*, Chicago, IL (2011): pp. 2951-2962.

[22] Dhakal RP, MacRae GA, Pourali A, Paganotti G. "Seismic fragility of suspended ceiling systems used in NZ based on component tests". *Bulletin of the New Zealand Society for Earthquake Engineering* 49.1 (2016): pp. 45-63.

[23] Drake RM, Bachman RE. "NEHRP provisions for 1994 for nonstructural components". *Journal of Architectural Engineering* 2.1 (1996): pp. 26-31.

[24] Echevarria AA, Zaghi AE, Soroushian S, Maragakis EM. "Seismic Fragility of Suspended Ceiling Systems". *Proceedings of the 15th World Conference on Earthquake Engineering*, Lisboa, Portugal (2012).

[25] ETABS. *CSI analyses reference manual for SAP2000, ETABS, SAFE and CSiBridge*. Computers and Structures, Inc. (2017).

[26] European Standard (BS EN 13964:2014). *Suspended ceilings – Requirements and test methos*. European Committee for Standardization (2014).

[27] FEMA E74. *Reducing the risks of non-structural earthquake damage – A practical guide*. U.S. Department of Homeland Security, Federal Emergency Management Agency (2011).

[28] FEMA. *Multi-harazd loss estimation methodology earthquake model, HAZUS-MH technical manual*. Federal Emergency Management Agency, Washington, DC (2005).

[29] Fiorino L, Mascillo V, Landolfo R. "Shake table tests of a full-scale two-story sheathing-braced cold-formed steel building". *Engineering Structures* 151 (2017): pp. 771-794.

[30] Fiorino L, Bucciero B, Landolfo R. "Evaluation of seismic dyanmic behavior of drywall partitions, façades and ceilings through shake table testing". *Engineering Structures* 180 (2019): pp. 103-123.

[31] Fiorino L, Shakeel S, Landolfo R. "Seismic behavior of a bracing system for LWS suspended ceilings: Prelimineary experimental evaluation through cyclic tests". *Thin-Walled Structures* 155 (2020).

[32] Flores, FX, Lopez-Garcia, D, Charney, FA. "Assessment of floor accelerations in special steel moment frames". *Journal of Contructional Steel Research* 106 (2015): pp. 154-165.

[33] Gilani AS, Glasgow B, and Ingratta T. "Seismic performance of directly hung suspended ceilings with engineered perimeter product". *The 14th World Conference on Earthquake Engineering*, Beijing, China (2008).

[34] Gilani AS, Reinhorn AM, Glasgow B, Lavan O, and Miyamoto HK. "Earthquake simulator testing and seismic evaluation of suspended ceilings". Journal of Architectural Engineering 16.2 (2010): pp. 63-73.

[35] Gilani AS, Takhiro SM, and Straight Y. "Seismic evaluation of drywall suspended ceilings using shake table testing and the finite element analysis". *In the second ATC & SEI Conference on Improving the Seismic Performance of Existing Buildings and Other Structures*, San Francisco, California (2015): pp. 471-482.

[36] Gupta A, Krawinkler H. *Seismic demands for performane evaluation of steel moment resisting frame structures*. Report No. 132. Department of Civil and Environmental Engineering, Stanford University, USA (1999).

[37] Huang WC, Hussainzada N, McClure G. "Experimental study on the seismic behavior of suspended ceilings". *Proceedings of the 3rd Specialty Conference on Disaster Prevention and Mitigation* (2013a).

[38] Huang WC, McClure G, and Hussainzada N. "Experimental study on the seismic performance of suspended ceiling systems in interaction with partition walls". *Proceedings of the 13th World Congress on Advances in Structural Engineering and Mechanics*, Jeju, Korea (2013b).

[39] ICC. *AC156 Acceptance criteria for seismic certification by shake-table testing of nonstructural components*. International Code Council Evaluation Service, Wihttier, CA (2010).

[40] Jovanović Đ, Žarković D, Vukobratović V, Brujić Z. "Hysteresis model for beam-to-column connections of steel storage racks". *Thin-Walled Structures* 142 (2019): pp. 189-204.

[41] Kehoe, BE and Freemand, SA. "A critique of procedures for calculating seismic design forces for nonstructural elements". *Proceedings of Seminar on*

Seismic Design, Retrofit, and Performance of Nonstructural Components, Applied Technology Council-29 (Vol. 1), California, USA (1998).

[42] Kehoe BE, Hachem M. "Procedures for estimating floor acceleration". *Proceedings of Seminar on Seismic Design, Performance, and Retrofit of Nonstructural Components in Critical Facilities*, ATC 29-2, Newport Beach, CA (2003): pp. 361-374.

[43] Lin, J and Mahin, SA. "Seismic response of light subsystem on inelastic structures". *Journal of Structural Engineering* 111.2 (1985): pp. 400-417.

[44] Luo Y, Mosqueda G, Han Q, and Zhao Y. "Shaking table tests examining seismic response of suspended ceilings attached to large-span spatial structures". *Journal of Structural Engineering* 144.9 (2018).

[45] Maddaloni G, Ryu KP, and Reinhorn AM. "Simulation of floor response spectra in shake table experiments". Earthquake Engineering & Structural Dynamics 40.6 (2010): pp. 591-604.

[46] Magliulo G, Pentangelo V, Maddaloni G, Capozzi V, Petrone C, Lopez P, Talamonti R, and Manfredi G. "Shake table tests for seismic assessment of suspended continuous ceiliings". Bulletin of Earthquake Engineering 10.6 (2012): pp. 1819-1832.

[47] Matsuoka, Y, Suita, K, Yamada, S, Shimada, Y, and Akazawa, M. "Nonstructural component performance in 4-story frame tested to collapse". *Proceedings of the 14th World Conference on Earthquake Engineering,* Beijing, China (2008).

[48] McCormick J, Matsuoka Y, Pan P, and Nakashima M. "Evaluation of non-structural partition walls and suspended ceiling systmes through a shake table study". *Structures Congress*, Vancouver, Bristish Columbia, Canada (2008):pp.1-10.

[49] Medina, RA, Sankaranarayanan, R, Kingston, KM. "Floor response spectra for light component mounted on regular moment-resisting frame structures". *Engineering Structures* 28 (2006): pp. 1927-1940.

[50] Minorski N. Non-linear mechanics. J.W. Edwards, Ann Arbor (1947).

[51] Miranda, E and Taghavi, S. " A comprehensive study of floor acceleration demands in multi-story buildings". *Proceedings of ATC&SEI Conference on Improving the Seismic Performance of Existing Buildings and Other Structures*, San Francisco California, December 8-11 (2009).

[52] Monir HS, Zeynali K. "A modified friction damper for diagonal bracing of structures". *Journal of Constructional Steel Research* 87 (2013): pp. 17-30.

[53] Motoyui S, Sato Y. "Numerical analysis for damage behavior of ceiling during earthquake". *The 63rd National Congress of Theoretical & Applied Mechanics* (2014) (in Japanese).

[54] Mualla IH, Belev B. "Performance of steel frames with a new friction damper device under earhtuqake excitation". *Engineering Structures* 24.3 (2002): pp. 365-371.

[55] Newmark NM, Hall WJ. "*Earthquake spectra and design*". EERI Monograph, Earthquake Engineering Research Institute, Berkeley, CA (1982).

[56] Ng, C-L, Xu Y-L. "Seismic response control of a building complex utilizing passive friction damper: Experimental investigation". Earthquake Engineering & Structural Dynamics 35.6 (2006): pp. 657-677.

[57] Niousha A."Invetigation on the vertical vibration characteristics of actual structure for earthquake observation records and impactor test". *Architectural Institute of Japan* 62 (1999): pp. 463-466.

[58] NIST. *Seismic Analysis, Design, and Installation of Nonstructural Components and Systems – Background and Recommendations for Future*

Work, NIST GCR 17-917-44. National Institute of Standards and Technology (2017).

[59] NIST. *Recommendations for improved seismic performance of nonstructural components, NIST GCR 18-917-43*. National Institute of Standards and Technology (2018).

[60] Oropeza, M, Favez, P, and Lestuzzi, P. "Seismic response of nonstructural components in case of nonlinear structures based on floor response spectra method". *Bulletin of Earthquake Engineering* 8.2 (2010): pp. 387-400.

[61] Pantoli E, Chen MC, Wang, X, Astroza R, Ebrahiman H, Hutchinson TC, Conte JP, Restrepo JI, Marin C, Walsh KD, Bachman RE, Hoehler MS, Englekirk R, Faghihi M. "Full-scale structural and nonstructural building system performance during earthquake: Part II – NCS damage states". *Earthquake Spectra* 32.2 (2016): pp. 771-794.

[62] Petrone C, Magliulo G, Lopez P, and Manfredi G. "Out-of-plane seismic performance of plasterboard partition walls via quasi-static test". Bulletin of the New Zealand Society for Earthquake Engineering 49.1 (2016): pp. 125-137.

[63] Politopoulos I, and Feau C. "Some aspects of floor of 1DOF nonlinear primary structures". *Earthquake Enigneering & Structural Dynamics* 26.8 (2007): pp. 975-993.

[64] Pourali A, Dhakal RP, MacRae G, and Tasligedik AS. "Fully floating suspended ceiling system: Experimental evaluation of structural feasibility and challenges". *Earthquake Spectra* 33.4 (2017): pp. 1627-1654.

[65] Qi L, Kunitomo K, Kurata M, and Ikeda Y. "Investigating the vibration properties of integrated ceiling systems considering interactions with surrounding equipment". *Earthquake Engineering & Structural Dynamics* 49 (2020).

[66] Qi L, Kurata M, Ikeda Y, Kunitomo K, and Takaoka M. "Seismic evaluation of two-elevation ceiling system by shake table test". *Earhtquake Engineering & Structural Dynamics* 50.4 (2021): pp. 1147-1166.

[67] Rahmanishamsi E, Soroushian S, and Maragakis EM. "Analytical model for the in-plane seismic performance of cold-formed steel-framed gypsum partition walls". Earthquake Spectra 33.4 (2017): pp. 1627-1654.

[68] Rihal SS, and Granneman G. *Experimental investigation of the dynamic behavior of building partitions and suspended ceilings during earthquakes*. Rep. ARCE R84-1. California Polytechnic State University, Pomana (1984).

[69] Rodriguez ME, Restrepo JI, and Carr AJ. "Earthquake-induced floor horizontal acceleration in buildings". *Earthquake Engineering and Structural Dynamics* 31.3 (2002): pp. 693-718.

[70] Ryu KP and Reinhorn AM. "Experimental study of large area suspended ceilings". *Journal of Earthquake Engineering* 23.6 (2019a): pp. 1001-1032.

[71] Ryu KP and Reinhorn AM. "Analytical study of large-area suspended ceilings". *Journal of Earhtuqake Enginnering* 23.6 (2019b): pp. 592-624.

[72] Sato, E, Furukawa, S, Kakechi, A, and Nakashima, M. "Full-scale shaking table test for examination of safety and functionality of base-isolated medical facilities". *Earthquake Engineering & Structural Dynamics* 40 (2011): pp. 1435-1453.

[73] SEAOC, Vision 2000 Committee. *Performance based seismic engineering of buildings*. Report prepared by Structural Engineers Association of California (1995).

[74] SEAOC. *Recommended lateral force requirements and commentary, 7th edition*. Seismology Committee Structural Engineers Association of California, San Franciso, CA (1999).

[75] Shimizu K, Miki H, Yamada S. *Seismic design for improvement construction method of ceiling of existing stations*. Quarterly Report of Railway Technical Research Institute 58.4 (2018): pp. 275-280.

[76] Singh, MP, Moreschi, LM, Suárez, LE, Matheu, EE. "Seismic design forces. I: Rigid nonstructural components". *Journal of Structural Engineering* 132.10 (2006): pp. 1524-1532.

[77] Singh, MP, Moreschi, LM, Suárez, LE, Matheu, EE. "Seismic design forces. II: Flexible nonstructural components". *Journal of Structural Engineering* 132.10 (2006): pp. 1533-1542.

[78] Singh M, Suarez L. "Seismic response analysis of structure-equipment systems with non-classical damping effects". *Earthquake Engineering and Structural Dynamics* 15.7 (1987): pp. 871-888.

[79] Somerville P, Smith N, Punyamurthula S, Sun J. *Development of ground motion time histories for phase 2 of the FEMA/SAC steel project SAC Background Document*. Report No. 1997 SAC/BD097/04 (1997).

[80] Soroushian S, Maragakis M, Jenkins C. "Capacity evaluation of suspended ceiling component, Part 1: Experimental Studies". *Journal of Earthquake Engineering* 19 (2015a).

[81] Soroushian S, Maragakis M, Jenkins C. "Capacity evaluation of suspended ceiling component, Part 2: Analyical Studies". *Journal of Earthquake Engineering* 19 (2015b).

[82] Soroushian S, Maragakis M, Jenkins C. "Capacity evaluation of suspended ceiling-perimeter attachments". *Journal of Structural Engineering* 142.2 (2015c).

[83] Soroushian S, Maragakis M, Jenkins C. "Axial capacity evaluation for typical suspended ceiling joints". *Earthquake Spectra* 32.1 (2016a): pp. 547-565.

[84] Soroushian S, Maragakis EM, Ryan KL, Sasaki T, Okazaki T, Mosqueda G. "Seismic simulation of an integrated ceiling-partition wall-piping system at E-Defense. II: Evaluation of nonstructural damage and fragilities". *Journal of Structural Engineering* 142.2 (2016b).

[85] Soroushian S, Maragakis M, Zaghi AE, Rahmanishamsi E, Itani AM, Pekcan G. "Response of a 2-story test-bed structure for the seismic evaluation of nonstructural systems". *Earthquake Engineering and Engineering Vibration* 15.1 (2016c): pp. 19-29.

[86] Soroushian S, Rahmanishamsi E, Jenkins C, and Maragakis EM. "Fragility analysis of suspended ceiling systems in a full-scale experiment". *Journal of Structural Engineering* 145.4 (2019).

[87] Sullivan, T, Calvi, P, Nascimbene, R. "Toward improved floor spectra estimates for seismic design". *Earthquake Spectra* 4.1 (2013): pp. 109-132.

[88] Surana, M, Pisode, M, Singh, Y, Lang, DH. "Effect of URM infills on inelastic floor respoonse of RC frame buildings". *Engineering Structures* 175 (2018): pp. 861-878.

[89] Villaverde R. "Seismic design of secondary structures: State of the art". *Journal of Structural Engineering* 123.8 (1997): pp. 1011-1019.

[90] Vukobratović, V and Fajfar, P. "A method for the indirect estimation of floor acceleration spectra for elastic and inelastic MDOF structures". *Earthquake Engineering & Structural Dynamics* 45.15 (2016): pp. 2495-2511.

[91] Wieser J, Pekcan G, Zaghi AE, Itani A, Maragakis M. "Floor accelerations in yiedling special moment resisting frame structures". *Earthquake Spectra* 29.3 (2013): pp. 987-1002.

[92] Yao GC. "Seismic performance of direct hung suspended ceiling systems". *Journal of Architectural Engineering* 6.1 (2000): pp. 6-11.

[93] Zaghi AE, Soroushian S, Echevarria AA, Maragakis EM, Bagtzoglou A. "Development and Validation of a Numerical Model for Suspended-Ceiling Systems with Acoustic Tiles". *Journal of Architectural Engineering* 22.3 (2016).

Abstract (in Korean)

최근 국내외 지진에서 발생한 비구조요소의 지진 피해는 막대한 경제적 손실을 야기하였으며, 건축물의 내진성능 확보에 있어 비구조요소 내진설계의 중요성을 명백히 보여주었다. 본 연구는 대표적 지진취약 비구조요소인 천장시스템에 대한 내진성능평가와 효과적인 내진시스템 개발을 위해 실대형 진동대 실험을 수행하였으며, 천장시스템에 작용하는 층운동(floor motion)에 대한 분석을 통해 설계법 및 절차를 제안하였다.

본 논문에서는 비구조요소에 작용하는 지진력의 특성을 분석하고자 최대 층응답가속도와 최대 비구조요소가속도에 영향을 미치는 주요 변수에 대한 연구를 수행하였다. 3차원 구조해석 모델을 활용한 선형 및 비선형 시간이력해석을 통해 최대 층응답 및 비구조요소가속도에 영향을 미치는 주요 구조동특성에 대한 분석을 수행하였으며, 포괄적인 계측지진기록에 대한 분석을 바탕으로 현행 설계기준에서 제안하는 등가정적설계하중의 한계를 분석하였다. 또한, 실대형 2층 철골구조물을 활용한 진동대 실험을 통해서 구조물과 비구조요소의 비선형거동이 층응답스펙트럼에 미치는 영향을 실험적으로 평가하였으며, 이를 통해 구조물의 연성도와 최대 층응답가속도 감소 간의 관계, 비구조요소의 핀칭(pinching) 이력거동이 최대 비구조요소가속도에 미치는 영향을 분석하였다.

본 연구에서는 다수의 천장실험체에 대한 진동대 실험을 수행하여 천장시스템의 파괴 메커니즘에 대한 규명 및 가속도 증폭, 고유진동수 및 임계감쇠비 등의 주요 설계 변수를 분석하였다. 본 실험에서는 직·간접 현수 천장시스템을 포괄하는 다양한 시스템에 대한 연구가 수행되었으며, 간접 현수 시스템에 대해서는 고유진동수를 예측할 수 있는 단자유도 해석모델을 제시하였다. 또한, 각 축에 대해 서로 다른

내진성능을 갖는 부착식 천장시스템의 거동특성을 규명하였으며, 칸막이벽 및 스프링클러 등을 활용한 시스템 규모의 천장실험체를 구축하여 천장의 내진성능에 영향을 미칠 수 있는 비구조요소 간 상호작용을 실험적으로 평가하였다.

본 연구에서는 천장시스템에 대해 새로운 두 가지 내진보강방법을 제안하였다. 이에 앞서, 현행 내진설계기준에서 제시하는 상세를 적용한 가새천장에 대한 실험을 수행하였으며, 천장프레임의 낮은 면내강성으로 인해 가새가 제공하는 거동 구속 효과가 제한적으로 발현되는 문제점을 확인하였다. 이를 보완하기 위하여 그리드(grid) 보강재를 적용한 가새천장시스템을 제안하였으며, 보강재가 천장프레임의 면내강성을 증대시킴으로써 전반적인 내진성능을 효과적으로 향상시킬 수 있음을 확인하였다. 또한, 비용효과적인 회전형 마찰 메커니즘을 도입한 마찰감쇠 천장시스템을 제안하였다. 제안된 시스템의 안정적 이력거동을 실험을 통해 검증하였으며, 마찰 감쇠장치의 우수한 에너지 소산능력을 활용하여 효과적으로 내진성능을 향상시킬 수 있음을 확인하였다. 비내진 천장시스템의 진자 거동을 활용한 마찰천장시스템에 대한 비선형 단자유도 해석모델을 제안하였으며, 철골프레임의 시각력해석을 통해 얻은 다양한 층운동을 기반으로 마찰천장에 대한 방대한 비선형해석을 수행하여 실제 구조물에 대해서도 충분히 적용 가능하며 만족할 만한 내진성능을 기대할 수 있음을 확인하였다. 구조물에 설치된 비선형 마찰천장의 정상상태응답을 시스템 등가선형화를 통해 분석하였으며, 마찰천장의 거동에 미치는 주요 영향 변수를 분석하였다. 마지막으로, 제안된 비선형 단자유도 모델과 주요 영향 인자들에 대한 분석결과를 활용하여 마찰천장시스템에 대한 설계 절차를 정립하였다.

주요어: 비구조요소, 천장시스템, 실대형 진동대 실험, 비구조요소 설계하중, 층응답스펙트럼, 마찰감쇠, 수치해석.

학번: 2018-32061